MICROSEISMICITY, FAULT STRUCTURE, & THE SEISMIC CYCLE: INSIGHTS FROM LABORATORY STICK-SLIP EXPERIMENTS

by

Thomas H. W. Göbel

A Dissertation Presented to the
FACULTY OF THE USC GRADUATE SCHOOL
UNIVERSITY OF SOUTHERN CALIFORNIA
In Partial Fulfillment of the
Requirements for the Degree
DOCTOR OF PHILOSOPHY
(GEOLOGICAL SCIENCES)

August 2013

We know truth, not only by reason, but also by the heart.

– Blaise Pascal –

There are problems to whose solution I would attach an infinitely greater importance than to those of mathematics, for example touching ethics, or our relation to God, or concerning our destiny and our future; but their solution lies wholly beyond us and completely outside the province of science.

– Carl Friedrich Gauss –

This dissertation is dedicated to my brother, Matthias Göbel. Thank you for your companionship on this quest – not beyond good and evil but surprised by joy.

Acknowledgments

The present work grew through the continuous support, and guidance of many people. My advisers Thorsten Becker and Charlie Sammis have provided invaluable guidance and mentorship throughout my research. Thorsten represents an example of steadfast scientific integrity, as well as the measure of hard work and quality commonly required to make meaningful scientific contributions. Thank you for everything. I thank Charlie for fostering my understanding of fractals, friction, fracture mechanics and in general "how things break". His humor, enthusiasm and encouraging words helped me to navigate through some strong headwinds. I am also indebted to Danijel Schorlemmer for his support during the preparation for my qualifying exam, the writing of our first paper, and introducing me to "the Pantry". The scope of the current research was broadened through the input of many USC faculty. Yehuda Ben-Zion, who stirred my interest in earthquake seismology, helped me tremendously in formulating testable hypotheses. I thank John Platt for his help with fault structure analyses, and Meghan Miller for her contribution to the seismological analysis. I would like to thank my committee members Amy Rechenmacher, Fred Aminzadeh, and Steven Nutt for their comments and invested time.

At the Earth Science department, I met some of the most colorful characters, which made gray days in our cubicles a lot brighter, and I am left with unforgettable memories. Many of my fellow graduate students became friends over the years, and it was a pleasure to share the joy of discovery as well as the hard-work during the pursuit of our degree. For all of this, I want to thank Melanie, Feng, Esther, Michael, Adam, Antoine, Shiqing, Amir, Attreyee, Rachel, Plamen, Whitney, Christiann, Jessica, Yaman, Jason, Zach, Iain, Lisa, Zi-Yu, Dao, and Dimitry. I also want to express my gratitude to the USC Earth Science staff, especially, John-Yu, John McRaney and Cindy Waite who relentlessly work to support students and faculty.

During my PhD years, I had the opportunity to spend many months conducting research in Germany. Most of the presented results are based on experiments that I conducted at GFZ-Potsdam in the Summers of 2009, 2011, 2012 and Fall 2010. While my trips to Germany were exceedingly productive in many ways, they also introduced a new level of stree on granite samples and on myself. For example, when I found out I should spend a semester at GFZ and had about two weeks to prepare. I would like to acknowledge the state-of-the-art experimental facilities of the rock mechanics lab at GFZ (Section 3.2). Much of the laboratory equipment was developed by

Sergei Stanchits, Arno Zang and Christian Wagner. Without their amazing, ground-breaking work, none of my experiments would have been possible. For valuable discussions, and greatly enhancing my understanding of the rock-mechanics micro-cosmos, I want to thank Georg Dresen. His ceaseless excitement about new projects was a strong motivation during the experimental series. Furthermore, I want to thank Gzergorz Kwiatek, Michael Nauman, Tobias Meier, Hiroki Sone, Erik Rybacki, Christoph Janssen, and Elma Charalampidou for strong technical and scientific support. The utilized samples were prepared by Matthias Kreplin and Stefan Gehrmann, and I want to thank Stefan for sharing his broad range of expertise from gardening and stock trading to earthquake physics during the many hours spend in the lab. Another highlight of my time at GFZ was of course the communal enjoyment of homemade cakes and pies for birthdays (or other appropriate excuses). I think this tradition should be adopted by any major research institution.

I want to express my gratitude to Jeremy Zechar who hosted me during a visit to ETH and with whom I worked on different projects over the years. His supportive mind set and positive criticism made my work at ETH productive and very enjoyable. I also want to thank Stefan Wiemer, Thessa Tormann, Markus, Matteo Spada, Jochen Woessner, Alba Zappone, and Phil Benson for animated discussions and collaborations during my time at ETH. During different conferences and visits to Lamont Daugherty Earth Observatory and Caltech, my work was enriched by conversations with Heather Savage, Paul Richardson, Peter Shearer, Egill Hauksson, and Felix Waldhauser. I want to thank Francis Su for his lecture on grace and his paper on teaching research (`http://www.math.hmc.edu/~su/`), which show where to find life even within the apparently inanimate realms of science.

My research was supported by the Southern Californian Earthquake Center, GFZ-Potsdam, a ThinkSwiss research fellowship, and a research grant of the Department of Earth Sciences at USC.

Lastly, I would like to include some personal remarks. I am deeply indebted to my entire family for their amazing support, which was a great source of strength throughout the years. Moreover, I want to thank Bob, Art and Chad for their mentorship. Much of the positive developments in my character, I owe to them and their invested time and prayer. On a related note, I want to thank Rankin Wilbourne, Francis Chan, Clark Peddicord, and Dallas Willard for providing spiritual nourishment. I also want to thank Jeff Still for stimulating breakfast-conversations before dawn. My life experienced a pervasive change through the exceedingly pleasant company of Juanita Rose. She is one of the greatest examples for a spirit-filled life, and I am thankful for every minute we

are allowed to spend together. I am extraordinary grateful for my fellow companions on this PhD journey: Micheal, Hsiang-Ling, Melanie and Felicity, and all the other amazing friends I was allowed to meet over the years: Solomon, Sheralyn, Ben Lah, Michele Schulker, Griffin, Johnny, Celia, Sheryl, Sam Daewong the mighty Bruin, Cheri, Leslie, Jocelyn, Winnie, Sammy, all the guys from the new and old 25th house, as well as from the OM-house in Schwammendingen, and Haus Nazareth in Berlin and my American family, the Thompsons. Most importantly, I thank God for his grace, purpose and vision that lead to lasting joy.

Contents

Abstract

The deformation along tectonic plate boundaries is associated with the storage and release of elastic energy. The abrupt release of strain energy results in seismic energy emission during fault slip, i.e., earthquake ruptures. The dynamics of these earthquakes, including the nucleation, propagation and arrest of ruptures, is closely tied to local fault zone properties. However, the details of how fault zone properties influence small and large earthquakes is insufficiently understood, partially due to limited observations of fault zone structure at seismogenic depths, and necessarily incomplete seismic catalogs. Here, we investigate the connection between micro-seismicity, and variations in fault stress and structure during series of stick-slip experiments on structurally-complex fault zones generated in natural granite samples. Within the present experimental series, we strove to mimic the natural faulting process by creating series of stick-slip events under seismogenic stress conditions on complex faults. Throughout the experiments, we monitored variations in stress, strain, and seismic activity. The latter was compared to post-experimental micro-structure of faults observed in computer tomography images and thin sections. Our laboratory-created faults exhibited many of the structural hallmarks of faults in nature. Moreover, the observed seismic event distributions show many similarities to natural seismicity, including Omori-Utsu type aftershock decays, Gutenberg-Richter frequency magnitude distributions, power-law off-fault activity decays, and fractal hypocenter distributions. The spatial and temporal variations in seismic event distributions in our experiments can be explained through variations in fault structure and stress. At high stresses and in the proximity to fault asperity regions, micro-seismic events tend to cluster, and show low b-values as well as high seismic moment release. Furthermore, our laboratory experiments provide insight into the creation of off-fault damage and resulting variations in micro-seismicity distributions. The off-fault micro-seismic events decay as a power-law at larger fault-normal distance with an exponent that is connected to fault roughness and normal stress. Our laboratory faults showed rapid structural evolution toward less complexity, however, evolutionary processes were predominantly limited to initial seismic cycles. Our results emphasize that small seismic events contain essential information about fault properties, e.g., roughness, structural heterogeneity and stress level, which in turn may control the dynamics of large earthquakes. A detailed analysis of micro-seismicity statistics and inferred fault properties therefore have the potential to significantly advance the seismic hazard assessment of active tectonic regions.

1 Introduction

Understanding seismic cycles, fault structures and stresses are fundamental problems in earthquake seismology and lithospheric dynamics. Faults are complex zones of strain accumulation, which accommodate the motion of tectonic plates in the upper 10s of kilometers of the Earth's crust. The stress distribution and structure of faults is generally heterogeneous, which is expressed in a complex distribution of seismic events in space, time and magnitude. Changes in seismic event statistics, e.g., Gutenberg-Richter b-values provide insights into local stress variations (Schorlemmer et al., 2005). However, a direct comparison between absolute fault stresses and seismic event distributions is complicated by the lack of observations at seismogenic depths. Similarly, the influence of fault structure on seismic event distributions is hard to assess in nature. Fault structural changes are commonly only observable under exhumed conditions far away from the actual seismic activity.

To study fault stresses and structure under *in situ* conditions and to understand their relationship to seismic event distributions, we conducted stick-slip experiments on complex, laboratory-created fault zones. Our experiments enabled us to connect fault structure observed in post-experimental CT-scans, applied stresses and acoustic emission statistics recorded during the experiments. Our earthquake analog experiments facilitate the documentation of stress, strain and seismic energy release over several seismic cycles, which cannot readily be done in nature.

Despite the apparent difference in scale, there are several interesting observations that make our acoustic emission (AE) studies important for the understanding of natural seismicity. For example, our results further highlight similarities between the statistics of AE events and natural micro-seismicity, as well as the structure of laboratory created and natural fault zones. Moreover, a recent study showed that the statistics of small, induced earthquakes, namely Gutenberg-Richter distributions and source scaling relations, are consistent with natural seismicity over a range of magnitudes from $M = -0.8$ to $M = -4.1$ (Kwiatek et al., 2010, 2011). The lower end of this magnitude range is on the order of laboratory stick-slip events. Gutenberg-Richter type frequency-magnitude distributions have been observed repeatedly for AEs in laboratory experiments (e.g. Scholz, 1968; Weeks et al., 1978; Amitrano, 2003; Goebel et al., 2012). Moreover, the scale invariance between seismic moment and corner frequency of micro-seismic events was confirmed in the laboratory during tests on dry rocks (Harrington and Benson, 2011). The sum of these

results suggests a similarity of physical processes involved in the creation of laboratory, induced and natural microseismicity.

In nature, fault slip and resulting seismic energy release can occur at a broad spectrum of velocities and magnitudes from slow slip events to large, destructive earthquakes (Peng and Gomberg, 2010). The arguably most studied slip events are large earthquakes with significant societal impact. However, large earthquakes are rare consequently they provide limited insight into the faulting process. Small earthquakes or microseismicity, on the other hand, occur frequently and can provide vital information about tectonic loading rates and static stress changes. Seismicity studies, e.g., of the densely instrumented Parkfield section of the San Andreas Fault, revealed the locations of fault asperities and stress variations over several seismic cycles (e.g. Malin et al., 1989; Wiemer and Wyss, 1997; Schorlemmer and Wiemer, 2005; Tormann et al., 2012), and provide valuable information about the deformation history and evolution of faults.

1.1 Fault zone structure and evolution

A better understanding of the interaction between earthquake dynamics and fault structure is vital for the estimation of likely sites and sizes of earthquakes. It is generally accepted that fault zones can only partially be described by planar, frictional interfaces and should rather be considered as complex zones of deformation (Figure 1.1). This complexity controls both fluid flow behavior and mechanical properties of faults. The structure of natural fault zones can conceptually be described by a fault core surrounded by a zone of distributed damage (e.g. Caine et al., 1996; Ben-Zion and Sammis, 2003). Fault cores contain a gouge layer, anastomosing principal and secondary zones of slip localization; and the damage zone consists of joints, pulverized rock and subsidiary faults over a wide range of length scales (e.g. Chester and Logan, 1986; Chester et al., 1993; Dor et al., 2006; Wibberley et al., 2008).

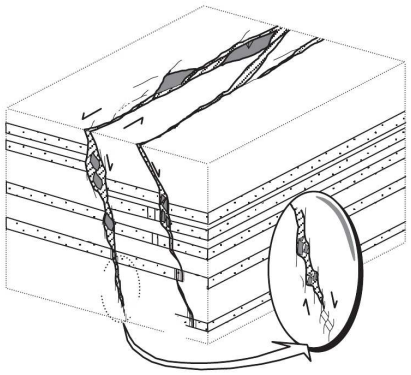

Figure 1.1: Schematic of fault zone complexity and fault growth mechanism (modified after Wibberley et al. (2008)). The inset shows the possibility for fault growth at the down-dip end.

Recent studies extended this simple model, suggesting that fault zones may consist of multi-

ple anastomosing fault cores that branch and re-connect, entraining blocks of fractured protolith (Faulkner et al., 2003, 2010). Consequently, fault structure varies substantially and shows a large dependence on protolith composition (e.g. Schulz and Evans, 2000; Faulkner et al., 2003). Current models of fault zone structure suggest that faults become less complex with larger displacements so that most of the slip on mature faults occurs within zones of highly localized strain (Chester et al., 1993; Ben-Zion and Sammis, 2003; Rockwell and Ben-Zion, 2007). This is supported by geologic observations of mature faults in Southern California (Chester and Chester, 1998) and a recent study based on across-fault seismicity distributions, which suggested that faults become progressively smoother even after they accumulated more than 100 km of slip (Powers and Jordan, 2010). Other studies, however, which examined the roughness of exhumed fault surfaces showed that large off-set faults remain in a state of consistent complexity (Sagy et al., 2007; Candela et al., 2012), possibly due to decreasing rates of abrasional smoothing caused by gouge lubrication (Brodsky et al., 2011) and rupture related fault re-roughening (Bhat et al., 2004; Klinger, 2010). At this point, the apparent conflict between seismicity data and fault roughness measurements has not been resolved.

The evolution as well as the structural and compositional heterogeneity of faults has seismogenic consequences. Recent results (e.g. Hori et al., 2004; Barbot et al., 2012; Noda and Lapusta, 2013) have shown that the distribution of fault patches that favor unstable (velocity-weakening) over stable (velocity-strengthening) slip along faults strongly influence earthquake distributions and the overall slip behavior of a fault. Earthquake ruptures and slip are, in addition to compositional heterogeneity, controlled by geometric heterogeneity of fault systems. The geometry of systems of faults controls local earthquake interactions and seismicity clustering (e.g. Ward, 2000; Rundle et al., 2004; Dieterich and Richards-Dinger, 2010). Models that include fault-system-induced interactions of earthquakes can produce seismicity characteristics similar to regional observations and replicate observed statistical relations, including aftershock clustering of natural seismicity (e.g. Ward, 2000; Rundle et al., 2004; Dieterich and Richards-Dinger, 2010). Consequently, a more detailed understanding of fault architecture and connected seismic event distributions is essential for seismic hazard assessment.

1.2 The role of acoustic emission studies in documenting fault structure

In most cases, fault structure can only be observed on inactive, exhumed fault branches and its connection to seismicity distributions cannot readily be studied in nature. Consequently, many seismicity studies have drawn from laboratory results to understand seismicity variations and their underlying mechanisms (Main et al., 1989; Wyss and Wiemer, 2000; Schorlemmer et al., 2005; Sobiesiak et al., 2007; Narteau et al., 2009). Laboratory studies highlight the influence of fault (Goebel et al., 2012) and material heterogeneity (Mogi, 1962), as well as applied stress (Scholz, 1968; Amitrano, 2003; Goebel et al., 2013d) on frequency-magnitude distributions of micro-seismic events. In the laboratory, seismic energy is predominantly radiated in form of high-frequency acoustic emissions (AEs) during micro-cracking and micro-slip. AEs mark distinct prefailure stages, that are connected to the redistribution of micro-crack activity during rupture nucleation (e.g. Lockner et al., 1991a). AE events initially occur distributed throughout the sample and then start to localize at the point of rupture nucleation and maximum stress (Lockner et al., 1991b). Prior to peak stresses, a general increase in AE rate and decrease in b-value is observed, which leads up to sample failure (e.g. Main et al., 1989; Meredith et al., 1990), and is explained by the growth and coalescence of the pre-existing micro-crack population (Main et al., 1992). AE events during stick-slip motion on rough fracture surfaces can be used to identify points of fault branching and increased geometric complexity (Thompson et al., 2009). Furthermore, AEs document micro-processes before stick-slip events (Weeks et al., 1978; Thompson et al., 2005; Goebel et al., 2012), a laboratory-analog for earthquakes (Brace and Byerlee, 1966; Byerlee, 1970). The following section elucidates conditions that lead to the creation of slip instability during laboratory experiments.

1.3 Mechanics of stick-slip

Stick-slip motion on interfaces is observed for a range of materials and conditions. It received special attention because of the suggestion that stick-slip motion on rock interfaces can serve as an analog for earthquake behavior (Brace and Byerlee, 1966). Brace & Byerlee suggested that the repeated accumulation of strain and successive release during earthquakes can be simulated by loading pre-cut or fractured rock surfaces resulting in series of laboratory stick-slip events. At high confining pressures, these surfaces are largely locked during stress increase and subsequently slip coinciding with an abrupt release of the stored stress. These slip events are connected to the

radiation of seismic energy and the formation of fault gouge (e.g. Weeks et al., 1978; Byerlee, 1970). Details about role of stick-slip experiments as earthquake analogs, and the conditions that favor slip instability over stable sliding are described in the following sections.

1.3.1 Controls on the occurrence of slip instability in frictional sliding experiments

In the laboratory, stick-slip can be considered an instability problem. For a simple frictional system, e.g., a slider-spring system, slip commences when the elastic forces exerted by the spring exceed the static friction along the interface of slider and the surface beneath. The occurrence of slip instability is due to a difference in static and kinetic friction, i.e., once the block starts to slide the friction drops suddenly to a lower level (Byerlee, 1970). The force in the spring is now greater than the force required for the block to maintain sliding, thus the system becomes unstable and the slider accelerates.

The frictional behavior of an artificial fault (saw-cut or fracture surface) is controlled by the frictional properties of the interface and the elastic properties of loading frame and sample. During triaxial compression tests, slip instability occurs when the decrease of frictional strength with displacement exceeds the rate of stress decrease which is controlled by the machine stiffness. The displacement over which the friction decreases from its static to dynamic value is given by the slip weakening distance, D_c. The transition from stable to unstable sliding is reached when the unloading rate, K, equals the strength decrease, $\Delta\tau$, over D_c (Dietrich, 1978). Thus, for stick-slip to occur the following inequality has to be satisfied:

$$K < \Delta\tau / D_c. \tag{1.1}$$

$\Delta\tau$ is connected to the decrease in friction $\Delta\mu$:

$$\Delta\tau = \Delta\mu\sigma_n, \tag{1.2}$$

where σ_n is the normal stress. The normal stress at the transition from stable to unstable sliding ($K = \Delta\tau / D_c$) is linearly related to the stiffness constant (K):

$$\sigma_n = \frac{D_c}{\Delta\mu} K. \tag{1.3}$$

This linear scaling of normal stress and machine stiffness at the transition from stable to unstable sliding was confirmed by experiments on granite samples (Dietrich, 1978). The magnitude of the decrease in friction is a function of surface properties, sliding velocity and time of contact.

An example for the formulation of a friction law that describes the decrease in friction due to a change in sliding velocity can be found in Dietrich (1978):

$$\Delta\mu = A\left(\log(Bt+1) - \log(B\frac{D_c}{V_l}+1)\right), \tag{1.4}$$

where t denotes the contact time, V_l is the loading velocity and A and B are constants with values of approximately 0.01–0.02, and 1.0–2.0, respectively (Dieterich, 1979). This version of the rate-and-state friction law highlights the initial increase in frictional resistance as function of logarithm of contact time and the final steady state friction as function of the new sliding velocity (V_l). To describe experimental observations, another formulation of the friction law (Dieterich-Ruina law) is commonly used (e.g. Ruina, 1983; Dieterich and Kilgore, 1994; Scholz, 1998):

$$\Delta\mu = a\ln\left(\frac{V}{V_0}\right) + b\ln\left(\frac{V_0\theta}{D_c}\right), \tag{1.5}$$

where V is slip velocity, V_0 is a reference velocity, and a and b are material dependent constants characterizing the degree of velocity strengthening or weakening due to changes in sliding velocity. The state variable, θ, evolves according to:

$$\frac{d\theta}{dt} = 1 - \frac{\theta V}{D_c}. \tag{1.6}$$

A requirement for slip instability to occur is that friction decreases due to a velocity step (velocity weakening) (e.g. Ruina, 1983; Dieterich and Kilgore, 1994). In that case, even an initially, stable-sliding surface can create stick-slip events if perturbed by a velocity increase that results in a drop in friction over D_c that exceeds the unloading stiffness of the system. The influence of contact time on initial frictional resistance was observed during asperity indentation tests confirming an increase with the logarithm of time (Engelder and Scholz, 1976).

Additionally surface roughness influences slip stability, i.e., rougher faults are generally observed to have larger D_c values than smoother fault (e.g. Dieterich, 1979; Okubo and Dieterich, 1984) so that the transition from stable to unstable sliding would occur at higher normal stresses.

1.3.2 Micro-processes during the initiation of stick-slip

Several processes were suggested to be active on a micro-scale during the initiation of stick-slip. Asperity indentation tests revealed a relationship between static friction and asperity hardness (Engelder and Scholz, 1976). The authors suggest that stick-slip was generally connected to brittle fracture of asperities which may result in the creation of distinct wear-grooves in case of sufficient hardness contrasts between asperity and the sliding surface (Engelder, 1974). Similarly, brittle asperity fracture was suggested to play a key role at the point of initiation of stick-slip for frictional sliding tests on granite surfaces (Byerlee, 1970), which generally produces a substantial amount of gouge. The generation of gouge is an indicator of asperity fracture but it does not provide evidence if these fracture processes are predominately active before, at the initiation or during stick-slip. Another important micro-scale process is asperity shear which leads to a detachment of junctions by overcoming adhesive forces, asperity ploughing and time-dependent asperity-creep (Engelder, 1974; Dietrich, 1978). A recent work showed the merit of AE studies in distinguishing the micro-processes that are active during stick-slip initiation (McLaskey and Glaser, 2011). The authors showed that both asperity shear and fracture are active during the initiation of stick-slip. Brittle rock samples with relatively higher asperity hardness exhibit brittle fracture of asperities whereas softer materials (e.g. synthetic polymers like acrylic glass) create stick-slip events at comparably low normal stress by shearing the points of contact between planar surfaces. This type of asperity failure creates micro-seismic events with predominant double-couple source mechanism similar to natural earthquakes.

In both laboratory and nature, the occurrence of slip-instability is not only sensitive to fault zone composition but also to gouge content. The composition, thickness and consolidation level of the gouge layer has a direct influence on the frictional stability of surfaces and the critical slip weakening distance (e.g. Dietrich, 1978; Marone et al., 1990; Marone and Kilgore, 1993; Saffer and Marone, 2003). Quartz rich granite powders, for example, exhibit velocity weakening which favors slip instability (e.g. Green and Marone, 2002) whereas phyllosilicates exhibit velocity strengthening which supports stable sliding (e.g. Moore and Lockner, 2004; Moore and Rymer, 2007; Faulkner et al., 2011).

1.3.3 Summary of controlling parameters of stick-slip

The occurrence of slip instability is controlled by material properties, loading conditions and the machine stiffness which supplies elastic energy to a propagating rupture (e.g. Byerlee and Brace, 1968; Dietrich, 1978; Lockner and Beeler, 2002). In nature, elastic energy is stored in the surrounding lithology of a fault. A slip instability occurs if a nucleating rupture patch reduces a fault segment's strength faster than the driving stress is reduced (Byerlee, 1970; Dieterich, 1979; Lockner and Beeler, 2002).

Following parameters influence slip stability and favor stick-slip type fault motion in lab-experiments:

1. high normal stress
2. low combined stiffness of sample and loading apparatus
3. large fault topography or roughness
4. long contact times due to slow loading rates or artificial hold times
5. fast loading rates which result in higher reduction in friction

As can be seen from this list, constant loading rates influence frictional stability in two ways: First, slow loading rates effectively increase hold-times and the initial frictional resistance, thus working in favor of instability, and second, slow loading rates also decrease the drop in friction at the initiation of sliding, favoring stable sliding. Within the range of confining pressures (10s–100s of MPa) and strain rates (10^{-6}–10^{-4} s^{-1}) that are common during triaxial compression tests, machine stiffness, confining pressure and material properties seem to influence the slip characteristics substantially more than differences in loading rates (Byerlee and Brace, 1968).

1.4 Summary of Dissertation Chapters

The present work focuses on 4 different aspects of AE analysis during laboratory, frictional sliding experiments: (1) the connection between fault structure and variations in AE statistics, (2) the connection between fault stress and b-values, (3) the similarities between microseismicity and fault structure in the laboratory and nature, and lastly (4) the relationship between fault roughness, stress and off-fault seismicity distributions. In the following, we will give a brief summary of each of these points.

1. - Chapter 3: The first study tested if changes in b-value, seismic moment release and event-densities are connected to along-strike fault heterogeneity. Fault heterogeneity was identified and documented in post-experimental computer tomography images. AE event statistics were analyzed over series of stick-slips on structurally complex fault zones. Major asperity regions, i.e., areas of comparably small fault zone width, were connected to low b-values, increased AE event densities, and high moment release. These asperity regions played an important role in controlling the nucleation spots of dynamic slip events.

2. - Chapter 4: We examined the relationship between cyclical stress changes and temporal variations in micro-seismic event statistics. The basis of this study were series of stick-slip experiments on structurally complex faults. We observed repeating AE patterns, namely, increasing AE-rates and seismic moments as well as decreasing b-values before failure events. b-values and differential stress were linearly related throughout most of the seismic cycle, so that an increase in stress resulted in a general decrease in b-value. Furthermore, we observed an abrupt increase in b-value after slip events. The amount of b-value increase was indicative of the effectiveness of a slip event in reducing the stress level on the fault. Our results support a connection between b-value variations and stress but also highlight the influence of fault zone complexity which can mask stress-driven b-value variations.

3. - Chapter 5: Within the scope of this study, we investigated similarities of micro-seismic event statistics and fault structure in laboratory experiments and nature. Our laboratory-created faults showed many structural characteristics of upper crustal faults including a damage zone, and areas of localized slip embedded in a gouge layer. In addition to the structural similarities, we observed many parallels between AE events and natural seismicity. AE event statistics could be described by both the Gutenberg-Richter frequency-magnitude distribution and Omori-Utsu

aftershock decay. Moreover, our experiments support a connection between low b-value regions and locations of geometric fault asperities, providing a physical explanation for observations of seismicity anomalies within the Parkfield region of the San Andreas fault (e.g. Wiemer and Wyss, 1997). These results emphasize the importance of stick-slip experiments for a better understanding of fault structure.

4. - Chapter 6 We examined the connection between predefined fault roughness and microseismic event distributions, showing that the roughness of saw-cut surfaces can be inferred from the distribution of AE off-fault activity during laboratory frictional sliding experiments. The AE activity at increasing fault-normal distances could be described by a power law with an exponent that varied systematically for different roughness. The observed variations in off-fault activity exponents are connected to changes in contact size distributions and the spatial extent of stress perturbations. Moreover, the contact size distributions were also sensitive to the applied normal stress resulting in a negative, linear relationship between normal stress and seismic off-fault activity distributions for faults with the same initial roughness. In **Chapter 7**, we extended the results from saw-cut surfaces to more complex fault zones that developed from incipient, saw-cut-guided fracture surfaces. We observed a strong, initial fault smoothing over the first stick-slip events expressed by a rapid increase in the off-fault activity exponent. The seismic activity decay during latter stick-slips remained at largely constant values which were related to the fault normal stress within a particular experiment. These series of experiments highlighted that both fault roughness and fault stress strongly influence the decay of seismic activity at increasing fault normal distances.

Chapters 3–7 are published (Goebel et al., 2012, 2013d) or in the process of being published (Goebel et al., 2013a,b,c). They include a description of the relevant experiments, methods and scientific background, thus, are self-contained, and can be read as individual papers.

Chapter 8 discusses the present experiments in the context of recent results from mining induced seismicity studies. This chapter also examines the current findings in light of a theoretical, minimum size for tectonic earthquakes, and possible breaks in scaling relations of source parameters as well as frequency-magnitude distributions from the laboratory to crustal scales.

2 Experimental method & data

This chapter gives a brief overview over the experimental methods and the collected data. More extensive details about the relevant experiments can be found in the Method sections of individual Chapters. We designed out experiment to mimic conditions within the seismogenic crust, for example, high confining pressures and slow loading rates as well as the strain accumulation along structurally, complex fault zones.

2.1 Rock specimens, sample geometry and loading conditions

The here presented series of experiments were conducted on cylindrical Westerly granite specimens. Westerly granite exhibits grain sizes between 0.05–2.2 mm with an average grain size of 0.75 mm (Byerlee and Brace, 1968; Stesky, 1978). It is isotropic and consists of 28% quartz, 33% plagioglase, 33% K-feldspar, 5% mica (3.5% biotite, 1.9% muscovite) (Chayes, 1950a).

We report on experiments with three different initial sample geometries (Table 2.1). The first set of experiments was conducted on intact samples which were fractured and then reloaded to create stick-slip events. It will be referred to as fracture experiments or experiments on fractured surfaces in the following. The fracture of intact samples led to a range of different fault orientations including faults that started to nucleate from within the upper boundary surface. If the faults penetrated the upper boundary surface, commonly, no stick-slips could be created due to the vertical confinement of the loading piston.

A second type of geometry consisted of samples that contained saw-cut notches at a thirty degree angle to the loading axis (Figure 2.1a). These notches focused most of the deformation toward the center of the samples, while still enabling us to create rough surfaces with complex structure. For these experiments, we always observed stick-slip behavior after fault locking and subsequent re-loading. The length of the notches of the saw-cut guided fracture experiments was varied between 1.5 to 2.3 cm to test the influence of different surface areas on sliding characteristics. The connected fracture surface sizes decreased accordingly from 5–3.4 cm (Table 2.1). The notches resulted in $\sim$1 mm wide gaps which were closed by inserting low-friction teflon sheets.

The third and last type of initial geometries were samples with simple, continuous saw-cuts. The resulting planar surfaces were ground using different size silicon-carbide abrasives to create a spectrum of initial roughness. Depending on loading rates, hold-time, normal stresses, and

Experiment ID	d [mm]	h [mm]	l_{RS} [mm]	N_{SS}	Description
01,02	40	107	80	0–1	fracture surface
04,05,07,08	40	107	34–50	3–6	saw-cut guided fracture
09,10,12,15,16	50	100	0	0–7	continuous saw-cut

Table 2.1: Overview of experiments conducted using three different initial geometries. Experiment ID: Index used to differentiate the different experiments. Depending on the chapter these indices are preceded by 'WG', 'W' or 'WGRN' which indicate rock type and sample geometry. d: sample diameter, h: sample height, l_{RS}: length of rough, laboratory-created fracture-surface, N_{SS} - number of stick-slip events with large stress-drops.

roughness these experiments showed a spectrum of behavior from creep, to frictional sliding at constant stress as well as series of stick-slip events. These type of experiments were basis of the analysis in chapter 6. Within this chapter, the experiments IDs were modified to express different roughness and confining pressures of the corresponding experiments (e.g. HR-HP for high roughness and high pressure and LR-LP for low roughness and low pressure etc.)

All of the here described experiments were conducted under triaxial compression and at room temperatures. Prior to loading, the specimens were oven-dried for at least 24 hours. The fracture-surfaces in both intact and notched samples were created at a confining pressure of 75 MPa. The laboratory faults were locked by increasing the confining pressure to 120–150 MPa, which was followed by axial loading resulting in frictional sliding, creep or stick-slip. Rock fracture and frictional sliding were performed with a 4600 kN MTS servo-controlled loading frame in a 200 MPa pressure vessel (Figure 2.1c).

2.2 Data

Throughout the experiments, we monitored mechanical and seismic data. Axial stresses were measured at an external load cell providing a precise estimate (uncertainty between 4–6 MPa) of the applied stresses. An example of a loading curve of a typical stick-slip sequence can be found in Figure 2.2a. At the beginning of each interslip period the stress increases linearly, then progressively deviates from linearity closer to failure, and shows a spectrum of slip events with small and large stress drops.

Local strains were measured using small (1×1 cm), two-component strain gauges that were attached directly to the rock surface. Generally, the strain measurements show similar characteristics to the previously described loading curves, i.e., both linear and non-linear strain increase before

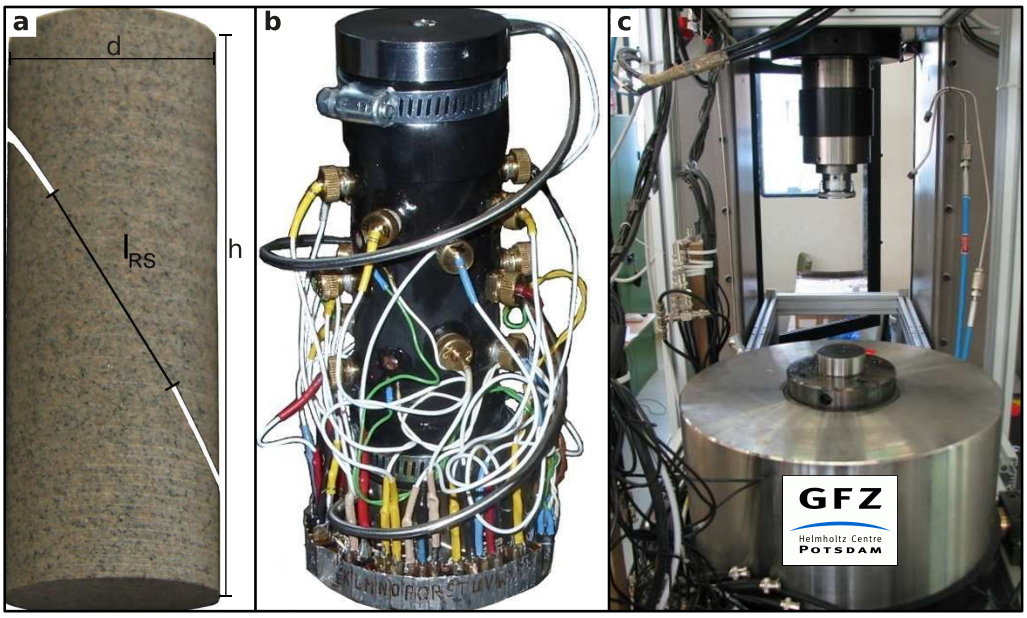

Figure 2.1: Photographic images of a Westerly granite sample, AE sensors and the loading rig. a): Westerly granite sample and saw-cut notches, b): Sample, rubber jacket, strain and piezo electric sensors, c): Loading frame and pressure vessel at GFZ-Potsdam, Germany.

stick-slip and a range of strain release events.

To determine variations in seismic velocities, we used piezo-electric transducers as active pulse senders. This enabled us to update the seismic velocity model every 10–300 sec, thus documenting dynamic changes in elastic properties of the specimens. The seismic velocities were generally sensitive to damage creation and the occurrence of stick-slip events (Figure 2.2b). The velocity measurements commonly exhibited a drop due to slip which was partially recovered during stress increase over the subsequent interslip period. Furthermore, we observed a strong seismic anisotropy due to axial loading stresses which was documented by the horizontal and vertical sensor pairs. We used the measured anisotropy as input for travel-time inversions which improved the accuracy of AE hypocenter locations to about 1–4 mm (for details about hypocenter determination see Appendix A).

Besides mechanical data and seismic velocities, we recorded and analyzed complete acoustic emission waveforms from 14 piezo-ceramic transducers. These transducers had resonance frequencies of 1 and 2 MHz. Our data acquisition system consisted of 8 high-speed digitizing boards with 80 GByte internal hard disk space. The internal hard drives prevent any type of data loss due to downtime during data streaming. Each channel was operated in a triggered mode at a sampling

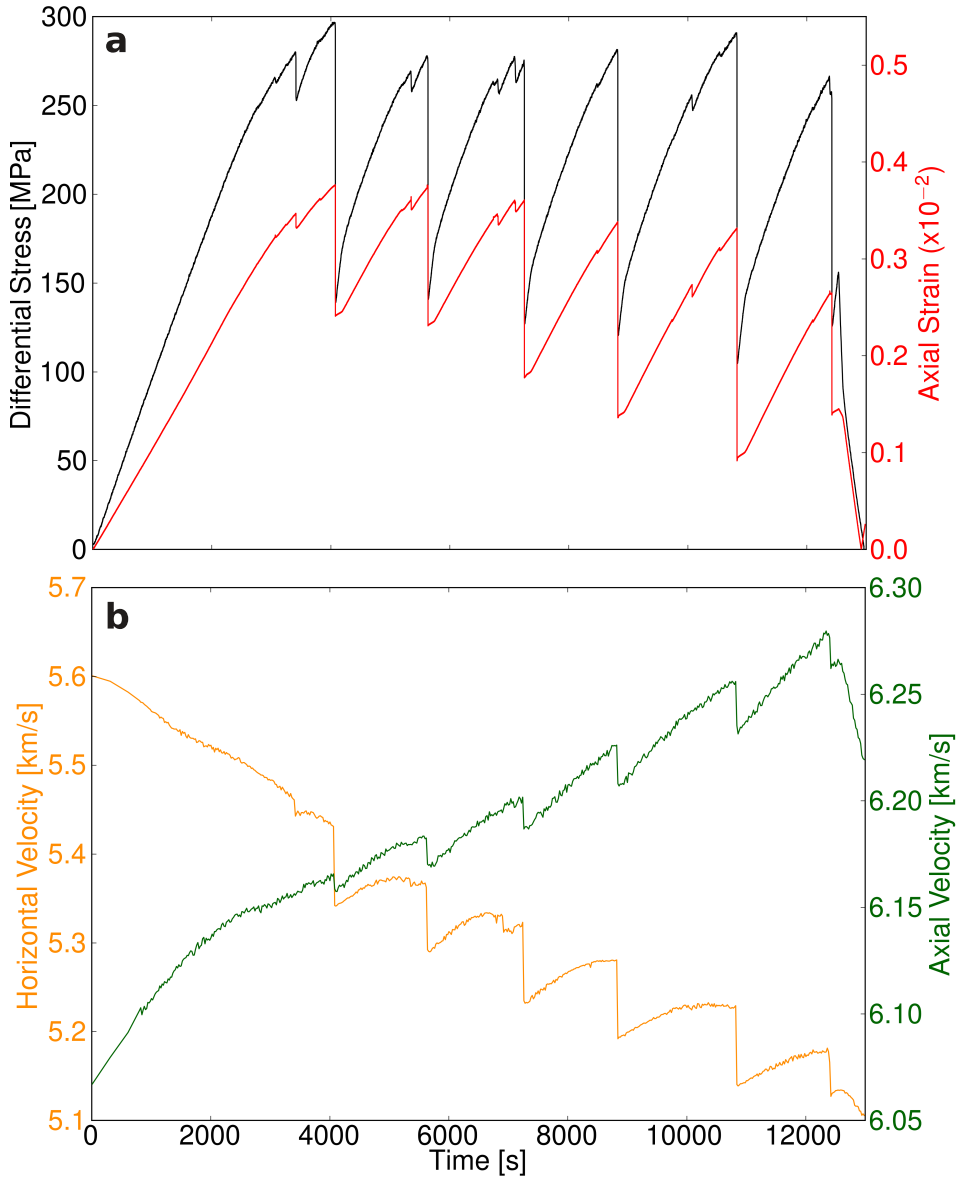

Figure 2.2: Example of differential stress, axial strain and seismic velocities for one of the saw-cut guided fracture experiments. All of the displayed data show clear evidence for series of stick-slip events. a): Differential stress (black curve) and local axial strain (red curve), b): Axial (green curve) and radial (orange curve) seismic velocities. Note the strong seismic anisotropy due to axial loading.

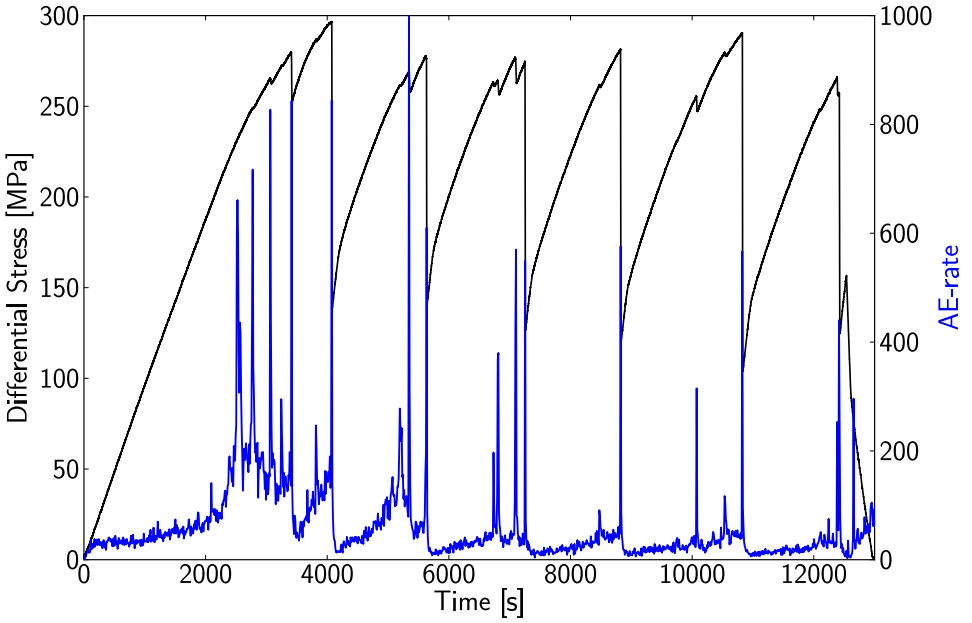

Figure 2.3: Example of differential stress (black curve) and AE-rate (blue curve) binned every 10 s for one of the saw-cut guided fracture experiments.

frequency of 10 MHz (corresponding to a time resolution of 0.1 ¯s) and an amplitude resolution of 16 bits.

Based on the recorded waveforms, we determined the number of AEs within specific time frames. The corresponding AE rates showed a general increase before small and large stress drop events and sharp peaks that coincided with the onsets of stress drops (Figure 2.3). We observed most AE events during experiments on fracture and saw-cut guided fracture experiments whereas continuous saw-cut surfaces created comparably less events with the lowest AE-rate for smooth, planar surfaces.

In addition to the precise location of each AE event and AE rates, we also determined their amplitudes based on the recorded waveforms following Zang et al. (1998):

$$A = \sqrt{\frac{1}{k}\sum_{i=1}^{k}\left(\frac{r_i}{10}A_{i_{\max}}\right)^2} \tag{2.1}$$

where $A_{i_{\max}}$ is the maximum amplitude of the AE waveform at each sensor, r_i is the distance between the source and the i^{th} receiver in millimeter and k is the total number of sensors used

for the amplitude calculation. The computed value is an average amplitude for the whole array assuming elastically propagating, spherical waves of a point source, corrected for geometrical spreading on a 10 mm reference sphere.

Based on AE amplitudes, we assigned magnitudes $(M = \log A)$ to each event. The utilized magnitude scale is specific for our laboratory set-up and, at this point, does not provide an estimate of the actual seismic moment or seismic energy release. Nevertheless, based on the local magnitude scale, we computed relative seismic moments which provide important insights into spatial and temporal variations of moment release during an experiment. Here, moment and magnitude are related over:

$$M_0 = 10^{CM}. \tag{2.2}$$

We chose $C = 3/2$ which is commonly used for real earthquake scaling relationships. Since our analysis focused on relative, spatial variations in M_0, the changes in C caused only an up or down scaling and had no influence on the detectability of moment variations.

The combination of magnitude information and AE hypocenter locations can provide important insights into fault zone properties. AE hypocenter locations generally focused within or in the proximity of the laboratory fault zones (Figure 2.4), and can be used to assess changes in fault orientation and fault structure.

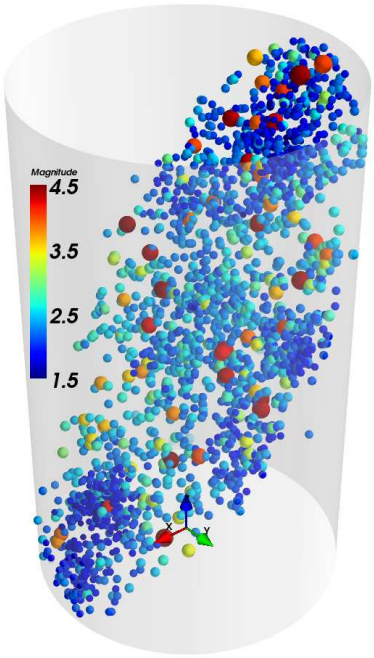

Figure 2.4: Example of AE locations and magnitudes of a frictional sliding experiment on a planar saw-cut surface with predefined roughness.

After completion of the experiments, we analyzed resulting fault zone micro-structures in thin-sections. We preserved the fault's micro-structure by introducing low viscosity epoxy resin which when cured, enabled cutting and grinding of the sample without changing the grain configuration. Accompanying the thin-section images, we created computer tomography images of the deformed samples. These images were taken using an X-ray computer tomography system (GE Phoenix X-ray nanotom 180 NF) equipped with a 180 kV/15 W nanofocus tube and a digital 5 Megapixel detector. The theoretical resolution of

CT-scans is $\sim$30 μm, but in practice the resolution may decrease due to boundary effects, small density contrasts between different grains and limited penetration for large sample sizes.

The here acquired spectrum of data is unique in its breadth and facilitates a direct connection between stress, strain, seismic data and post-experimental fault structure. Furthermore, the repeated occurrences of stick-slip events provide the opportunity to study fault properties over many successive seismic cycles which is generally not possible in nature.

3 Identifying fault heterogeneity by mapping spatial anomalies in acoustic emission statistics

3.1 Abstract

Seismicity clusters within fault zones can be connected to the structure, geometric complexity and size of asperities which perturb and intensify the stress field in their periphery. To gain further insight into fault mechanical processes, we study stick-slip sequences in an analog, laboratory setting. Analysis of small scale fracture processes expressed by acoustic emissions (AEs) provide the possibility to investigate how microseismicity is linked to fault heterogeneities and the occurrence of dynamic slip events. The present work connects X-ray computer tomography (CT) scans of faulted rock samples with spatial maps of *b*-values (slope of the frequency-magnitude distribution), seismic moments and event densities. Our current experimental set-up facilitates the creation of a series of stick-slips on one fault plane thus allowing us to document how individual stick-slips can change the characteristics of AE event populations in connection to the evolution of the fault structure. We found that geometric asperities identified in CT-scan images were connected to regions of low *b*-values, increased event densities and moment release over multiple stick-slip cycles. Our experiments underline several parallels between laboratory findings and studies of crustal seismicity, for example, that asperity regions in lab and field are connected to spatial *b*-value anomalies. These regions appear to play an important role in controlling the nucleation spots of dynamic slip events and crustal earthquakes.

3.2 Introduction

Fault systems contain geometric and structural complexities on multiple scales. The San Andreas fault system, for example, consists of several sub-parallel faults which accommodate the relative movement of the Pacific and North-American plates. The strain accumulation and release in connection with the movement of tectonic plates result in the creation of broad fault zones which evolve over time. The slip distribution along plate boundaries can be explained to first order by geometrically simple systems of planar faults (e. g. Ben-Zion and Sammis, 2003) but the spatial distribution of earthquake hypocenters reveals a picture of great complexity. Seismicity within the continental crust, which is connected to both frictional and fracture processes, is strongly influ-

enced by fault zone geometry, segmentation, and roughness (e. g. Aki, 1979, 1984; Malin et al., 1989; Zhang et al., 1991; Dieterich and Smith, 2009; Powers and Jordan, 2010).

Within the scope of this study, we investigated the connection between the spatio-temporal distribution of microseismicity and structural heterogeneities of fracture surfaces during laboratory stick-slip experiments. In particular, we concentrated on the influence of geometric fault asperities, which are commonly seen as areas of increased fault strength and resistance to slip. The term asperity has been used in seismological studies to describe highly stressed, locked fault patches. These patches are observed to produce large co-seismic moment release during earthquake propagation but can also be linked to rupture nucleation and arrest (e. g. Kanamori and Stewart, 1978; Kato et al., 2010). In laboratory studies, areas of increased fault strength may be connected to inflections, unbroken asperities, as well as healed or branching faults (e. g. Scholz, 2002; Lei, 2003; Lei et al., 2004; Thompson et al., 2009). We define asperities as areas of large sliding resistance and more specifically as load-bearing points of contact between rock surfaces (Jaeger and Cook, 1979) as a result, for example, of locally increased positive fault topography. The regions of geometric asperities can be identified using CT-scan images and can be connected to episodic locking, enhanced strain accumulation and fault rupture.

Fault plane asperities have been studied at crustal and laboratory scales. The latter aims to mimic similar conditions to those inside of the seismogenic crust. An advantage of laboratory experiments is that experimental set-ups can be adapted to study isolated processes, e. g. the role of an asperity region in creating macroscopic slip events. Rock mechanics experiments have been essential in extending the understanding of physical processes involved in earthquake ruptures. Brace and Byerlee (1966) demonstrated that stick-slips during triaxial compression tests of simulated faults may be considered as analogous to earthquakes. Furthermore, the widely used rate and state friction laws were based on laboratory observations (Dietrich, 1978; Ruina, 1983) and have since been applied to describe parts of complex fault behavior.

3.2.1 Acoustic emissions in laboratory experiments

Non-elastic deformation of rock specimens in the brittle regime is connected to microcracking events that emit elastic waves similar to seismic waves during crustal earthquakes. The hypocenters and amplitudes of these acoustic emissions (AEs) have been determined with increasingly high accuracy and applied to the description of fracture processes of intact rock (e. g. Zang et al., 1998;

Lei et al., 2004). AEs show a high degree of localization during the initiation of catastrophic failure (Lockner et al., 1991a). Scholz (1968) and Amitrano (2003) demonstrated that the frequency magnitude distribution (FMD) of AEs during loading of intact samples follows a power law similar to the Gutenberg-Richter distribution of natural seismicity with a decreasing slope (b-value) with increasing differential stress. b-values also exhibit a characteristic minimum before the failure of intact rock samples that has been linked to stress-driven microcrack corrosion and coalescence (e. g. Main et al., 1989; Meredith et al., 1990). The authors suggest a negative correlation between b-values and the level of stress.

In addition to fracture experiments, many studies focused on the investigation of naturally and artificially created faults during triaxial compression. Amitrano and Schmittbuhl (2002), for example, observed a damage zone containing a gouge layer, as well as regions of high and low crack density during frictional sliding of rough fracture surfaces. A detailed micro-analysis showed many mode II cracks that accommodated the fault displacement. Sammonds and Ohnaka (1998) conducted experiments on saw-cut faults with pre-defined roughness which showed that b is related to the fractal dimension of the surface topography during frictional sliding with lower b-values for smoother surfaces. Thompson et al. (2009) showed that AE hypocenters during stick-slips on natural fracture surfaces cluster close to asperities. They identified asperities using both CT-scan images and AE event locations and suggested that asperity regions in laboratory experiments are analogous to locked patches of crustal faults in that they are barriers to fault slip.

3.2.2 Spatial b-value mapping

The role of fault zone complexity in the creation of crustal seismicity and its connection to rupture nucleation spots is an area of active research. Ben-Zion and Sammis (2003) argued that faults evolve toward geometric simplicity with increasing total offset ("slip age"). The authors suggest geometrical and material heterogeneity of planar faults as a mechanism that leads to complex seismicity clustering. In subduction zones, fault plane asperities have been identified by high seismic moment release. Corresponding aftershocks are suggested to create areas of high b-values (Sobiesiak et al., 2007). The nucleation spots of ruptures have been linked to fault plane asperities, for example for the Parkfield section of the San Andreas Fault (Schorlemmer and Wiemer, 2005). An investigation of spatial b-value variations along the Parkfield section revealed a pronounced low b-value anomaly that coincides with a fault plane asperity (Wiemer and Wyss, 1997; Schorlemmer

et al., 2004a). This area also produced large co-seismic slip during the 2004 M=6.0 Parkfield earthquake (Schorlemmer and Wiemer, 2005). A detailed mapping of fault plane asperities could play an important role in seismic hazard assessment. While variations in seismic b-values have been associated with asperities in natural faults, there is a lack of additional data to validate this interpretation. The physical mechanisms involved in their creation remain unclear, for example, if low b-values are a consequence of regional fault criticality, or the failure of one or more large asperities on a rough fault.

We extend previous studies by connecting detailed b-value maps with *in situ* fault structure observations. While many laboratory experiments were focused on the mechanism of rock fracture, we put our emphasis on the analysis of AEs during stick-slip sliding. We created naturally faulted surfaces and observed the AE build up with approaching dynamic slip events as well as AEs occurring immediately after slips. AE events can be related to both fault morphology and branching (e. g. Lei et al., 2004; Thompson et al., 2009). AE hypocenter locations and amplitudes were analyzed within the framework of a single fault zone, thus isolating the influence of asperities from other suggested geometrical heterogeneities like fault branching. We developed a method to create several stick-slips on one fault to test the persistence of major asperities.

AE patterns were related to fault heterogeneities as revealed by CT-scan images and microstructural analysis. In this study, results from three stick-slip experiments are presented. Initially, we describe the mechanical details of fault creation and the following stick-slip events. We then show the applicability of concepts and statistical relations derived from crustal seismicity to our data, namely to the microseismicity which occurred in connection with stick-slips. The main part of this study is focused on the identification of fault plane asperities using b-values, seismic moment release, and event densities of AEs, and to compare it to CT-scans. Lastly we look at the evolution of the fault plane structure with successive stick-slip events.

3.3 Method

3.3.1 Rock sample and loading

We present results from triaxial compression experiments conducted on three, cylindrical Westerly granite (WG) specimens (40 $\times$ 107 mm). Westerly granite, which is a good representative of the continental, seismogenic crust, is isotropic and consists of 28% quartz, 33% plagioglase, 33% K-

feldspar, 5% mica (3.5% biotite, 1.9% muscovite) (Chayes, 1950a) with an average grain size of 0.75 mm (Stesky, 1978).

Rock fracture and frictional sliding were performed with a 4600 kN MTS servo-controlled loading frame and a 200 MPa pressure vessel. All experiments were conducted at previously oven dried samples to avoid additional complexity and to facilitate the interpretation of results. An elastic rubber jacket was installed around the specimens to prevent any fluid penetration during the experiments. The axial force was measured by an external load cell. Both vertical and horizontal strain were determined by local strain gauges and larger scale deformation braces (similar to LVDTs). The maximum displacement, which was limited by the strength of the rubber jacket, was $\sim$ 6 mm depending on the experimental set up and rock sample preparation. We used piezoceramic sensors with 1 mm thickness and a resonance frequency of 2 MHz for AE recording and ultra-sonic pulse generation. Samples were drilled from homogeneous granite blocks, without any visible cracks. The end surfaces were cut and ground parallel to $\pm$ 0.03–0.1 mm. For specimens WGRN04 and WGRN05, we introduced saw-cut notches in a 30° angle to the loading axis on opposite sides of the samples. An approximately 1 mm wide gap was created due to the thickness of the cutting disc which was filled with low friction teflon sheets. The notches provided a guide for fracture propagation resulting in the localization of deformation between their ends.

Post experimental microanalysis of fault structure and crack network was performed using a X-ray computer tomography system (GE Phoenix X-ray nanotom 180 NF) equipped with a 180 kV/15 W nanofocus tube and a digital 5 Megapixel detector. The theoretical resolution of CT-scans is $\sim$30 μm, but in practice the resolution decreases due to boundary effects, small density contrasts between different grains and limited penetration for large sample sizes. Scanning of samples by X-rays allows visualizing density contrasts on gray-scale images because the absorption of the electromagnetic waves depend on material contrasts (density, atomic number), thickness, and radiated X-ray energy.

3.3.2 Fracture of intact rock and stick slip events on fault

We developed a three-step procedure, in which initially the intact part of the rock samples were fractured during axial loading at constant strain rates of $\dot{\epsilon} \sim 3 \cdot 10^{-6}$ s^{-1} (20 ¯m/min) and confining pressure of $P_c = 75$ MPa (Figure 3.1 left). As a second step, we locked the fault by an increase in confining pressure to 150 MPa and during the final step resumed axial loading which

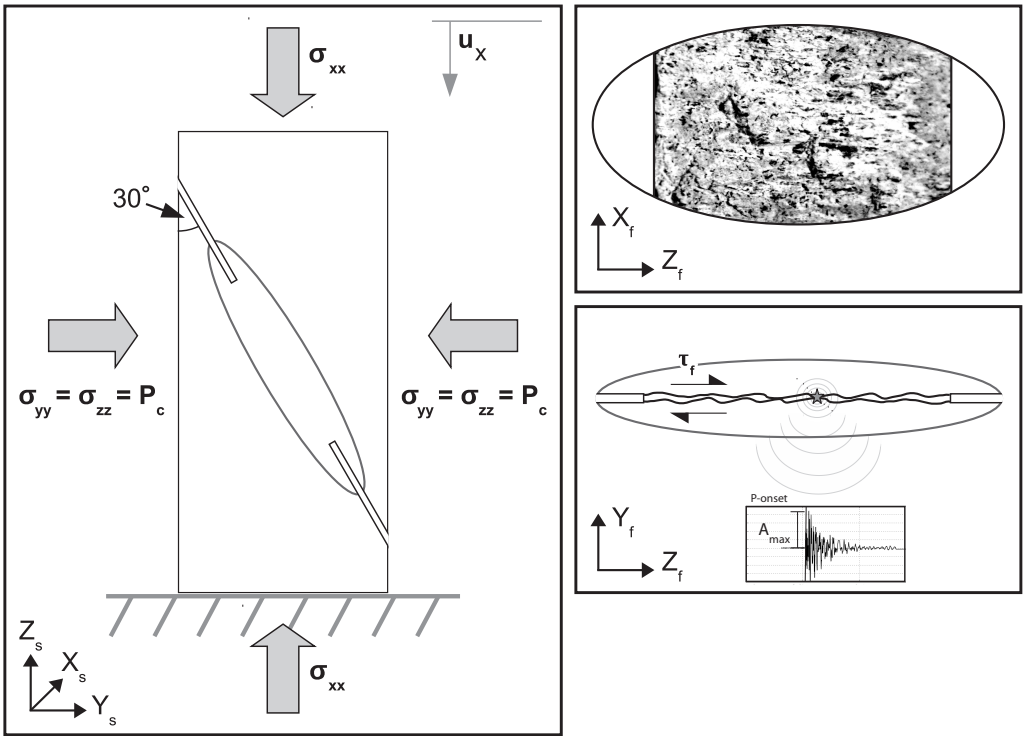

Figure 3.1: left: Schematic diagram of loading conditions and stresses. Arrows in lower left specify the sample specific coordinate system. right: Sliding of fault with naturally developed roughness in fault specific coordinate system which is also used for the later AE representation.

led to a reactivation of the fault (Figure 3.1 right) in form of a series of stick-slip events. The uncertainty in stress, confining pressure and displacement were estimated to be 6 MPa, 0.5 MPa and 3 μm respectively. Initial experiments were conducted on completely intact samples followed by a later set of experiments on notched specimens. The failure process of intact samples from our earlier experiments (not shown) resulted in complex fault structures that contained multiple fracture surfaces. The introduction of notches provided a key improvement in our experimental set-up and ensured the reproducibility of results. The naturally developed laboratory faults had a simpler structure and a single fault plane with predictable orientation. This information could be used to optimize the locations of AE sensors on the sample periphery.

Figure 3.2 shows the loading curve during fault activation of WGRN05 with characteristic stick-slip behavior. We observed an initial linear increase of stress and strain which was followed by a growing deviation from linearity leading up to stress drop events which were connected to macroscopic slip of the entire fault. Six abrupt slip events with stress drops ($\Delta\sigma$) between 132–181 MPa and duration of max. 0.1 s were observed during frictional sliding of sample WGRN05 (Figure 3.2).

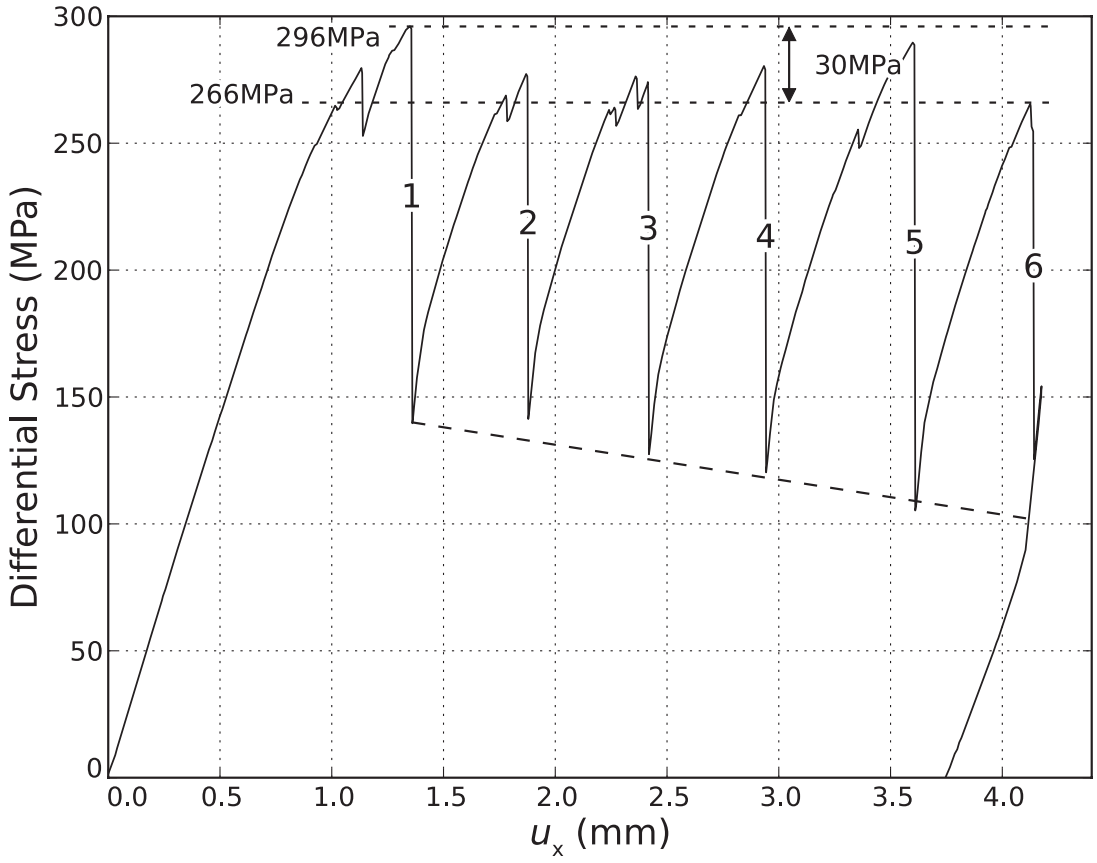

Figure 3.2: Differential stress and axial displacement (u_x) for experiment WGRN05 with characteristic stick-slip behavior. The slip events with large stress drops are labeled from 1 to 6. All slip events with large stress drops nucleated within a differential-stress window of 30 MPa (upper dashed lines). The residual stress decreased systematically after each successive stick slip as indicated by the downward sloping dashed line.

All slip events occurred within a differential-stress-window of 30 MPa between peak stresses of 266–296 MPa without any systematic changes in the maximum fault strength. The largest stress drop was connected to slip event 5. The residual stress after each of the slips decreased systematically (downward sloping, dashed line in Figure 3.2), which is likely to be connected to fault smoothing with successive slip events.

Table 3.1 shows loading conditions and number of slip events for the three different samples that were used in this study. The specimen WGR01 had no notches but a through going fracture surface with natural roughness and a coefficient of friction of about 0.66. It produced one slip event with a large stress drop. This stress drop was preceded by about 60 min of frictional sliding at a consistently high differential stress level which was interrupted by several smaller slips. The notched samples, WGRN04 and WGRN05, produced three and six stick-slip events, respectively,

	Sample	l_{rs} cm	l_n cm	$P_{c_{frac}}$ MPa	$P_{c_{slide}}$ MPa	$\sigma_{max_{frac}}$ MPa	$\sigma_{max_{slide}}$ MPa	$u_{x_{max}}$ mm	N_{slips}
1	WGR01	8.5±0.15	-	75±0.5	150±0.5	780±6	570±6	3.1	1
2	WGRN04	5±0.15	1.5±0.15	75±0.5	150±0.5	610±6	400±6	3.0	3
3	WGRN05	4.2±0.15	1.9±0.15	75±0.5	150±0.5	505±6	295±6	4.1	6

Table 3.1: Overview of experiments and boundary conditions conducted on samples WGR01, WGRN04, and WGRN05. WGR01 was fractured in its intact condition while WGRN04 and WGRN05 contained notches. l_{rs}: approximate length of the rough fracture surface, l_n: length of each notch, $P_{c_{frac}}$: confining pressure during fracture stage, $P_{c_{slide}}$: confining pressure during frictional sliding of the fractured surfaces, $\sigma_{max_{frac}}$: maximal differential stress during fracture stage, $\sigma_{max_{slide}}$: maximal differential stress during sliding, $u_{x_{max}}$: maximum vertical displacement, N_{slips}: number of abrupt slip events with large stress drops.

with stress drops between 115–217 MPa. The maximum differential stress during fracture and sliding phases decreased from WGR01 to WGRN05 as a result of specimen weakening due to longer notches. The maximum axial displacement was between 3.0 and 4.1 mm.

3.3.3 AE data

The main focus of this study was to connect AE properties (namely magnitude, density, *b*-value, and location) to specific heterogeneities of the fault zone. We recorded and analyzed complete acoustic emission waveforms from 16 piezo-ceramic transducers with a resonance frequency of about 2 MHz using eight high-speed digitizer cards with 80 GByte internal hard disk space. The internal hard drives prevent any type of data loss due to downtime during streaming. Each channel was operated in a triggered mode at a sampling frequency of 10 MHz (corresponding to a time resolution of 0.1 ¯s) and an amplitude resolution of 16 bits. Large deformation during fracture and shear caused significant changes in elastic moduli, hence also in seismic velocities. To account for these variations during hypocenter determination, velocities were computed every 5 to 30 s from onset times of high-voltage pulses transmitted by piezo-ceramic sensors. This technique improved the location accuracy to about 1–4 mm. Further details about the AE-system can be found in Stanchits et al. (2006).

The amplitude of each AE event was determined similarly to Zang et al. (1998):

$$A = \sqrt{\frac{1}{k}\sum_{i=1}^{k}\left(\frac{r_i}{10}A_{i_{max}}\right)^2} \tag{3.1}$$

where $A_{i_{max}}$ is the maximum amplitude of the AE waveform at each sensor, r_i is the distance

between the source and the i^{th} receiver in millimeter and k is the total number of sensors used for the amplitude calculation. The computed value is an average amplitude for the whole array assuming elastically propagating, spherical waves of a point source, corrected for geometrical spreading on a 10 mm reference sphere.

Within the framework of this study we distinguished between AEs which were described by their locations, magnitudes, and origin times and macroscopic, dynamic slip events with specific stress drops, durations, and onsets of stress drops. Dynamic slip events were associated with a whole set of AE events, consisting of AE- "fore-", "main-" and "aftershocks". The nucleation spots of macroscopic slip events were defined as âĂIJmainshocksâĂİ. They were easily detectable due to abrupt increases in AE rates, their temporal proximity to the onsets of large stress drops, their distinct waveforms as well as their large amplitudes. An initial mainshock selection was performed by identifying the largest magnitude AE within a 0.2 s time window around the onset of stress drops. This time window accounts for the different sampling rates and synchronization uncertainties of AE and stress data. The mainshock identification was then confirmed by analyzing the waveforms associated with slip onsets and by comparing them to a waveform of a typical AE event. The two signals showed very distinct characteristics (Figure 3.3) in terms of duration and amplitude. A commonly observed AE event exhibits a burst signal of high frequency, with high, initial amplitudes which decay rapidly within less then 0.050 ms. AE waveforms of slip events generally show larger amplitudes that are clipped on all channels due to the limited dynamic recording range of the AE system. The signal can have a total duration of up to 10 ms. Right after the sliding, several aftershock AEs might be hidden in the coda of the large event, for which recordings were momentarily clipped by the large signal, as is common for actual earthquake studies. However, this temporary loss of recording ability did not affect our statistical studies or the identification of the mainshocks.

In the context of a mainshock, we then defined aftershocks as AE-events in an 8 s time window after the origin time of the mainshock. Foreshocks were defined as AEs that occurred from 20 s after the previous slip until 0.2 s before the current slip event. For the spatial analysis of foreshocks, we selected AEs with larger magnitudes and small residuals from the travel-time inversion of the location algorithm to ensure the highest possible accuracy of hypocenter determination. We decided to choose a sufficiently small aftershock period to avoid any mixing of different event populations. Figure 3.4 shows an example of the AE activity binned to 0.1 s before and after the

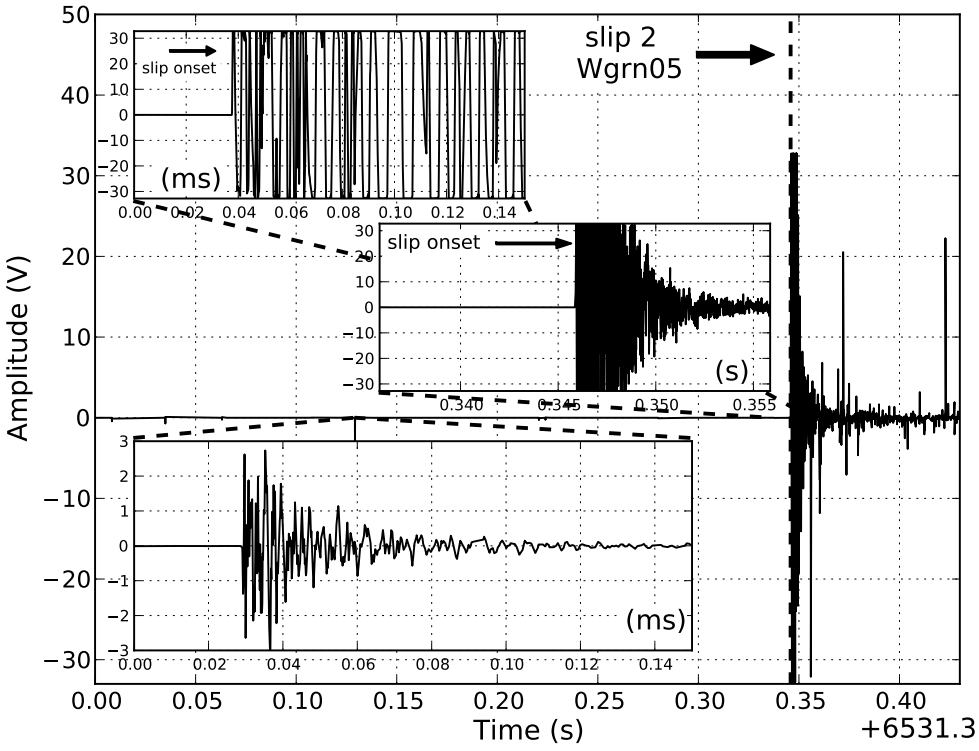

Figure 3.3: AE waveforms within a ∼0.5 s (main axis), 20 ms (center) and 0.15 ms (upper insert) time window of slip event 2 of experiment WGRN05 as well as a waveform of a 'typical' AE event (lower insert). The waveforms connected to slip onsets were clearly distinguishable from commonly observed AEs by their amplitude and duration. Note that time scales are in ms for upper and lower insert.

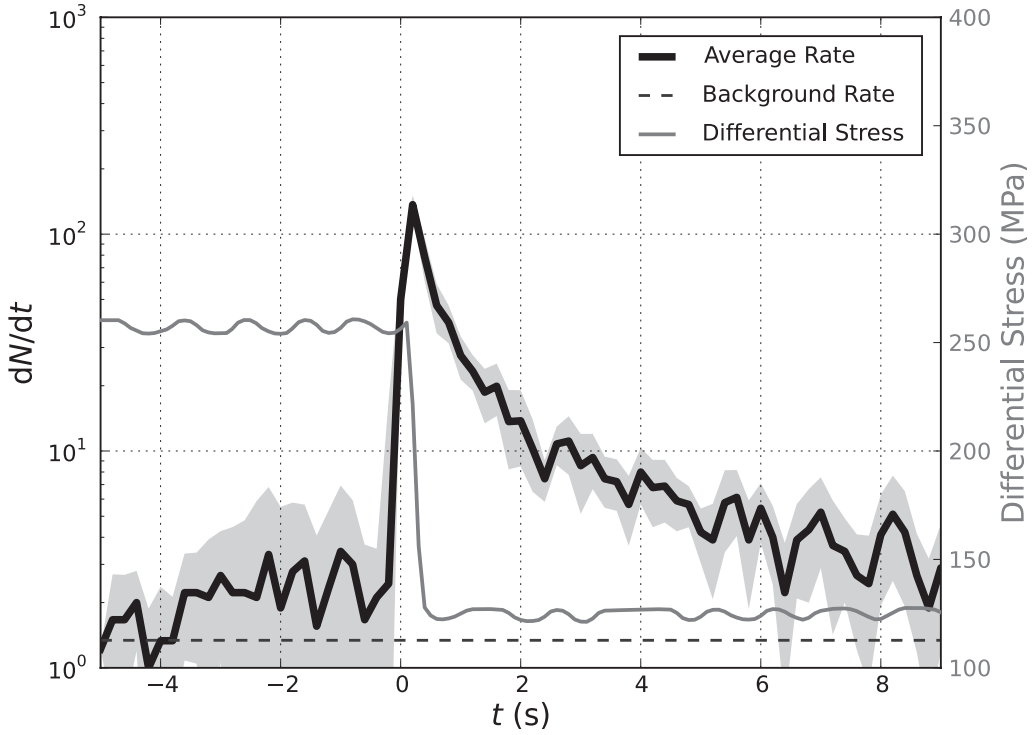

Figure 3.4: Differential stress (gray line), AE-rate average (black line), standard deviation (shaded gray region) and background rate (dashed gray line) for all slip events of WGR01, WGRN04 and WGRN05 within a 15 s time window of slip onsets, stacked to t=0. The origin times of slip events were determined from the stress drop onsets and compared to AE data. The highest AE-rates occurred within less than 100 μs of the stress drops.

origin time of macroscopic slip. The AE-rates right before the slip events were low compared to aftershock rates. The onsets of stress drops coincided with a sharp peak in AE-rates (within sampling accuracy of 0.1 s for stress and AE-rate). We observed a rate decrease with time after slip until it reached approximately pre- slip rates.

Based on AE amplitudes, we assigned magnitudes ($M = \log A$) to each event on an experiment-specific scale and seismic moments using

$$M_0 = 10^{CM}. \tag{3.2}$$

Here, we chose $C = 3/2$ which is commonly used for real earthquake scaling relationships. Our analysis focused on relative, spatial variations in M_0 which is why changes in C cause only an up or down scaling but have no influence on the detectability of spatial variations. Both magnitude and seismic moment were computed on an experiment-specific reference scale.

Frequency-magnitude distributions of AE-events follow a power law of the form

$$\log N = a - bM \tag{3.3}$$

where b is the slope of the number of events (N) vs. magnitude (M) and a provides an estimate for the productivity analogous to the Gutenberg and Richter (1944) relationship. To compute b-values, we use the maximum-likelihood approach (Aki, 1965).

$$b = \frac{1}{\overline{M} - M_c} \log(e) \tag{3.4}$$

where M_c is the magnitude of completeness estimated by the maximum curvature of the distribution, corrected for bin-size (Utsu et al., 1965; Guo and Ogata, 1997) and $\overline{M}$ is the mean magnitude. For a reliable b-value estimate we required distributions to contain at least 150 AEs.

We performed a detailed analysis of spatial AE-clusters by first projecting all AEs into the fault coordinate system using the best-fit fault plane vectors which are the eigenvectors of the covariance-matrix of AE locations obtained by singular value decomposition. We then computed b-value, AE event density, and moment release maps based on events in the proximity of the fault plane by creating a 2D grid with 0.1 mm node spacing. We determined b for frequency-magnitude distributions for the N (with $N \geq 150$) closest AEs to each node within a maximum radius of $r_{max} = 7$ mm or $r_{max} = 10$ mm, respectively, depending on the overall AE activity in a specific foreshock time window. This method provides an optimized resolution for b-value estimates while accounting for a changing AE event density in different parts of the fault. Nevertheless, each b-value still represents a volume rather than one specific point on the fault surface.

We computed the seismic moment release per volume (M_0/V) between slip events by summing the seismic moment within spheres of constant radius centered at fault plane nodes. AE event density (ϕ) maps were created by counting events within spherical subvolumes of the fault plane which were then corrected for volume size and length of the time windows of fore- and aftershock occurrences.

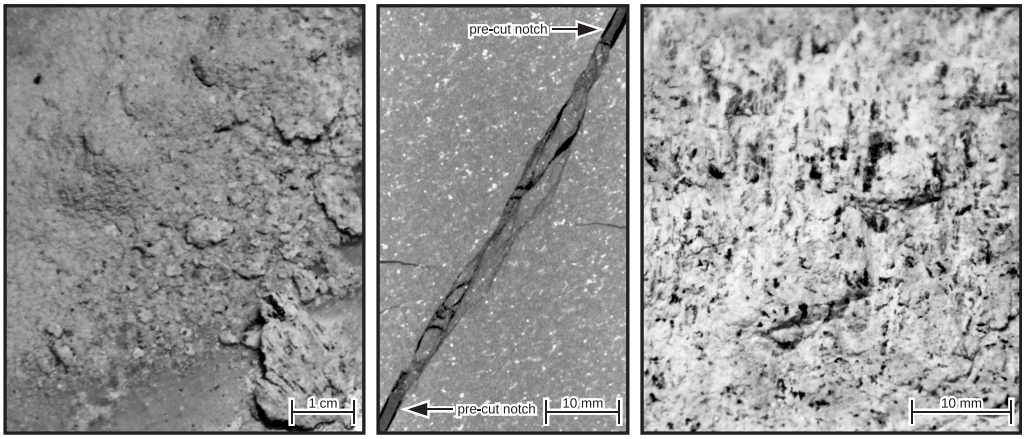

Figure 3.5: (Left) Photo of gouge, which was produced within the fault zone during the 6 stick slips of WGRN05, consisting of ultra-fine and larger grains. Larger rock flag at lower right shows evidence of slickensides and black elongated grains as a result of slip under high normal stress. (Center) CT image of the fault structure with scale in mm after the completion of the experiments. The fault width and gouge layer thickness varied along the fault. (Right) Photo of fault surface with many slip-parallel slickensides and topographic relief changes of up to 2 mm.

3.4 Results

3.4.1 Fault topography and microstructure

Post experimental inspection of the samples showed areas of complex fault structure consisting of gouge, a damage zone containing microcracks with varying density, and the host rock which was characterized by little damage. The initial grain-size distribution after fracturing decreased substantially during frictional sliding due to comminution, leading to the creation of large amounts of ultra-fine rock powder. The combination of grain comminution and the localized occurrences of AE events close to the central fault plane as well as the decrease of the residual friction with progressive stick slips suggested an ongoing reshaping of the fault surface. The successive stick-slip events lead to an accumulation of fine-grained gouge on the fault surfaces (Figure 3.5 left) as a result of asperity grinding and grain-size reduction. We observed both highly fractured fine grained gouge and individual larger rock particles that were produced through the propagation of larger cracks into the host rock. Different grain sizes may be an expression of different stages of damage evolution.

We performed a CT-scan of sample WGRN05 after experiment completion which revealed a heterogeneous fault structure with different size cracks between the ends of the notches. We identified a fault zone with one or possibly several through-going fault surfaces that accommodated

the macroscopic slip. Several subsets of cracks formed a zone of highly fractured rock of variable thickness (Figure 3.5 center). This zone was up to ~ 1 cm wide. We observed an anomalously thin part of the fault zone towards the center of the sample. This area could have led to episodic fault locking and enhanced microcracking in the vicinity due to stress intensification. Visual inspection of fault topography after the experiments (Figure 3.5 right) supports the theory of the existence of large asperities on the fault surface: several areas of increased roughness and larger relief changes were observed forming points of contact between the two host rock surfaces of the sample. Despite the complex fault structure, we observed many slip-parallel slickensides of up to 0.5 cm length. Slickensides in laboratory experiments are connected to dynamic slip events (Engelder, 1974) and are also encountered in exhumed, natural faults.

3.4.2 Stress drop and duration

The loading curves of our sliding experiments showed sudden slips with large stress drops in addition to many smaller slip events with varying stress drops. We investigated the connection between stress drops and duration of macroscopic slip events by compiling data from samples WGR01, WGRN04 and WGRN05 (Figure 3.6). The confining pressure for all three rock specimen was 150 MPa but in contrast to WGRN04, and WGRN05, WGR01 did not contain any notches. The sliding experiment of WGR01 was dominated by an extended period of high differential stresses with relatively small stress changes of ~ 20 MPa. We observed several small slips that may have prepared the fault for the large slip event which occurred after ~ 60 min. Experiments performed on WGRN04 and WGRN05 produced slip events in a systematic fashion without extended preparatory periods. For all three specimens, we observed two different groups of slip events: (1) slips with $\Delta\sigma \gtrsim 130$ MPa which were always abrupt with max. durations of less than 0.1 s, (2) low stress drop events ($\Delta\sigma \lesssim 50$ MPa) with longer durations. The slip events with largest stress drops exhibited also sudden onsets and the shortest durations. Small stress drop events showed longest duration of up to 6 s. (The accuracy of the duration of large stress drop events was limited by the sampling rate of the load-cell so that all values between 0.06–0.1 s could be seen as upper limits.) Abrupt and slower slip events occurred at similar stress levels. This emphasizes that not only the far-field stress levels determine the onsets of slip events but also geometric fault heterogeneities may have an important influence on the locations of rupture nucleation points and times.

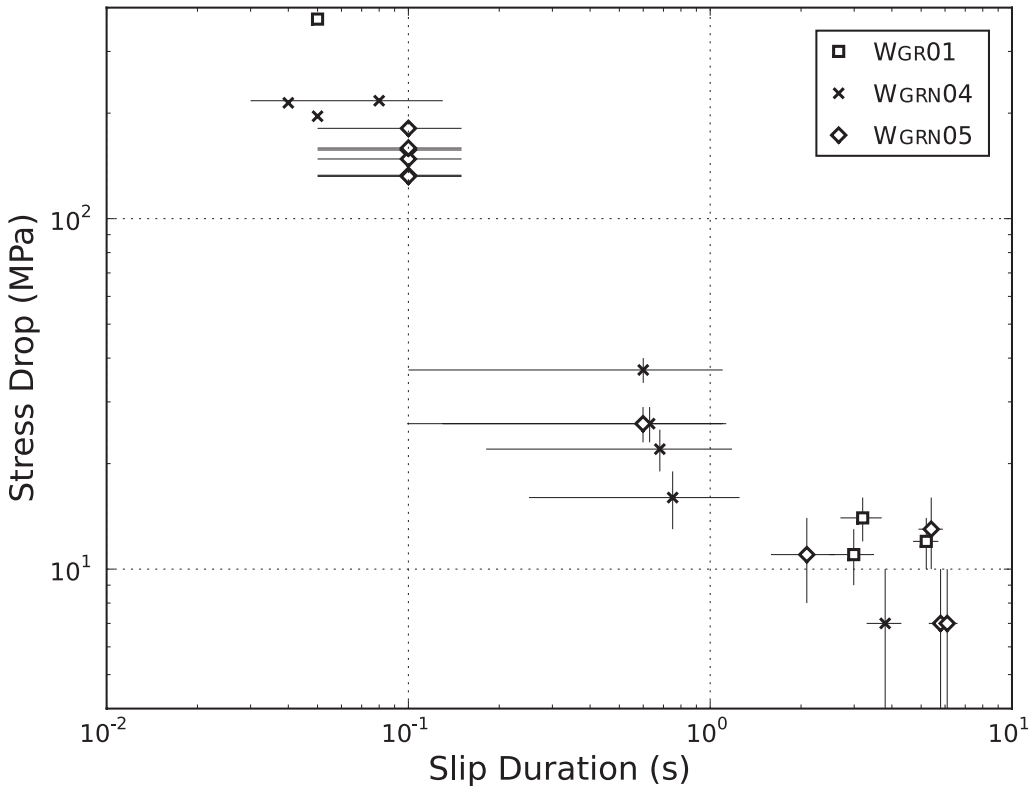

Figure 3.6: Stress drop ($\Delta\sigma$) and duration of slip events for three different samples. Vertical errors represent uncertainties in stress measurements while horizontal uncertainties are estimated errors for onset picks of stress drop start and end which are larger for small stress drops due to a smaller signal to noise ratio. Slip events with large stress drop had a maximum duration of 0.1 s. Decreasing stress drops were connected to increasing slip durations of up to 6 s. The duration uncertainty for all large stress drops was 0.1 s while low stress drop events had estimated uncertainties of 0.5 s.

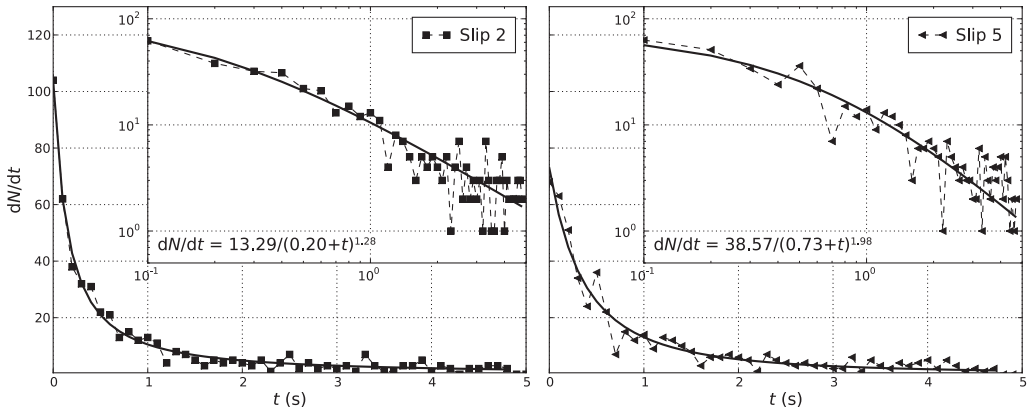

Figure 3.7: AE aftershock rates for slip events 2 and 5 plotted in linear and logarithmic scale.

3.4.3 Aftershock rates and locations

We computed AE-rates by summing events in 0.1 s bins for a 5-second period after each slip event. Figure 3.7 shows aftershocks after slip event 2 and 5 of WGRN05 in linear and logarithmic scale as an example of a typical rate decay after slips. The AE-rate decreased rapidly for the first 0.2–1 s followed by a more gradual decrease over several seconds until reaching the pre-slip rates. To quantify this behavior we use the Omori-Utsu law (Utsu, 1962) which captures both a power law decay and an initial period for which the rate is lower than predicted by a power law:

$$\frac{\mathrm{d}N}{\mathrm{d}t} = \frac{K}{(c+t)^p} \tag{3.5}$$

where $\frac{\mathrm{d}N}{\mathrm{d}t}$ is the aftershock rate and t is the time after slip. K, c, and p are empirical fitting parameters. K is related to the productivity of the aftershock sequence, c describes the length of the time window of initial deviation from power law decay and p is the rate decay exponent. Slip event 2 of WGRN05 had a significantly shorter period of deviation from the power law compared to slip event 5 resulting in a smaller c-value. The overall productivity and rate of decay was higher for aftershocks of slip 5.

Table 3.2 shows results from the analysis of the aftershock rates of all slip events of WGRN04 and WGRN05. WGRN04 showed p-values close to unity except for slip 3 where we observed a high p-value of 1.21. c-values varied between 0.19 and 0.34 and K-values changes between 15.71 and 20.11. The observed activity, N_{tot}, and peak rate, ($\frac{\mathrm{d}N}{\mathrm{d}t}(t=0)$) right after slip event occurrence decreased for each successive slip event of WGRN04.

WGRN04	K	c	p	N_{tot}	N_0
1	20.11 ± 0.64	0.20 ± 0.02	1.09 ± 0.05	751	114
2	15.71 ± 0.63	0.19 ± 0.02	1.01 ± 0.06	590	87
3	19.01 ± 1.61	0.34 ± 0.05	1.21 ± 0.10	550	68
WGRN05	K	c	p	N_{tot}	N_0
1	21.11 ± 1.27	0.32 ± 0.03	1.53 ± 0.09	655	116
2	13.29 ± 0.57	0.20 ± 0.02	1.28 ± 0.08	542	104
3	10.61 ± 0.50	0.18 ± 0.03	1.24 ± 0.09	492	86
4	13.44 ± 0.53	0.17 ± 0.02	1.10 ± 0.07	505	94
5	38.57 ± 10.8	0.73 ± 0.13	1.98 ± 0.23	518	68
6	14.97 ± 0.45	0.15 ± 0.01	1.10 ± 0.05	609	122

Table 3.2: Parameters K, c, p of Omori law fit for slip events of experiments WGRN04 and WGRN05. c is in seconds and both N_{tot} and N_0 number of events. N_{tot} is the total number of events within an aftershock sequence and N_0 is the initial and also maximum number of events within an aftershock sequence.

The decay rate p and delay time c for specimen WGRN05 decreased systematically from slip event 1–6 except for slip event 5 which was connected to anomalously high parameters in the Omori-Utsu law. The recorded number of AEs within the aftershock sequence 5, N_{tot}, exceeded the two preceding ones despite exhibiting a comparably low initial AE-rate, ($\frac{\mathrm{d}N}{\mathrm{d}t}(t=0)$). Small $\frac{\mathrm{d}N}{\mathrm{d}t}(t=0)$ and high Omori-Utsu parameters for aftershock sequence 5 could be an indication of a large amount of small events that were not recorded during the period right after the slip onset which would explain high K-values despite lower observed activity N_{tot}. Slip event 5 produced also the largest stress drop of all events possibly connected to a change in fault roughness, e. g. due to the fracture of a large asperity. Hence both mechanical and AE aftershock data could be explained by the failure of a fault asperity. There are strong trade-offs between the parameters of the Omori-Utsu law and $\frac{\mathrm{d}N}{\mathrm{d}t}(t=0)$ (and hence K, given c and p) is difficult to estimate. If we fix c to 0.2, for example, the trend in p is less clear. We leave statistical exploration of significance to a latter stage when more experiments are available.

Figure 3.8 shows the locations of main- and aftershocks for the three slip events of WGRN04 and the six slip events of WGRN05 in the fault coordinate system. Hypocenter locations were projected onto the fault plane and are viewed, looking onto the fault plane (top in Figure 3.8) and looking at a side view of the fault plane (bottom in Figure 3.8). The AE activity was very low within 0.1 s after the mainshock occurrence possibly due to events that were hidden within the mainshock coda. Thus the nucleation spot of a macroscopic slip event (red stars in Figure 3.8) could simply be defined as the hypocenter location of the largest amplitude event during that

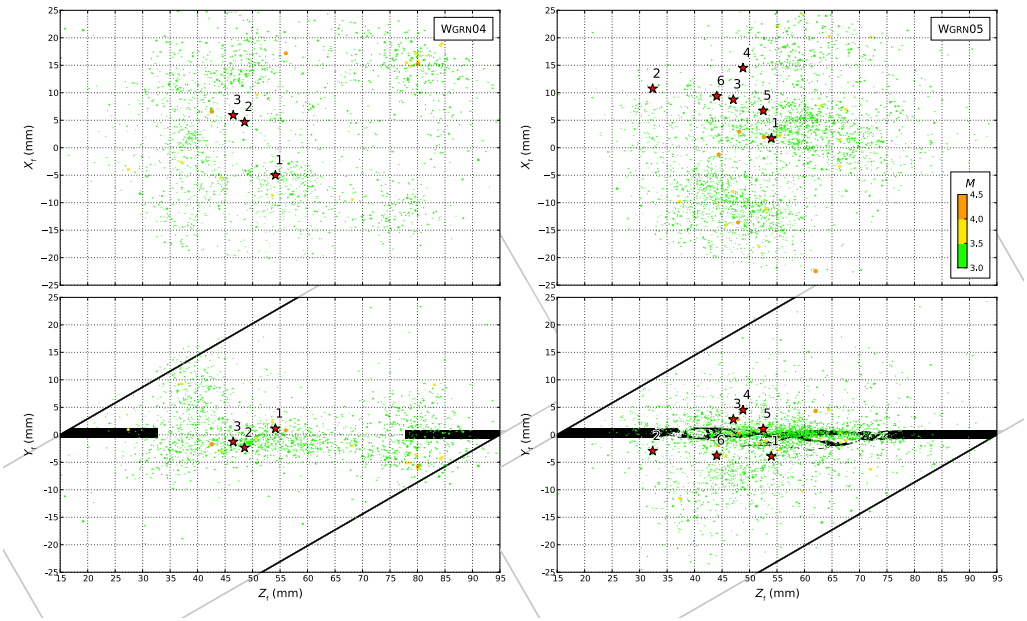

Figure 3.8: Upper plots show AEs (main- and aftershocks) projected onto fault plane, lower plots image AEs within a plane normal to the fault for samples WGRN04 (left) and WGRN05 (right). The red stars indicate the location of the large amplitude AEs coinciding with the onset of the stress drops for all slip events. Dots are aftershocks to slip events colored with size. The nucleation points of stick-slips cluster within similar regions for individual experiments except for event 2 of WGRN05.

0.1 s time frame. The mainshocks were clustered between $[Z_f = 46,\ X_f = -7]$ and $[54, 6]$ in a $\sim 0.5\,\mathrm{cm}^3$ volume for WGRN04 and $[44, -4]$ and $[53, 5]$ in a $\sim 1.5\,\mathrm{cm}^3$ volume for WGRN05 close to the fault plane. Slip event 2 of WGRN05, which nucleated in the lower part of the sample, formed an exception. Common nucleation spots of macroscopic slips could indicate a common mechanism for their creation, for example the rupture of strong fault plane heterogeneities or areas with increased roughness. The aftershocks in both experiments occurred throughout the sample with a small degree of localization on the fault plane. This could be caused by enhanced micro-cracking during strain release and lower differential stresses after slip events. The following section will focus on a detailed analysis of fault geometry and its changes with successive slip events of WGRN05 and WGRN04.

3.4.4 AE-based asperity detection

We now concentrate on the identification of larger-scale asperities and their role during the nucleation process of the six slip events of WGRN05. We analyzed the spatial distribution of foreshock

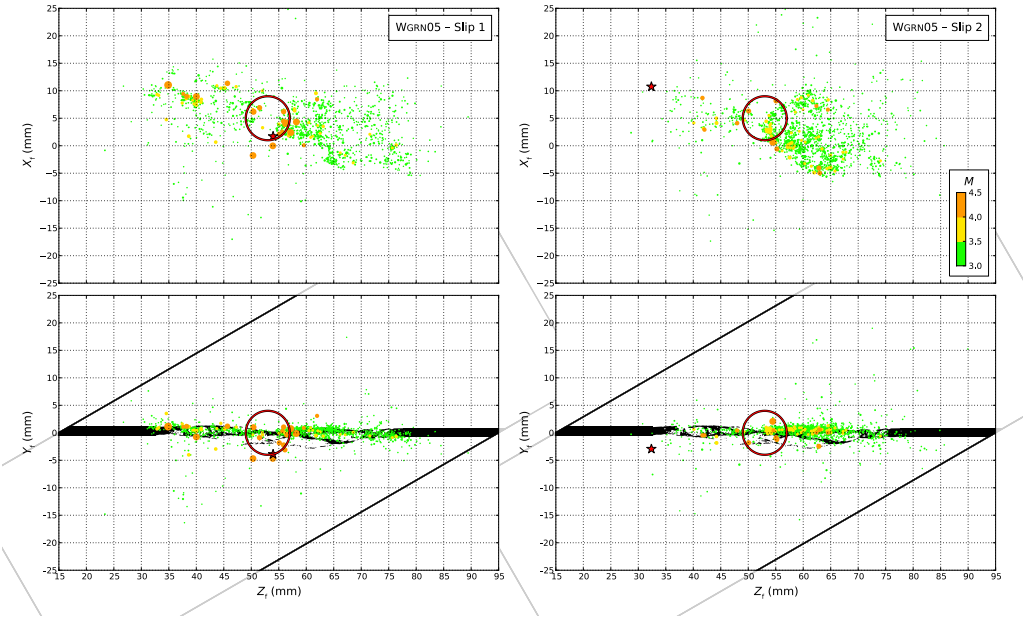

Figure 3.9: Examples of AE foreshock activity based on slip event 1 and 2 of WGRN05. The red circle highlights an area of a relatively sharp contrast between low and high AE activity. Many large amplitude events were produced in the periphery of this area before each of the slip events.

behavior preceding slip events of WGRN04 and WGRN05. One prominent feature of the spatial distribution of foreshocks was an abrupt change from high to low activity which was observed within the same area over multiple slip events. Figure 3.9 shows an example of the foreshock activity to slip event 1 and 2 of WGRN05 which changed from high at $[Z_f = 55,\ X_f = 3]$, to almost no at $[52,5]$ to little activity at $[45,5]$ along the Z_f-axis. The variation in AE activity could be a result of different fault-plane roughness along this path. The activity contrast is likely to be connected to an asperity region highlighted by a red circle in Figure 3.9. Large magnitude foreshocks nucleated close to the asperity boundaries, probably due to crack initiation and growth in preparation of asperity failure. The mainshocks of slips 1, 3, 4, and 6 were located close to an activity 'gap' region. The asperity seemed to control the nucleation spots of most slip events so that during locked periods large foreshocks nucleated predominately in its proximity.

3.4.5 Mapping b-values, AE-event density and moment release

Figure 3.10 shows the AE event density, b-value, and moment release for the foreshocks of slip 1 of WGRN05. The foreshocks were clustered within several areas with elevated event densities.

Largest AE event densities were measured at $[Z_f = 37, X_f = 8]$, $[62, 3]$, and $[72, -2]$. The large heterogeneity of AE densities points towards the existence of a few, larger-scale asperities which caused AEs to cluster in their proximity. One area of anomalously low b-values was located about 5 mm to the left of the high event density region $[42, 7]$ and a second low b-values area was located at $[56, 5]$. The center of the previously identified asperity region was located between these two regions. To emphasize differences in b-values we compared the frequency-magnitude distributions (FMD) of AEs within and outside of the asperity (Figure 3.10 lower left). The FMD for AEs connected to the asperity contained relatively more large-magnitude events which caused the large difference of ~ 0.5 in b-values. The mainshock occurred well within a zone of low b-value. Similarly to the event density and b-value maps, the moment release was dominated by two main areas centered at $[45, 7]$ and $[56, 5]$.

To investigate if low b-value regions and high event densities were always located close to the asperity and to determine the corresponding relative locations of the slip nucleation points, we performed a spatial b-value mapping for foreshocks of all six slips of WGRN05 and plotted the contour lines of the mean AE densities for each slip event (see Figure 3.11 for examples of b-value maps for slip event 2, 3, and 5 of WGRN05). The nucleation points of 5 out of the 6 slip events of WGRN05 were within an area of low b-values. For the first three slip events the highest fore- and aftershock densities were centered at similar points just to the right of the asperity. Aftershock locations started to deviate from foreshock locations after slip event 3. Areas of high aftershock densities still seemed to border low b-value regions but were now shifted to the lower left, centered at $[45, -8]$. The asperity region (red circle in Figure 3.11) can be identified through combining information of event density and b-value maps. An overlap between high foreshock densities and low b-values, bordering high aftershock densities, was an indicator for the location of an asperity region close by. High aftershock densities seemed to occur at its outer edges. These observations underline that the asperity caused relatively larger-magnitude AEs to nucleate at its boundaries, creating areas of relatively lower b-values and elevated fore-and aftershock densities.

Figure 3.12 shows AE event densities and b-values for WGRN04. The aftershocks following slip 1 exhibited highest densities above and below a region with several relatively low b-values of less than 0.74. We identified an asperity region by applying similar criteria (a combination of low b-value, increased moment release, and event density) as for WGRN05. These areas were characterized by low b-values and an abrupt change from low to high foreshock activity. Initially,

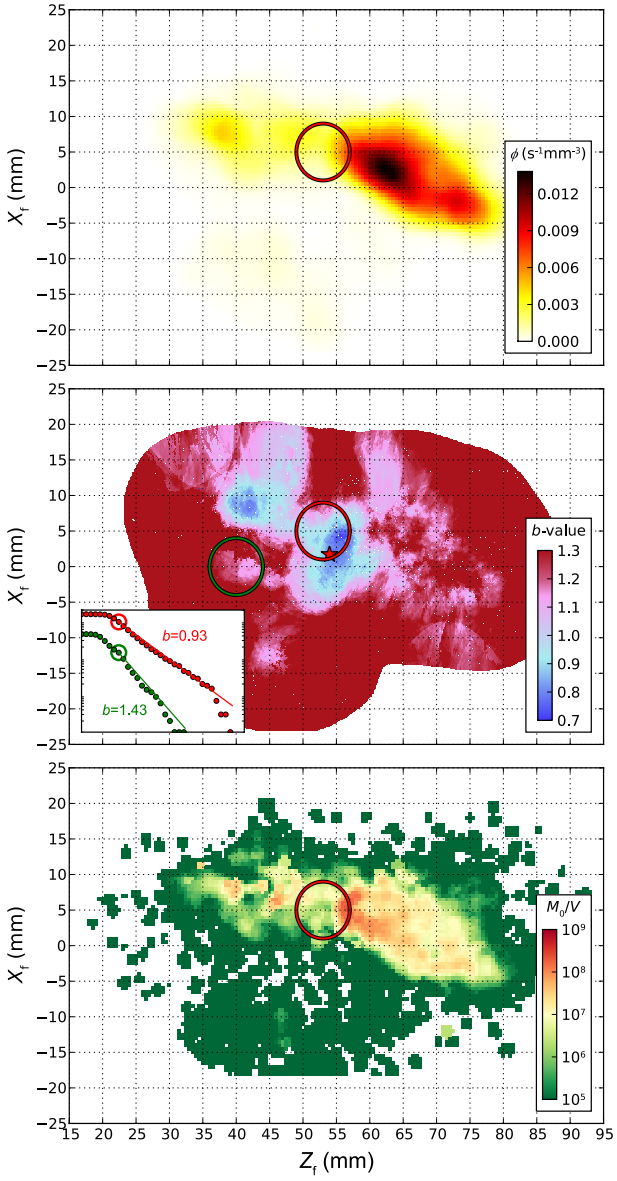

Figure 3.10: Examples of AE-event density (ϕ), b-value and moment release maps computed for AEs occurring before slip event 1 of experiment WGRN05. Slip event one (red star) nucleated close to or from within an area of high ϕ, M_0 and low b-value. The fmds for high and low b-value regions are compared (lower left in central subplot). The asperity region is connected to low b-values, high event density and moment release.

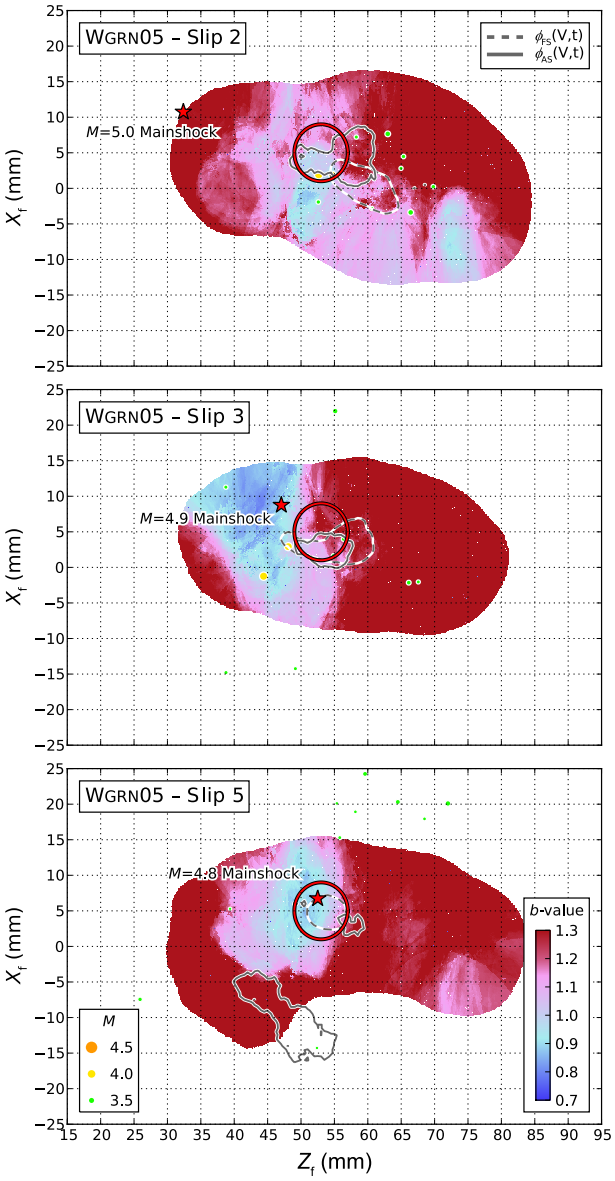

Figure 3.11: *b*-value maps based on foreshocks, contours of fore- (dashed line) and aftershock (solid black line) densities, hypocenters of 10 largest aftershocks and the mainshock nucleation points of slip events 2, 3 and 5 of experiment WGRN05. The size of the aftershocks is indicated by legend at the lower right. The previously identified asperity region is indicated by the red circle. Low *b*-value regions are situated at the border of high AE activity regions of both fore- and aftershocks which mark similar regions for the first three pre-slip periods and are deviating significantly for events 4-6.

we observed about four different low b-value anomalies on the fault plane which suggested several candidate regions that met our asperity criteria. The decrease in complexity of b-value maps after the first slip enabled the identification of one specific asperity centered at $[50, 4]$. The highest fore- and aftershock densities (centered at $[55, -8]$, $[47, 15]$ for slip 1, $[55, -8]$, $[38, 0]$, $[40, 0]$, $[45, 5]$, for slip 2, and $[55, -8]$, $[42, -12]$, $[40, -3]$, $[40, 5]$, $[50, 15]$ for slip event 3) were located around the asperity. Again, the highest fore- and aftershock densities occurred in different fault regions indicating a shift in activity as a consequence of stress transfer between some areas of the fault plane during slip.

To provide information on the location of asperities, AE event-density maps image the degree of clustering of seismic activity within certain time frames of a particular experiment. Figures 3.11 and 3.12 show contours of the mean densities before (solid contour lines) and after (dashed contour lines) the slip events of WGRN04 and WGRN05. The foreshock densities of WGRN04 showed a larger spatial variation with successive slips while the foreshocks to slip events of WGRN05 were centered approximately at the same point. We observed an evolution of the AE densities of WGRN05 to a broader spatial distribution so that larger parts of the fault plane were covered by high AE activity while individual spots with high densities contributed less to the total activity (Figure 3.12). During the first two slips, only one major cluster was active, located towards the center of the sample. With each successive slip, the AE activity became more distributed and separate clusters were formed. The gradual increase in activity in different fault areas indicates a smoothing process, resulting in a distributed set of small-scale asperities that carried the load and contributed to the AE activity. This process was most visible for slip events 1 to 3 of WGRN04.

To compare information of AE locations with post-experimental fault microstructure, we superimposed AE hypocenters on the CT-images of WGRN05. We show results for two exemplary slip events (slip event 2 and 5) of WGRN05. Figure 3.13 shows the foreshocks of slip event 2 colored with magnitude. AE hypocenter locations follow the larger-scale fault structure. Most AEs could be linked to specific cracks. The uncertainty in hypocenter determination of 3 mm lead to a slightly larger spread of AEs compared to the discrete microcrack traces of the CT images. The demonstrated fault structure is a compilation of many fracture and slip events while the AEs were taken from a narrow zone corresponding to the CT slice during one specific time window only. These effects explain the differences between fault structure and AE locations.

Several large foreshocks (yellow and orange dots) nucleated in fault proximity on larger-scale

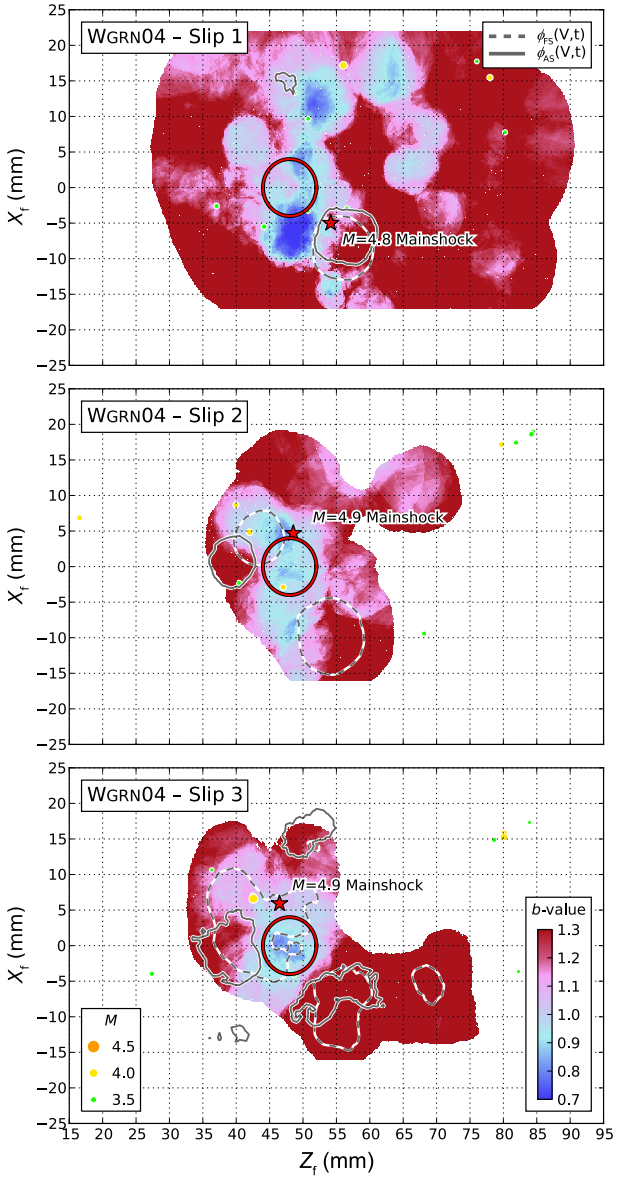

Figure 3.12: *b*-value, fore- and aftershock densities, main and largest aftershock locations plotted similarly to figure 3.11 but now for three different slip events of experiment WGRN04. A combination of *b*-value maps, AE-event densities and foreshock locations enables the identification of an asperity region (red circle) which is also the nucleation spot of macroscopic slip events.

flaws. Less AE activity was observed close to the notches and away from the fault plane. Several AE-clusters were distributed along the fault, perhaps caused by small-scale fault heterogeneities. The previous area of high foreshock activity contrast was also observed on the fault plane at $[26, 45]$, highlighted by a red circle in Figure 3.13. Three larger foreshocks (at $[27, 43]$, $[25, 43]$, $[24.5, 43.5]$) occurred just below this region and a dense cluster of large amplitude events above it occurred at $[27.5, 47]$. The spatial 'gap' in AE activity coincided with an area of narrow fault zone, visible in the CT-images. The other parts of the fault zone were wider, consisting of a gouge layer between many small and large cracks. The change from larger fault zone width and multiple fault planes to a narrow zone could be responsible for the enhancement of microcracking and seismicity in this area.

Figure 3.14 shows a superposition of the CT scan and foreshocks prior to slip event 5. The overall seismic activity was smaller and more localized than before slip event 2. We observed several large foreshocks which pre-dominantly nucleated within or close to the asperity region. The mainshock originated on the fault plane within the asperity. High activity inside the asperity and large-magnitude events can be connected to continuous fracture or grinding of the previously identified asperity region leading up to slip event 5. The combination of seismic and fault structural information revealed that the region of low b, high seismic moment, and high AE-event-density was connected to an anomalously thin part of the fault zone. Asperity regions were characterized by small fault zone width, without anastamosing cracks and possibly bare rock surfaces that were in contact and caused the fault to be locked in this region.

3.5 Discussion

Within the scope of the described experiments, we found some compelling similarities between microseismicity occurrences during sliding of fracture surfaces and crustal seismicity: (1) Laboratory AE records can be separated into fore-, main-, and aftershocks based on their origin times, rates, and magnitudes. We observed a comparatively low rate during foreshock periods that accelerated almost instantaneously during mainshock occurrence which is usually the largest magnitude AE of the sequence. (2) The aftershock rate decay after macroscopic slip can be described by the Omori-Utsu law. (3) The frequency-magnitude distribution of micro-seismicity in our experiments followed a Gutenberg-Richter distribution with an average value of $b \approx 1.1$ and a range between

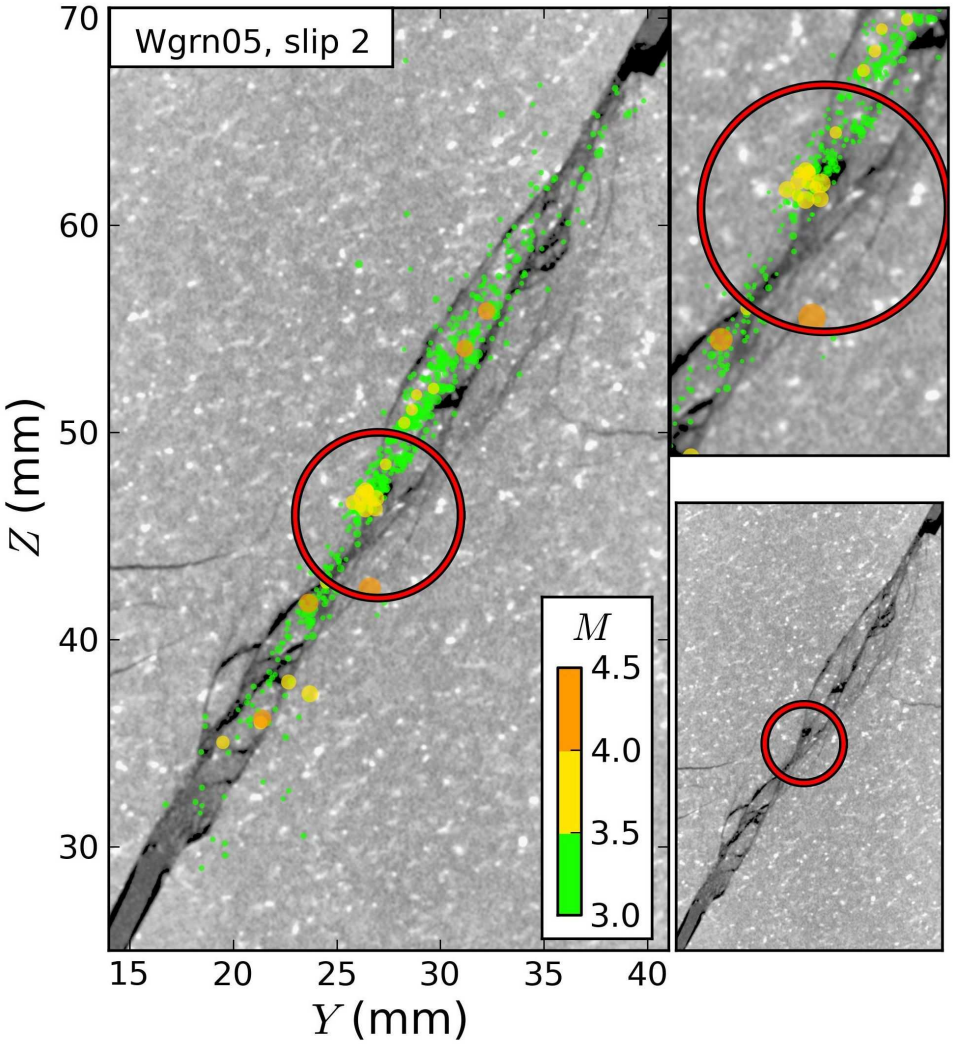

Figure 3.13: CT-scan of central part of sample obtained after the experiments and AE-hypocenters (colored dots) for the stick periods before slip event 2 of WGRN05. The colors of hypo-center locations corresponds to their magnitudes. The red circle highlights the likely site of a large asperity which was centered at [27,45].

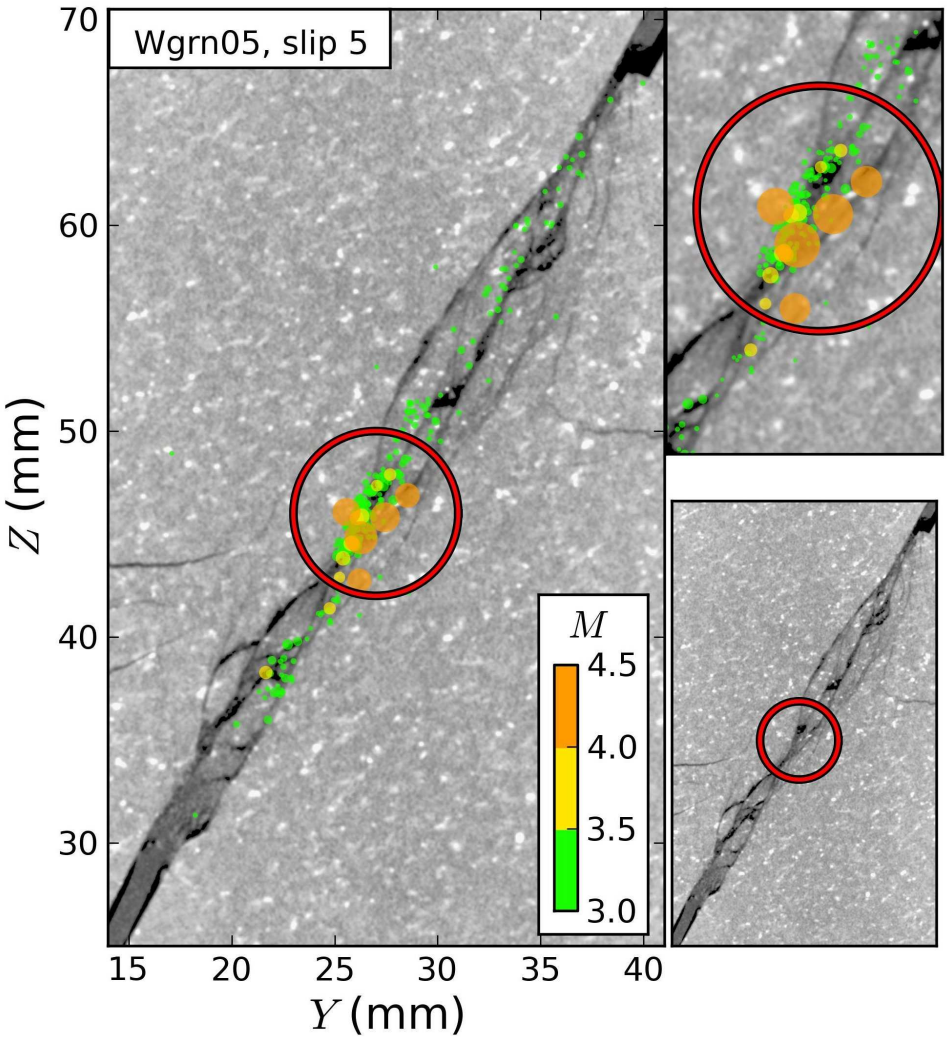

Figure 3.14: CT-scan and AE hypocenters colored according to magnitude for foreshocks to slip event 5 of WGRN05. Most of the AE activity is concentrated within the asperity region indicated by a red circle.

0.7 and 1.3, which is similar to values observed for earthquake catalogs. b-values were higher for aftershock sequences than for foreshocks which is in agreement with Weeks et al. (1978). (4) Similarly to studies conducted on natural seismicity, we performed a detailed b-value mapping based on AEs that occured before macroscopic slip events. The spatial mapping revealed a connection between asperity regions and areas of low b-values. This connection has also been observed for areas of increased fault strength within the continental crust (Wiemer and Wyss, 1997; Wyss et al., 2000; Schorlemmer and Wiemer, 2005). The spatial variations of b-values before slip onsets seem to be a promising tool for the characterization of fault heterogeneity. Absolute b-values cannot be meaningfully compared between laboratory experiments and real earthquakes (or even between different earthquake catalogs) because they depend partly on magnitude definitions.

We observed higher AE foreshock densities and high moment release associated with asperity regions. Slip events nucleated in the proximity or from within asperity regions, coinciding with areas of low foreshock b-value. A precise estimate of size and location of asperities was limited by the spatial resolution of b-value maps. The analysis of foreshock hypocenter distributions demonstrated that large events occurred preferably at the boundaries of asperity regions. Both low and high foreshock activity regions are found within or close to asperity regions forming a distinguishable contrast which was not observed in other areas of the fault.

The foreshock densities changed abruptly close to the asperity region before most of the macroscopic slips. Slip event 5 of WGRN05 resembled an exception in that most of the activity was focused within the asperity region prior to slip. This event was connected to low post-rupture strength and the largest stress drop. Slip event 6 again was preceded by the same characteristics of low b, high AE density at asperity edges, and higher moment release. This indicates that the geometric asperity remained largely stationary within the amount of applied displacement despite of high AE activity close by and many slip events which nucleated in its proximity.

In the absence of large, geometric heterogeneity, for example, during fracture experiments of homogeneous rock samples, stress concentrations identified by AE clusters are usually localized at the outer sample surface (Lockner et al., 1991a). During our experiments we did not observe AE clustering at the sample boundaries or in proximity to the tips of the notches, but rather AEs appeared to localize close to the fault and clustered in certain areas on the fault plane. The fact that AE activity occurred localized within a zone of high damage is also connected to a lack of a characteristic length scale of AEs. Both AE-based FMDs and b-values, computed from events

within a volume close to the fault surface, did not show a preferred AE magnitude. The region around the fault axis was dominated by high damage, i.e. crushed grains and high micro-crack densities as a result of a series of stick-slips. Initial grain size distributions were unlikely to have had a significant influence on micro cracking and AE magnitudes after several slip events and sample fracture. This supports our interpretation that fault plane asperities were one main factor in controlling the locations and size of AEs.

Our experiments provide the possibility to monitor the evolution of a natural fracture surface to a fault zone that contains a gouge layer, a damage zone, and the intact host rock. The largely persistent asperity regions were closely connected to the creation of macroscopic slip events. The faults of both experiments, WGRN04 and WGRN05, showed evidence of smoothing with successive slip events which could be recognized by more distributed micro-seismicity occurrences and lower residual stresses after slip events.

We observed a set of small and large slip events with various stress drops. Slip events within one experiment had the potential to grow both small or large at similar bulk stresses. This indicates that additionally to far field stress levels local stress field perturbations as a result of geometric fault heterogeneity seem to have a large influence on slip event size, stress drop, and duration. Large slip events were connected to differential stress drops between 130–370 MPa, corresponding to a drop in shear stress between 57 and 160 MPa. The small slip events had a maximum differential stress drop of $\sim$ 40 MPa. Slip events could be separated into small stress drop events with long duration and large stress drop events that had short slip durations ($\Delta t \leq 0.1$ s). This difference could possibly be used to evaluate if slip events are likely to grow to large sizes before the rupture actually stops. Stress drops of slip events with short durations were larger than for mining-induced seismicity which exhibits shear stress drops of up to 70 MPa (McGarr et al., 1979). A true comparison between natural and laboratory stress drops is limited because of the large influence of the loading frame stiffness on lab-results (Brace and Byerlee, 1966).

One major difference between our stick-slip events and natural seismicity is that none of the macroscopic slips were contained within the fault surface but rather caused slip along the entire fault. In contrast to strike-slip earthquakes, which usually nucleate and stop within the fault zone, the end of our ruptures were limited by the sample dimensions and would otherwise extend further. This poses a problem on the estimation of earthquake-equivalent seismic moment and rupture area for our laboratory slip events, and could partially be responsible for high stress drops.

Even though we found many similarities between AE statistics and those of crustal seismicity, the majority of AE source types differ from crustal earthquakes. AE moment tensors usually contain large isotropic components. These could be a result of micro-mechanical processes only observable at lab scales, for example, damage and surface creation due to tensile cracking and grain fracture. Despite the deviations of AE sources at the smallest scale, some of the larger magnitude AE events can be modeled as double couple sources (Zang et al., 1998; Thompson et al., 2009).

3.6 Conclusions

We conducted triaxial compression experiments on three Westerly granite samples with and without notches and recorded mechanical and seismic data throughout each experiment. During triaxial loading of the previously created fault, several macroscopic slip events occurred with small and large stress drops. Larger slip events had shorter slip duration with increasing stress drops which could possibly be used to determine the size of a rupture before it actually stopped. The two experiments on notched rock specimens (WGRN04, WGRN05) produced a series of nine stick-slip events. Eight out of these nine events nucleated within areas of high foreshock moment release, AE-event density, and low b-value. We demonstrated similarities between microseismicity connected to stick-slips and natural seismicity. An asperity region was identified in CT-scan images of specimen WGRN05 by anomalously thin fault zone width. The asperity definition based on AE data coincided with the same area. The overall AE distribution indicates a fault smoothing process after several stick-slips as a result of the failure of large asperities which probably let to a broader distribution of the stress on many load bearing asperities.

Larger scale asperities which approach their critical strength are connected to locally more abundant high amplitude AE events and to the nucleation spots of large slips. Highly stressed asperities cause events to grow larger once they nucleate, providing an explanation for relatively lower b-values. The regions of spatial seismicity anomalies show the same characteristics during several stick-slip sequences, indicating the persistence of fault-plane heterogeneity over extended periods. We note a similarity between the current laboratory findings and seismicity based asperity characterization at the San Jacinto-Elsinore fault system (Wyss et al., 2000), the Hayward fault in Northern California (Wyss, 2001) and the Parkfield section of the San Andreas fault (Wiemer and Wyss, 1997; Schorlemmer et al., 2004a). These studies showed that crustal scale asperities are

connected to low b-value anomalies and can influence the nucleation points and slip distribution of large-magnitude earthquakes. High-resolution mapping of b-values, seismic moment, event density, and the identification of connected areas with large contrasts in seismic activity could be used to further improve asperity identification based on natural seismicity.

4 Acoustic emissions document stress changes over many seismic cycles in stick-slip experiments

4.1 Abstract

The statistics of large earthquakes commonly involve large uncertainties due to the lack of long-term, robust earthquake recordings. Small-scale seismic events are abundant and can be used to examine variations in fault structure and stress. We report on the connection between stress and micro-seismic event statistics prior to the possibly smallest earthquakes: those generated in the laboratory. We investigate variations in seismic b-value of acoustic emission events during the stress build-up and release on laboratory-created fault zones. We show that b-values mirror periodic stress changes that occur during series of stick-slip events, and are correlated with stress over many seismic cycles. Moreover, the amount of b-value increase associated with slip events indicates the extent of the corresponding stress drop. Consequently, b-value variations can be used to approximate the stress state on a fault: a possible tool for the advancement of time-dependent seismic hazard assessment.

4.2 Introduction

Seismicity provides the most readily available information about crustal stress heterogeneity and stress orientations (e.g. Gephart and Forsyth, 1984; Michael, 1987; Schorlemmer et al., 2005; Narteau et al., 2009). Recent studies of natural and induced micro-seismicity (Schorlemmer et al., 2004a; Bachmann et al., 2012; Tormann et al., 2012) have drawn from laboratory insights (Scholz, 1968; Main et al., 1989; Meredith et al., 1990; Lockner et al., 1991b; Lei et al., 2000; Amitrano, 2003) to interpret spatial b-value (slope of the frequency-magnitude distribution) variations in terms of crustal stress changes. Increasing stresses in laboratory experiments on intact samples cause b-values to drop prior to failure. This drop is observed for a range of rock types (e.g. Main et al., 1989; Thompson et al., 2006). In the Earth's continental crust, low b-value anomalies have been widely observed, e. g. in California (Wiemer and Wyss, 1997; Wyss et al., 2000; Wyss, 2001) and also for induced micro-seismicity with magnitudes down to $M = -4.4$ (Kwiatek et al., 2010). Regions of low b-value can be connected to fault-structural heterogeneity and local stress concentrations which cause seismic events to grow to relatively larger sizes once they start to

nucleate (Goebel et al., 2012).

While spatial variation in b-value have already been used to formulate forecasts for large earthquakes ($M \geq 5.0$) in a time-independent sense (Schorlemmer et al., 2004b; Wiemer and Schorlemmer, 2007; Gulia et al., 2010), temporal variations in b are more controversial, partially due to a lack of long-term, homogeneous earthquake recordings. A recent study suggested that there is no statistical-significant predictive power in temporal variations of b-values, at least for predictions of earthquakes with $M = 4.0$–6.2 (Parsons, 2007). Others, however, view decreasing b-values as a possible precursor for the occurrence of large earthquakes (i. e. events with $M \gtrsim 6.0$) (Wyss, 1990; Imoto, 1991; Nanjo et al., 2012). Part of the current controversy is due to *a-posteriori* observations about phenomena preceding individual seismic events that would not withstand rigorous, statistical testing. Such observations are likely biased because of the intentional search for anomalies. Furthermore, the interpretation of b-value variations in nature is non-unique due to the intrinsic complexity of the faulting process, and the lack of supportive observations, e. g. of stress variations in borehole measurements. This emphasizes the importance of a detailed understanding of the mechanisms behind b-value variations.

Within the framework of our experiments, we are able to overcome some of these obstacles. We examine physical conditions that cause b-values to decrease during several seismic cycles on laboratory faults, which cannot readily be done in nature. Despite the inherent difference in scale between laboratory and natural seismicity, several similarities have been highlighted by recent studies. In particular, sample-scale faults in the laboratory show structural similarities to upper-crustal faults (Amitrano and Schmittbuhl, 2002) and the statistics of laboratory acoustic emission (AE) events exhibit patterns similar to natural seismicity (Goebel et al., 2012).

High-frequency AE events in laboratory tests are associated with the formation of and slip on micro-cracks. This type of micro-seismic event activity can be associated with distinct pre-failure stages during loading of intact samples (Lockner et al., 1991b; Lei et al., 2000). The macroscopic failure of intact samples is generally preceded by abruptly increasing AE-rates, increasing micro-seismic moment release, and decreasing Gutenberg-Richter b-values (Main et al., 1989; Meredith et al., 1990; Sammonds et al., 1992; Liakopoulou-Morris et al., 1994). A possible explanation for the connection between b and stress is the extension of pre-existing micro-crack populations by stress-corrosion and crack-coalescence leading up to the failure of intact samples (Main et al., 1992).

Previous laboratory experiments predominantly focused on macroscopic failure of intact samples or stick-slip motion of planar interfaces. We expand on these experiments through creating structurally-complex fault systems starting from incipient fracture surfaces and by documenting variations in stress and AE statistics during series of stick-slip events.

4.3 Experimental setup, methods, and AE-data

In the following, we describe loading conditions and sample geometry which were chosen to represent natural faulting conditions as closely as possible. We report on four triaxial experiments (W4, W5, W7, W8), conducted on cylindrical (radius = 2 cm, height = 10.7 cm) specimens at constant loading rates ($\dot{\epsilon} \sim 3 \cdot 10^{-6}$ s^{-1}) at GFZ-Potsdam, Germany. All experiments were performed on oven-dried samples at room temperatures, with constant confining pressures ($P_c = 150$ MPa). We introduced 1.5–2.5 cm deep saw-cut notches at a 30° angle to the loading axis to localize faulting at the center of the specimens during initial fracture and subsequent stick-slip sliding. The results presented here are from the stick-slip sliding stage of previously fractured specimens. Our initial condition, i. e. an incipient fracture surface that develops into a fault zone, can be seen as an analog for the structural complexity of natural fault zones. To monitor micro-crack formation and sample deformation, strain gauges and AE sensors were glued to the specimen surface (Suppl. Figure 1 left). We employed a high-speed (10 MHz sampling frequency) and accuracy (16 bits amplitude resolution) AE system, enabling the documentation of micro-mechanical processes that occurred in temporal proximity to slip instabilities. AE events were recorded using a miniature seismic-array, consisting of 16, one-component, piezo-electric transducers. The location-uncertainty of AE hypocenters was estimated at 1–4 mm, depending on the proximity of the event to the edge of the array. The total number of successfully located AEs from each sample was between 34,141 and 97,847, which allowed robust measurements of b-value as a function of time. Variations in b-value were determined using a moving time window that contained an equal number of AE events. This optimized the temporal resolution of b-value computations while ensuring the same statistical significance of each value. We also scrutinized the effects of different sample sizes and sampling techniques on b-value trends to ensure reliability and consistency (see Section 4.6 at the end of this Chapter).

4.4 Results

If b-value is indeed an indicator of stress (Schorlemmer et al., 2005), we expect to observe a systematic relation between b and stress for stick-slip cycles on a fault during our experiments. Figure 1 shows results from experiment W5, which are typical of all experiments. The differential stress shows a characteristic saw-tooth pattern of gradual increase followed by an abrupt decrease during slip. At the same time, b-values decrease with increasing stresses and abruptly increase when the stresses drop during a slip event. The stress curve shows six slip events with large stress drops (LSDs), some of which were preceded by small stress-drop events (SSDs). The loading curve preceding the first three LSD events exhibits many SSDs. The b-value curves also show more fluctuations during these early cycles. Fluctuations in b are strongest during the first stick-slip cycle and decrease with successive LSDs so that the last three stick periods show a smoother, monotonic decrease. This evolution may be related to progressive fault smoothing, which is also indicated by decreasing residual stresses with successive LSD events.

Figure 4.2 shows b as a function of normalized stress (fraction of maximum stress) for the six LSD events in experiment W5. The relationship between b and stress is approximately linear for high differential stresses above $\approx$ 55% of the peak stress. Below this value, only few AE events were observed and b-values tend to show more scatter. This scatter is likely related to AEs that occurred due to the reduction of pore space at the initial stage of a loading cycle.

The three other experiments confirmed the relationship between b-value and stress (Suppl. Figure 5). This relationship was most pronounced for experiment W8 whereas experiment W4 showed the smallest change in b-value with larger applied stresses and the scatter in b-value was comparably large. The scatter at elevated stresses in Figure 4.2 and during the other experiments may be related to larger fluctuations in b associated with geometric complexity especially before the initial LSD events of an experiment.

We also investigated if b values carry additional information during high-stress regimes, for example about the amount of stress release connected to SSD or LSD events. We estimated the stress-drop related increases in b-value from the difference between minimum before and maximum b-value after a stress-drop event. The SSD events produced relatively smaller increases in b while LSD events caused a larger upward jump in b-values (Figure 4.3). On average, the b-value jumps are higher for larger stress drops and exhibit a positive correlation with a Pearson's corre-

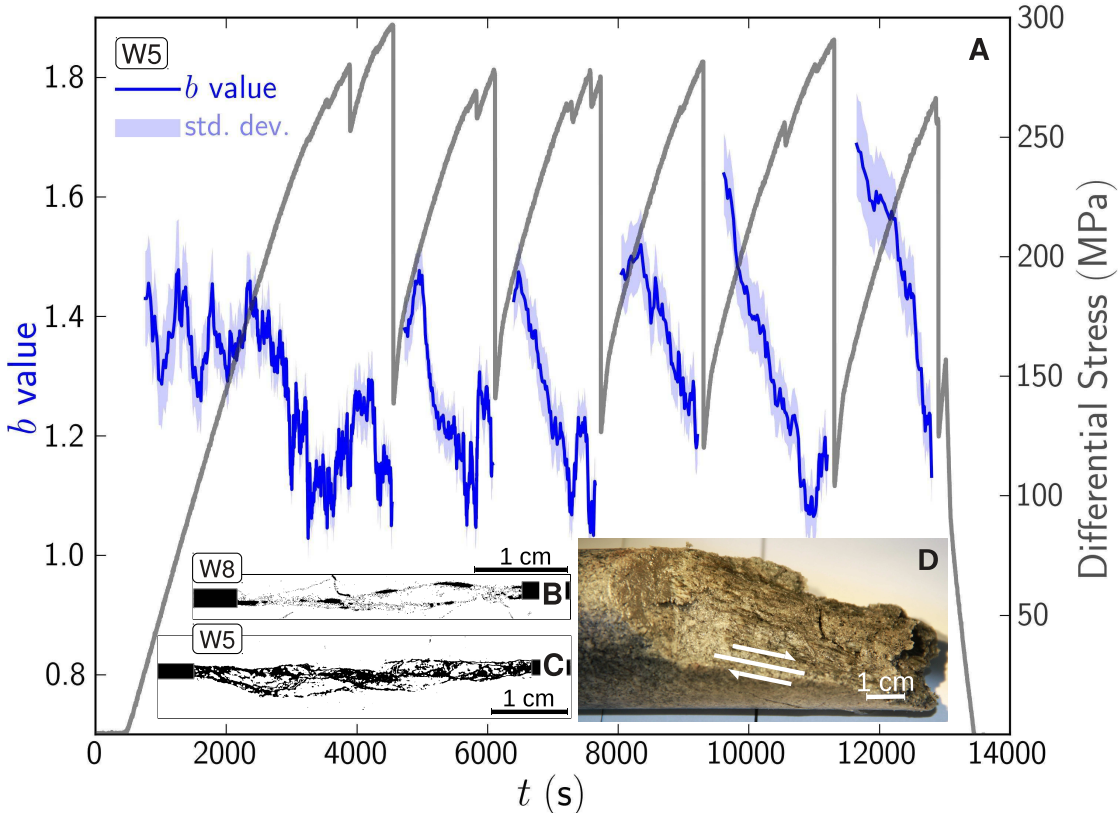

Figure 4.1: Influence of cyclical stress changes during stick-slip type fault movement on temporal b-value variations. **A,** Both, differential stress (gray line) and b-values (blue line), exhibit a characteristic saw-tooth pattern but with opposite sense (experiment W5). b-values were computed for 1200 AE sample windows and a 50 event step size. Standard errors in b are indicated by blue-shaded areas. **B, C,** Post-experimental X-ray computer tomography images of fault zones at the center of the respective samples. The damage zone complexity varied between samples with relatively longer (W5), compared to relatively shorter fracture surfaces (W8). **D,** Photographic image of post-experimental slip surface with slip-parallel lineations.

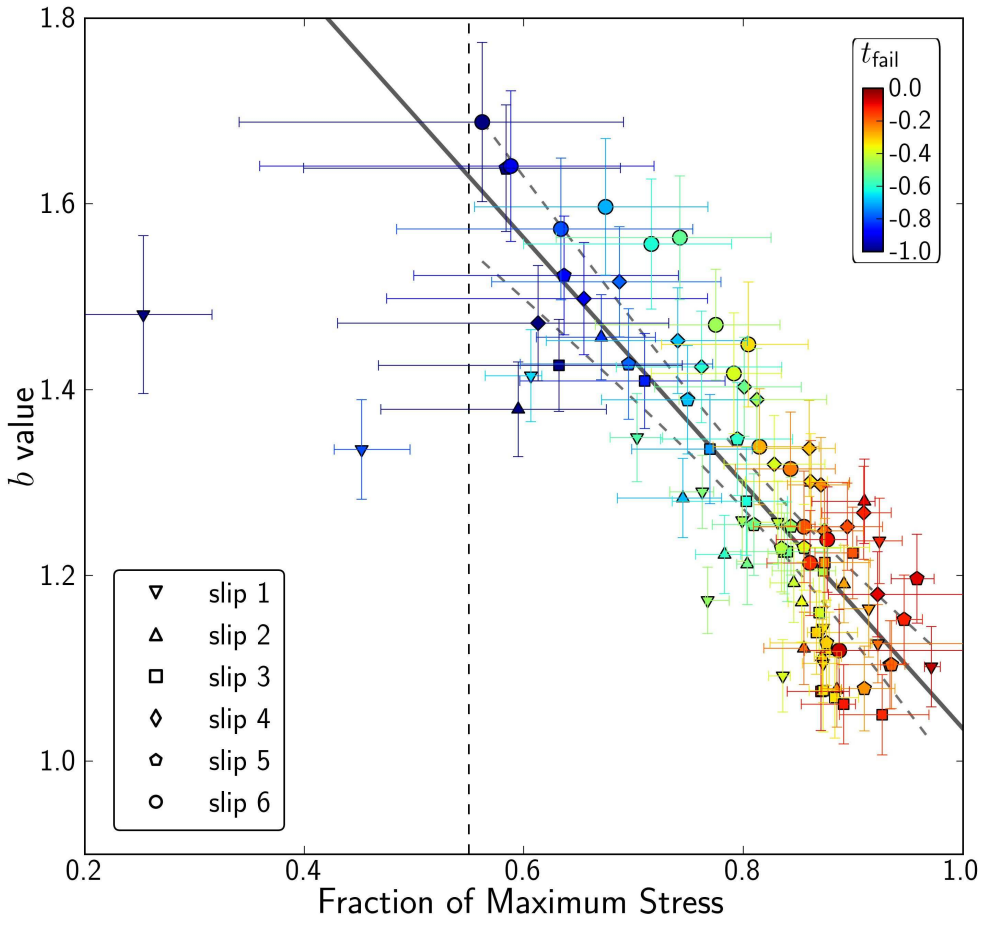

Figure 4.2: b-values drop closer to failure and show an inverse, linear relationship with the differential stress. Depicted are results of all six stick-slips of experiment W5, normalized according to the maximum stress. The markers are colored according to the normalized time to failure (t_{fail}) and the marker symbols indicate individual stick-slip sequences. The curved dashed lines are the 95% confidence bounds of the regression line, and the vertical dashed line shows the 55% limit of the maximum stress used for the linear regression. The horizontal error bars show the extent of the stress window from which AEs were used for b-value computations. The vertical error bars are the standard error in b. For the linear regression using 1200 AE events for each b-value, we determined a Pearson's r of -0.84 which was significant at a 99% level.

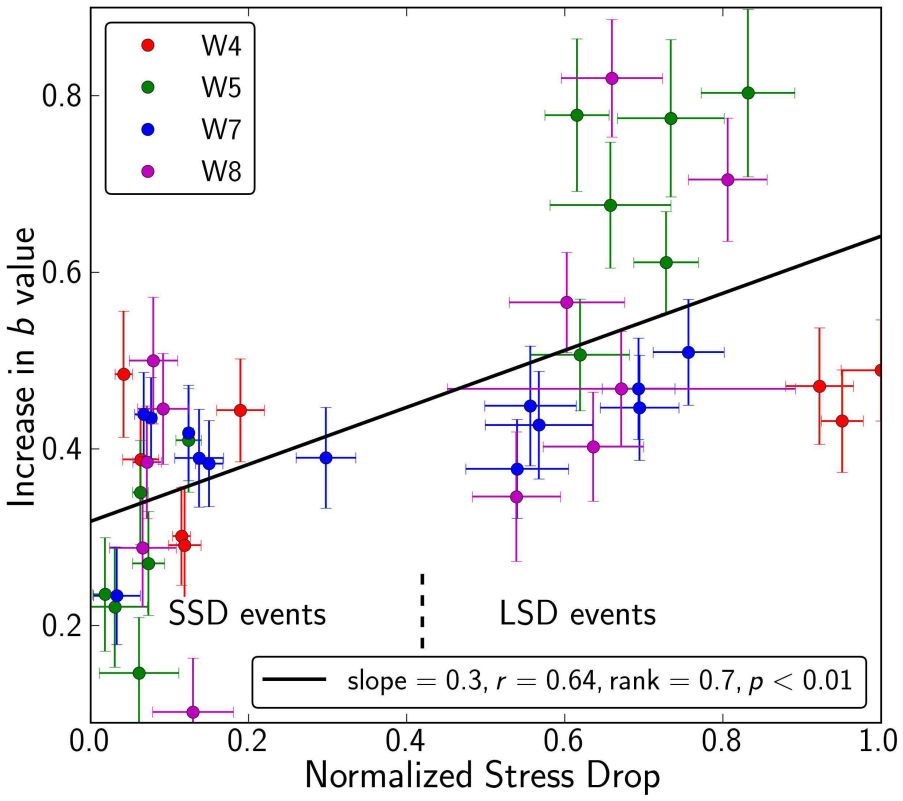

Figure 4.3: b value increase as function of connected stress drop for all experiments (see upper left legend for marker symbols). Stress drops and b value increase showed a linear correlation with Pearson's $r = 0.64$ (Spearman's rank = 0.7) which was significant on a 99% level. Error bars show statistical error in b-value estimates and the stress range that corresponds to the AE samples used for b-value computations.

lation coefficient of $r = 0.64$ for a sample size of $N_{\mathrm{AE}} = 600$. We explored this correlation over a range of sample sizes ($r = 0.53$ for $N_{\mathrm{AE}} = 300$, $r = 0.57$ for $N_{\mathrm{AE}} = 1200$ and $r = 0.57$ for $N_{\mathrm{AE}} = 3000$) confirming the connection between b-increases and stress-drops. Furthermore, we tested if this relation is also observed for shear stress drops which were computed for the effective fracture surface area, corrected for slip after each successive slip event (Scott et al., 1994; Tembe et al., 2010). The linear regression between slip-corrected shear stress drop and b value increase was characterized by a correlation of $r = 0.65$ which was significant at a 99% level. Thus, the amount of increase in b after slip appears to be related to the stress-release due to slip.

Assuming that the number of SSD events can serve as a proxy for the degree of structurally related complexity, we performed a systematic analysis of the connection between geometric com-

plexity and *b*-value variations. Stick-slip events that were preceded by fewer SSDs showed higher linear correlation coefficients between *b* and stress (Suppl. Figure 8), consistent with the hypothesis that *b*-value-stress relations are more pronounced for structurally less complex faults. Additionally, the times of *b*-value minima were closer to the LSD for stick-slips with fewer SSDs (Suppl. Figure 7). The *b*-value-stress relations depended also on the lengths of the laboratory faults, i. e. they were less linear for longer faults (Suppl. Figure 5). This is consistent with our observation that longer fracture surfaces showed more structural complexity in post-experimental X-ray computer tomography scans (Figure 4.1B–C), and structural complexity can obscure *b*-value-stress relations.

To investigate the importance of observational scales on the *b*-stress relation, we compared results from a LSD with a SSD event as well as with the failure of an intact sample (Figure 4.4). For the LSD and SSD event, we limited our observations to one dominant asperity region within the laboratory-created fault zone, identified through areas of low *b*-value, high seismic moment, and large AE density gradients (Goebel et al., 2012). The temporal variations of *b*-values based solely on AEs within asperity regions in Figure 4.4 show a clear monotonic decrease with increasing stresses before both SSD and LSD event, similar to the fracture of the intact sample, but on a different time scale. The previously observed variations in *b* on short time scales before the LSD events, which seemed to be connected to SSD events (see Figure 4.1), have largely disappeared, presumably because the SSD events occurred outside the asperity area under study. The similarity in the temporal evolution of *b* value before an initial fracture and the fracture of a single asperity suggest that the underlying micro-mechanical processes are similar. The additional complexity observed during slip on a rough fault plane are probably due to fault-structural heterogeneity.

4.5 Discussion and Conclusion

It is commonly assumed that *b*-values are stable in time and only reflect spatial variations in stress (Wiemer and Wyss, 1997; Westerhaus et al., 2002; Schorlemmer and Wiemer, 2005; Parsons, 2007). We observed that *b*-values vary significantly within a seismic cycle in stick-slip experiments and that the amount of increase in *b* after a slip event is related to the stress-drop (or the equivalent residual stress state on the fault after slip). This is consistent with a recent study of changes in *b*-value following the 1989 M6.9 Loma Prieta and the 2004 M6.0 Parkfield event which suggested that a rapid return of *b*-values to pre-failure levels indicate that the local stress field has not been

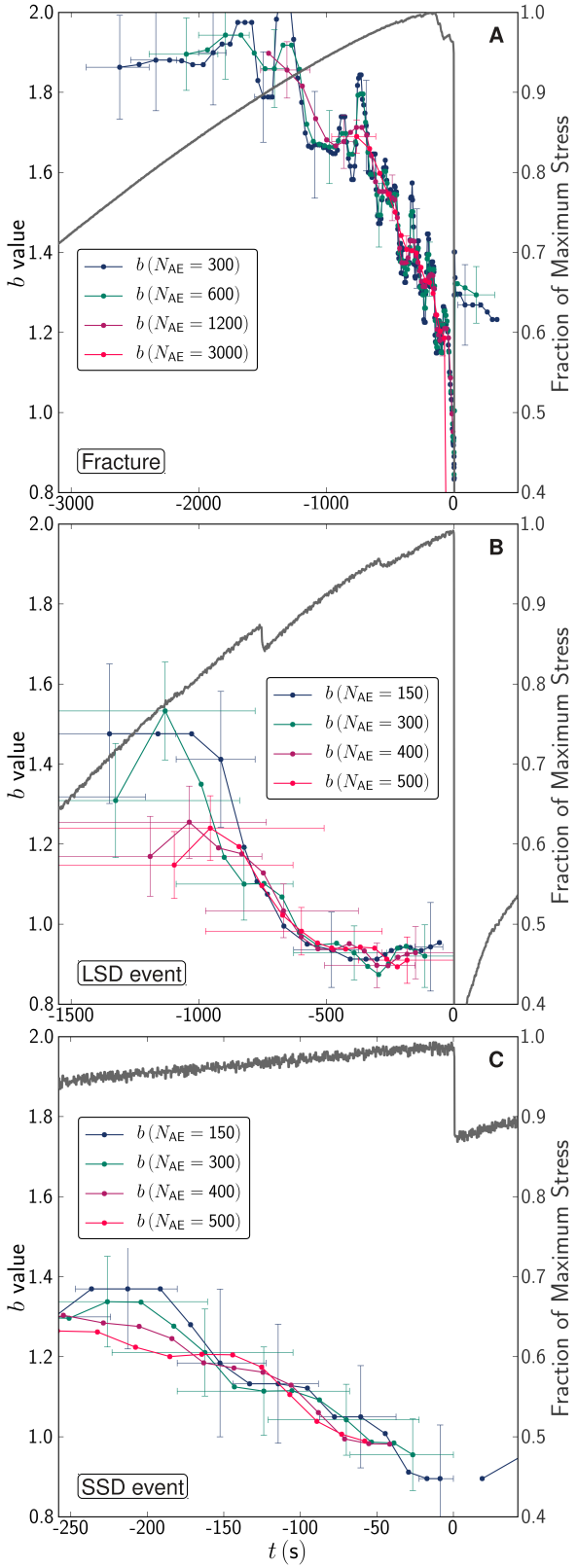

Figure 4.4: Comparison between b-value decrease preceding the initial fracture of an intact sample with b-value decrease in the neighborhood of a large asperity on a natural fault surface. b-values showed a characteristic decrease before the fracture of the intact sample (A) and before the occurrence of a LSD (B) as well as a SSD (C). The depicted LSD event corresponds to stick-slip event 5 of experiment W5 shown in Figure 4.1. b-value curves for the LSD and SSD event were computed based on AE events that were connected to an asperity region (see text for details). Stresses are normalized to peak stress of individual failure events.

reset and stresses quickly return to pre-failure levels (Tormann et al., 2012). Our results suggest that the magnitude of increase in *b*-value after failure can be associated with the effectiveness of a large earthquake to release stored shear stress on a fault. Relatively small amounts of stress release during a seismic event could possibly be caused by large structural heterogeneity within a fault zone.

The observed connection between decreasing *b*-values and increasing differential stresses substantiates previous findings of a *b*-value-stress dependence (Scholz, 1968; Amitrano, 2003; Schorlemmer et al., 2005). Our results are also in agreement with a stochastic model that explores variations of the Gutenberg-Richter relationship in the context of an inhomogeneous medium (Scholz, 1968). This model predicts that *b*-value is inversely related to the applied stress so that seismic events have a higher probability to grow to larger sizes if the stress level in the medium is high. Consequently, we also expect that an increase in the stress level on the fault, for example, by changing the fault angle or increasing the confining pressure would lead to a general decrease in *b*-value. The role of increasing confining pressures in reducing *b*-values has been shown during fracture and successive frictional sliding of granite samples (Amitrano, 2003).

Our results provide an explanation for the observed decrease in *b*-value in the source regions prior to large earthquakes (Nanjo et al., 2012). We suggest that the underlying physical processes governing *b*-value variations affect *b*-values on different time scales and over different fault volumes. Disregarding the importance of temporal and spatial scales may lead to a loss of physically driven *b*-value variations. *b*-values are more strongly correlated with stress for faults with less structural complexity and stick-slip sequences with simple, monotonic stress curves, i.e., without SSD events. This suggest that *b*-value-stress relations depend on fault complexity and are more strongly connected for smoother fault surfaces.

Natural faults are likely to contain additional complexity that cannot readily be explored within the framework of the current set of experiments. Our results suggest that this complexity could partially be reduced by choosing an adequate subscale of a fault volume for the analysis of temporal *b*-value variations, providing a possible means to explore the relative stress state of a fault segment and its position within the seismic cycle. Furthermore, a detailed understanding of temporal *b*-value variations is important for intermediate and long-term earthquake forecasting efforts, especially time-dependent forecast models for hazard assessment.

4.6 Supplementary Information: Acoustic emissions document changes in stress over many seismic cycles in analog experiments

In chapter 4, we investigated temporal changes in *b*-value (slope of the frequency magnitude distribution) during series of stick-slip events on complex, laboratory created fault zones, showing that *b*-value and differential stress are correlated over multiple seismic cycles. Within the scope of this supplementary material, we describe more details of the experimental setup, the acoustic emission (AE) recording system and the sample preparation. Furthermore, we show details of variations in stress, *b*-value, and seismic moment and analyze the *b*-stress relationships for different periods, i.e., for entire experiments, individual stick-slip events within an experiment and at periods of elevated stress closer to failure. Lastly, we explore the influence of fault complexity on *b*-stress relationships.

4.6.1 Experimental set-up and sample geometry

In this section, we briefly discuss sample preparation, loading conditions, and acquisition of AE data. A more detailed treatment of the experimental setup can be found in Stanchits et al. (2006) and Goebel et al. (2012). Within the scope of the current experimental series, we used homogeneous, undamaged Westerly granite samples. Westerly granite exhibits grain sizes between 0.05–2.2 mm with an average grain size of 0.75 mm (Stesky, 1978). The experiments were conducted at room temperatures on previously oven-dried samples. Initially, we fractured the intact part between two pre-cut, 30° notches at a confining pressure of 75 MPa. We then locked the created laboratory fault zone by increasing the confining pressure to 150 MPa and reactivated the fault by resuming axial loading. The reactivation stage was characterized by a stick-slip type fault motion in which episodes of stress increase alternate with macroscopic slip events, releasing the stored elastic energy. The length of the saw-cut notches increased systematically from 1.5 to 2.3 cm with the four successive experiments (W4, W5, W7, W8). The connected fracture surface sizes decreased accordingly from 5–3 cm (Table 4.1). The notches resulted in $\sim$1 mm wide gaps which were closed by inserting low-friction teflon sheets. The length increase of the saw-cut notches resulted in lower peak axial stresses prior to sample failure during fracture and frictional sliding.

Table 4.1 shows the mechanical data and loading conditions of the fracture and frictional sliding stage of the four experiments, conducted at triaxial loading conditions, constant hydrostatic

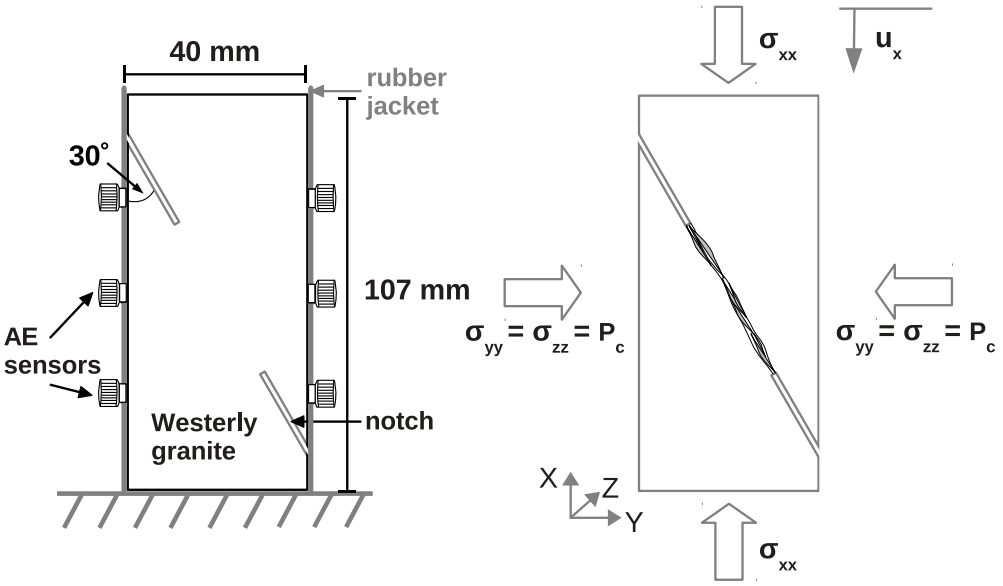

Figure 4.5: Schematics of sample geometry and dimensions (left) as well as loading conditions (right). Initially, the intact part of the sample was fractured, the fault was then locked by an increase in confining pressure after which axial loading was resumed until a series of stick-slips occurred.

confining pressures and constant vertical displacement rates ($\dot{\epsilon} \sim 3 \cdot 10^{-6}$ s^{-1}).

Seismic waveforms of AE events were recorded using a 3D transducer array of 16 piezo-electric sensors. Full AE waveforms were digitized with a 10 MHz sampling frequency corresponding to a time resolution of 0.1 μs and an amplitude resolution of 16 bits. Based on the AE records which contain between 34,141 and 97,847 events, we computed the average amplitude from the maximum amplitude of each channel in volts and corrected for geometric spreading between source and receiver. Based on these amplitudes, we assigned magnitudes, $M = \log\left(\frac{A}{A_c}\right)$, where A_c describes a reference value in volts and seismic moments to each event at an experiment-specific scale. We investigated the temporal variations of b-values which are defined as the slope of the AE frequency-magnitude distributions:

$$\log N = a - bM, \tag{4.1}$$

where N is the number of AE events of larger or equal magnitude than M and a is a constant representing the AE activity. For reliable b-value estimates, we required distributions to contain at least 200 AE events. b-values were computed using the maximum-likelihood method (Aki, 1965; Utsu et al., 1965; Bender, 1983), assuming that the magnitudes of AE events were largely

Sample	l_{RS} (cm)	$P_{c_{frac}}$ (MPa)	$P_{c_{slide}}$ (MPa)	$\sigma_{max_{frac}}$ (MPa)	$\sigma_{max_{slide}}$ (MPa)	$U_{x_{max}}$ (mm)
W4	5.0±0.15	75±0.5	150±0.5	635±6	365±6	3.0±0.003
W5	4.2±0.15	75±0.5	150±0.5	510±6	296±6	4.1±0.003
W7	3.7±0.15	75±0.5	150±0.5	450±6	293±6	4.3±0.003
W8	3.0±0.15	75±0.5	150±0.5	380±6	288±6	3.7±0.003

Table 4.1: Mechanical data and loading conditions of the four presented experiments. The length of the saw-cut notches was gradually increased from W4 to W8 which led to a net reduction of the rough surface area. l_{RS}: approximate length of the rough fracture surface, $P_{c_{frac}}$: confining pressure during fracture stage, $P_{c_{slide}}$: confining pressure during frictional sliding of the previously generated fault, $\sigma_{max_{frac}}$: maximal differential stress during fracture stage, $\sigma_{max_{slide}}$: maximal differential stress during sliding, $U_{x_{max}}$: maximum vertical displacement of loading piston.

independent at the considered time scales:

$$b = \frac{1}{\overline{M} - M_c} \log(e). \tag{4.2}$$

Here, $\overline{M}$ is the mean magnitude, $e = \exp(1)$ and M_c is the magnitude of completeness corrected for bin size to account for possible biases of discrete magnitude bin size (Utsu et al., 1965; Guo and Ogata, 1997). For the temporal analysis we associated each b-value with the temporal mean of each sample window and both minimum and maximum values are shown (e. g. Figure. 4.6), demonstrating the extent of the corresponding time window.

Based on the relative magnitudes, which ranged from 0.84 to 5.0, we computed b values for certain time and stress windows. We scrutinized the influence of a variety of sample sizes and sampling techniques to avoid imaging artifacts within b value trends. We determined the magnitude of completeness (M_c) for the entire duration of each experiment, assuming constant array geometry and detection sensitivity, by determining the deviation from linearity of the cumulative frequency-magnitude distributions (FMDs). An accurate estimation of b values was ensured by using the maximum-likelihood method (Aki, 1965; Utsu et al., 1965; Bender, 1983), and verified through inspection of large sets of FMDs and corresponding power-law fits (e. g. Figure 4.6).

4.6.2 b value trends during a single stick-slip sequence

We show the details of b values and stresses for the example of stick-slip sequence 5 of experiment W5. During loading of the structurally complex fault zone, we observed two small stress-drop

events (SSDs) at $t = 10,100$ s and $10,500$ s and one large stress-drop event (LSD) which occurred at $t = 10,800$ s (Figure 4.6). b values generally decreased with larger stresses and closer proximity to failure. They also showed some short period variations, i. e. a local b value minimum followed by an increase in b that coincided with the onsets of SSDs. Expectedly, such features were most pronounced for small sample sizes of b computations. Thus, also small-scale stress perturbations had an influence on the frequency-magnitude distributions of AEs and produced a characteristic trend of decreasing b before and higher b values after the SSDs, similar to the observed long-term trends.

Nevertheless, a longterm decrease in b was observed for all sample sizes and was generally higher than the estimated standard errors in b. The overlap and extent of time windows used for b value computations were also smaller than the observed variations in b values.

Furthermore, we analyzed the difference between FMDs which are the basis for b value computations. FMDs were determined for three different time frames at the center and toward the end of an inter-slip period as well as immediately after the onset of the LSD (Figure 4.6c). The slope of the FMDs was lowest several hundred seconds before the slip onset. Here, we also observed a pronounced increase in the right tail (between $M = 3.5$–4.9) of the FMD. The relative proportion of small magnitude AEs was higher at low stress level and smaller during the high-stress regime. The highest FMD-slopes were observed in the third time window starting at ~ 2 s after the LSD.

4.6.3 Comparison between seismic moments and b values

Once the fault started to slip, we expected large magnitude AEs to occur in greater abundance thus perturbing the b value curves downward. To investigate whether b value trends were influenced by LSD associated AE events, we removed all AEs in temporal proximity to slip onsets. This was done by excluding AEs within a period from 0.5 s before, until 20 s after slip onsets which is when the AE rates returned to the background rate. We then stacked b values computed from the residual record (Figure 4.7). b values were compared between all inter-slip periods by using AEs within a constant-length, sliding time window. Initial inter-slip periods were excluded due to their untypical variations in AE rate and b value. Again, b values decreased with increasing stresses while average seismic moment, computed by summing the moment within constant time windows and normalizing by the corresponding AE number, increased over similar periods. A b value maximum of 1.55 was observed $\sim$ 1200 s before slip onset, followed by a steady decrease to $b = 1.2$ at

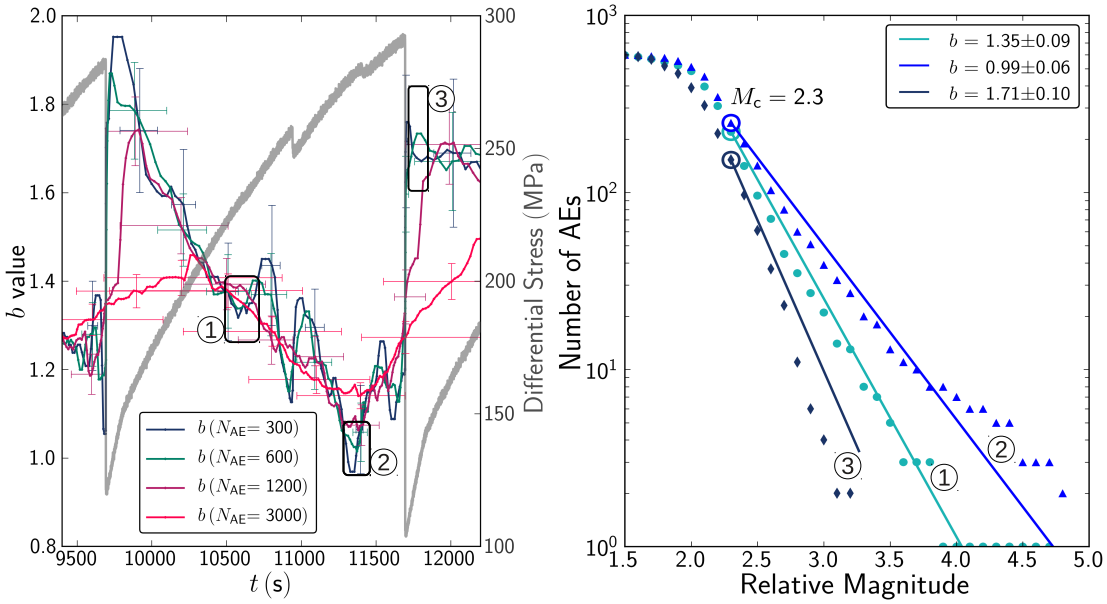

Figure 4.6: Temporal changes in b and differential stress for one stick-slip period (left). b values were computed for four different sample sizes and curves are colored accordingly. The gray frames, labeled from 1 to 3, highlight b values for which the FMDs are shown in the right plot. Vertical errors are standard errors in b, horizontal error bars indicate the extent of the sliding time windows of AE sampling used for b value computation which stopped close to a LSD and started again right after (see text for explanation). The height of the frames corresponds to the standard error in b and the width to the length of the corresponding time windows. (c) FMDs for three different periods but with the same sampling ($N_{AE} = 600$), taken from the intermediate (1, light blue dots), high (2, dark blue triangle) and low stress regimes (3, black diamonds) during and right after inter-slip period between LSD 4 and LSD 5.

$t \approx -200$ s. This decrease was followed by slightly higher b values leading up to slip onsets. For b values averaged over inter-slip periods of all experiments we observed a decrease from 1.41 at $t \approx -1100$ s to 1.2 at $t \approx -400$ s, followed by a minimum which lasted until the onset of the LSDs. The seismic moment showed a long-term non-monotonic increase up to $\sim$ 420 s before failure which also marked the time of maximum moment release (Figure 4.7 bottom). This was followed by a period of rather abrupt, large changes with moment maxima at ≈ -300 s and ≈ -180 s and minima at ≈ -390 s to ≈ -350 s and ≈ -250 s to ≈ -180 s. The average seismic moment showed more short-period variations than the b value curves. Some of these variations were connected to SSDs. These findings underline the previous trends, which indicate a more abundant occurrence of large magnitude AEs during high-stress periods. b value curves were slightly smoother and less dominated by SSDs than seismic moment curves. The persistent observation of long-term decrease in b values shows that they were not simply caused by large AE events associated with LSD events but rather highlight the occurrences of relatively larger proportion of high-magnitude AEs closer to slip events.

4.6.4 Correlating stresses and b values

We tested if b values and stress can be described by an inverse relationship. We used AE sample sizes of 600 (left plot in Figure 4.8) and 3000 (right plot in Figure 4.8) events for b value computations. The corresponding stress levels were taken at the temporal mean of the respective AE samples used to calculate the b value. For each stick-slip cycle, we adapted the step-size of the sliding sample window to show the same number of b values. This allows for an easier comparison of b-stress trends between different stick-slip events. The linear Pearson correlation coefficients (r) for the linear-regressions of the entire experiment W5 were $r = -0.77$ for $N_{\mathrm{AE}} = 600$ and $r = -0.78$ for $N_{\mathrm{AE}} = 3000$. The standard errors decreased slightly from 0.11 to 0.07 for larger sample sizes. The scatter in b values was reduced for the larger sample size resulting in slightly better correlation while slope and intercept of the linear regression remained unchanged. Thus, the long-term trend could be described by a simple linear relationship. However, we also observed deviations from linearity at the beginning and end of an inter-slip period as well as within the high-stress regimes especially for $N_{\mathrm{AE}} = 600$. For simplicity, we decided to describe the correlation between stresses and b values with a linear model. However, other models might perform equally well or better at the cost of increasing the model complexity.

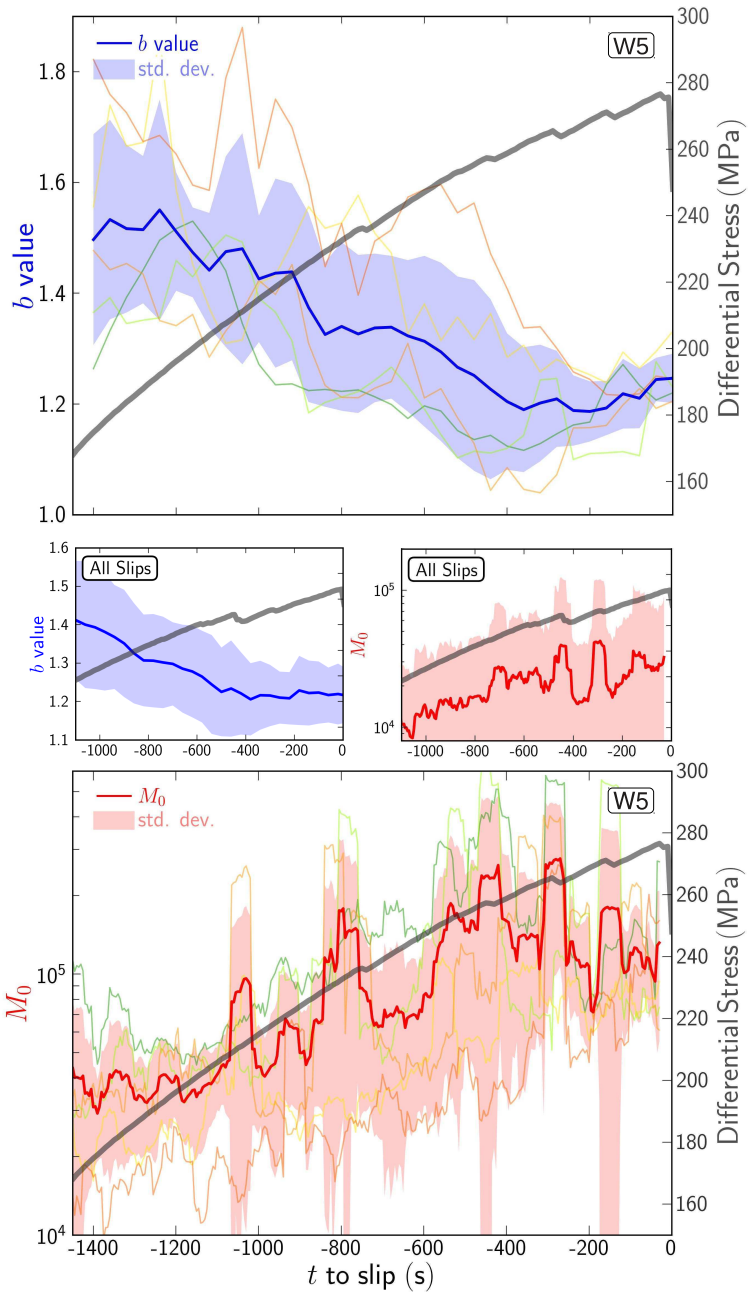

Figure 4.7: b values (top) and average seismic moment (bottom) for inter-slip periods excluding AE events in immediate temporal proximity to LSDs during experiment W5 (larger axes) and for all experiments (insets). For the larger frames, we used averaged b values and moments over inter-slip periods of experiment W5 excluding the first inter-slip period (see text for details). For the insets, we averaged over the inter-slip periods of all experiments. The shaded areas depict standard deviations from the averaged values. The onset of slip events is at $t = 0$.

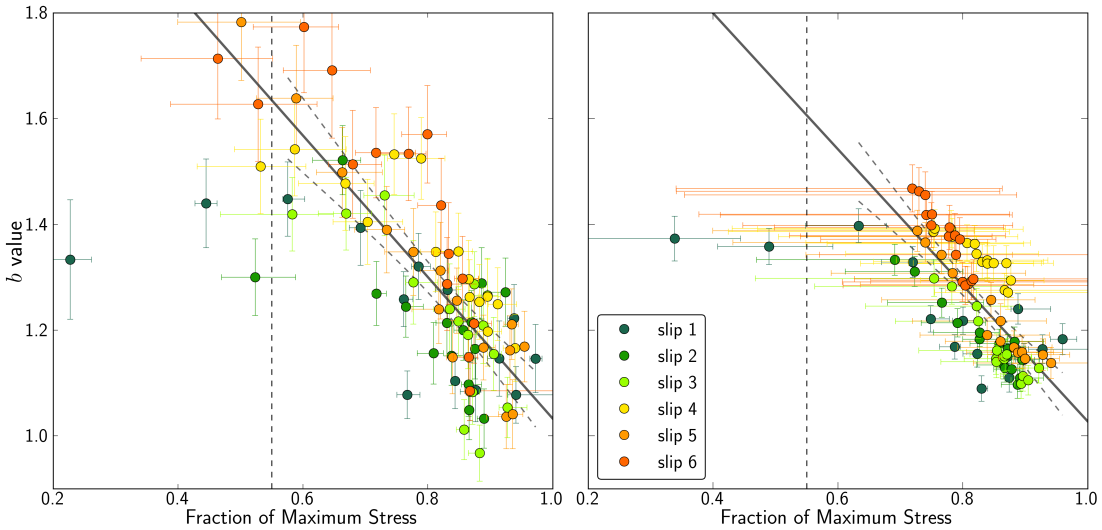

Figure 4.8: Linear regression of normalized differential stress and b value for all six stick-slips of W5 using a sample size of 600 (left) and 3000 AEs (right). The regression parameters for b and stress above 55% of the peak-stress were Pearson's $r = -0.77$ and $r = -0.78$ which were both significant at a 99% level, and the standard error of the modeled b values were 0.11 and 0.07. The markers are colored according to individual slip events. Vertical error bars indicate standard error in b value estimates and horizontal error bars show the range of stress from which AE events were sampled for b value computations. The dashed lines are the 95% confidence bounds of the regression line. The utilization of larger sample sizes improved the linear regression and the large scatter observed for smaller sample sizes was reduced especially for the low-stress regime.

We also tested if b values changed systematically with successive stick-slip events of different experiments. To this end, we display b value-stress relations for which b values again were computed from a constant number of AEs but adapted for different stick periods to display equal numbers of b values (Figure 4.9). Stresses were normalized to the peak-stress of individual inter-slip periods.

The previously established connection between stress and b, i. e. decreasing b values with increasing stresses was still observed, but with different degree of scatter and deviations from a simple linear relation, depending on individual experiments. Except for W4, b values decreased predominately monotonically during individual inter-slip periods. b values showed the largest scatter during individual inter-slip periods of experiment W4 and W7. These experiments also had the lowest correlation coefficients. W8 showed the highest correlation coefficient and a low standard error thus deviating the least from a linear trend whereas W4 deviated the most. The latter showed some local increases in b, partially caused by SSD occurrences.

4.6.5 b value and stress behavior within the high-stress regime

In this section, we investigate the more complex behavior within the high-stress regime. We focus on changes in the position of the b value minima within a stick-slip sequence, and the relation between stress release and b value increase.

We show two examples of temporal b value changes and variations with stress for individual inter-slip periods (Figure 4.10). Stick-slip events 1 and 6 of experiment W7 can be seen as end member cases in terms of the extent of non-linear deformation prior to failure. b values for stick-slip 1 decreased until $\sim$ 1600 s before failure which corresponds to $\approx$ 66% of the inter-slip period. This was followed by a complex behavior of repeated b value increase and subsequent decrease within the high-stress regime. This regime was connected to at least 5 SSDs which could be partially responsible for some of the variations in b. Within the final 300 s before failure (7% of inter-slip period), there was a decrease in b values from 1.28 to 1.17 while b values increased on an intermediate scale, starting at ≈ -1400 s (32% of the inter-slip period). The three SSDs with the largest stress drops were connected to noticeable b value jumps, however, not all b value fluctuations could be connected to changes in far-field stress. The statistically significant correlation coefficient was -0.56 for stick-slip event 1 of experiment W7 with partially large scatter and deviations from linearity especially above 85% of the peak stress.

The right side of Figure 4.10 shows the relatively less complex behavior of b value and stress

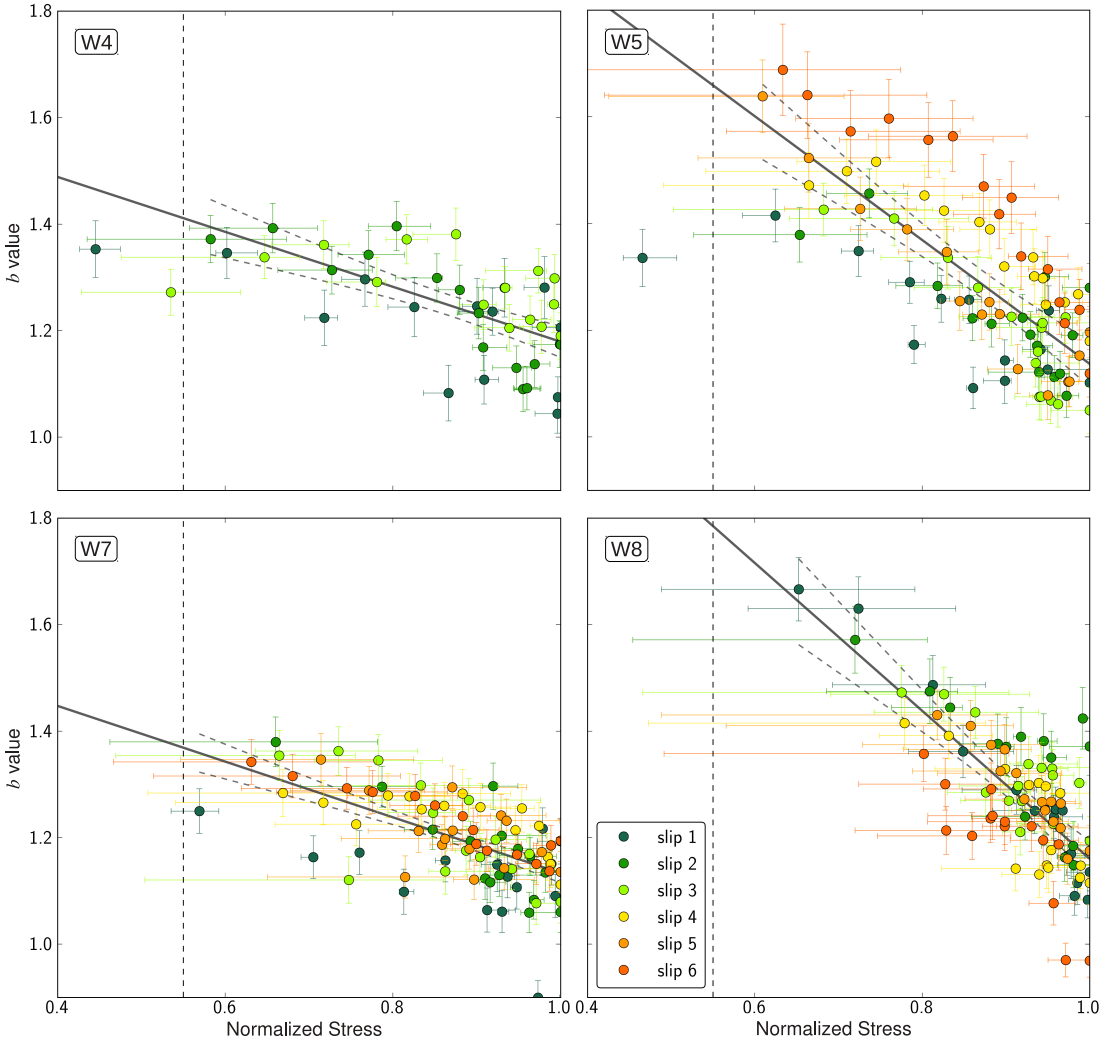

Figure 4.9: b values and stress normalized by peak-stresses of individual stick periods of all four experiments. b values were computed based on constant numbers of AEs. Error bars show standard error in b and extent of sample window for b value computations. b values decreased systematically with higher stresses. This decrease showed the smallest deviation from a linear trend for W8. The corresponding Pearson's r values were -0.62, -0.71, -0.64 and -0.77 and standard errors of the estimated dependent variable were 0.08, 0.11, 0.07 and 0.08.

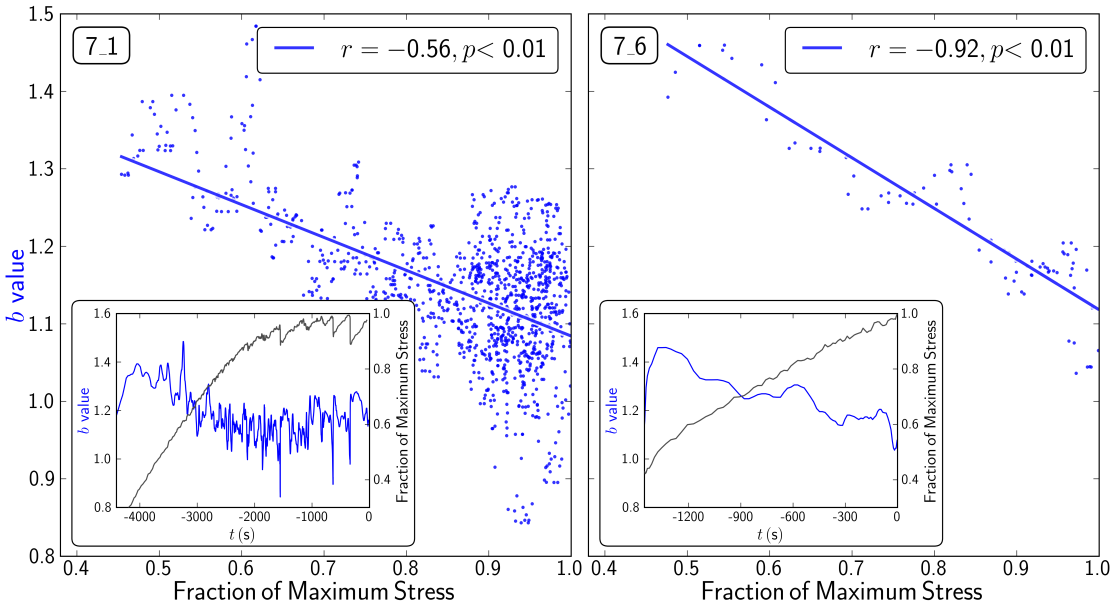

Figure 4.10: Examples of b value trends and stress for individual inter-slip periods for experiment W7. Shown here are both temporal trends (main axis) and b value-stress relations (insets) of slip event 7_1 (left) and 7_6 (right) which could be seen as end-member cases in terms of complexity in both stress and b value curves. b values were computed using 600 samples. The legend at the top right of each axis shows Pearson's r and significance of correlation, p.

during stick-slip 6 which had no SSDs. The b values decrease from a maximum of $b = 1.47$ at $t = -1390$ s to $b = 1.05$ approximately 20 s before failure. b value and differential stress showed a negative, linear relation with a coefficient of correlation of -0.92.

Naturally, there also existed a range of behavior between the two end-member cases. Inter-slip periods differed from one another by the degree of deviation from a linear relationship between stress and b value, the number of SSDs and the complexity of b values within the high-stress regime including the position of b value minima. The latter will be investigated in the following.

Figure 4.11 shows a systematic compilation of the positions of b value minima for all inter-slip periods. They were grouped according to the number of SSDs observed during the corresponding inter-slip period. The number of SSDs can be seen as a proxy for the amount of complexity during the high-stress regimes. Commonly, the times of b value minima averaged over inter-slip periods with the same number of SSDs (colored frames) occurred closer to failure if less SSDs were observed and also for smaller sample sizes of b value computations. The minima of b values based on sample sizes between 300–1200 AEs occurred, on average, at $t \geq -150$ s for inter-slip periods without SSDs while increasing numbers of SSDs also led to an increase in temporal distance to

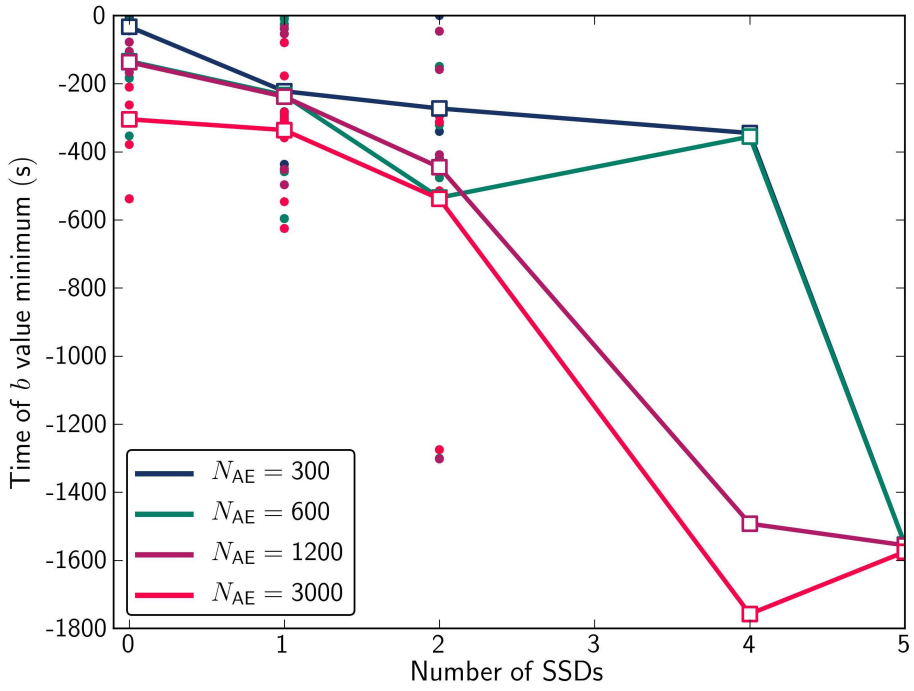

Figure 4.11: Times of b value minima relative to failure as function of number of SSDs for individual slip events (dots) and averaged over inter-slip periods with the same number of SSDs (frames). Colors are according to the employed sample sizes. The averaged times are connected by solid lines. This figure highlights both the influence of the amount of SSDs and sample sizes on the time of b value minima.

failure. With increasing number of SSDs, the average time of b value minima changed systematically, for example, for a sample size of 1200 AEs from $t = -150\,\mathrm{s}$, to $-240\,\mathrm{s}$, $-450\,\mathrm{s}$, -1500 s, and ultimately to $-1550\,\mathrm{s}$. The confidence in the last two data points is somewhat reduced because they were based solely on one inter-slip period while the others were averaged over 5–8 inter-slip periods from different experiments. Based on the observed systematic changes we identify two controlling parameters for the location of b value minima, i. e. (1) the number of SSDs as a proxy for the degree of complexity within the high-stress regimes and (2) the sample size used for b value computations which can lead to an over-smoothing of b value trends as well as mixing of AE events from different inter-slip periods which is seen for the pink curve in Figure 4.11. Less complex stress curves were connected to b value minima that occurred in close temporal proximity to failure.

If the complexity in the stress curve is indeed systematically connected to b value variations, we

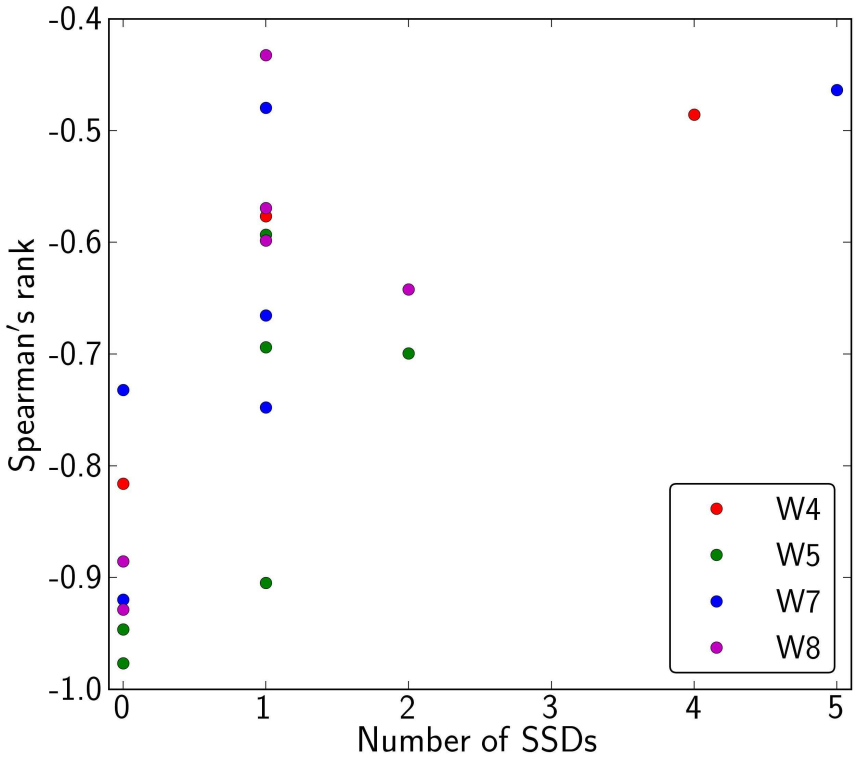

Figure 4.12: Change in correlation coefficient (Spearman's rank) as function of number of SSDs during individual stick-slip sequences of all experiments. The quality of correlations decreased with increasing numbers of SSDs which can be seen as a proxy for complexity of the temporal variations of differential stress within a stick-slip cycle.

would expect to also observe systematic changes in the quality of b-stress correlations. To investigate this hypothesis, we grouped the correlation coefficients (here we preferred to use Spearman's rank which is less sensitive to strong outliers, but the more commonly used Pearson's r showed similar results) according to the number of observed SSDs within each stick-slip cycle (Figure 4.12). The correlation coefficient increased on average with more SSDs so that the highest-quality correlations were observed for stick-slip sequences with the least complexity and vice versa. Stick-slip sequences with one SSD showed lower correlations as stick-slips with no SSDs but corresponding correlation coefficients showed also very low absolute values thus slightly deviating from the general trend. Nevertheless, the systematics of correlation coefficients and number of SSDs support the hypothesis that details of the b value-stress relationship partially depend on the observed level of complexity.

5 A comparison of seismicity characteristics and fault structure between stick-slip experiments and nature

5.1 Abstract

Fault zones contain structural complexity on all scales. This complexity influences fault mechanics including the dynamics of large earthquakes as well as the spatial and temporal distribution of small seismic events. Incomplete earthquake records, unknown stresses, and unresolved fault structures within the crust complicate a quantitative assessment of the parameters that control seismicity. To better understand the relation between fault structure and seismicity, we examined dynamic faulting under controlled conditions in the laboratory by creating saw-cut-guided natural fractures in cylindrical granite samples. The resultant rough surfaces were triaxially loaded to produce a sequence of stick-slip events. During these experiments, we monitored stress, strain and seismic activity. After the experiments, fault structures were imaged in thin-sections and using computer tomography. The laboratory fault zones showed many structural characteristics observed in upper crustal faults including zones of localized slip embedded in a layer of fault gouge. Laboratory faults also exhibited a several millimeter wide damage zone with decreasing micro-crack density at larger distances from the fault axis. In addition to the structural similarities, we also observed many parallels between our observed distribution of acoustic emissions and natural seismicity. The acoustic emissions followed the Gutenberg-Richter and Omori-Utsu relations commonly used to describe natural seismicity. Moreover, we observed a connection between along-strike fault heterogeneity and variations of Gutenberg-Richter b value. As suggested in natural seismicity studies, areas of low b value marked the nucleation points of large slip events and were located at large asperities within the fault zone that were revealed by post-experimental tomography scans. Our results emphasize the importance of stick-slip experiments for the study of fault mechanics. The direct correlation of acoustic activity with fault zone structure is a unique characteristic of our laboratory studies that has been impossible to observe in nature.

5.2 Introduction

It is generally accepted that natural fault zones can only partially be described by planar, frictional interfaces, and should rather be considered as complex zones of deformation. This complexity

along with inherent fault properties such as frictional behavior controls the mechanical response of faults when subjected to tectonic loading stresses. Recent results (e.g. Hori et al., 2004; Barbot et al., 2012; Noda and Lapusta, 2013) have shown that the distribution of materials that favor unstable (velocity-weakening) over stable (velocity-strengthening) slip along faults strongly influences earthquake distributions and the overall slip behavior of a fault. In addition to rheological heterogeneity, earthquake ruptures and slip are also controlled by geometric heterogeneity within the fault zone.

On a larger scale, models that include fault-system-induced interactions of earthquakes can produce seismicity characteristics similar to regional observations and replicate observed statistical relations, including aftershock clustering, of natural seismicity (e.g. Ward, 2000; Rundle et al., 2004; Dieterich and Richards-Dinger, 2010). Consequently, fault complexity is connected to internal fault properties (e.g. structural and rheological heterogeneity) and external processes (e.g. pore-pressure changes, stress changes induced by other earthquakes). This study focuses on a comparison between intrinsic fault zone properties in the laboratory and nature, with special emphasis on structural similarities.

The structure of natural fault zones can conceptually be described by a fault core surrounded by a zone of distributed damage (e.g. Caine et al., 1996; Ben-Zion and Sammis, 2003). A fault core contains a gouge layer, anastomosing principal and secondary zones of slip localization. The surrounding damage zone consists of joints, pulverized rock, and subsidiary faults over a wide range of length scales (e.g. Chester and Logan, 1986; Chester et al., 1993; Faulkner et al., 2003; Dor et al., 2006) and see Wibberley et al. (2008); Faulkner et al. (2010) for reviews. The structure of fault zones can vary substantially and shows a large dependence on protolith composition (e.g. Schulz and Evans, 2000; Faulkner et al., 2003). This structural heterogeneity strongly affects seismic activity along faults. Micro-seismicity is suggested to be connected to fault heterogeneity and has been used to map fault asperities (Malin et al., 1989; Wiemer and Wyss, 1997; Schorlemmer and Wiemer, 2005). Seismicity studies also provide details about changes in strain accumulation and fault properties at depth (Nadeau and McEvilly, 1995, 1999). Fault-normal seismicity profiles have been used to infer the width of the fault core and fault roughness, as well as progressive fault smoothing with larger displacements (Powers and Jordan, 2010).

Many of these seismicity studies have drawn from laboratory results to understand seismicity variations and their underlying mechanisms in nature (see also Main et al., 1989; Wyss and

Wiemer, 2000; Schorlemmer et al., 2005; Sobiesiak et al., 2007; Narteau et al., 2009). Laboratory studies highlight, for example, the influence of stress (Scholz, 1968; Amitrano, 2003) and compositional heterogeneity (Mogi, 1962) on frequency-magnitude distributions of micro-seismic events. In the laboratory, seismic energy is predominantly radiated in form of high-frequency acoustic emissions (AEs) during micro-cracking and micro-slip. These AEs mark distinct prefailure stages before sample fracture that are connected to sample dilation and rupture nucleation (e.g. Lockner et al., 1991a). AEs are initially distributed throughout the sample and then start to localize when approaching the point of rupture nucleation and maximum stress (Lockner et al., 1991b). Prior to the point of peak stress and failure a general increase in AE rate and decrease in b value is observed (e.g. Main et al., 1989; Meredith et al., 1990; Zang et al., 1998), which is explained by the growth and coalescence of the pre-existing micro-crack population (Main et al., 1992). AE events during stick-slip motion on rough fracture surfaces can be used to identify points of fault branching and increased geometric complexity (Thompson et al., 2009). Furthermore, AEs document micro-processes before a stick-slip event (Weeks et al., 1978; Thompson et al., 2005; Goebel et al., 2012), which is commonly considered as laboratory-analog for earthquakes (Brace and Byerlee, 1966; Byerlee, 1970).

In experiments, the occurrence of slip instability is controlled by material properties, loading conditions and the machine stiffness which supplies elastic energy to a propagating rupture (Dietrich, 1978; Lockner and Beeler, 2002). Variations in machine stiffness (Lockner and Byerlee, 1990) and fault roughness evolution (Voisin et al., 2007) can cause a transition between stable and unstable sliding. In nature, elastic energy is stored in the surrounding lithology of a fault. A slip instability occurs if a nucleating rupture patch reduces a fault segment's strength faster than the driving stress is reduced (Byerlee, 1970; Dieterich, 1979; Lockner and Beeler, 2002).

This emphasizes some of the analogies between experiments and nature, and highlights the importance of a detailed description of slip instability in the laboratory. The nucleation of slip instability can be described as a function of changes in sliding velocity and interface properties which evolve over time. For a comprehensive review of laboratory derived rate-and-state friction laws and their role in earthquake mechanics see Marone (1998) and Scholz (1998). In the laboratory, the occurrence of a slip instability is sensitive to fault zone composition. Quartz rich granite powders, for example, exhibit velocity weakening which favors slip instability (e.g. Green and Marone, 2002) whereas phyllosilicates exhibit velocity strengthening which supports stable

sliding (e.g. Moore and Lockner, 2004; Moore and Rymer, 2007; Faulkner et al., 2011).

Most previous laboratory studies investigated sliding characteristics and frictional properties of planar material interfaces. This study focuses on the mechanical properties and structures of faults that develop from saw-cut guided, natural fracture surfaces, thus providing the opportunity to study naturally-created fault complexity. Furthermore, our experiments produced a series of stick-slip events under upper crustal stress conditions, thus enabling us to study the mechanical and seismic consequences of early stages of fault evolution. In the following, we emphasize observed similarities between laboratory experiments and nature. Initially, we show parallels in fault structure and off-fault damage production, which will be tied to observed acoustic emission statistics which show temporal and spatial clustering analogous to natural seismicity. Lastly, we consider fault evolutionary processes in the laboratory, which can be assessed by systematic changes in the spatial distribution of acoustic emissions.

5.3 Method

In this section, we will describe the sample preparation, loading conditions, and AE data analysis. A more detailed treatment of AE acquisition system and experimental setup can be found in Stanchits et al. (2006) and Goebel et al. (2012), respectively. We report on 4 experiments performed on cylindrical (radius = 40 mm, height = 107 mm) Westerly granite specimen at the German Research Centre for Geosciences (GFZ). The grain size of Westerly granite samples varies between 0.05 and 2.2 mm with an average grain size of 0.75 mm (Stesky, 1978).

The experiments were conducted at room temperature and room-dry conditions. To accurately monitor elastic and inelastic sample deformation, AE sensors and strain gauges were glued directly to a specimen's surface. We designed the experiments so that most of the macro- and micro-fracture activity was focused within the central region of each specimen away from the sample boundaries. This was accomplished by introducing saw-cut notches with different lengths (1.5 to 2.3 cm) at a 30° angle to the loading axis prior to the experiments. An overview of loading conditions can be found in Table 5.1 and a schematic representation of the sample geometry is depicted in Figure 5.1a. The experiments were conducted under triaxial loading conditions at constant confining pressures ($\sigma_{xx} = \sigma_{yy}$). Vertical displacement rates were held constant at $\dot{\epsilon} \approx 3 \cdot 10^{-6}$ s^{-1}. The laboratory fault zones were created by initial, saw-cut-guided fracture, followed by fault locking

Sample	l_n (cm)	l_{RS} (MPa)	$P_{c_{frac}}$ (MPa)	$P_{c_{slide}}$ (MPa)	$\sigma_{max_{frac}}$ (MPa)	$\sigma_{max_{slide}}$ (mm)	$U_{x_{max}}$
WGRN04	1.5±0.7	5.0±0.15	75±0.5	150±0.5	635±6	400±6	3.0±0.003
WGRN05	1.9±0.7	4.2±0.15	75±0.5	150±0.5	510±6	296±6	4.1±0.003
WGRN07	2.2±0.7	3.7±0.15	75±0.5	150±0.5	450±6	293±6	4.3±0.003
WGRN08	2.5±0.7	3.0±0.15	75±0.5	150±0.5	380±6	288±6	3.7±0.003

Table 5.1: Loading conditions and mechanical data of the 4 presented experiments. The length of the saw-cut notches was gradually increased from WGRN04 to WGRN08 which led to a net reduction of the rough surface area. l_n: notch length l_{RS}: approximate length of the rough fracture surface, $P_{c_{frac}}$: confining pressure during fracture stage, $P_{c_{slide}}$: confining pressure during frictional sliding of the previously generated fault, $\sigma_{max_{frac}}$: maximal differential stress during fracture stage, $\Delta\sigma_{max}$: maximal differential stress during sliding, and $U_{x_{max}}$: maximum vertical displacement of loading piston.

due to pressure increase (from P_c = 75 to 150 MPa), and lastly fault reactivation in form of stick-slip motion (Goebel et al., 2012).

In contrast to an idealized model of stick-slip motion with linear stress increase and constant failure stresses, we observed a range of complexities in the stress curves of our tests (Figure 5.1b). The stress increase before failure showed large amounts of inelastic deformation. At the same time, we observed small, abrupt stress drops possibly due to local failure events and variations in both peak and residual stress after slip. Figure 5.1b shows differential stress and strain during the reloading of a previously faulted sample that led to the creation of 6 stick-slip events with large stress drops (LSD events) some of which were preceded by smaller stress drop (SSD) events. The alternation of gradual stress increase and abrupt release of the stored elastic energy during slip is typical for all experiments.

5.3.1 Acoustic emission recordings and magnitude determination

To monitor seismically active deformation during stick-slip, we used a 16 channel seismic array of piezo-electric transducers with a resonance frequency at 2 MHz. We recorded full seismic waveforms at 10 MHz sampling frequency corresponding to a time resolution of 0.1 μs. The amplitude resolution was 16 bits. AE hypocenter locations were determined from first arrival times and active velocity measurements using transducers as ultrasonic-pulse senders. The location uncertainty was estimated at 1–4 mm, depending on the proximity of an event to the edge of the array.

The average amplitudes of the recorded AE events were computed from the maximum amplitudes at each channel in volts and corrected for geometric spreading between source and receiver.

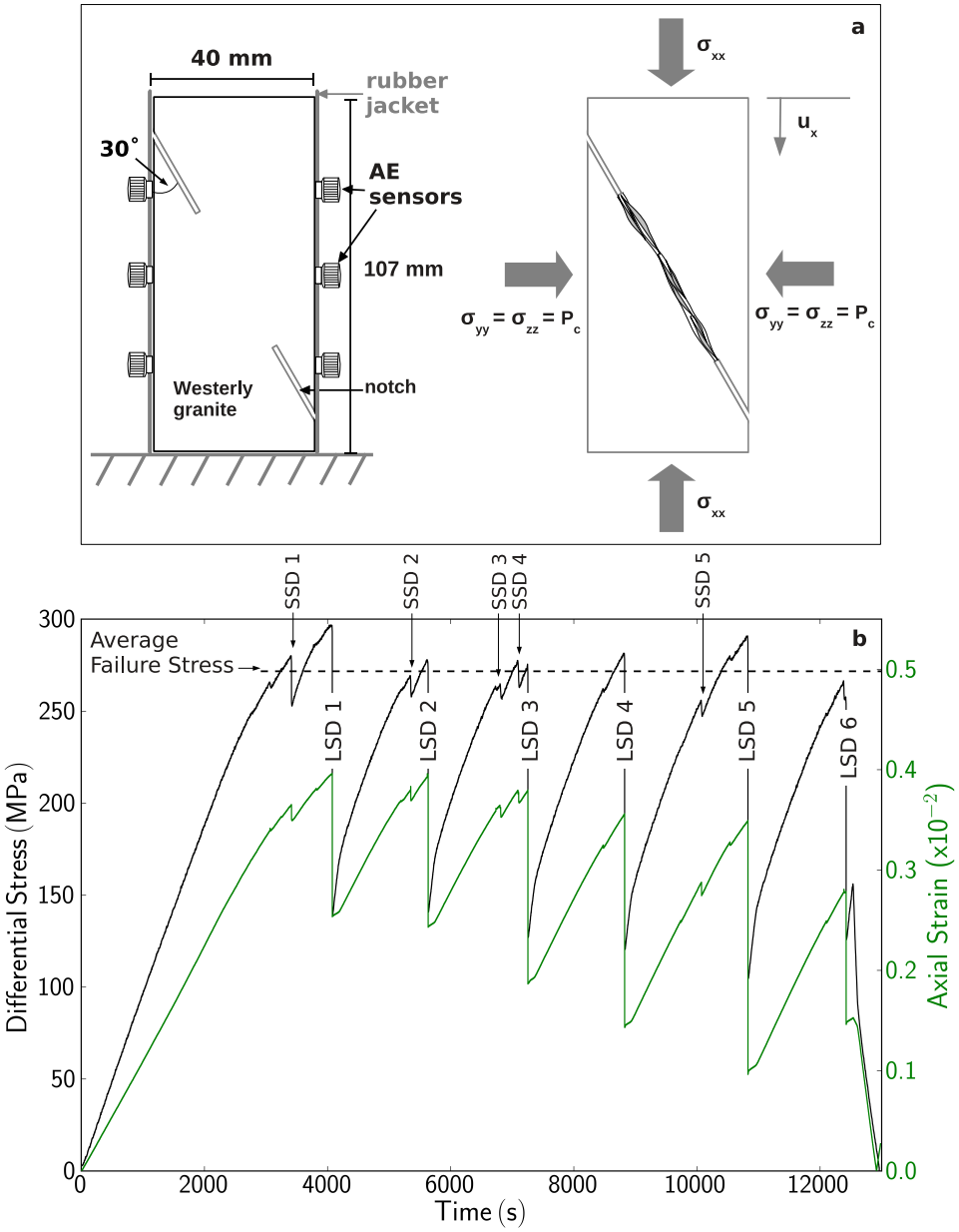

Figure 5.1: (a): Sample geometry and loading conditions of the triaxial tests. (b): Variations in stress and strain with small stress drop (SSD) and large stress drop (LSD) events during 6 stick-slip cycles.

Based on the corrected, averaged amplitudes (A), we assigned magnitudes:

$$M = \log_{10}\left(\frac{A}{A_c}\right) \tag{5.1}$$

where A_c describes a reference value.

5.3.2 Statistical analysis of acoustic emission data

In the following, we will describe the details of the statistical description of AE distributions in space and time as well as of the frequency-magnitude distribution (FMD). The latter can be characterized by a power-law with an exponent (b value) that describes the relative proportion of small vs. large magnitude events (Ishimoto and Iida, 1939; Gutenberg and Richter, 1944):

$$\log N = a - bM, \tag{5.2}$$

where N is the number of AE events with magnitudes that are larger than or equal to M and a is a constant representing the seismic activity. For reliable b value estimates, we required AE distributions to contain at least 150 events. b values were computed using the maximum-likelihood estimator (Aki, 1965; Utsu et al., 1965; Bender, 1983):

$$b = \frac{1}{\overline{M} - M_c} \log_{10}(e). \tag{5.3}$$

Here, $\overline{M}$ is the mean magnitude, $e = \exp(1)$ and M_c is the magnitude of completeness corrected for bin size to account for possible biases of discrete magnitude bin sizes (Utsu et al., 1965; Guo and Ogata, 1997). We estimated M_c through the inspection of large sets of FMDs and determined the deviation from linearity of the cumulative histograms. We used a constant value for M_c assuming no significant changes in completeness. This is supported by a stable array sensitivity and consistent, high-quality seismic records throughout the experiments. The total number of successfully located AE events for each experiment varied between 34,141 and 97,847, with relative magnitudes ranging from 0.84 to 5.0. While the minimum magnitude was likely related to the smallest detectable crack size, the maximum magnitude was limited by the analog input range of the digitizing cards. Based on the large AE data sets, we computed spatial variations in b value within the fault zone. To this end, we used the N nearest events to each point within

a homogeneous 2D grid (0.1 mm grid spacing) that was located within the best-fit fault plane. Computing b values based on a nearest neighbor approach ensures the same statistical significance and similar uncertainties at each grid point, while also increasing the spatial resolution especially in areas of high AE density (for details about spatial b value mapping and different methods see e.g. Wiemer and Wyss (2002)). b values were only computed for grid nodes that had sufficient AE events ($N > 150$) within a spherical volume with maximum radius of 5 mm. N was then varied between 150 to 600 events to test the stability of spatial b value patterns.

To describe aftershock rates after LSD events we used the Omori-Utsu relation:

$$\frac{\mathrm{d}N}{\mathrm{d}t} = \frac{K}{(c+t)^p} \tag{5.4}$$

where $\mathrm{d}N/\mathrm{d}t$ is the aftershock rate and t is the time after slip. K, c and p are empirical fitting parameters. K is generally related to the productivity of an aftershock sequence, and is suggested to depend on mainshock magnitude (Utsu et al., 1965). c describes the length of the time window of initial deviation from a power-law decay and is typically small (e.g. $\lesssim$1 day for Japan (Ogata, 1999)). p is the rate decay exponent which is generally close to 1, and can vary between 0.5 and 1.9, especially during spatial mapping of aftershock parameters (Ogata, 1999; Wiemer and Katsumata, 1999). To estimate the empirical fitting parameters of aftershocks within the time interval $[t_\mathrm{a}, t_\mathrm{b}]$, we maximized the likelihood function suggested by Ogata (1999):

$$\log L(K, c, p; t_\mathrm{a}, t_\mathrm{b}) = N \log K - p \sum_{i=1}^{N} \log(t_i + c) - K\Lambda(c, p, t_\mathrm{a}, t_\mathrm{b}), \tag{5.5}$$

where

$$\Lambda(c, p, t_\mathrm{a}, t_\mathrm{b}) = \begin{cases} \log(t_\mathrm{b} + c) - \log(t_\mathrm{a} + c), & \text{for } p = 1 \\ \left((t_\mathrm{b} + c)^{1-p} - (t_\mathrm{a} + c)^{1-p}\right)/(1-p), & \text{for } p \neq 1 \end{cases} \tag{5.6}$$

To find the parameters that maximize this function, we used a simplex optimization algorithm, and explored the parameter space to ensure the robustness of the maxima. The parameter uncertainties are estimated by bootstrap re-sampling. A performance test of the fitting algorithm can be obtained from a Kolmogorov-Smirnov-test (KS-test) that compares modeled and observed AE aftershock times (Woessner et al., 2004). The KS-test indicates if modeled and observed data

originated from the same distribution. High values underline that the Omori-Utsu relationship is a valid model for the description of the observed aftershock rates.

To assess variations in the spatial distribution of AE events we computed the fractal dimension for events within individual interslip periods. To this aim, we estimated the sample densities at varying scales using the pair correlation function (Feder, 1988; Schroeder, 1991), and determined the number of AE events within spherical volumes with increasing radii r_i:

$$\mu(R < r_i) = A_H r_i^{D_H} \tag{5.7}$$

where R is the distance vector between the current sample and all other AE events, μ is the AE density, A_H is a prefactor and D_H is the fractal dimension, computed from the linear part of the power-law distribution of μ and r (Wyss et al., 2004). The radius r was logarithmically binned so that its values appear equally-spaced in log-space. As a result, less weight is given to data at large distances, adding to the robustness of the least-square estimates of fractal dimensions. The pair correlation function is analogous to the correlation integral (Grassberger, 1983) used to estimate fractal dimensions of hypocenter locations in nature (e.g. Hirata, 1989). We tested a range of different values for AE sample sizes, concluding that results were stable for more than 1000–3000 events depending on the AE catalog size. Uncertainties in D_H were estimated by bootstrap re-sampling and the reliability of fractal dimension estimates was tested using known fractal geometries, i.e. the Sierpinski gasket (Schroeder, 1991).

5.4 Results

5.4.1 Post-experimental fault structure

To examine parallels between laboratory experiments and natural faulting, we monitored fault development starting from an incipient fracture surface. After completion of the experiments, we analyzed micro-structures based on fault parallel and orthogonal thin-sections of multiple specimens. Prior to this analysis, specimens were confined by the initial rubber tubing and additional steal clamps to preserve the post-experimental sample configuration in as much as possible. Small movements along the fault were unavoidable due to elastic rebound of samples and rubber jackets after pressure removal, so that off-sets and crack width in thin-sections and CT-scans deviated

slightly ($<$1 mm) from the *in-situ* conditions. To avoid any further movement, specimens were impregnated with low-viscosity, colored (blue) epoxy-resin, immediately after the experiments. The usage of the blue epoxy allowed for a clear distinction between connected pore-space and sample mineralogy.

Sample fracture and successive stick-slip events resulted in damage creation that led to the formation of distinguishable structural features. The center of the faults were generally marked by a gouge layer containing larger clasts and localized zones of fine-grain material (Figure 5.2c). The clasts show strong size-variations (from $\sim$5–500 μm) due to varying stages of grain comminution and spatial-heterogeneous strain accumulation within the fault zone. Analogous to models of natural faults, we sub-divided our laboratory fault-structures into 3 major zones: (1) A fault core with a width that varied between 0.3 to 1 mm containing clasts of variable grain-size and several zones of localized slip with very fine-grained material ($>$20 μm). The fault core shows evidence of shear deformation in form of zones of localized slip and Riedel shears within the core's gouge layer. (2) At larger distance from the fault axis, we observed a zone of enhanced damage and micro-cracking. This damage zone was characterized by grain boundary cracks, inter- and transgranular cracks, as well as the removal of grains from the edge of the damage zone and subsequent assimilated into the gouge layer. Many of the larger flaws within the fault core and transitional damage zone showed a preferred, low-angle ($<$30°) orientation with regard to the fault axis. These cracks exhibited extensional and shear components, similarly to the observations of Riedel shears (Figure 5.2b) and joints in nature. (3) The gouge layer and damage zone were embedded into the country rock which appeared largely undamaged within the thin-sections.

We analyzed the density of micro-cracks at increasing distances to the fault axis (Figure 5.3), identified by the blue-colored epoxy resin. For the micro-crack density analysis, we removed all loose gouge particles from the fault surface to provide a clearer distinction between gouge and transitional damage layer. The crack density was computed from the ratio of cracks to intact material for each fault-parallel thin-section image slice. The resulting density profile was then smoothed using a 15 sample moving average filter. Micro-crack densities were generally highest close to the fault core and decreased with large fault normal distances. This suggests that most of the damage is caused by deformation processes within or at the edge of the fault core and that these processes result in pervasive damage creation even at distances of several millimeters. In addition the fault core related damage zone, we observed secondary zones of increased crack

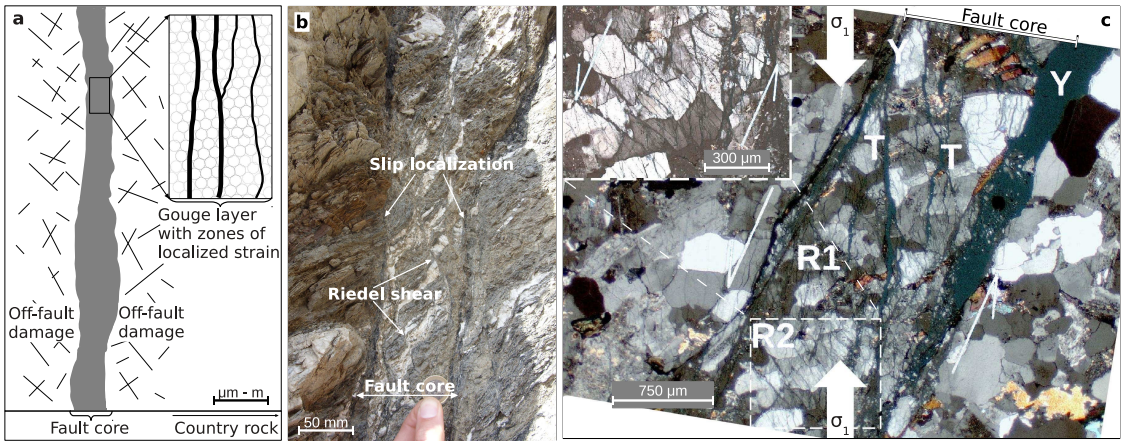

Figure 5.2: Comparison between natural and laboratory fault structures. (a): Schematic of natural fault structure. (b): Photographic image of a natural fault zone that contains a gouge layer and zones of localized slip as well as Riedel shears within the gouge layer. (c): Microscopic image of post-experimental thin-section of a laboratory fault zone. The fault contains a gouge zone, off-fault damage as well as Riedel shears (R1 and R2 see inset), principal slip zones (Y), and tensional cracks (T) sub-parallel to the direction of maximum stress.

densities around larger flaws within the transitional damage zone (see Figure 5.3a). Areas at large distances (>1.7 mm) from the gouge/damage zone interface showed little to no visible damage in thin-sections. The connected AE activity, however, which was largest close to the fault axis and decreased with larger distances, extended out to ∼15 mm emphasizing the distribution of faulting induced micro-cracking (Figure 5.3c).

5.4.2 AE distributions in time and space

In the following, we discuss the connection between *in-situ* recordings of AE events and post-experimental fault structures. Besides the micro-structural analysis of thin-sections, we examined the structure of faults in post-experimental X-ray computer tomography (CT) scans. CT-scans, which image density contrasts between pore-space and the rock-matrix, show a range of deformation induced features. These features include preferred zones of slip highlighted by black, linear zones as well as high AE activity in Figure 5.4 and anastomosing, secondary cracks within a broader damage zone. The previously observed gouge layer is not clearly identifiable. However, we can determine the width of the fault damage zone outlined by the anastomosing crack network. This width varies between 1.5 mm and 4.5 mm, similarly to observations in thin-sections. The thinnest part of the damage zone is located close to the center of the specimen at Y = 25–30 mm and

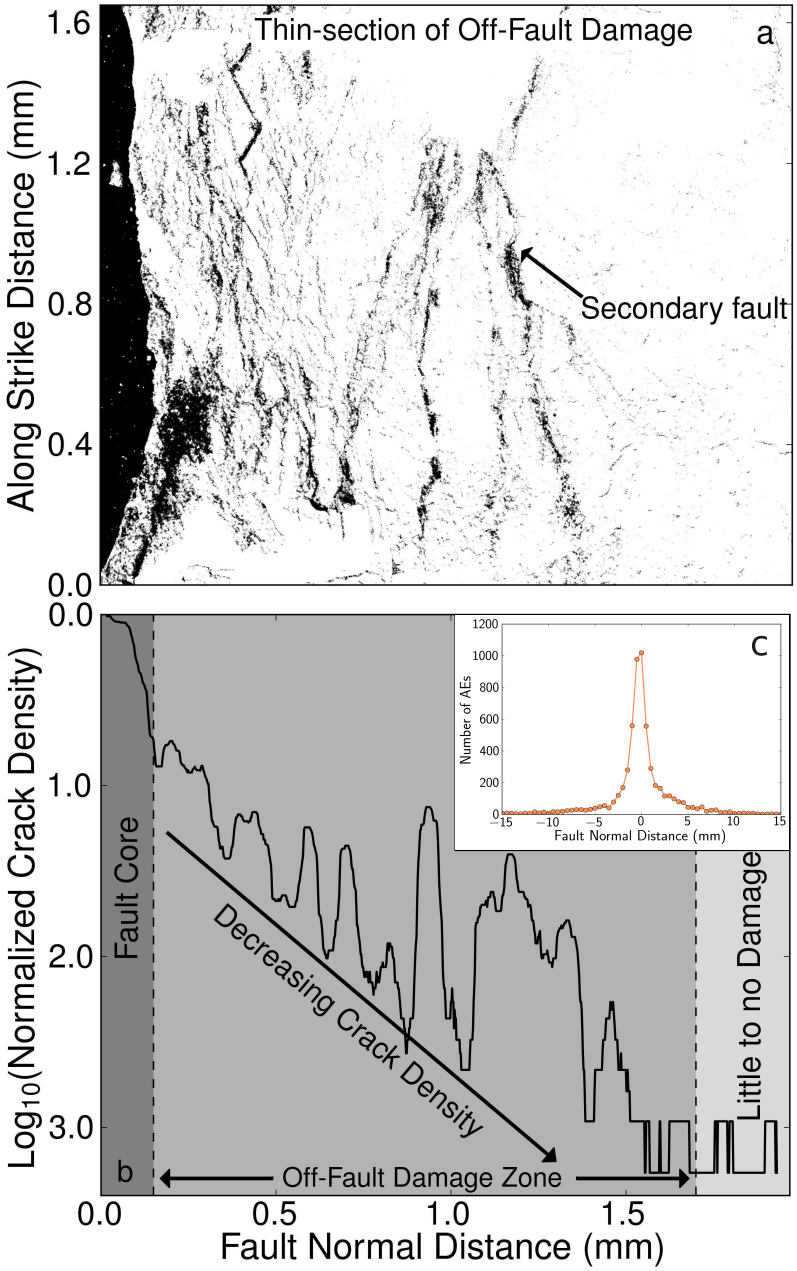

Figure 5.3: Micro-crack density distribution as function of fault normal distance. (a): Cracks and pore-space within a thin section of a typical, fault-adjacent region. The fault gouge was removed. (b): Crack density at increasing fault normal distance and fault structural units (i.e. fault core, off-fault damage zone, country rock with little damage). (c): Across-fault profile of AE activity for all AE events within a typical interslip period. The AE activity was binned every 0.5 mm.

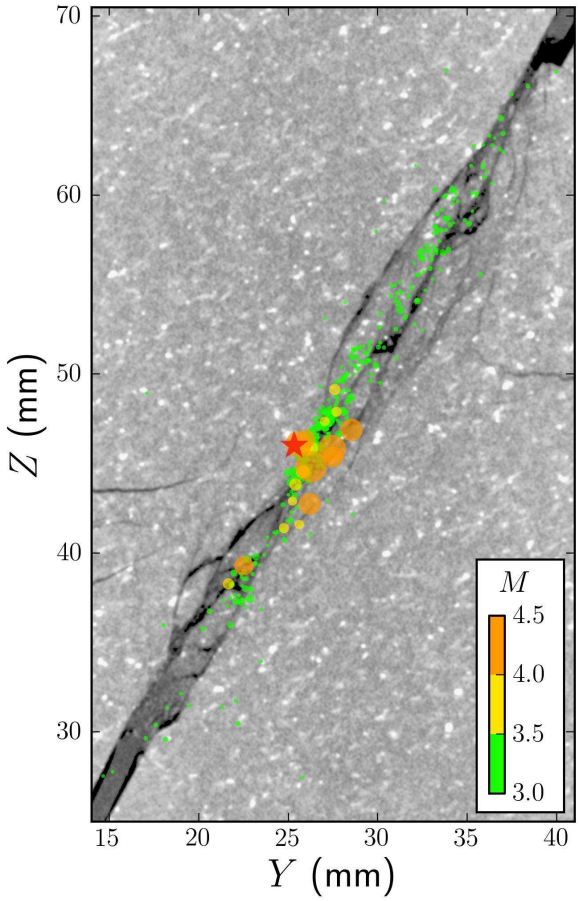

Figure 5.4: AE hypocenter distribution and magnitudes (colored dots) superimposed on a post-experimental CT-scan image that shows fault structure and width. The displayed crack network is connected to the cumulative damage creation of sample fracture and 6 successive stick-slip events whereas the shown AE events occurred within a ∼15 min period leading up to a LSD event. The AEs occurred within a 5 mm slice centered at the CT-image position. The red star shows the nucleation point of the LSD event. (modified from Goebel et al. (2012))

Z = 42–47 mm in Figure 5.4. AE hypocenter locations, which are generally guided by the fault orientation, cluster within this area. These AE clusters showed relatively larger magnitudes at higher stresses closer to failure. The nucleation point of the following LSD event is located within this area in immediate proximity to a cluster of large magnitude events. This highlights the close connection between fault structure and AE activity during loading and stress increase on our laboratory faults. Thin parts of the fault zone seem to locally intensify loading stresses which would explain the relatively large AE activity and event magnitudes in this area as discussed in Goebel et al. (2012).

Besides the spatial variations of the AE activity, we also observed systematic temporal changes in AE rates associated with LSD events. AE event rates were comparably low before, and showed a sharp peak at the onset of LSD events which was followed by a gradual decrease over several seconds (Figure 5.5). The onset of LSD events was also connected to large-amplitude AE waveforms,

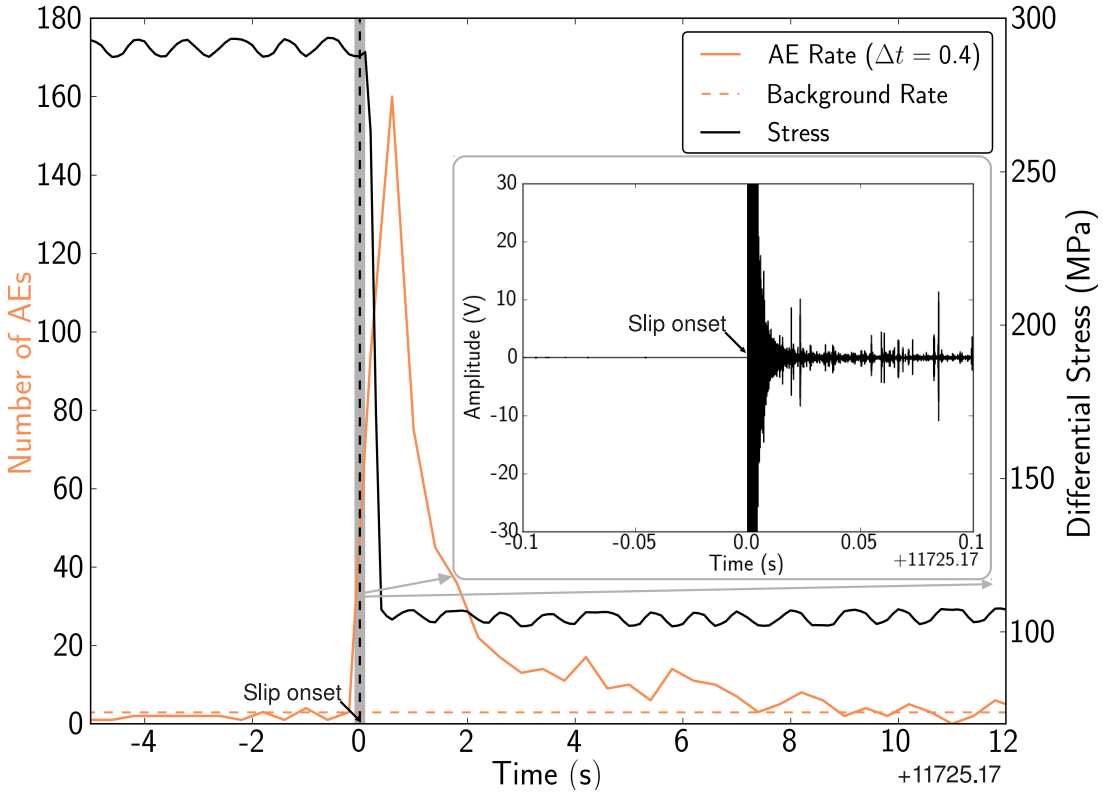

Figure 5.5: 'Mainshock' identification based on AE rate peaks and waveform recordings (inset). AE rates, computed for time bins of $\Delta t = 0.4$ (orange line), show a sharp increase at the time of slip while stress (black, solid line) drops abruptly. The apparent shift between the onset of stress-drop and peak AE rate is caused by time binning and the saturation of the recording system immediately after slip. After the slip onset, AE rates decreased gradually reaching the pre-failure rate at ∼10 s.

which led to a ∼5 ms long saturation of the recording system. Even though these waveforms appeared mostly clipped, their first-arrival times enabled an accurate determination of slip onset times and locations of slip nucleation patches. After ∼5–10 ms, individual AE events could again be recorded and located. The AE activity decayed with time after the LSD onsets and reached the pre-failure level within ∼10–20 s. These AE events will be called aftershocks in the following.

AE aftershock rates decayed rapidly within the first few seconds after the LSD events and then more gradually over the next ∼20 s. This behavior can be described by the Omori-Utsu relationship. Our analysis revealed that the Omori-Utsu parameters are very sensitive to the beginning of an aftershock period, whereas the end of the aftershock interval changed the results only marginally. We generally attained the most stable results by setting the beginning of an aftershock sequence to the LSD onset times and the end to 30 s after slip onset. To exemplify the quality

of aftershock fitting and the analogy to natural aftershock sequences, we plotted the cumulative aftershock rates of a typical LSD event as well as aftershock rates of the M = 6.0, 2004 Parkfield event (Figure 5.6 inset). Both events exhibited relatively high KS-statistics (p-value = 0.5 and 0.9) showing that the Omori-Utsu relationship is a valid model for the description of both data sets. Aftershock sequences during our experiments were limited to faults that developed from incipient fracture surfaces and were not observed during experiments on saw-cut surfaces. This highlights the importance of fault structural heterogeneity for the temporal clustering of AE events.

Besides the generally observed Omori-Utsu aftershock decay, we were also interested in a comparison of frequency-magnitude distributions (FMD) in the laboratory and nature. Figure 5.7 depicts an example of a typical FMD of AE events that occurred within an interslip period. The FMDs generally show similar characteristics to Gutenberg-Richter type FMDs with a pronounced power-law fall-off over more than one order of magnitude. The extend of the power-law decay is seen at both the approximately straight part of the FMD in log-log space and the stability of b values within this range of magnitudes (Figure 5.7 inset).

We investigated spatial variations in b values within the interslip periods of LSD events. Spatial b value maps were characterized by localized regions of low b (Figure 5.8b). These regions varied in size and shape, however, the centroid position remained largely stable over many successive stick-slip events. This result was independent of the number of AE events used for b value computations, even if varying the number of AEs between 150–600 (Goebel et al., 2012). Low b value regions were generally coinciding or adjacent to regions of high seismic moment release (Figure 5.8c) suggesting that the occurrence of large AE events played a substantial role in creating low b value regions. We compared FMDs within a low b value area and a 'typical' fault region (Figure 5.8b inset). The 'typical' fault region was associated with a substantially smaller amount of large magnitude AE events ($M > 3.0$). Events with M = 4.0–4.9 were missing entirely during that period which provides an explanation for the large differences in b value.

Our observations agree in several respects with spatial b value maps of the Parkfield section of the San Andreas fault (Figure 5.8a). Both maps depict regions of anomalously low b value within a broader region of higher b values. In both cases, the difference between low and high b value regions is ≈0.4–0.5, and the regions of low b value mark the likely areas of future, large seismic events. The total range of b value variations is generally slightly higher during our experiments (0.7–2) than in nature (0.5–1.3). This shows that a direct comparison between absolute b values is

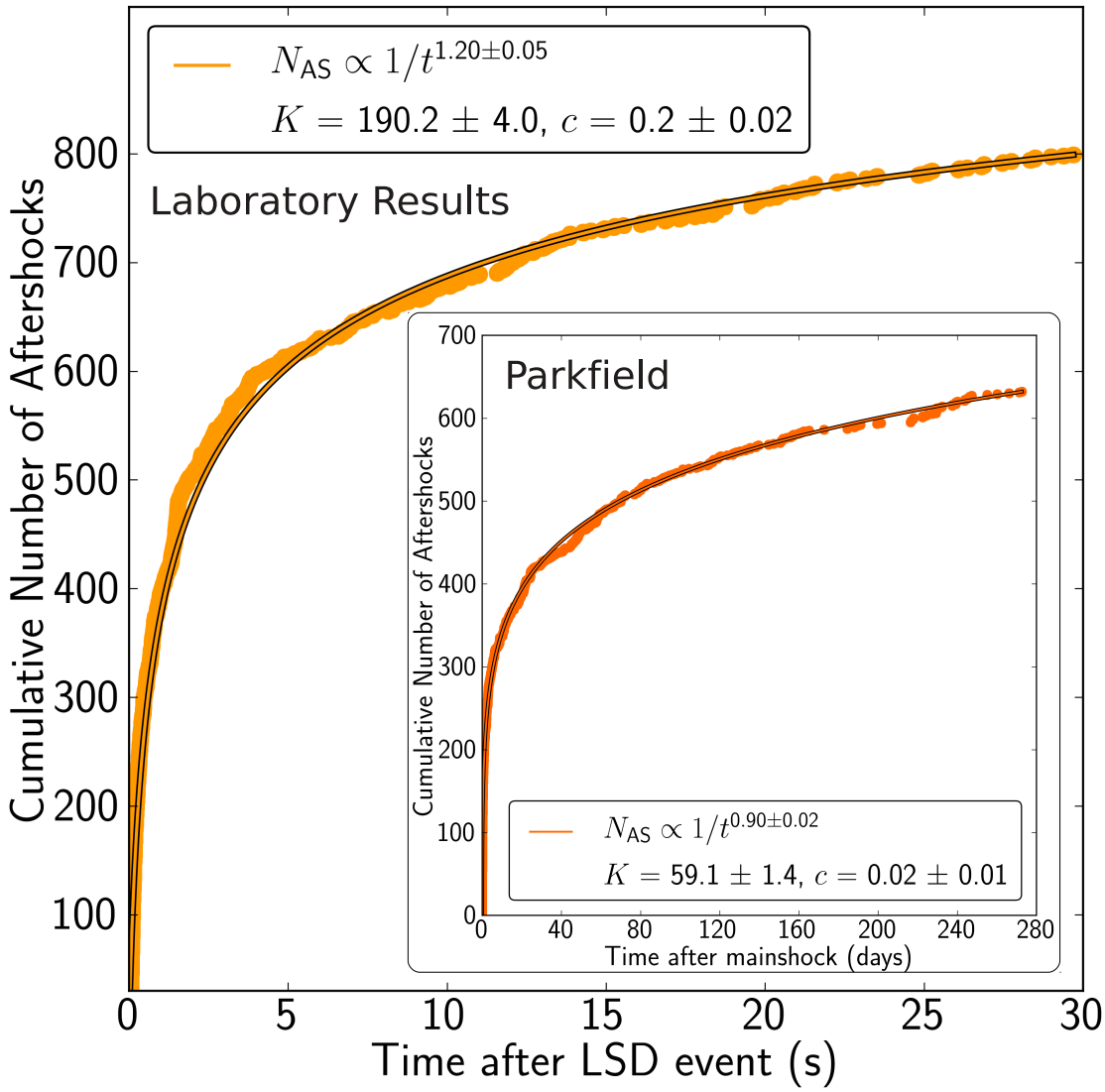

Figure 5.6: AE aftershocks decay as a power-law with time from the LSD event. This could be described by the Omori-Utsu relationship. The orange markers represent a typical, cumulative aftershock rate 30 s after a LSD event, and the orange curve shows the corresponding fit. The inset shows the cumulative aftershock rate and Omori-Utsu fit in a 280 day period after the $M = 6.0$, 2004 Parkfield event.

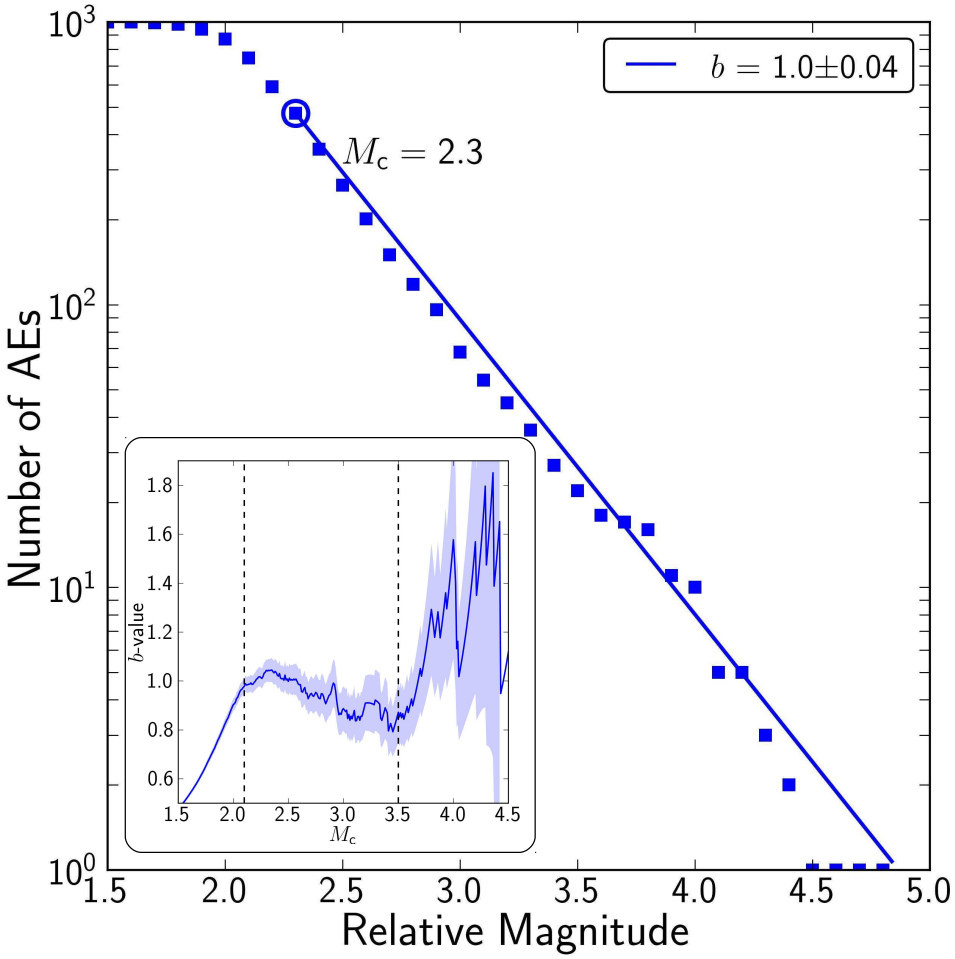

Figure 5.7: Frequency-size distributions of AEs in laboratory stick-slip experiments can be described by a power-law similar to the Gutenberg-Richter relationship with a slope $b = 1 \pm 0.04$. This power-law spans $\approx$1.2 orders of magnitude (inset).

not possible. The differences in b value are likely due to different types of recording systems as is between different seismicity catalogs and corresponding magnitude scales. Nevertheless, relative variations in b value may be an expression of similar underlying micro-processes in nature and laboratory experiments.

5.4.3 Fractal dimensions of AE events

While fault structures can only be assessed directly after completion of an experiment, for example, by using CT-images and thin-sections, AE events provide information about *in-situ* deformation and can thus be used to monitor changes in fault structure. We investigated the tendency of AEs to localize close to the fault plane to assess the changes in the spatial extend of micro-cracking with each successive stick-slip event. To this end, we computed the fractal dimensions of AE hypocenter distributions (D_{H}) for each interslip period. In general, fractal dimensions of seismic events can vary between about 1 and 3. Strongly localized event clusters can drop below values of $D_{\mathrm{H}} = 1$ (depending on observational scales), linear clusters have fractal dimensions slightly greater than 1 and event clusters that occur along a plane show values of $D_{\mathrm{H}} \gtrsim 2$ (e.g. Mandelbrot, 1982). Based on these considerations, we expect volume-filling distributions of AEs to have fractal dimensions substantially larger than 2 which decrease once AEs start to preferably occur along the fault surface. In practice, decreasing fractal dimensions can be connected to both localization at a surface and hypocenteral clustering at points within the surface.

We conducted 3 control experiments on planar, saw-cut surfaces with specific roughness created by surface grinding with silicon carbide powder (Figure 5.9). These experiments showed AE distributions with fractal dimensions below 2 in all cases, thus the AE populations did not fill the entire fault plane. The smooth surface exhibited a lower fractal dimension ($D_{\mathrm{H}} = 1.48$), compared to the rough surfaces ($D_{\mathrm{H}} = 1.79$–1.82). Following the observed connection between D_{H} and fault roughness, we analyzed variations in D_{H} with successive LSD events. Figure 5.9b shows D_{H} for 6 successive stick-slip events. The fractal dimension decreased systematically and approached a value of $D_{\mathrm{H}} \approx 2$ in the interslip period before the 6. LSD event. Similarly, the fractal dimensions decreased with successive stick-slips during the other experiments from values between $D_{\mathrm{H}} \approx 2.5$ to ≈ 2.0 (Figure 5.9c), highlighting a generic tendency of AEs to localize close to or within the fault zone.

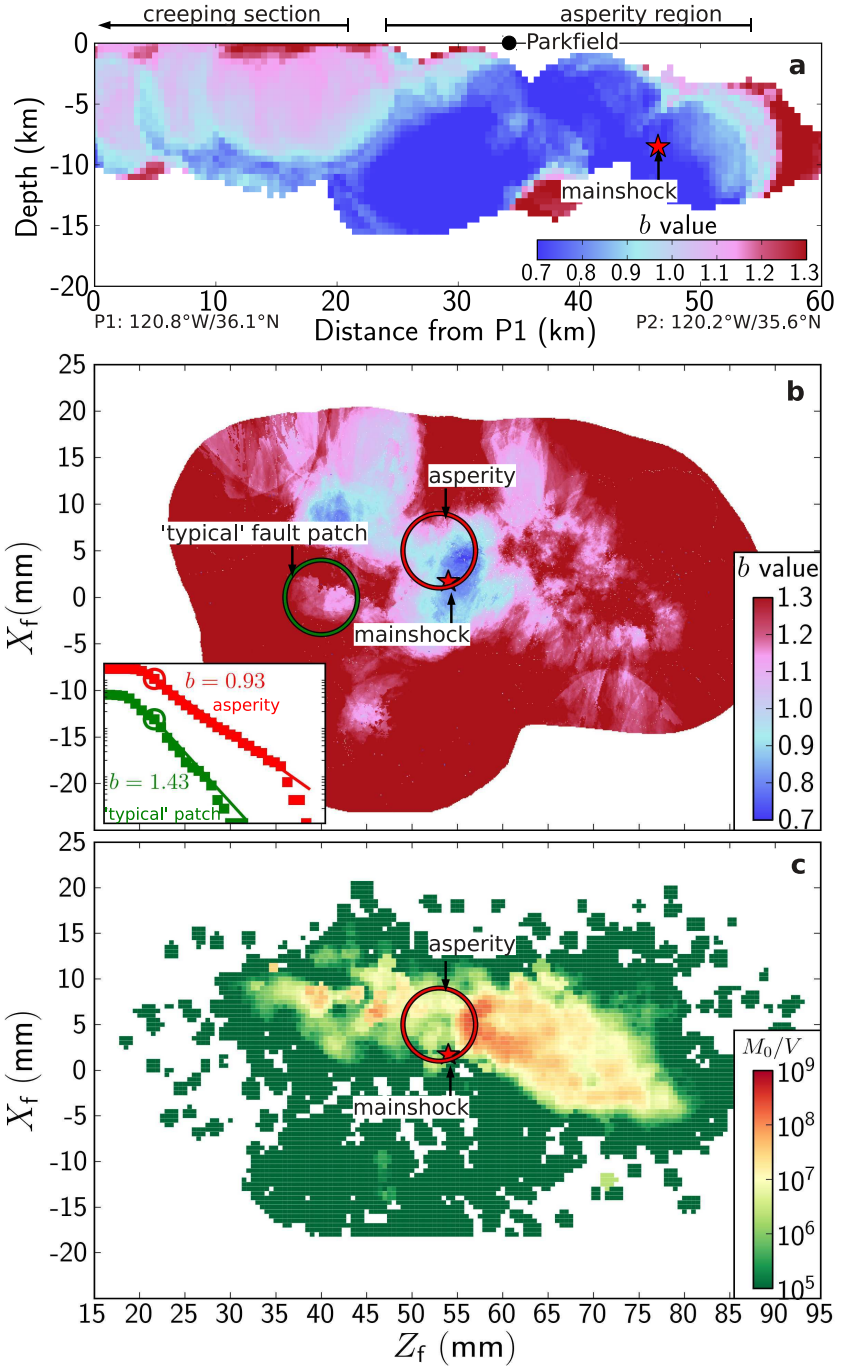

Figure 5.8: A comparison between b value maps at Parkfield and in the laboratory. a): b value map of the Parkfield section of the San Andreas fault modified after Schorlemmer and Wiemer (2005). The red star marks the hypocenter location of the 2004, $M = 6.0$ mainshock. b): Spatial b value map and frequency-magnitude distributions of an asperity region (inset, red markers) and a normal fault region (inset, green markers). c): Map of seismic moment release per fault volume computed for events close to the fault surface. (Figures (b) and (c) were modified from Goebel et al. (2012), which corresponds to Chapter 3 of the current work.)

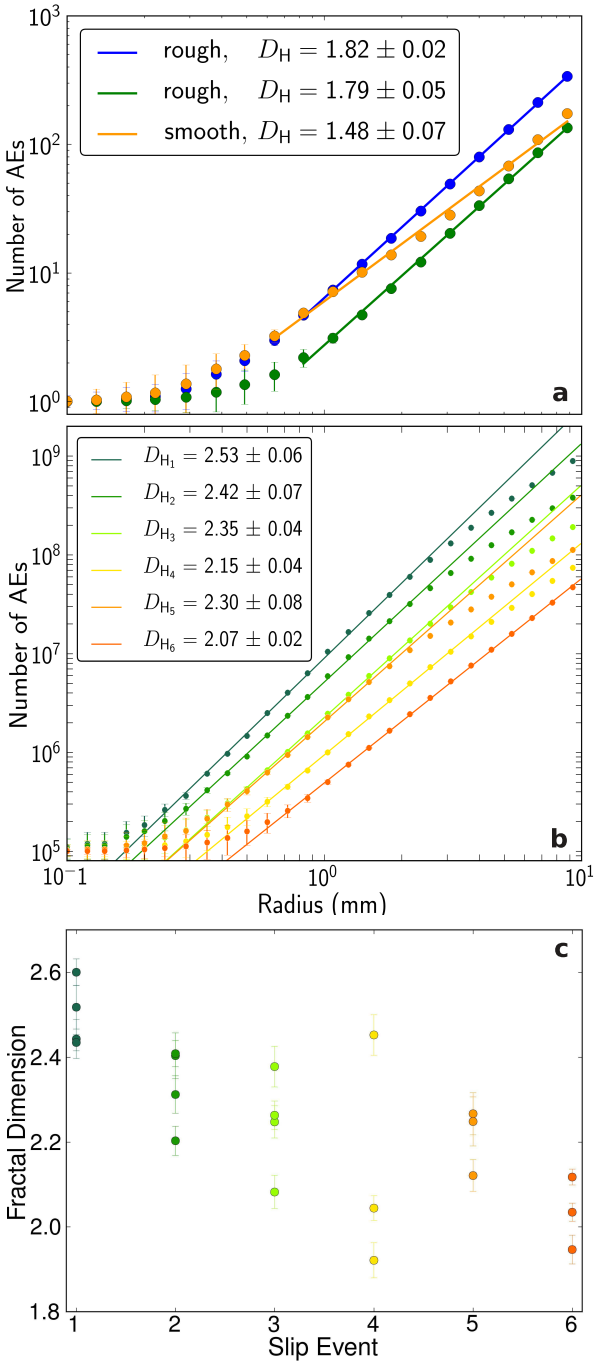

Figure 5.9: Changes in the AE hypocenter distributions (described here by their fractal dimension) with successive stick-slip events. (a): Fractal dimension of AEs recorded during loading of planar surfaces with pre-defined roughness. (b): Number of AE event pairs within increasing radii and corresponding fractal dimension computed from the linear part of the distributions. (c): Changes in fractal dimension with successive stick-slips. The number of markers (3–4) per slip event represent fractal dimensions for interslip periods of different experiments.

5.5 Discussion

5.5.1 Seismic event statistics in laboratory experiments and nature

Our experiments reveal many similarities between the distribution of AE events during laboratory stick-slip events and natural seismicity. The recorded AE populations can be described by the two fundamental relationships of statistical seismology: the Gutenberg-Richter and Omori-Utsu relationship (Omori, 1894; Utsu et al., 1965; Ogata, 1999). A spatial mapping of the seismic b value revealed that areas of low b-value mark the nucleation points of stick-slip events, which is similar to the observed connection between low b value regions and mainshock locations in nature (Westerhaus et al., 2002; Wyss and Matsumura, 2002; Schorlemmer and Wiemer, 2005; Wyss and Stefansson, 2006). We also illustrated that areas of low b values are associated with higher seismic moment release and relatively more large-magnitude AE events observed in FMDs. Larger AEs tend to cluster at relatively thin parts of the faults during periods of elevated stress before failure (see Figure 5.4). Thus, seismic event clustering is a result of the interaction between fault structural heterogeneity and loading stresses. More specifically, load bearing asperities may produce clusters of relatively larger-magnitude events during the stress increase of an advancing seismic cycle. Similarly, fault asperities may play a key role in generating areas of low b value in nature (Wiemer and Wyss, 1997).

Besides the power-law distribution of FMDs and AE aftershocks, we showed that AE hypocenters are fractally distributed, which is also observed for natural seismicity (e.g. Aki, 1981; Hirata, 1989; Wyss et al., 2004). In the laboratory, fractal dimensions are observed to decrease rapidly before sample fracture caused by AE localization close to the point of fracture nucleation (Lei et al., 1992; Lockner and Byerlee, 1995; Zang et al., 1998). Our results, on the other hand, highlight a connection between fractal dimension and fault roughness. We observed that rough, pre-cut surfaces generally produce AE hypocenter populations with larger fractal dimensions than smooth, pre-cut surfaces. Similarly, we interpret the observed decrease in D_{H} with successive stick-slip events on incipient fracture surfaces as an expression of progressive fault smoothing and reduction of structural complexity. This emphasizes a possible role of our experiments in guiding fractal dimension analysis for the assessment of fault roughness evolution in nature.

Our laboratory experiments revealed a general connection between fault structure and seismic event distributions suggesting that fault roughness and heterogeneity can control both the spatial,

temporal, and frequency-magnitude distributions of seismicity.

5.5.2 Fault structure and slip localization

Natural fault zones are generally complex but show distinguishable structural features, i.e. one or more fault cores, a gouge layer, zones of localized slip surrounded by a broader zone of deformed rocks (e.g. Chester et al., 1993; Schulz and Evans, 2000; Ben-Zion and Sammis, 2003; Faulkner et al., 2003, 2010). Within the scope of the current experimental series, we showed that similar structural features can be produced after only few stick-slip events on fault zones that developed from incipient fracture surfaces. Analogous to natural faults which are surrounded by a broad zone of damage and fractures (e.g. Mitchell and Faulkner, 2009; Savage and Brodsky, 2011; Faulkner et al., 2010), we observed a wide zone of micro-cracking which extends out to several millimeters at places. This zone shows decreasing micro-crack and AE activity with increasing fault normal distances. Similar observations, i.e. decreasing crack densities away from the faults axis, were also made within process zones of controlled, shear-fracture experiments (Zang et al., 2000; Janssen et al., 2001). These studies highlight the importance of fracture processes during the formation of faults and secondary cracks which can exhibit their own zones of intensified mico-cracking.

Besides the direct analysis of fault structures in thin-sections and CT-scans, we investigated the spatial distribution of AEs and its connection to fault roughness. Systematic changes in fractal dimension of AE events with successive stick-slip events are interpreted as being caused by fault smoothing and reduction in fault complexity. This type of fault evolution is likely associated with the formation of zones of slip localization, observed in post-experimental thin-sections. Consequently, the deformation history of the samples during our stick-slip events includes an initial stage during which the faults are relatively rough, AE activity is high and the seismic events occur distributed. The second stage of fault formation is characterized by progressive fault smoothing and the AE hypocenters start to localize at, or within, the fault zone. During this stage, zones of localized slip form which probably accommodate most of the total displacement along the fault. We hypothesize that slip starts to localize early within thin zones of fine grain material during our experiments. This is supported by the corresponding rapid decrease in D_{H} within the first 3 LSD events.

Localized zones of high deformation are not only limited to stick-slip experiments but are also observed after sample fracture and subsequent frictional sliding experiments (Amitrano and

Schmittbuhl, 2002). The authors identified localized shear bands (∼0.1 mm) that consist of thin layers of elongated, smaller grains within a wider gouge layer (∼1 mm). Local shear bands in granular layers and porous rocks are likely transient deformation features at low strains which may mark different stages of strain localization (Aydin and Johnson, 1983; Hirth and Tullis, 1989; Mair et al., 2000). The stick-slip events during our experiments commonly produce through-going zones of strain localization and localized slip. For a more quantitative assessment of structural difference between different stages of slip localization, more experiments with a spectrum of strains and slip modes are required. Nevertheless, the observed structural similarities of laboratory-created and natural fault zones emphasize the importance of laboratory analog experiments for the understanding of fault formation. Moreover, our experiments provide insight into how complexity controls physical properties of faults.

5.5.3 Subsidiary faults and aftershock distributions

Part of the structural complexity of natural fault zones is generated by secondary fault structures in the vicinity of the main fault. One example for the existence of secondary fault branches is the Parkfield section of the San Andreas fault (Figure 5.10b). Similarly, our laboratory-created fault zones are connected to secondary cracks and slip surfaces which can accommodate parts of the total displacement. The 3-D representations of laboratory faults reveal the overall topography (Figure 5.10c), however, the complex network of anastomosing cracks is best visualized by extracting their traces from 2-D CT-images (Figure 5.10d). This representation elucidates that part of the fault's topography is due to different branches of smaller cracks with sub-parallel or low-angle orientation to the main slip surface identified by high AE activity. During our experiments, secondary structural features, for example, anastomosing crack networks are likely required for the creation of SSD events and aftershocks which are both not observed during stick-slip on simple, planar saw-cut surfaces.

Thus, our results suggest that the existence of aftershock sequences in the laboratory is linked to fault structural complexity. Similarly, aftershock sequences may be closely linked to fault complexity in nature. In nature, aftershocks are related to the slip distribution during the mainshock (e.g. Wiemer and Katsumata, 1999; Woessner et al., 2006) as well as mainshock induced changes in fault strength (e.g. Beroza and Zoback, 1993) and redistribution of stress (e.g. Mendoza and Hartzell, 1988). Aftershocks can also occur on secondary faults with different orientations from

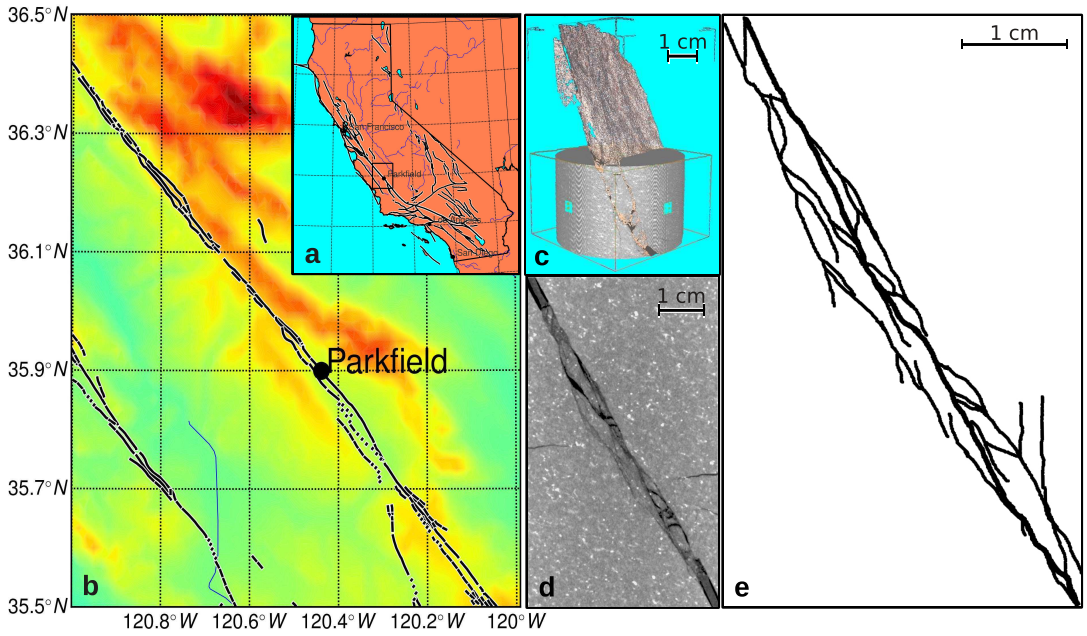

Figure 5.10: Traces of main faults and subsidiary faults in nature and in the laboratory. (a): Map of California with major fault traces (Californian Fault Traces, 2010). The black rectangle marks the region plotted in (b). (b): Fault traces including subsidiary faults close to the Parkfield section of the San Andreas fault. Background colors represent elevation between 100 to 1200 m. (c): 3-D image of a laboratory fault highlighting varying fault topography and secondary cracks seen at the outer boundaries. (d): CT-scan slice of the sample's center. (e): Traces of faults and secondary cracks based on the CT-image in (d).

the principal slip surfaces (Mendoza and Hartzell, 1988; Oppenheimer, 1990).

5.6 Conclusion

We documented the formation of laboratory fault zones from incipient fracture surfaces by means of post-experimental fault-structural analysis and through the analysis of AE distributions. Our results underline many structural similarities between laboratory-created and natural fault zones, for example, a fault core containing a gouge layer and zones of slip localization, a damage zone with decreasing crack densities at increasing fault normal distances and secondary, anastomosing cracks in the proximity of the main slip surface. Moreover, we observed several analogies between the statistics of AE events and natural seismicity: 1) AE events are fractally distributed in space, 2), show Omori-Utsu aftershock decay, and 3), Gutenberg-Richter frequency-magnitude distributions. Our experiments emphasize that AE clustering in time and space is connected to fault complexity. The spatial clustering of AEs before slip events is associated with fault asperity regions. Temporal clustering, i.e. aftershock sequences is related to the existence of fault structural complexity in

stick-slip experiments.

Our results also highlight a connection between fault roughness and the fractal dimension of AE hypocenters, and suggest that changes in fault roughness due to successive stick-slip events can induce progressive localization of AEs. Consequently, roughness may be a controlling parameter for the spatial distribution of seismicity in the proximity of both laboratory and natural faults. Our experiments highlight the importance of laboratory investigations of fault complexity when assessing physical mechanisms that cause variations in micro-seismicity. Furthermore, they can advance the understanding of fault formation, and evolution with larger displacements as well as the complex interplay between fault driving stresses and fault heterogeneity before stick-slip events and earthquakes.

6 Seismic event distributions and off-fault damage during frictional sliding of saw-cut surfaces with predefined roughness

6.1 Summary

The motion along upper crustal faults in response to tectonic loading is controlled by both loading stresses and surface properties, for example, roughness. Fault roughness influences earthquake slip distributions, stress-drops, as well as possible transitions from stable to unstable sliding which is connected to the radiation of seismic energy. The relationship between fault roughness and seismic event distributions is insufficiently understood, in particular, the underlying mechanisms of off-fault seismicity creation in the proximity of rough faults are debated. Here, we investigate the connection between roughness and acoustic emission density with increasing fault-normal distance during loading of surfaces with predefined roughness. We test the influence of fault roughness and normal stress variations on the characteristics of acoustic emission off-fault distributions. To this end, two sets of experiments were conducted: one to investigate the influence of initial surface roughness at constant confining pressure, and the other to investigate the influence of fault-normal stresses at constant roughness. Our experiments reveal a power-law decay of acoustic emission density with distance from the slip surface. The power-law exponents are sensitive to both fault roughness and normal stress variations so that larger normal stresses and increased roughness lead to slower AE density decay with fault-normal distance. This emphasizes that both roughness and stress have to be considered when trying to understand micro-seismic event distributions in the proximity of fault zones. Our results are largely in agreement with theoretical studies and observations of across-fault seismicity distributions in California suggesting a connection between off-fault seismicity and fault roughness over a wide range of scales. Seismicity analysis including a possible mapping between off-fault activity exponents, fault stresses and roughness, can be an important tool in understanding the mechanics of faults and their seismic hazard potential.

6.2 Introduction

Much of the deformation at tectonic plate boundaries is focused within zones of relative weakness, i.e., faults. Fault zones accumulate strain over time and release it over a spectrum of slip events of different size and velocity (e.g. Peng and Gomberg, 2010). The characteristics of these slip

events may be a function of fault roughness over a range of scales (e.g. Chester and Chester, 2000; Dieterich and Smith, 2009; Candela et al., 2011a,b). The roughness of natural fault zones varies from the sub-grain scale (micro- to centimeter scale) to the scale of large bends and deflections (1–100s km), like the Big Bend of the San Andreas fault.

The details of how different scale roughness or fault topography influences the dynamics of earthquakes and fault mechanics is not entirely understood. At the scale of laboratory experiments (millimeter to decimeter scale), the static coefficient of friction is suggested to be independent of roughness if normal stresses are high (Byerlee, 1970). Nevertheless, small scale roughness, i.e., the roughness of planar, ground surfaces ranging from micrometers to millimeters influences the frictional properties of rock samples in many different ways. For example, the break-down slip-distance required for the coefficient of friction to drop during the initiation of slip depends on the initial surface roughness (e.g. Dieterich, 1979; Okubo and Dieterich, 1984). Consequently, larger roughness can increase the stability of motion along a fault in that it favors stress release through the creation of small slip events instead of unstable slip events, i.e., stick-slips. This is supported by the observation of relatively high b-value (larger proportion of small seismic events) of acoustic emission events on rough compared to smooth faults (Sammonds and Ohnaka, 1998). Besides the influence on seismic event size distributions, roughness also influences the stress drop of slip events at laboratory scale (Okubo and Dieterich, 1984) and at the scale of natural faults (Candela et al., 2011a). Similarly, the distribution of slip on faults is related to roughness, assuming that local stress variations are connected to fault roughness (Candela et al., 2011b). A direct connection between local stress heterogeneity and fault roughness has been observed through mapping the size distributions of contacts on translucent material interfaces (Dieterich and Kilgore, 1996). Rougher faults are associated with smaller effective contact area, and the stresses at individual asperities are higher, whereas smooth surfaces exhibit more contacts over which the loading stresses are distributed. Thus, in addition to the distribution of slip, roughness influences the distribution of stress and strength along faults. This is also the case in the presence of gouge for which roughness increases the amount of stress required to shear a gouge layer (e.g. Sammis and Steacy, 1994; Rathbun et al., 2013).

The roughness of natural faults has been studied and mapped extensively for exhumed faults, revealing self-affinity of slip surfaces with similar roughness exponents and slip related surface smoothing in direction of slip (e.g. Power et al., 1987; Sagy et al., 2007; Candela et al., 2009; Grif-

fith et al., 2010; Candela et al., 2012). Faults with larger cumulative displacements are generally smoother in direction of slip than faults with small displacements (below 10–100 m) and appear polished at the smallest wavelengths (Sagy et al., 2007; Brodsky et al., 2011; Candela et al., 2012). Progressive fault smoothing is most likely caused by abrasional wear, which could be a mechanism for fault evolution (Brodsky et al., 2011). Sagy et al. (2007) pointed out that the fault smoothing process might be limited to the first $\sim$100 m of fault displacement after which fault roughness remains largely constant. Systematic changes in fault roughness due to slip may be associated with a tendency of faults to evolve into a state of less complexity and more localized slip (e.g. Chester et al., 1993; Ben-Zion and Sammis, 2003; Rockwell and Ben-Zion, 2007).

Fault evolution has also been documented as function of step overs per length scale and cumulative geologic offset (Wesnousky, 1988). Moreover, a decrease in the complexity of splay orientations may indicate that faults evolve to less geometric complexity (Wechsler et al., 2010). However, these geologic observations are limited to fault traces or exhumed fault surfaces, thus providing little insight into 3-D fault topography and fault structure at seismogenic depths. At these depths, microseismicity provides the most readily available information about fault properties. A recent study highlighted a possible connection between fault structure and across-fault seismicity distributions in California (Powers and Jordan, 2010). The authors suggested that fault smoothing, inferred from off-fault seismicity distributions, is active even at large fault displacements, i.e., for faults that exhibit cumulative offsets of 5–315 km. In their study, Powers & Jordan use a connection between fault roughness and off-fault seismicity distributions described theoretically by Dieterich and Smith (2009). The latter investigated stress interactions and sliding characteristics of simulated 2–D faults with random, fractal roughness in a purely elastic medium. The introduction of fault roughness and resulting geometric irregularities was associated with stress heterogeneity, including off-fault stresses. These off-fault stresses depended strongly on the fractal character of the fault geometry. The off-fault stress relaxation rates, $\dot{S}_{\mathrm{R}}$, were predicted to decrease as a power-law with distance from the fault, y:

$$\dot{S}_{\mathrm{R}} = kG\beta y^{-(2-H)}, \tag{6.1}$$

where G is the shear modulus, β is a prefactor that controls the total power of the spectrum, k is a constant that depends on fault slip rate, and H is the Hurst exponent which describes the fractal roughness. In the brittle seismogenic crust, off-fault stresses are likely released in form of

secondary cracks within the fault's damage zone. Consequently, the resulting seismicity distribution follows a power-law with an exponent that is linearly related to fault roughness assuming that the surfaces are in contact everywhere. This has been tested for faults in California, confirming a general power-law decay of near-fault seismicity (Powers and Jordan, 2010; Hauksson, 2010). Furthermore, Powers and Jordan (2010) quantify the linear relation between off-fault seismicity exponent and fault roughness assuming that the 2-D fault roughness model can be applied to strike-slip faults. They obtain:

$$\gamma = 2 - H, \tag{6.2}$$

where γ is the power-law exponent of seismicity decay with fault-normal distance.

To test this hypothesis, we performed frictional sliding experiments on planar fault surfaces with predefined roughness. Previous studies on natural seismicity (Powers and Jordan, 2010; Hauksson, 2010) could not establish a direct connection between seismicity and roughness because fault roughness can only be assessed for exhumed faults whereas seismicity typically occurs at several kilometers depths. Our experiments enable us to investigate both roughness and seismic off-fault activity in form of acoustic emission (AE) events under seismogenic conditions. AEs have proven to be effective in documenting both fault structure and stresses in a range of experiments. Spatial variations in the statistics of AE events during earthquake analog experiments were observed to be connected to along-strike fault structural heterogeneity and asperity locations (Goebel et al., 2012). Moreover, AE analysis can provide vital insights into the stress variations during macroscopic failure of rock samples (e.g. Scholz, 1968; Main et al., 1992; Goebel et al., 2013c) and micro-failure of asperities (McLaskey and Glaser, 2011).

In the following, we scrutinize the existence of off-fault micro-cracking through AE event and thin-section analysis. We then investigate the characteristics of the off-fault activity distribution, including a detailed test for power-law behavior. This is followed by a study of controlling parameters on off-fault activity, namely, variations in roughness and normal stress. Lastly, we discuss our findings with regard to the understanding of natural seismicity variations.

6.3 Experimental data and method

We report on five frictional sliding experiments on homogeneous, isotropic Westerly granite samples. Westerly granite exhibits varying grain sizes between 0.05 and 2.2 mm with an aver-

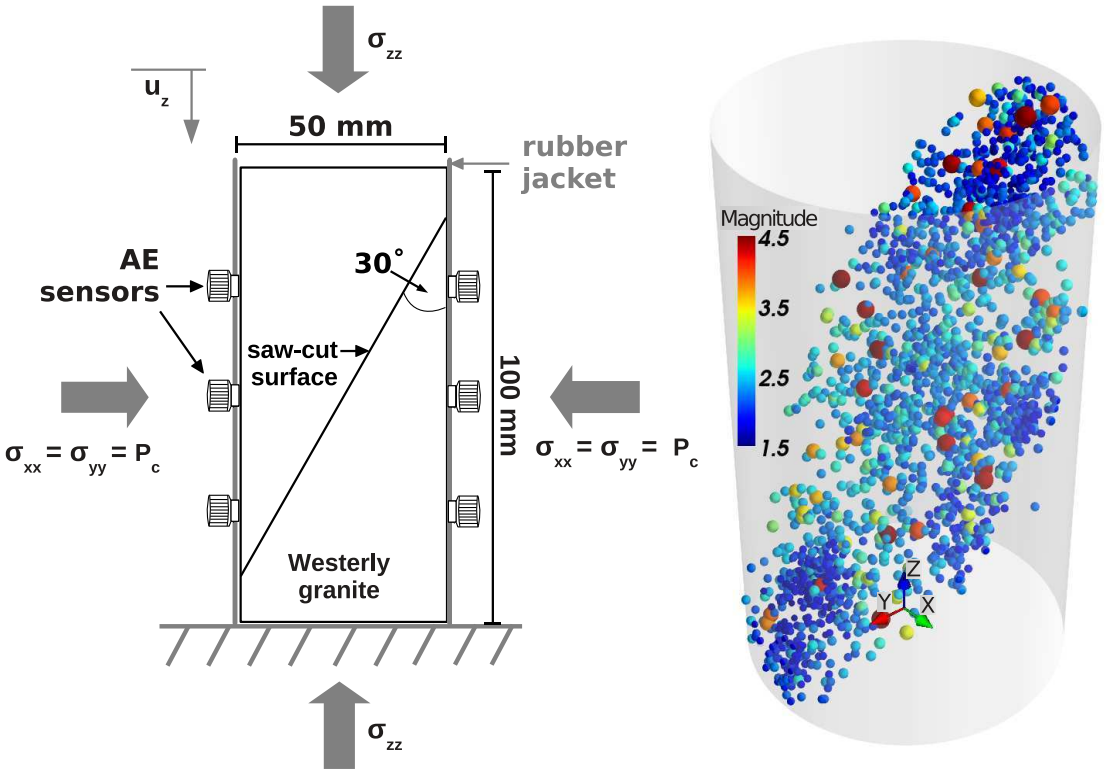

Figure 6.1: Sample geometry and loading conditions for saw-cut faults with different initial surface preparation (left). AE hypocenter locations highlight orientation of the fault at a 30° angle to the loading axis. Marker colors correspond to relative AE magnitudes estimated on a transducer-specific scale.

age grain size of 0.75 mm (Byerlee and Brace, 1968; Stesky, 1978). The employed cylindrical (height = 100 mm, radius = 25 mm) samples were prepared with saw-cuts at a 30° angle to the loading axis (Figure 6.1). The resulting surfaces were ground using different grain-size silicon-carbit abrasives. An overview of abrasive sizes, loading conditions, resulting stresses and displacements can be found in Table 6.1. All experiments were conducted at a constant axial displacement rate of 20 ¯m/min ($\dot{\epsilon} \sim 3 \cdot 10^{-6}$ s^{-1}). Within the present work, we strove to investigate the influence of different fault properties on AE distributions in isolation. To this end, we conducted two sets of experiments: the first set at constant confining pressure to test the influence of different initial roughness (experiments: LR1-LP, HR2-LP, HR1-LP, where LR and HR denote low and high roughness, and LP low pressure), and the other set (experiments: HR1-HP, HR1-IP, HR1-LP, where HP, IP, LP denote high, intermediate and low pressure) with the same initial surface finish to test the influence of different confining pressures and connected fault stress level.

We imaged the initial surfaces for each choice of abrasive using a White Light Interferometer

(Zygo7300). Interferometry imaging is based on the interference pattern of a reference green light beam with a beam that reflects off a rough surface. By vertical movement of the sample and simultaneous image capturing, the interference, intensity envelope, and thereby the relative height of the imaged surface at each pixel is determined. A vertical resolution down to 0.1 nanometer was estimated by scanning a flat, reference surface (Silicon Carbide) with an estimated roughness of ~ 6 order of magnitudes below the roughness of the initial surfaces used in our experiments.

We computed two different measures of initial surface roughness: The first measure was the root-mean-square (R_{rms}) which provides an estimate of the deviation from an average roughness profile:

$$R_{\mathrm{rms}} = \sqrt{\frac{1}{n}\sum_{i=1}^{n}(p(z_i) - \bar{p})^2}, \tag{6.3}$$

where $p(z)$ is the roughness profile. The other measure of roughness was computed from the power-spectral density of Fourier-transformed, roughness profiles, which were stacked for individual scans. This method provides an estimate of roughness as function of wavelength. Straight parts of the log-transformed power-spectra indicate self-affine scaling of wavelength and power. This can be quantified by computing the Hurst exponent (H):

$$P(\lambda) = \beta\lambda^{1+2H}, \tag{6.4}$$

where $P(\lambda)$ is the power at wavelength λ and β is a pre-factor that is related to the absolute vertical topography (Feder, 1988; Amitrano and Schmittbuhl, 2002; Candela et al., 2009). The Hurst exponent itself shows the distribution of power over different wavelength, i.e., the relative power at small compared to large wavelengths. Instead of the Hurst exponent, one can express this relationship also by the roughness exponent α (e.g. Power and Durham, 1997) which is linearly related to H (e.g. $\alpha = 1 + 2H$ for power spectral slopes) (e.g. Feder, 1988). The Hurst exponent commonly occupies values between 0–1. A Hurst exponent of unity ($\alpha = 3$) indicates self-similar roughness scaling, whereas values of H below unity are connected to self-affine surfaces. For natural faults, H commonly ranges between 0.6–0.8 but also shows anisotropic behavior, i.e., smaller Hurst exponents in direction of slip (e.g. Sagy et al., 2007; Candela et al., 2009, 2012; Renard et al., 2013).

Frictional sliding of the rough surfaces under high pressures resulted in large AE catalogs con-

taining 1,268 to 10,907 events. The AE events had an amplitude range of about 4 orders of magnitude. Events were located by travel-time inversion of automatically picked first P-wave arrivals. We used AE sensors both as receivers and active pulse senders. The latter was to estimate seismic velocity changes throughout the experiments to improve the AE location accuracy. Similarly to Lockner et al. (1991a), we limited our analysis to high quality events, i.e., AEs that were recorded at 8 stations or more and a travel-time residual $\leq 0.5\ \mu s$. In general, the location uncertainty was estimated between 1 and 4 mm, depending on the extent of fault-induced velocity perturbations and the proximity of an event to the edge of the sample. Average uncertainties could be lower for certain regions and experiments, especially for simple geometries like saw-cut samples.

6.4 Across-fault activity profiles and power-law parameter estimates

To analyze spatial characteristics of AE catalogs for experiments with different roughness, we projected the recorded AE events into a fault-specific coordinate system and computed across fault activity profiles. The AE activity was generally symmetric with respect to the fault axis allowing for a stacking of AE events from both sides of the fault. We deployed two methods to quantify the distribution of events with distance to the slip surface. The first method follows previous studies of natural seismicity (Felzer and Brodsky, 2006; Powers and Jordan, 2010; Hauksson, 2010). It is based on an estimate of the linear density of AEs (linear density distributions will be referred to as LDDs in the following) by sampling a constant number (N) of nearest neighbor events starting from the fault center (Silverman, 1986). We then determined the area covered by each sample from the distance of the N^{th} event and normalize by the total fault area and duration of the experiment. Changes in N mainly influence the smoothness, and distribution tail whereas the slope remains largely stable for large sample sizes.

We also computed cumulative distributions of AE events as function of distance to the slip surface. The advantage of this method is that it is not prone to binning artifacts. Moreover, cumulative distributions depict many details of the trends in the data especially toward the tail of the distribution. The LDDs, on the other hand, represent the data in a smoothed form which can be advantageous to diminish the influence of individual outliers. Furthermore, LDDs depict regions of constant AE density as horizontal trends in the data and power-law cut-offs can be estimated from the deviation from linearity of the activity fall-off close to the fault center. The slope below

the power-law cut-off can be determined by least-squares fitting since every data point contains the same number of seismic events hence same statistical significance.

Due to the consistent curvature of cumulative distributions, it is more complicated to estimate the power-law cut-off. For this reason, we compute the minimum cut-offs for our data ($Y_{\min}$) using the maximum Kolmogorov-Smirnoff distance (KS-distance) between the observed distribution and modeled power-law distribution at varying values of $Y_{\min}$ (Clauset et al., 2009). The best parameter estimates of $Y_{\min}$ and γ will minimize the KS-distance between model and observation. The maximum likelihood estimate (MLE) of the power-law exponent is given by (e.g. Newman, 2005; Clauset et al., 2009):

$$\gamma = 1 + n \left[\sum_{i=1}^{n} \ln \frac{Y_i}{Y_{\min}} \right]^{-1} . \tag{6.5}$$

Here, $Y_{\min}$ is the minimum bound, γ is the power-law exponent, n is the number of data points above $Y_{\min}$, and Y_i are the observed distance values above $Y_{\min}$. The MLE is independent of sampling and less sensitive to variations in the distribution's tail compared to least-square estimates of binned, log-transformed data (Clauset et al., 2009). For the MLE, we can estimate the goodness-of-fit using a Monte-Carlo re-sampling approach: We created synthetic data using the best-fit power-law parameters, computed the corresponding KS-statistics and compared it to the KS-statistic of the observed data set (Clauset et al., 2009). The goodness-of-fit (p-value) is then simply the fraction of cases for which the synthetic KS-distances are larger than the empirical distance. Large p-values (here we choose a value above 0.1 following Clauset et al. (2009)) suggest that a power-law distribution is a plausible hypothesis whereas small p-values would require the rejection of the power-law hypothesis.

6.5 Results

The triaxial loading of our five samples resulted in different deformation characteristics along the saw-cut surfaces. An overview of the total vertical displacements, initial surface treatment and the stress conditions on the faults can be found in Table 6.1. The normal stresses varied between 178 and 244 MPa for different experiments with the largest normal stress for experiment HR1-HP which also exhibited the largest confining pressure. The initial stress increase was predominantly linear for all experiments (Figure 6.4c). This was followed by extended periods of non-linear stress increase accompanied by higher AE activity. Experiment LR1-LP produced three stick-slip events

Sample	σ_n [MPa]	τ [MPa]	μ	P_c [MPa]	U_{max} [mm]	mesh-size	abrasive grain-size [μm]
LR1-LP	221±4	175±4	0.79	120±0.5	4.76±0.003	F290	16.5–59
HR2-LP	222±4	177±4	0.79	120±0.5	3.32±0.003	F80	150–212
HR1-LP	178±4	101±4	0.57	120±0.5	1.02±0.003	F60	212–300
HR1-IP	225±4	160±4	0.71	133±0.5	5.03±0.003	F60	212–300
HR1-HP	244±4	162±4	0.67	150±0.5	2.25±0.003	F60	212–300

Table 6.1: Stress state, displacements and surface preparation of all experiments. σ_n - normal stress, τ - shear stress, μ - coefficient of friction, P_c - confining pressure, U_{max} - maximum vertical displacement, mesh-size and abrasive grain-size describe the silicon carbit powder used to grind the inclined saw-cut surfaces.

with shear stress drops in the range of $\approx$ 107–173 MPa. For this experiment, we determined the normal stress in Table 6.1 from the average, peak stress before the three stick-slip events. To ensure comparability, we only analyzed AE events that occurred before the first stick-slip event and compared the corresponding AE distribution to the initial surface roughness. At the beginning, we will focus on experiments HR2-LP, HR1-LP, and LR1-LP, which were conducted at the same confining pressure ($P_c = 120$ MPa) but different surface finish. LR1-LP resembles a polished surface with no apparent topography whereas both HR2-LP and HR1-LP appeared rough during visual inspection before the experiments.

6.5.1 Initial surface roughness

We determined the initial roughness of the three different surface-finishes with mesh-sizes F290, F80, and F60 (see also Table 6.1 for different experiments and corresponding mesh-sizes). The power-spectra of all surfaces exhibited several decades of self-affine scaling between wavelength and power (Figure 6.2a). highlighting the fractal character of the roughness within that scale range. The smooth surface (F290) showed a characteristic roll-off and flattening of the spectrum above $\sim$ 0.1 mm. The rough surfaces started to deviate from linearity of the power-spectra at larger wavelengths ($\lambda > 0.2$ mm). The flattening of power spectra at large wavelength is related to the planarity of the surfaces which introduces a maximum wavelength of roughness and a corresponding roll-off in power (Persson et al., 2005). Below the roll-off wavelength, F290 appears smoother (less power) at all wavelength than F80 and F60, and also above, F290 shows smaller power at the largest wavelengths. F80 and F60 exhibit very similar power-spectra that only deviated at the largest wavelengths.

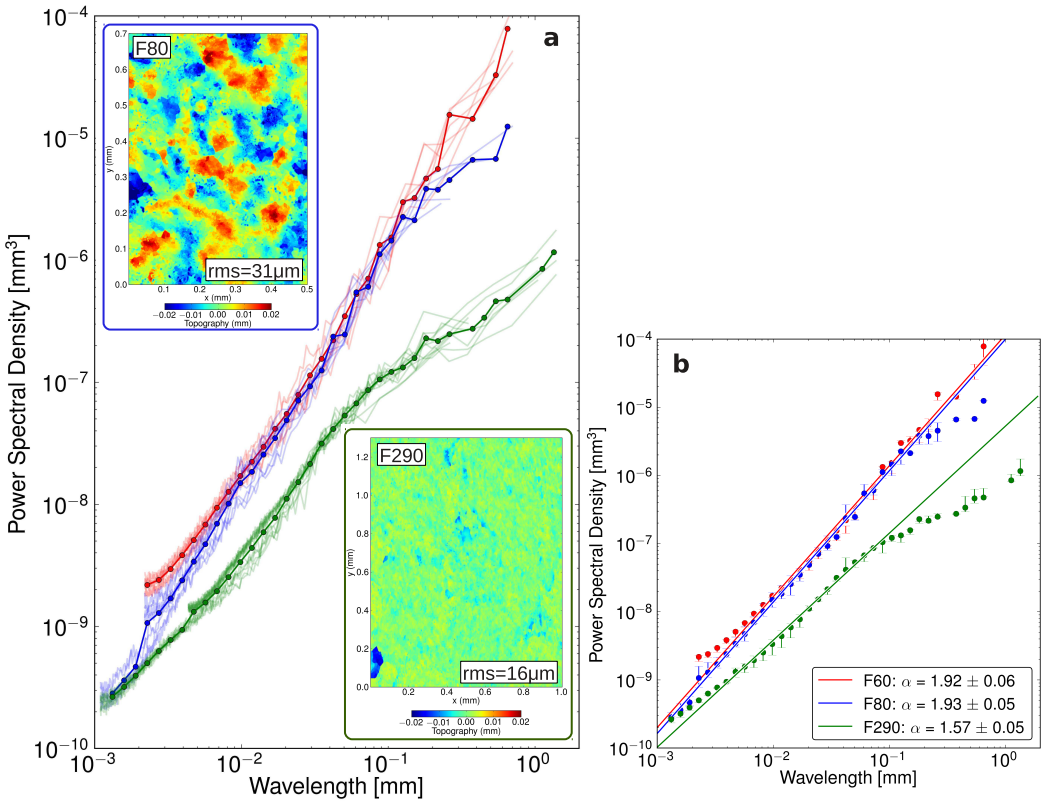

Figure 6.2: Power spectral density as function of wavelength for smooth and rough faults. a): Stacked power spectra for different roughens profiles of surface F290, F80 and F60 (see legend in b). The surface IDs correspond to the mesh-sizes in Table 6.1. The experiments were prepared in the following manner: F290 - LR1-LP, F80 - HR2-LP, F60 - HR1-HP, HR1-IP, and HR1-LP. Upper and lower insets depict the topography within the initial roughness of a rough and a smooth surface. b): Least-square fits of average power-spectral density of all scans of the individual surfaces. F80 and F60 have comparable roughness exponents whereas F290 has a substantially smaller exponent.

To understand the possible role of fractal roughness in controlling seismic off-fault activity, we are interested in changes in slopes of the power-spectra. To this end, we computed the roughness exponents, α, for the fractal range of power-spectra (Figure 6.2b). F60 and F80 exhibited largely identical values of $\alpha = 1.92$ and $\alpha = 1.93$ respectively, whereas F290 exhibits a substantially smaller value of $\alpha = 1.57$.

6.5.2 AE hypocenter locations, off-fault micro-cracks and loading curves

To test if seismic event distributions and off-fault activities are connected to different roughness, we analyzed high precision AE catalogs. AE events generally highlight the orientation and extent of the saw-cut surfaces (Figure 6.3). We scrutinized the quality of surface finish before and during

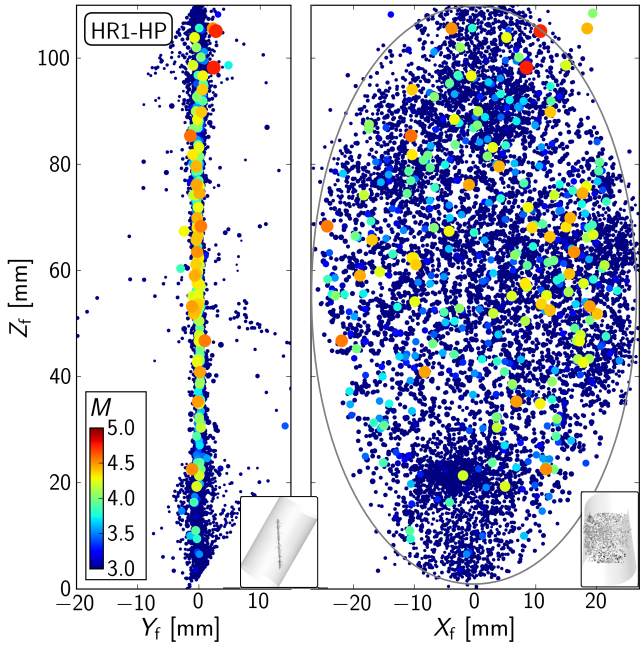

Figure 6.3: AE hypocenter locations of experiment HR1-HP, projected into the fault coordinate system and viewed in a plane perpendicular (left) and parallel (right) to the saw-cut surface. Marker colors correspond to AE magnitudes on a scale that is specific to the present experimental set-up.

the experiments. The latter was accomplished by comparing the extent of AE hypocenter locations with the faults' surface area, which was a good indicator for surface planarity and homogeneous surface contacts. Experiments with localized AE clustering, which is indicative of uneven surface finish resulting in partial loading of the surfaces, were not included in this study.

Figure 6.3 (left) highlights the orientation and extent of the AE event populations of experiment HR1-HP. AEs occurred in a narrow zone of a few millimeter width around the fault axis. Large magnitude events predominantly occurred on the fault plane whereas smaller magnitude events were located at maximum fault-normal distances of $Y_f = 10$–20 mm from the fault plane, thus suggesting pervasive micro-cracking away from the fault.

We test the existence of off-fault micro-cracks through inspection of post-experimental thin-sections and histograms of the AE activity with increasing Y_f. The thin-section images revealed a network of cracks and connected pore-space that extended out to a fault-normal distance of $\sim$10 mm (Figure 6.4a). Similarly, the largest AE activity was observed within the first 5–10 mm (Figure 6.4b). Within this range of fault-normal distances, the AE activity decreased rapidly until it reached an approximately constant rate for $Y_f > 10$ mm. Thus, both AE event distributions and thin-sections provide evidence for the existence of seismically active micro-cracks at distances up to $\sim$18 mm from the fault axis.

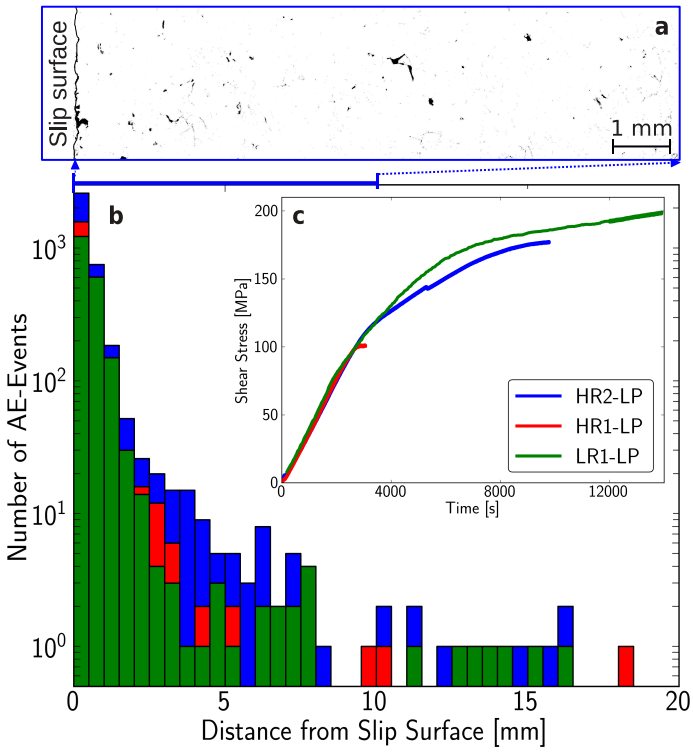

Figure 6.4: a): Post-experimental micro-crack distribution in a fault-perpendicular thin-section. Here, we only show the relevant microcracks which appear as black, linear features in a thinsection. b): Seismic activity histograms as function of distance from the slip surface for three surfaces with different initial roughness (see legend or Table 6.1 for mesh-sizes used for surface grinding). All surfaces show clear evidence of seismic activity away from the slip surface. This activity decayed the fastest for the smooth surface and slower for the rougher surfaces. c): Changes in fault shear-stress during loading of the three different, rough surfaces.

6.5.3 Across-fault activity profiles and power-law exponent estimate

In the following, we will compare the two aforementioned methods to quantify off-fault activity distributions. We start by computing LDDs using constant AE sample sizes of $N = 20$ events (Figure 6.5a). Expectedly, this method depicts a plateau in the AE activity close to the fault axis at distances of $Y_f \lesssim 0.4$–0.7 mm. This is followed by a rapid decrease in AE density at larger distances. We estimated the slope of this decrease (γ) using a least-squares fit. The power-law exponents are similar for the two rough surfaces (HR2-LP: $\gamma = 2.63 \pm 0.17$, HR1-LP: $\gamma = 2.52 \pm 0.42$) whereas the smooth surface (LR1-LP) exhibits a substantially higher exponent of $\gamma = 3.5$. To test the stability of these results, we compute the power-law exponent using the MLE (Eq. 6.5). The MLE power-law fit and cumulative distribution of each of the three experiments is shown in Figure 6.5b. The minimum cut-off values Y_{min} were computed by minimizing the KS-distance between observed and modeled distributions. These values were also used to define the resolution limit of both cumulative and AE density distributions. For details about the role of Y_{min} and its connection to hypocentral uncertainties, see section 6.5.4. The power-law exponent increases for the different experiments from $\gamma = 2.57$ for HR2-LP to $\gamma = 2.74$ for HR1-LP and lastly to $\gamma = 3.11$

for experiment LR1-LP. In comparing the least-squares and maximum likelihood estimates, we notice an apparent difference for the experiments with relatively small sample sizes (HR1-LP, LR1-LP) while HR2-LP exhibits largely constant exponents. The discrepancy is likely due to a combination of binning artifacts in the LDDs and large uncertainties of least-squares fit for small sample sizes. The latter can result is insufficient data spread for a reliable least-square fit of LDDs. For example, the data points of experiment HR1-LP are concentrated between 0.7 and 2 mm, providing a small range for a least-square fit and a relatively large error of 0.42. Small changes in the furthest data points can thus influence the power-law exponent substantially. The MLE, on the other hand, is insensitive to binning artifacts and outliers in a distribution's tail (Clauset et al., 2009).

To further investigate the relative differences in the observed distributions, we computed the power-law exponent as function of increasing values of $Y_{\min}$ between 0.1 and 3 mm (Figure 6.6). We expect γ to increase rapidly when approaching the true $Y_{\min}$ value from below and to stay roughly constant above, over the range where the power-law holds. This behavior could be observed for experiment HR1-LP which approached a value of $\gamma \sim 2.7$ for $Y_{\min} > 0.5$, and is in agreement with the predominantly linear trend of the cumulative distribution on logarithmic scales (Figure 6.5b). The other two experiments exhibited trends in γ that are stable over shorter ranges (i.e. 0.7–1 for LR1-LP and 0.5–1 for HR2-LP). The combination of stability of γ and statistical error give an estimate for possible range of $Y_{\min}$. Above $Y_{\min} = 1.5$, the uncertainty in γ becomes too large, providing an upper bound for $Y_{\min}$. Consequently, one can determine, that within the possible range of $Y_{\min}$, LR1-LP has the largest value of $\gamma \approx 3$–3.1 while HR1-LP shows lower values ($\gamma \approx 2.6$–2.75) and HR2-LP consistently shows the lowest values ($\gamma \approx 2.3$–2.55).

6.5.4 Testing the power-law hypothesis

We tested if the observed distributions can be described by a different model, for example, a simple summation of normal distributions which represent Gaussian-uncertainties in hypocenter locations. To this end, we created random uniformly-distributed hypocenter locations within a fault zone with varying widths, $w = 0.1$–5.1. Instead of discrete event locations, we prescribed each hypocenter a random Gaussian uncertainty with varying width (Figure 6.7a) and computed the cumulative distributions and power-law exponents for the resulting synthetic distributions (Figure 6.7b). As a reference, we also plotted the cumulative distribution and γ as function of $Y_{\min}$

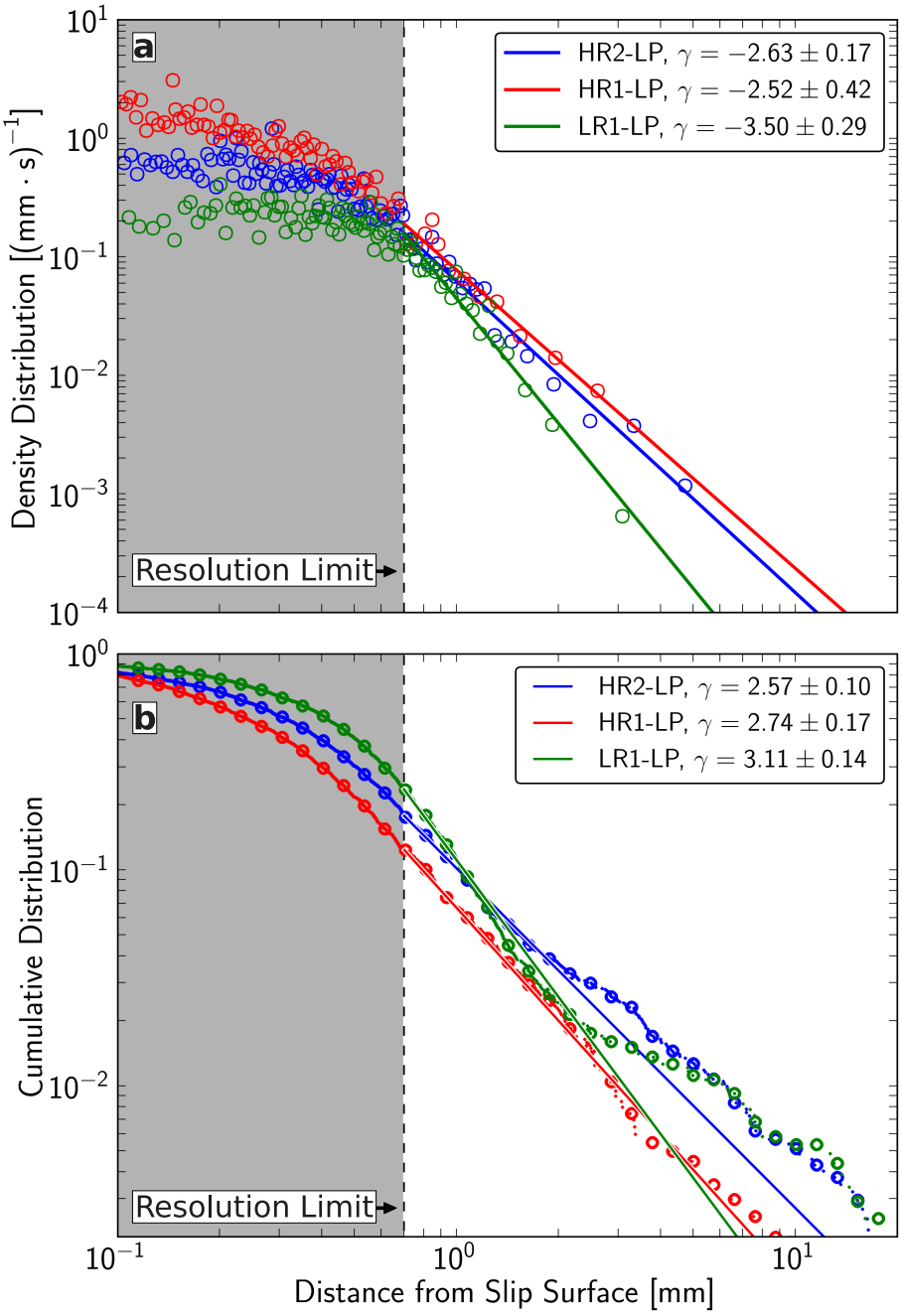

Figure 6.5: a): AE density distribution as function of fault-normal distance, estimated by LDDs. The corresponding power-law exponents for each experiment are shown in the legend on the upper right. The shaded, gray area depicts the lower resolution limit of across fault activity profiles which is defined by the lower bound of the power-law as discussed in the text. b): Cumulative distributions of seismic activity as function of fault-normal distance and MLE of corresponding power-law exponents. The distributions are depicted for log-bins between 0.1 to 20 mm and exponents are computed for activity above minimum cut-off.

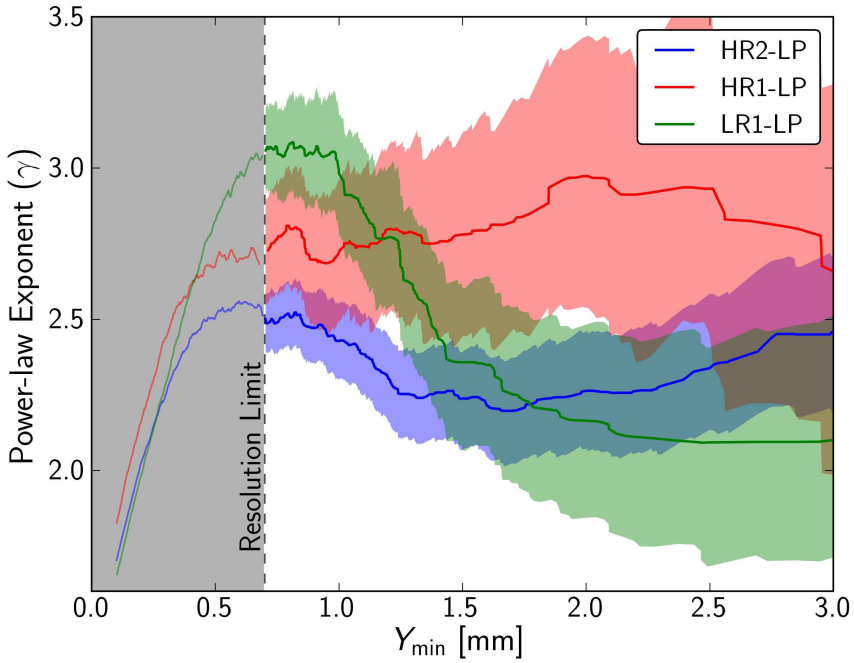

Figure 6.6: Changes in power-law exponent α as function of minimum cut-off Y_{min}. The stability of α above the estimated minimum cut-off ($Y_{\text{min}} = 0.7$) is a good indication about the range of the power-law behavior.

for one of the observations (HR1-HP). The synthetic Gaussian distributions generally overpredict the number AE events close to the slip surface while decaying too rapidly at larger distance thus providing a poor fit to the observation. The corresponding estimates of γ express the continuous curvature of the synthetic distributions, i.e., they never show the plateau of constant exponents characteristic for power-law behavior. Thus, hypocentral uncertainties alone cannot explain the observed across-fault activity profiles.

After ruling out that the observed distributions are simply caused by Gaussian errors, we tested the hypothesis that the observed distributions are a convolution of hypocentral uncertainties and a power-law distribution. To this end, we randomly sampled fault-normal distances from power-law distributions with the empirically determined exponents. We then assigned a value of Gaussian uncertainty to each distance value and computed the resulting cumulative distribution and power-law exponent (Figure 6.8). The resulting distributions mimic the characteristics of the observed distribution including the region of high AE density close to the fault axis, a gradual roll-off zone and transition into a power-law dominated distribution at increasing fault-normal distances. The

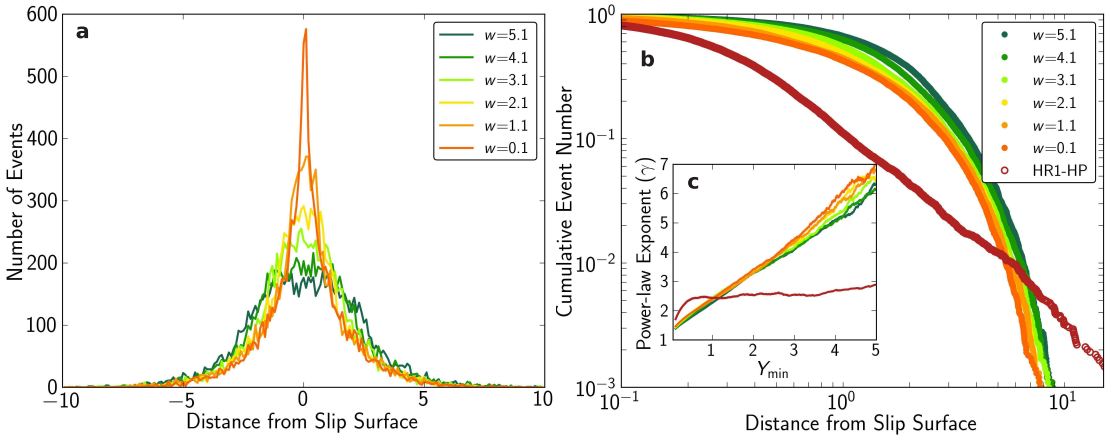

Figure 6.7: a): Simulated Gaussian distributions for different fault widths (w) see text for details. b): Cumulative, synthetic Gaussian distributions for different fault widths (colored markers) and power-law distribution with exponent and minimum cut-off that resemble the observed values. The inset (c) displays differences in exponent as function of minimum cut-off assuming a power-law model for the data. The red line shows observed values of γ as function of Y_{min} for experiment HR1-HP, highlighting that the Gaussian distributions are a poor description of our data.

convolution of power-law and Gaussian uncertainties changes the parameter estimates of an initial power-law in two different ways: First, it generally leads to a slight overestimate of the power-law exponent due to the faster decay of Gaussian distributions at intermediate distances. This is most pronounced for large power-law exponents. Second, large normal distribution widths systematically increase the roll-off zone and connected minimum cut-offs of the initial power-law. Nevertheless, the depicted distributions highlight that the observed data could be modeled by convolving power-law with normal distributions. Figure 6.8 shows the best-fit (minimum KS-distance) distribution exemplified for experiment HR2-LP which has a Gaussian-width of $\sigma \approx 2$ mm.

We systematically tested the connection between the observed parameter estimates Y_{min}, γ and the parameters of the synthetic distributions γ^* and σ, where γ^* is the exponent of the initial power-law and σ is the width the normal distribution. The latter gives an estimate of the expected hypocentral uncertainty. We simulated a range of distributions with increasing Gaussian widths and estimated the minimum cut-offs (Y_{min}) using the minimum KS-distance between synthetic and modeled distribution (Figure 6.9b). Following this method, the theoretical prediction of the Gaussian uncertainty for a power-law with lower cut-off $Y_{\text{min}} = 0.7$ convolved with a normal distribution is $\sigma = 1.4$–2 mm depending on the power-law exponent. These values are in approximate agreement with AE location errors ($\sigma \approx 1.7$ mm) estimated for known sensor locations that were

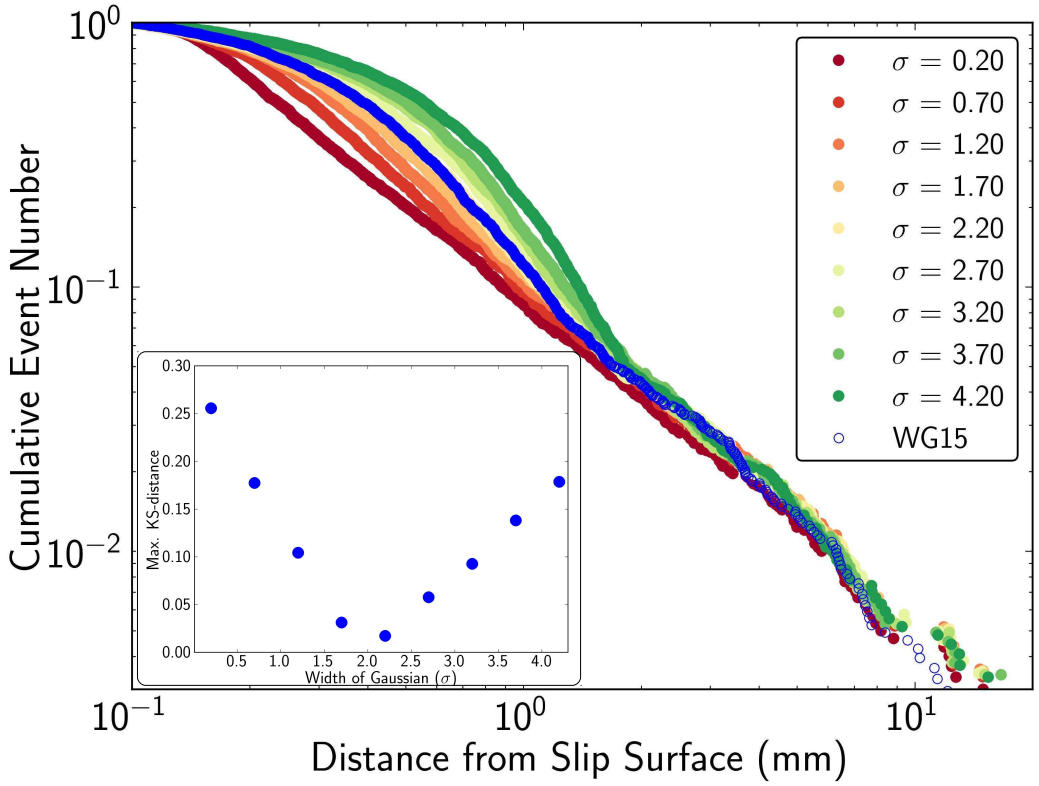

Figure 6.8: Observed (blue circles) and synthetic distributions (colored markers) computed from power-laws with Gaussian uncertainty. The best-fit synthetic distribution was estimated by minimizing the KS-distance between the different distributions (inset).

Sample	γ	γ^*	p-value	α	N_{AE}	N_{AE}/s
LR1-LP	3.11±0.15	2.85±0.15	0.14	1.57±0.05	1978	0.14
HR2-LP	2.56±0.10	2.42±0.10	0.11	1.93±0.05	3787	0.33
HR1-LP	2.74±0.17	2.56±0.17	0.64	1.92±0.06	2073	0.67
HR1-IP	2.55±0.12	2.42±0.12	0.36	1.92±0.06	1268	0.01
HR1-HP	2.48±0.06	2.36±0.06	0.53	1.92±0.06	10907	1.63

Table 6.2: Results of off-fault activity and roughness analysis for all experiments. γ - observed off-fault activity exponent, γ^* - off-fault activity exponent corrected for Gaussian uncertainty, p-value - goodness-of-fit, α - roughness exponent, N_{AE} - total number of observed AE events, N_{AE}/s - AE-rate per second.

used as active sources.

Assuming that the width of the Gaussian remains constant for all experiments, which is supported by constant array sensitivity, we could also test the influence of the normal distribution on the observed power-law exponents (Figure 6.9a). As previously noted, the observed power-law exponent (γ) was slightly higher than the true power-law exponent (γ^*) due to the presence of Gaussian uncertainty. The computed synthetic distributions suggest an approximately linear relationship between γ and γ^*, enabling a simple correction of the observed exponents. This correction is slightly larger for higher exponents whereas small exponents are less influenced by the Gaussian uncertainty and consequently deviate less from the true value. In the following, we will use the value of the power-law exponent corrected for Gaussian uncertainty of hypocenter locations (see Table 6.2 for both γ and γ^*).

We estimated the goodness-of-fit for the observed power-law exponent resulting in p-values between 0.11–0.64. This supports that a power-law is a valid hypothesis for the observed distributions since none of the power-law fits can be rejected at the chosen confidence level. The computed p-values are related to the extent of the power-law, which is seen at both the degree of linearity of cumulative distributions (Figure 6.5) and the stability of γ-values as function of Y_{min} (Figure 6.6). For example, experiment HR2-LP depicts a comparably low p-value (0.11) and corresponding larger fluctuations in γ as function of Y_{min}, whereas HR1-LP showed a higher p-value (0.64) and stable values of γ above Y_{min}. The computed p-values are somewhat sensitive to the number of samples within the observed distributions especially in case of very small sample-sizes which can lead to an unrealistic inflation of p-values (Clauset et al., 2009). A combination of the here proposed measures can largely prevent miss-interpretations of p-values, and should generally be applied to seismicity fall-off studies.

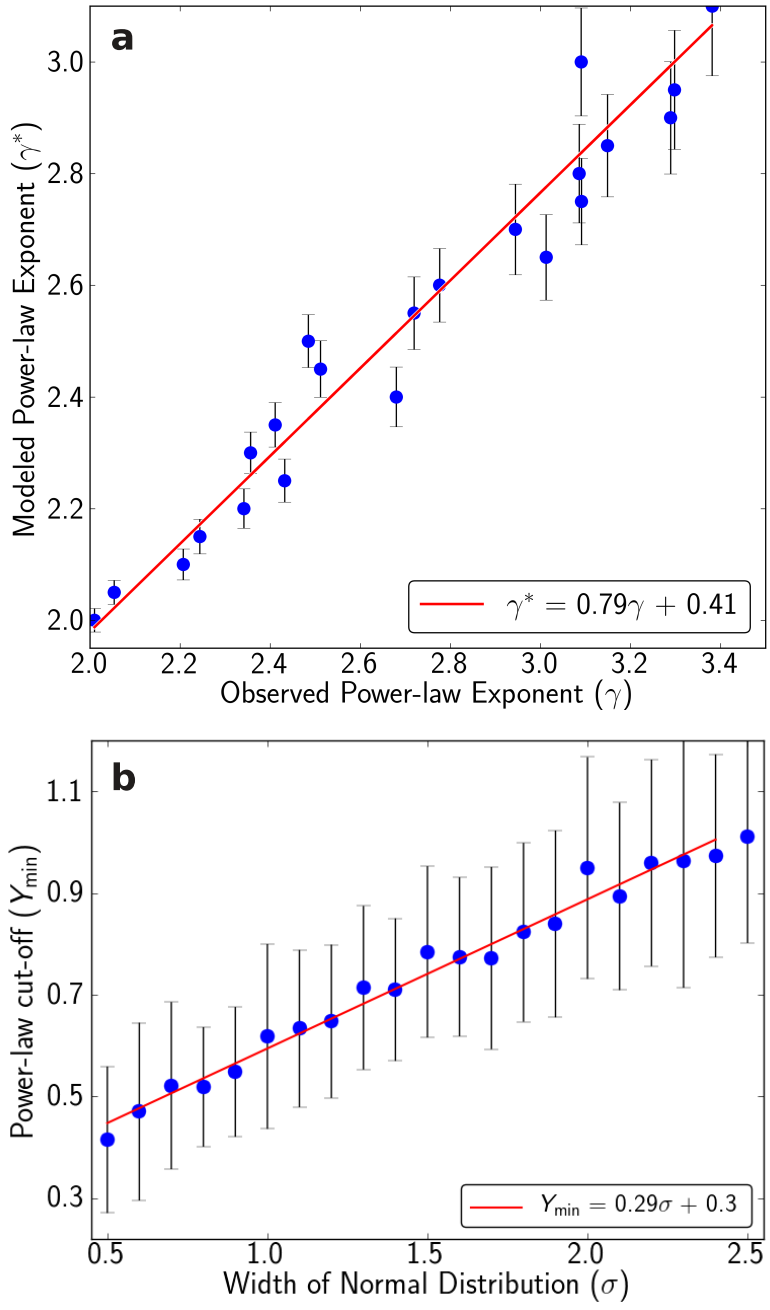

Figure 6.9: Changes in power-law parameters due to the presence of Gaussian uncertainty. a): Connection between true (γ^*) and observed (γ) power-law exponent assuming constant Y_{min} and σ. b): Influence of σ on Y_{min}. For our experiments a value of $Y_{min} = 0.7$ suggests a hypocentral uncertainty between 1.4–2.0 mm.

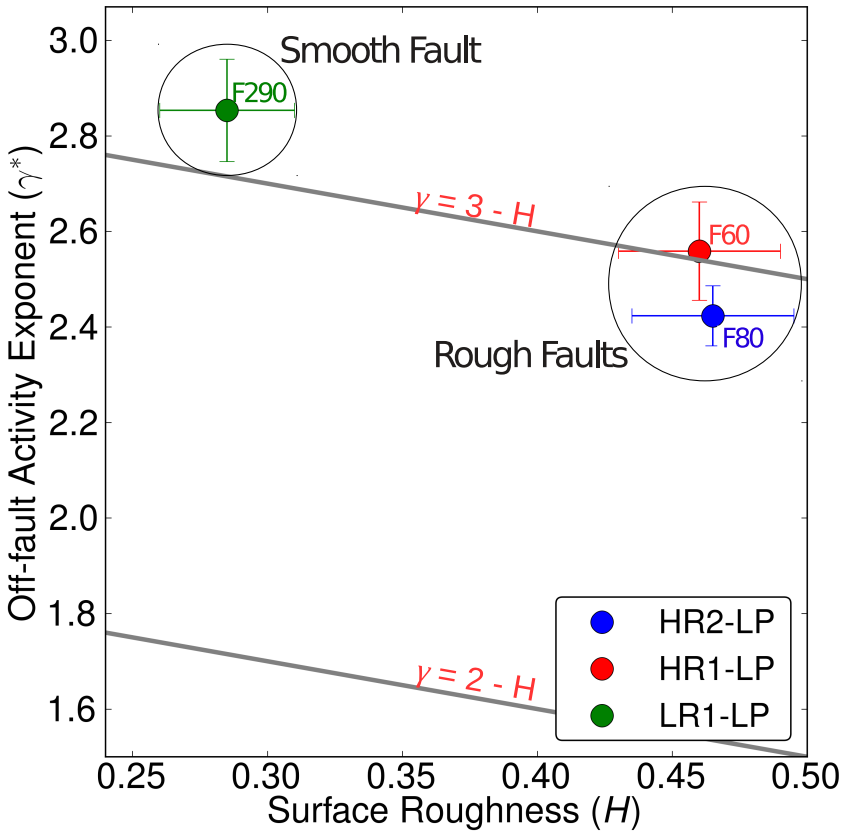

Figure 6.10: Increasing surface roughness results in decreasing off-fault activity exponents. Rough faults (HR2-LP and HR1-LP) are highlighted by a dark circle to the right and the smooth fault (LR1-LP) is located at the upper left. The labels next to the markers correspond to the abrasive mesh-size used for initial surface preparation. Grey lines show the theoretical prediction of a connection between roughness and off-fault activity. The corresponding equations are depicted above the gray lines.

6.5.5 Roughness and off-fault AE distributions

We now test the initial hypothesis that seismic off-fault activity is connected to the fractal roughness of a slip surface. Figure 6.10 shows the off-fault activity exponents as function of Hurst exponent. The smooth fault is connected to a higher γ value while the Hurst exponent is substantially lower, which is in agreement with the hypothesis. The two rough surfaces, which exhibited a similar value of H, showed slightly different values of γ but both were substantially lower than the value for the smooth surface. The model in Dieterich and Smith (2009) suggests that the Hurst exponent should be linearly related to the off-fault activity exponent, γ in 2-D (Eq. 6.2). We included this relationship in Figure 6.10. Our results support a similar linear relationship, however, with a different regression intercept. Thus, a relationship of the form: $\gamma = 3 - H$ describes our data

better. This discrepancy is likely due to the difference in geometric dimensions between model and laboratory fault zones, which results in a variation of the spatial extent of stress perturbations (see Discussion for details).

6.5.6 Normal stress and off-fault AE distributions

Considering the difference in off-fault activity exponents between HR2-LP ($\gamma = 2.56$) and HR1-LP ($\gamma = 2.74$) at similar initial roughness, other mechanisms appear to influence γ as well. In the context of the current experimental series, a variation in fault stresses is a likely candidate that may change the off-fault activity. We investigated the influence of different normal stresses by conducting three experiments with the same initial roughness ($\alpha = 1.92$) but different confining pressures. Starting with experiment HR1-LP ($P_c = 120$ MPa), we increased the confining pressure to $P_c = 133$ MPa for experiment HR1-IP, and $P_c = 150$ MPa for experiment HR1-HP. The power-law exponent of the off-fault activity changed with increasing confining pressures from 2.74 to 2.55 and 2.48 (Figure 6.11). The respective goodness-of-fit values (p-values) can be found in Table 6.2.

The power-law exponents decrease in an approximately linear fashion with increasing normal stresses (Figure 6.12). This indicates that faults under higher normal stresses can appear 'seismically rougher', in the sense that relatively more of the seismic activity is located at larger distances from the slip surfaces (see inset in Figure 6.11), and the off-fault activity exponents become smaller. The rate of change in γ due to the observed range of normal stress increase ($\sim 4 \cdot 10^{-3}$ MPa) can also account for the difference in γ between HR2-LP and HR1-LP ($\Delta\gamma \sim 0.18$) due to a change in normal stress of $\Delta\sigma_n = 44$ MPa. These considerations are under the assumption of a simple linear relationship between increasing normal stresses and γ. More complex interactions between fault roughness and stress state may also result in a more complex relationship between these quantities and the off-fault activity exponents (see Discussion).

6.6 Discussion

6.6.1 Influence of roughness on seismic off-fault activity

Our results are in agreement with theoretical predictions of a connection between surface roughness and the rate of stress relaxation with increasing fault-normal distance (Dieterich and Smith,

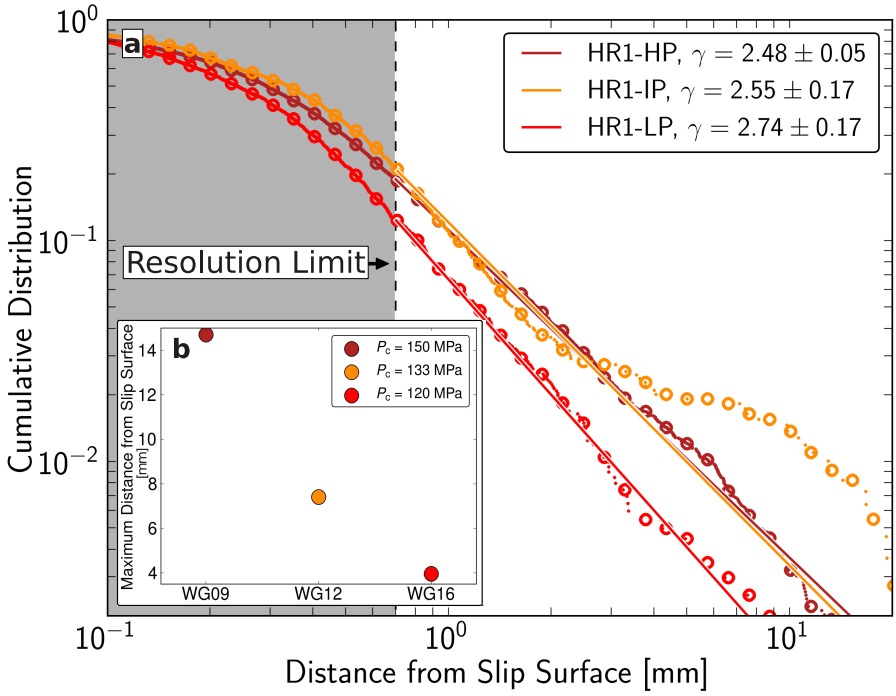

Figure 6.11: Influence of confining pressure on seismic off-fault distribution and maximum AE event distance from the fault axis a): Cumulative distribution of AE events as function of distance from the slip surface for 3 experiments with different confining pressure (HR1-LP: $P_c = 120$ MPa, HR1-IP: $P_c = 133$ MPa, HR1-HP: $P_c = 150$ MPa) but same initial roughness. b): Maximum distance of the furthest off-fault events. Here, we used the average distance of the furthest 50 AE events in millimeter to diminish the influence of individual outliers.

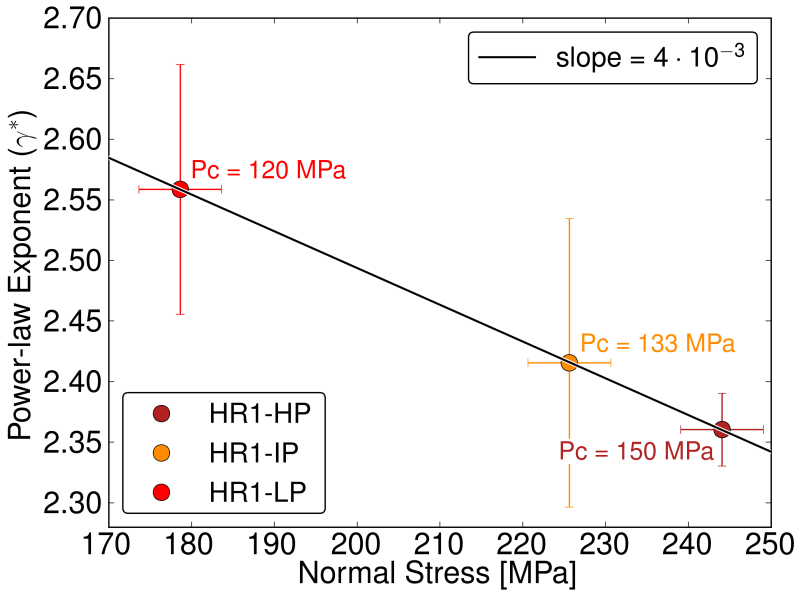

Figure 6.12: Increasing normal stresses lead to a decease in the off-fault activity exponent (γ). The three markers correspond to three experiments conducted at different confining pressures.

2009). While these stresses could not be measured directly, the observed AE event distributions and post-experimental thin-sections (see Figure 6.4a) are a good indicator for a stress release in form of brittle micro-cracking and associated seismic energy release. Fault roughness and connected geometric interaction at irregularities are likely involved in the creation of pervasive off-fault damage out to distances of ∼10–20 mm. This process can, in addition to dynamic ruptures, play an important role in the creation of damage zones in the vicinity of natural faults (Dieterich and Smith, 2009). Laboratory experiments (e.g. Zang et al., 2000; Janssen et al., 2001) and geologic observations of natural faults indicate that fault wall-damage zones show crack densities that decrease exponentially, or as a power-law, with distance from the fault (e.g. Anders and Wiltschko, 1994; Mitchell and Faulkner, 2009; Savage and Brodsky, 2011). This type of damage is likely related to high strain at a propagating rupture tip and deformation around the fault as slip increases (e.g. Kim et al., 2004; Griffith et al., 2009; Xu and Ben-Zion, 2013). The here discussed off-fault damage would predominantly be created during interseismic periods on rough faults and background stresses close to the critical stress. Within the scope of the current experimental series, we did not observe a systematic connection between the maximum range of the off-fault power-law and the outer length-scale of the fractal fault geometry, as hypothesized by Dieterich and Smith (2009). This may be due to limited ranges of wavelengths over which the roughness of our sur-

faces can be considered as fractal. Moreover, the AE events at the farthest distance from the fault axis are likely associated with small-scale sample heterogeneities that radiate seismic energy at locally-high stresses. This is especially visible for smooth faults with comparably localized AE activity, e.g., LR1-LP which produced AE activity that was higher than predicted from a power-law at large distances to the slip surface. For rougher faults, finite sample sizes may additionally influence the distribution at large distances ($Y_f \gtrsim 20$ mm).

We tested a proposed theoretical model that suggests a linear relation between fractal roughness and off-fault activity decay exponent, implying that rougher faults exhibit increased spatial extents of significant off-fault stresses (Dieterich and Smith, 2009). This model and observations of actual seismicity led Powers and Jordan (2010) to posit that the relationship between off-fault activity exponent and fault roughness goes roughly as $\gamma = 2 - H$, where H is the Hurst exponent characterizing fault roughness. This scaling was based on the assumption that the 2-D approximation of Dieterich and Smith (2009) model holds approximately also in 3-D. Instead, our results suggest a scaling closer to the form $\gamma = 3 - H$ for fractally-rough surfaces in 3-D, and this would also explain some of the larger off-fault activity exponents found in Powers and Jordan (2010). The faster decay of off-fault stresses with fault-normal-distance in 3-D is consistent with the inference that stress should decay with distance (r) from asperities as $1/r^3$ in 3-D as opposed to $1/r^2$ in 2-D. Consequently, we use a more general form for the relationship between roughness and off-fault activity:

$$\gamma = c_g - H, \tag{6.6}$$

where c_g is the geometric dimension (see e.g. Mandelbrot, 1982; Turcotte, 1997).

6.6.2 Influence of normal stress and contact size distributions

In addition to the described influence of fault roughness, fault-normal stress was observed to change the decay-rate of off-fault seismicity. Within the range of the here observed stresses, the normal stress showed an approximately linear relationship with γ, so that at higher stresses, a larger proportion of AEs occurred at increased fault-normal distances. Higher stress levels were also connected to an increase in the maximum distance of AEs (Y_{max}) from the fault axis.

The connection between roughness and fault stresses, and the resulting seismic event distributions is generally complex. Stress variations and the frequency-size distributions of seismic events

have been investigated for fractally-rough faults (Huang and Turcotte, 1988). The authors computed random 2-D fractal surfaces to simulate combined stress-strength distributions on faults with different roughness exponents. They showed that the frequency-size distributions of seismic events follow a power-law with an exponent (b-value) that is inversely proportional to the ambient stress level. Besides the correlation with stress, their model predicts a dependence of b-values on the fractal dimension of the initial stress-strength distributions.

Moreover, the normal stress distribution on a fault is strongly dependent on the amount and size of contacts. The scaling of these stress distributions ($H_{\text{œ}}$) is suggested to be related to the initial fractal roughness (H_{r}) over: $H_{\text{œ}} = H_{\text{r}} - 1$ (Hansen et al., 2000), for surfaces that are perfectly mated. This relationship is strongly dependent on the ratio of effective contact area to total fault area so that the corresponding scaling of $H_{\text{œ}}$ changes in a non self-similar fashion during contact area increases with larger normal stresses (Schmittbuhl et al., 2006). The here tested model (Dieterich and Smith, 2009) does not account for the changes in the amount of effective surface area. Previous experiments on analog materials revealed that contact area increases with larger fault-normal stress and that the corresponding contact size distributions exhibit smaller scaling exponents for some materials, e.g., acrylic and glass (Dieterich and Kilgore, 1996). Lower scaling exponents are connected to an increase in the proportion of large contacts which is in agreement with our results, assuming a direct connection between the spatial extent of off-fault stress relaxation and on-fault asperity-size distributions. Consequently, the growth and coalescence of asperities is likely responsible for the observed changes in γ at increasing normal stresses.

Furthermore, the model in Dieterich and Smith (2009) does not account for possible size variations of seismic events that are connected to off-fault stress relaxation. A possible difference in AE sizes can influence both the off-fault activity exponent and the maximum extent of the distributions. This can be explored theoretically by linking event sizes to relative off-fault stress level assuming constant strength and experimentally by studying b-value variations as function of fault-normal distance. The latter requires very large AE catalogs, due to the power-law decay with distance from the slip surface which are not available within the scope of current experimental series.

For a more comprehensive understanding of underlying mechanisms of seismicity variations, a model that elucidates the influence of fractal roughness and stress changes on both off-fault activity and b-value is desirable.

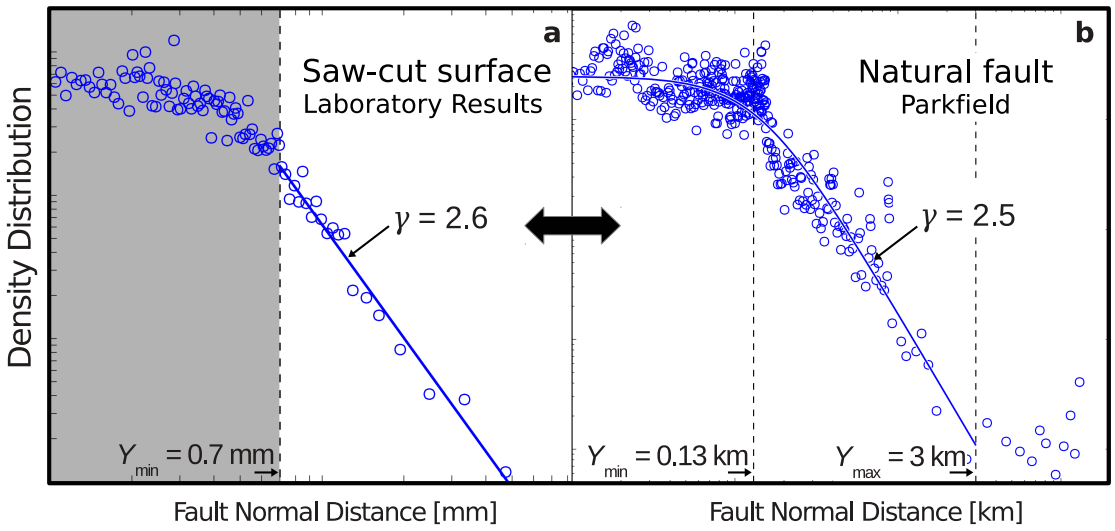

Figure 6.13: Off-fault activity profiles show similar characteristics in laboratory and nature. a): AE event density as function of fault-normal distance for a planar fault with predefined roughness. Y_{min} is the minimum power-law cut-off which is controlled by the hypocentral uncertainty. b): Seismic event density profile for the Parkfield section of the San Andreas fault (modified after Powers and Jordan (2010)). Y_{min} is related to the half-width of the fault core. Y_{max} marks the transition to the background seismicity.

6.6.3 Understanding off-fault density distributions of natural seismicity

The observed across-fault AE activity profiles show strong similarities to observations of natural seismicity (Figure 6.13). In both cases, we observe an initial flat part of the distributions which is connected to constant AE density. The natural seismicity profiles are characterized by an inner (Y_{min}) and outer scale (Y_{max}), as well as a power-law fall-off that can be described by an exponent (γ). At large fault-normal distances ($Y > Y_{\text{max}}$), one can observe a transition from power-law decay to the seismic background activity. The inner scale may indicate the half width of the inner fault zone or fault core (Powers and Jordan, 2010). Our experiments highlight that the inner scale is also strongly influenced by hypocentral uncertainties which may lead to an inflation of the inferred fault zone width. The outer scale is not resolvable in our experiments due to limited sample dimensions. Our range of off-fault activity exponents (2.36–2.85) is within the upper range of those observed for Californian faults. The corresponding faults are considered mature faults with large cumulative offsets, comparably low complexity and increased smoothness. This indicates that mature faults can possibly be simulated in the laboratory by planar surfaces with little to no large-wavelength roughness. Young faults are suggested to have substantially lower values of γ indicating high fault complexity and roughness (Powers and Jordan, 2010).

6.7 Conclusion

We conducted two sets of frictional sliding experiments on Westerly granite samples with predefined, initial roughness. The first set was conducted at constant confining pressure and different initial surface preparation revealing a correlation between surface roughness and seismic off-fault activity. Analogous to observations of natural seismicity, the seismic off-fault activity in our laboratory experiments can be described by a power-law. We show that the corresponding exponent is related to roughness so that $\gamma = 3 - H$, where H is the Hurst exponent.

We conducted a second set of experiments at constant roughness revealing an approximately linear dependence of γ on normal stress. The combined influence of normal stress and roughness can explain the observed off-fault activity for all experiments. Our results substantiate previous findings suggesting a linear relationship between off-fault activity and roughness (Dieterich and Smith, 2009; Powers and Jordan, 2010). They also highlight the importance of the stress state on the fault in controlling seismicity distributions. For a comprehensive understanding of underlying mechanism of seismicity distributions the interplay between fault driving stresses and roughness has to be considered. The direct connection between off-fault seismicity exponents, fault stresses and roughness potentially allows for a direct mapping of fault zone properties based on microseismicity statistics, thus providing a tool for the understanding of the fault mechanics and local hazard potential.

7 Off-fault damage and acoustic emission distributions during the evolution of structurally-complex faults over series of stick-slip events

7.1 Summary

Tectonic faults, which consist of zones of distributed and localized deformation, show structural complexity at many different scales. Variations in fault structure, e.g. fault roughness, influence the location and dynamics of large earthquakes as well as the distribution of small seismic events. In nature, roughness and seismicity distributions can rarely be studied simultaneously. Consequently, little is known about their interplay over successive seismic cycles. Here, we investigate the connection between fault structure and near-fault distributions of acoustic emission events over series of stick-slip cycles in the laboratory. We conducted a set of experiments on rough fault zones that developed from an initial, fracture surface while monitoring stress and seismic activity. We determined across-fault acoustic emission distributions from high-accuracy hypocenter locations during individual interslip periods. The characteristics of these distributions were closely connected to different structural units of the faults. For example, the core deformation zone was characterized by consistently high seismic activity, whereas the off-fault damage zone displayed a power-law decay of seismic activity with increasing distance from the fault core. The exponent of the off-fault power-laws changed systematically with successive stick-slip events so that later interslip periods exhibited higher exponents, i.e., more rapid spatial decay of seismic off-fault activity. The faster spatial decay and connected localization closer to the slip surfaces is likely an expression of decreasing fault zone complexity and roughness. Our results indicate a close relationship between fault structure, stress and seismic off-fault activity. A more extensive mapping of seismic off-fault activity-decay has the potential to significantly advance the understanding of fault zone properties including roughness variations and stress-states.

7.2 Introduction

The complexity of strain accumulation along fault systems, which mark the boundaries between tectonic plates, poses a challenge for the predictability of earthquakes. Earthquake rupture ini-

tiation and propagation is strongly influenced by the frictional properties and structure of faults. Faults are zones of high strain within the upper crust, consisting of a fault core surrounded by a zone of distributed damage (e.g. Caine et al., 1996; Ben-Zion and Sammis, 2003). This damage zone consists of joints, cracks, pulverized rock, and subsidiary faults over a wide range of length scales, and the embedded fault core contains a gouge layer, as well as anastomosing principal and secondary zones of slip localization (e.g. Chester and Logan, 1986; Chester et al., 1993; Faulkner et al., 2003; Dor et al., 2006; Wibberley et al., 2008; Faulkner et al., 2010). The structure of fault zones can vary substantially along fault-strike and shows a large dependence on protolith composition (e.g. Schulz and Evans, 2000; Faulkner et al., 2003). Current models of fault zone structure suggest that faults are heterogeneous but become less complex with increasing displacements so that most of the slip on mature faults occurs within zones of highly localized strain (e.g. Chester et al., 1993; Chester and Chester, 1998; Ben-Zion and Sammis, 2003). This is supported by geologic observations of 'mature' fault zones in Southern California (e.g. Chester and Chester, 1998; Rockwell and Ben-Zion, 2007). Fault evolution has additionally been documented by decreasing numbers of fault step-overs (e.g. Wesnousky, 1988), and decreasing geometric disorder of fault surfaces traces (Wechsler et al., 2010). These studies generally indicate a continuous evolution toward less complexity even after large amounts of slip (1–300 km) have been accumulated. This is in agreement with results from seismicity inferred fault smoothing which appears to be active at displacements of up to $\sim$ 300 km (Powers and Jordan, 2010). Other studies, however, examined roughness of exhumed fault surfaces showing that large off-set faults remain in a state of consistent complexity (Sagy et al., 2007; Candela et al., 2012), possibly due to decreasing rates of abrasional smoothing caused by gouge lubrication (Brodsky et al., 2011) or rupture related fault re-roughening (Bhat et al., 2004; Klinger, 2010).

The documentation of fault evolution is vital for the understanding of many upper crustal processes. For example, fault roughness influences the characteristics of strain release during fault slip including slip distributions, stress drops and off-fault stresses (Power and Tullis, 1995; Dieterich and Smith, 2009; Candela et al., 2011a,b; Dunham et al., 2011). Moreover, the degree of slip localization and roughness reduction of evolving fault zones governs many fault processes including a fault's hydrology, fault zone growth, earthquake-rupture dynamics and the near-fault distribution of seismic events (e.g. Ben-Zion and Sammis, 2003; Wibberley et al., 2008; Faulkner et al., 2010; Powers and Jordan, 2010). Similarly, the geometry of systems of faults controls

local earthquake interactions and seismicity clustering. Models that include these fault-system-induced interactions can produce seismicity characteristics similar to regional observations and replicate observed statistical relations of natural seismicity, including aftershock clustering (e.g. Ward, 2000; Rundle et al., 2004; Dieterich and Richards-Dinger, 2010). Consequently, a more detailed understanding of fault evolution and its controls on seismic event distribution is essential, not least, for seismic hazard assessment.

Geologic observations of fault zone structure are commonly limited to inactive, exhumed fault branches, so that an investigation of fault structure, fault evolution and associated variations in seismicity distributions is not straightforward. To overcome these limitations, we study fault evolution and seismic event distributions on complex fault zones in analog experiments under upper crustal stress-conditions. We present results from series of stick-slip experiments on laboratory-created fault zones during which we document stress, strain and seismic activity as well as post-experimental fault structures. In a previous study (Goebel et al., 2013b), we tested the connection between roughness and seismic off-fault distributions on planar surfaces with pre-defined roughness showing that the off-fault activity can be described by a power-law which is controlled by fault roughness and normal stress. We extend this study through the creation of series of stick-slip events on structurally complex fault zones that developed from incipient fracture surfaces. Our experiments are designed to mimic structural complexity and stress conditions characteristic for upper-crustal faulting processes. The current study is divided into three parts: Initially, we analyze the characteristics of fault-normal distributions of acoustic emissions. We then investigate the corresponding changes with successive stick-slip events and possible evidence for fault evolution. Lastly, we examine the connection between different structural units, variations in normal stress and across-fault activity profiles.

7.3 Data and Method

We show results from four frictional sliding experiments (WG04, WG05, WG07, and WG08) on Westerly granite surfaces, loaded under triaxial compression. Prior to loading, the rock samples were prepared with saw-cut notches at a 30° angle to the loading axis to concentrate deformation toward the center of the samples. Initially, we fractured the intact part between the notches. We then increased the confining pressure to lock the faults and loaded the samples axially resulting

Sample	l_{RS} [cm]	σ_{diff} [MPa]	U_z [mm]	σ_n [MPa]	τ [MPa]
WG04	5.0±0.15	365±6	3.0±0.003	261±6	198±6
WG05	4.2±0.15	296±6	4.1±0.003	372±6	276±6
WG07	3.7±0.15	293±6	4.3±0.003	237±6	170±6
WG08	3.0±0.15	288±6	3.7±0.003	280±6	224±6

Table 7.1: Mechanical data and loading conditions of the four presented experiments. The length of the saw-cut notches increased from WG04 to WG08 which led to a reduction of the length of the rough, surface area. Initially, samples were fractured at P_c = 75 MPa and then reloaded at 150 MPa. l_{RS}: approximate length of the rough fracture surface, σ_{diff}: maximal differential stress during sliding, U_z: maximum vertical displacement of loading piston, σ_n: normal stress, and τ: shear stress. σ_n and τ were corrected for notch length and change in fault area due to slip (see text for details).

in series of stick-slip events (see Goebel et al. (2013c) for more details about sample geometry and loading). The current study focuses on results from the stick-slip sliding phase of these experiments. This phase was generally conducted at a constant axial displacement rate (20 $\mu m/min$, and corresponding strain-rate $\dot{\epsilon} \sim 3 \cdot 10^{-6}\ s^{-1}$) and constant confining pressure (P_c = 150 MPa). Changes in differential stress were determined from the measurements of an external load cell. Fault normal stresses were computed under consideration of changing fault geometries, i.e., we corrected for different notch depths and changes in effective fault surface area due to slip (Scott et al., 1994; Tembe et al., 2010). A summary of loading conditions, sample geometry and stresses can be found in Table 7.1.

The deformation along the complex laboratory-created fault zones was connected to a high acoustic emission (AE) activity. To document the AE activity, we employed a high-speed (10 MHz sampling frequency) and accuracy (16 bits amplitude resolution) data acquisition system (Stanchits et al., 2006). AE events were recorded using a miniature seismic-array, consisting of 16, one-component, piezo-electric transducers. AE event locations were determined from travel-time inversions of automatically picked first arrival times. The location-uncertainty of AE hypocenters was estimated at 1–4 mm, depending on the proximity of an event to the limits of seismic array coverage. The total number of located AEs varied between 34,141 and 97,847 for the different experiments (see Goebel et al. (2013c) for details).

For the analysis of AE distributions as function of fault normal distances, we largely follow Goebel et al. (2013b). Initially, we project the recorded AE hypocenters into a best-fit fault coordinate system. We then stack the AE activity from both sides of the fault while ensuring the symmetry

of across-fault activity profiles (see below for details) and determine AE density distributions as function of fault normal distances, analogous to Hauksson (2010) and Powers and Jordan (2010).

The off-fault density distributions could be described by a power-law with an exponent that was determined by the maximum likelihood method (e.g. Newman, 2005; Clauset et al., 2009). The corresponding minimum bound of the power-law was estimated through maximizing the fit between observed distributions and modeled power-law behavior. Here, we used the Kolomogorov-Smirnov distances, i.e., the maximum distance between two (observed and modeled) cumulative distributions, as a measure of goodness-of-fit. A more detailed description of the here employed tests for power-law behavior and corresponding parameter estimates can be found in Goebel et al. (2013b).

7.4 Results

Stick-slip type fault motion, which is characterized by increasing stress during interslip periods and abrupt stress drops due to fault slip, is considered a close, laboratory analog to natural earthquake behavior (Brace and Byerlee, 1966). We strove to mimic the natural faulting process through creating series of stick-slip on structurally complex fault zones allowing for abrupt earthquake-like stress release and fault evolution over several seismic cycles. As a consequence, the differential stress-curves during our experiments were generally characterized by: (1) gradual increases which were linear at first and progressively deviated from linearity at elevated stresses close to failure and (2) sudden stress drops with magnitudes ranging from 4–220 MPa. We observed two predominant populations of stress drops, i.e., large stress drop (LSD) events with magnitudes from 118–220 MPa and small stress drop (SSD) events with magnitudes from 4–65 MPa. In contrast to naturally-fractured surfaces , tests on planar, saw-cut surfaces (Goebel et al., 2013b) resulted in single stress drop events for individual stick-slip cycles and the described complexity in both stress curves and fault structures was absent. Thus, the two types of stress drop events, which occurred at similar stress level (Figure 7.1), are likely associated with fault structural complexity.

Besides variations in fault stresses, we investigate changes in AE densities as function of fault normal distance with successive stick-slip events. To this end, we separate the initial AE record into event populations associated with individual stick-slip cycles (see Figure 7.1). The period between successive stick-slip events will be referred to as interslip periods (ISPs) in the following. To

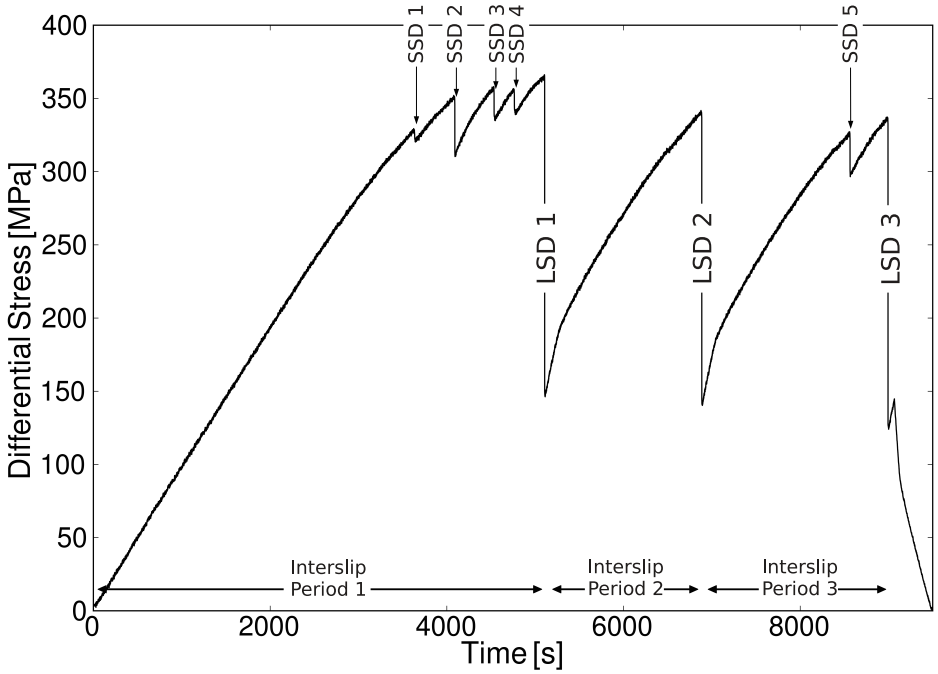

Figure 7.1: Loading curve for experiment WG04 which resulted in three large stress drop (LSD) and five small stress drop (SSD) events. The extend of the interslip periods (ISPs) between LSD events is indicated by black arrows at the bottom of the figure.

investigate the connection between AE event occurrences and fault structure during stress increase, we excluded AE events that occurred in close temporal proximity to stress drop events from the analysis. These type of events were characterized by a pronounced aftershock-like rate-decay with increasing times from stress drop onsets (Goebel et al., 2012, 2013d).

Initially, we will discuss the changes in across fault AE distributions with successive stick-slips using experiment WG04 as an example. We will then show results form the other experiments and highlight general trends.

7.4.1 Acoustic emission hypocenter locations

AE event populations during frictional sliding experiments provide insight into the stress state on faults and fault segments. AE hypocenters can also highlight fault orientation and structure. Figure 7.2 shows AE event locations during the three ISPs of experiment WG04, displayed in a best-fit fault coordinate system. AE events generally outline the orientation and width of a zone of high strain and brittle deformation, i.e., the fault zone that developed from an initial fracture

surface. Most of the deformation is localized within a plane connecting the two saw-cut notches which were introduced prior to the experiment. Furthermore, AE activity indicates some degree of fault curvature and variable fault zone widths between 10 to 20 mm. Besides the near-fault AE activity, we also observed AE events that were connected to secondary faulting, and more distributed activity at larger distances from the fault axis. The highest AE activity was observed during the first ISP whereas later ISPs showed less activity and more pronounced AE clustering in different areas of the fault.

7.4.2 Acoustic emission across-fault activity

To understand changes in fault structure, we investigate the distribution of AE events as function of fault normal distance. In case of a direct connection between fault structural evolution and AE activity, we expect to observe a systematic change in AE distributions with successive stick-slip events. Figure 7.3 shows histograms of AE distributions with fault normal distance (Y_f) for different ISP events during experiment WG04. The largest activity is generally located at the center of the fault zone and decreases with larger distance from the fault axis. Again, we observe evidence for secondary faulting highlighted by a local maximum of AE event numbers at $Y_f = 13$ mm. The AE activity associated with secondary faulting decreased with successive stick-slip events.

The AE activity histograms (Figure 7.3 left) are influenced by fault curvature which led to an artificial broadening of the zone of high AE activity. We removed the influence of long wavelength curvature by shifting individual segments of across-fault activity profiles. To this aim, we estimated the fault-perpendicular shift required to maximize the symmetry of activity profiles for segments that were binned every 5 mm. The symmetry between the two sides of the fault was determined through comparing the corresponding cumulative distributions and the maximum Kolomogorov-Smirnov distance (KS-distance). The center of a particular profile, which is the point of maximum symmetry, is found by minimizing the KS-distance of the shifted profiles. Expectedly, the histograms with removed fault curvatures (Figure 7.3 right) showed narrower distributions as well as a better alignment around the fault axis. The previous characteristics of activity distributions, e.g., secondary faulting and activity decay with distance, were largely conserved.

To quantify the AE hypocenter distributions, we computed the density of AEs as function of fault normal distance during individual ISPs. AE densities were determined by sampling a constant number of nearest-neighbor events with respect to their distance from the fault axis, and

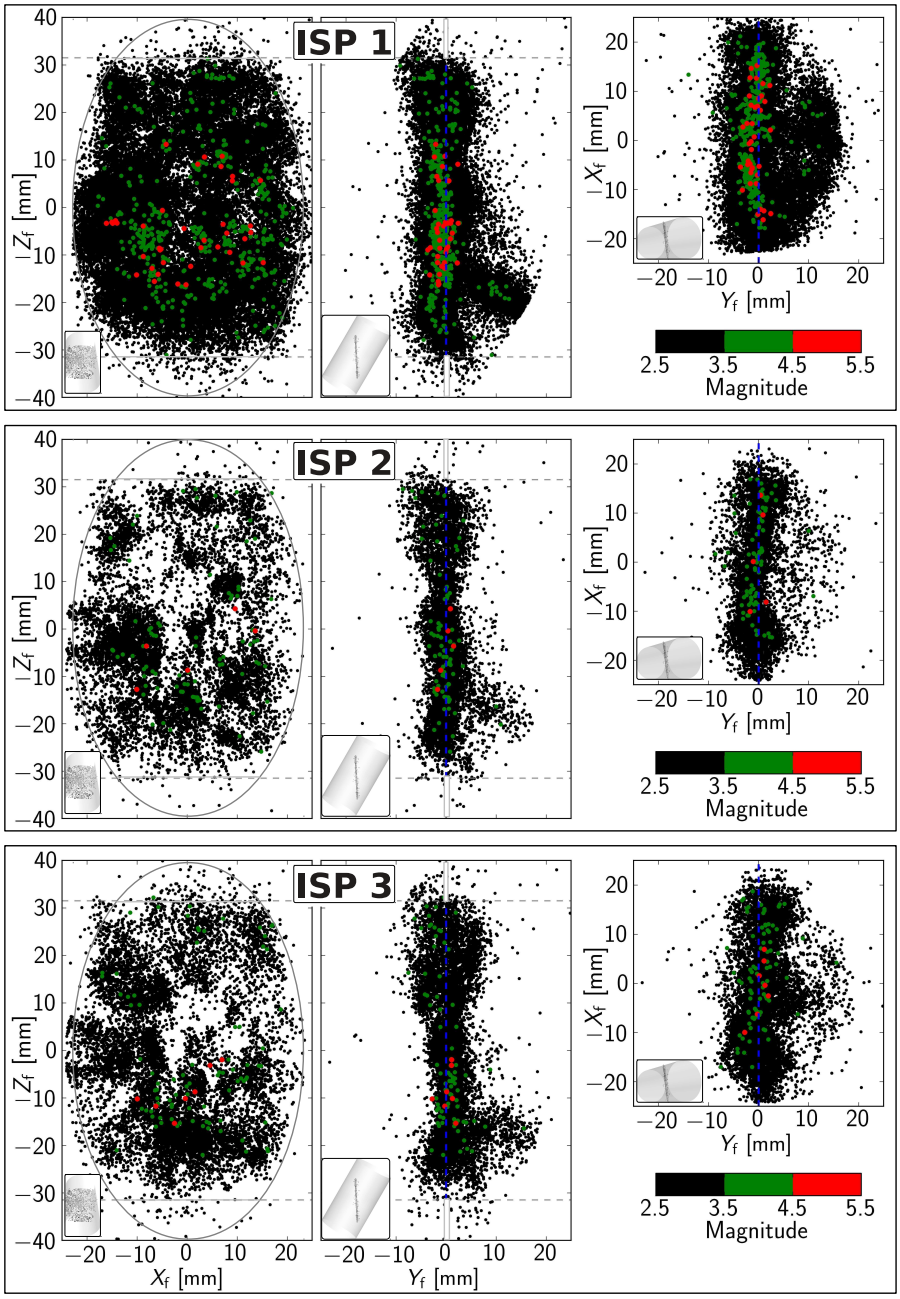

Figure 7.2: AE hypocenters of experiment WG04 projected into a best-fit fault coordinate system and viewed in a plane parallel (left column) and perpendicular to the fault. The fault perpendicular views show AE events along the longer (center column), and the shorter fault axis (right column) which has the same extent as the sample diameter. The three different frames mark three different interslip periods from top to bottom (labeled from ISP1–ISP3 analogous to Figure 7.1). The markers are colored according to magnitude, and the extent of the saw-cut notches is indicated by gray, dashed lines

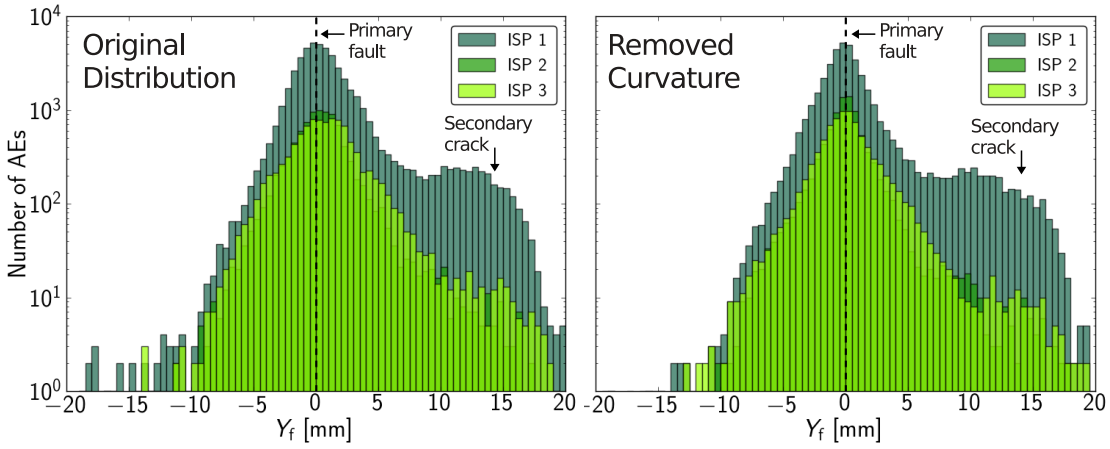

Figure 7.3: Histogram of AE activity as function of fault normal distance for all three ISPs of experiment WG04, before (left) and after (right) correcting the profiles for fault curvature.

computing the corresponding area covered by each sample (Silverman, 1986). The resulting values were then normalized by effective fault area and ISP duration. The so determined AE density distributions depict areas of constant AE activity as approximately constant values whereas AE activity-decays can be identified by decreasing densities. Possible power-law activity-decrease is displayed by a linear trend between density and fault normal distance on logarithmic scales. The initial ISP of experiment WG04 showed a plateau of AE density close to the fault axis out to a distance of about 2 mm (Figure 7.4 top). This was followed by a roll-off region between 2–2.7 mm, and a power-law decay out to distances of $Y_f \sim 7$ mm. The previously observed secondary AE-activity was also visible but did not influence the power-law slopes close to the fault. This was scrutinized by computing power-law exponents without AEs of the region of secondary cracking. The exponents of the power-law, which were estimated by the maximum likelihood method (e.g. Clauset et al., 2009), decreased systematically with successive stick-slip events ($\gamma = 2.67 \pm 0.05$ for ISP 1, $\gamma = 3.31 \pm 0.1$ for ISP 2, and $\gamma = 3.6 \pm 0.08$ for ISP 3, Figure 7.4) indicating the occurrence of a relatively larger proportion of AEs close to the fault and a more rapid density decay during later ISPs.

To investigate the variations in AE density distributions in more detail, we computed different values of the power-law exponent, γ^*, for varying minimum power-law cut-offs, Y^*_{min} (Figure 7.4 insets). In case of power-law distributed data, we expect to observe a rapid increase in γ^* below Y_{min}, followed by a largely constant value over the extend of the power-law and larger fluctuations in the distribution's tail. The corresponding standard deviation of γ^*, computed within

a sliding Y^*_{min}-window (see black dots within the insets of Figure 7.4), is expected to show a minimum close to Y_{min} and remain close to its minimum value over the region of constant γ^*. The insets in Figure 7.4 largely confirm this expectation, and underline the previous trend of increasing γ with successive stick-slips as well as a slight extension of the power-law range. Y_{min} increased systematically with successive stick-slip events from 2.7 for ISP 1 to 4 for ISP 2, and 5.3 for ISP 3. The uncertainties in γ are generally smaller, compared to uncertainties in Y_{min} which may contains large errors depending on the character of the roll-off region. Consequently, we estimate uncertainties in Y_{min} up to $\sim$ 0.5 mm. The lower bound is an important parameter in distinguishing the power-law distributed, off-fault activity, and the 'on-fault' activity which consists of the regions of constant AE density and the roll-off region. In the following, we will refer to AE events that occurred at fault normal distances above Y_{min} as off-fault activity.

7.4.3 Changes in off-fault activity exponents with successive stick-slip events

We scrutinized if the observed trend of decreasing off-fault activity exponents can be observed for all four experiments. Figure 7.5 shows the changes in γ as function of ISPs for all experiments. Experiments WG04, WG07, and WG08, display a similar relative trend in γ, i.e., comparably low values at the beginning, followed by an increase over the next 1–3 ISPs. WG05, WG07 and WG08 approached an approximately constant value for the latter ISPs. This is indicated by the solid lines in Figure 7.5 which mark the average value of γ for ISPs above 1. We observed a substantial difference in the average value of γ between the experiments. The lowest values of γ was connected to experiment WG05. For this experiment, γ also deviated from the previous trend of initial increasing power-law exponents. In the following, we investigate this behavior in more detail by comparing experiment WG05 and WG07, which exhibited similar initial sample geometry (i.e. length of saw-cut notches) and experienced similar loading stresses.

In spite of similar initial sample geometry, the natural fracture process of the intact part between the end of the notches can result in different fault geometry and orientation. If this is the case, these differences should also be detectable through mapping the principal orientation of AE hypocenter populations. In the following, we assume that AE event populations of individual ISPs highlight the regions of largest strain accumulation and the principle slip surfaces within the fault zone. Shifts in the AE hypocenter locations can thus be used to infer a variation of principle slip surface orientation and the connected stress state of the fault. To understand the stress state on

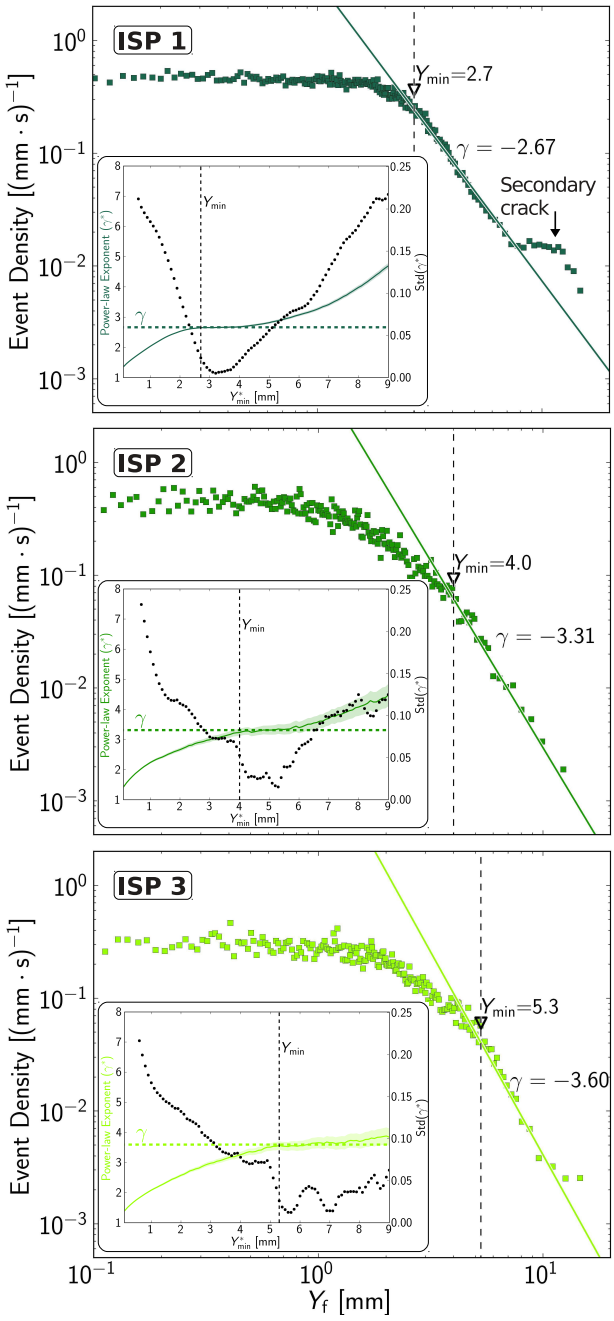

Figure 7.4: AE event density as function of fault normal distance for the three ISPs of experiment WG04. Power-law exponents are displayed in the upper right of each frame and minimum bounds of the power-law behavior are marked directly on the curves. The insets highlight the changes in γ for different values of Y_{min}. The estimated values of Y_{min} and γ are highlighted by a black and a colored, dashed line in the insets.

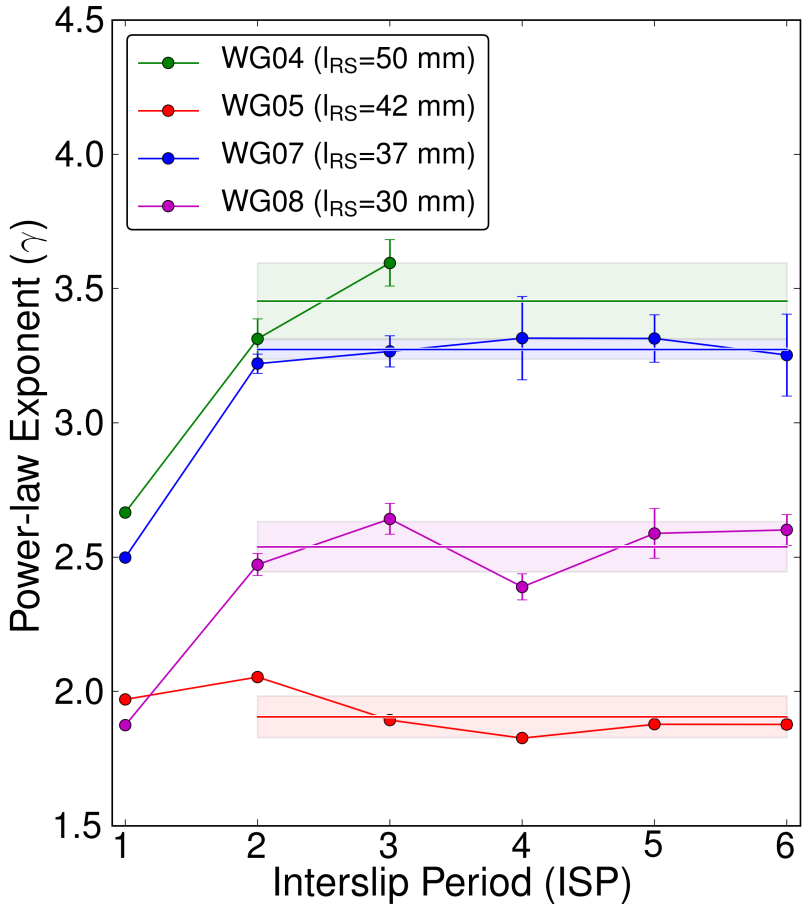

Figure 7.5: Changes in off-fault activity exponent (γ) with successive stick-slip events. Markers are colored according to the different experiments. The horizontal lines represent the average value of γ for the later ISPs (excluding the first ISP). The shaded area around these lines is the corresponding standard deviation. γ changed rapidly during the initial ISPs and then approaches similar values for later ISPs.

the fault, we are mainly interested in the angle between the principle slip surfaces inferred from the dominant orientation of AE hypocenters, and the loading axis. This angle, which, besides the applied loading stresses, is the primary control on fault stresses, will be referred to as the fault angle, or μ_f, in the following.

The comparison between WG05 and WG07 revealed a substantial difference in μ_f between the two experiments (Figure 7.6). For experiment WG05, the best-fit fault coordinate system was oriented at $\approx 40°$ angle during the initial ISP. This angle decreased systematically with successive stick-slip events down to $\mu_f \approx 35°$ during the last ISP. Experiment WG07, on the other hand, showed an approximately constant fault orientation of $\approx 27°$. In addition to the change in μ_f, there was a visible difference in the amount of off-fault activity between WG05 and WG07 so that WG05 showed substantially higher AE activity at larger distances from the fault surface. This difference is also supported by the previously described average values of γ.

To further test for possible differences in fault orientation, fault structure, and changes in principle slip surfaces between WG05 and WG07, we analyze post-experimental computer tomography (CT) images (Figure 7.7). The CT-images generally depict the cumulative damage creation as a result of sample fracture and subsequent stick-slip events. The CT-scans reveal slightly larger fault angles of WG05 compared to WG07. Furthermore, we observed a comparably broad zone of high crack-density for experiment WG05 whereas WG07 exhibited a more localized damage-zone (Figure 7.7 insets). To compare these results to our prior estimates of μ_f, we highlighted the corresponding angles in both CT-images. The damage-zone orientation and width within the CT-scan of experiment WG05 make it plausible that the principle slip surface could have migrated from 40° to 35° during a series of stick-slip events. The damage-zone width of WG07, on the other hand, is comparably narrow, underlining the more pronounced stability of principal slip surface orientations and μ_f. Our estimate of μ_f based on AE hypocenters about one degree lower than expected from CT-images, but is in agreement with a plausible range of $\mu_f = 27°$–$30°$ based on the observed width of the fault zone in CT-images. Due to the cumulative character of the damage within the CT-images a precise estimation of the fault angles for each ISP is not possible. Nevertheless, the slightly larger angle between fault and loading axis for experiment WG05 together with the broader damage zone support the previously suggested differences in μ_f between WG05 and WG07.

Figure 7.8 provides an overview of the angles between vertical loading axis and slip zones,

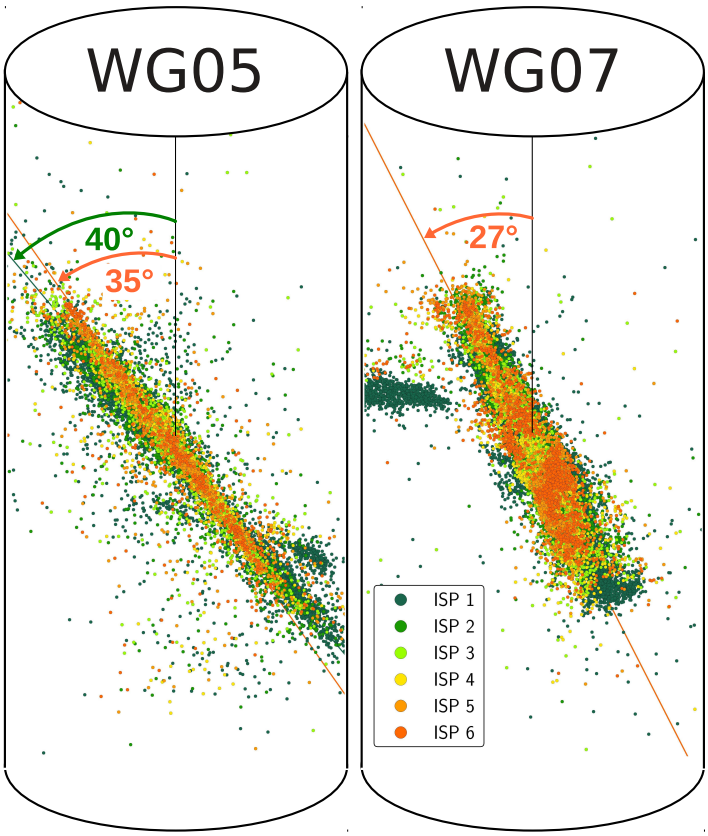

Figure 7.6: Changes in fault orientation inferred from AE populations for experiment WG05 (left) and WG07 (right). The marker colors correspond to AE events recorded during the individual ISPs of an experiment. Fault angles are highlighted by colored arrows between loading axis and AE locations. WG05 showed relatively larger fault angles which decreased with successive stick-slip events whereas WG07 showed an approximately constant value of 27°. WG07 shows evidence for AE activity that is related to secondary faulting below the end of the upper notch (area of dark, green AE event population).

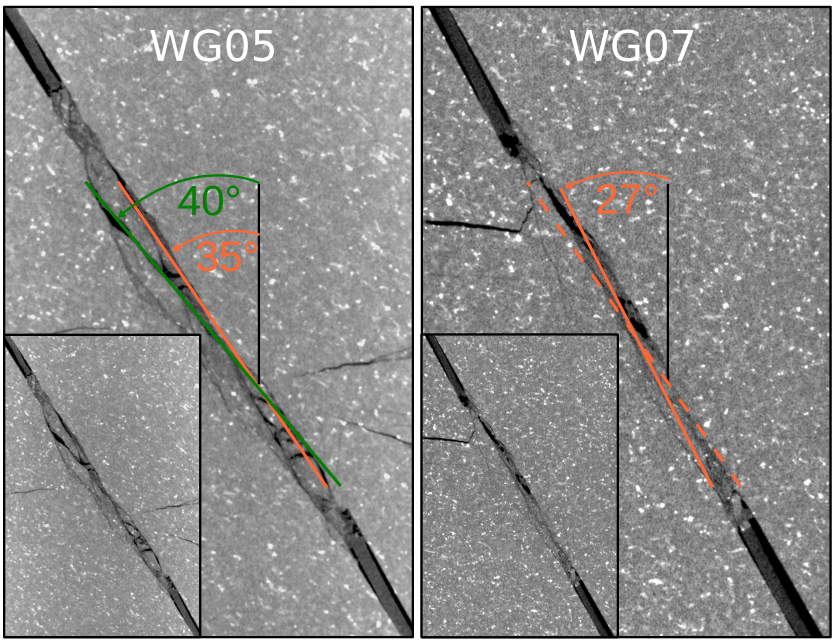

Figure 7.7: Fault structure and orientation in post-experimental computer tomography scans of WG05 (left) and WG07 (right). The fault angles are highlighted by solid green and orange lines. For a comparison, we also highlighted a 35° angle for WG07 by an orange, dashed line. The insets show the original fault structure without marked fault angles.

inferred from AE hypocenter populations. Generally, the values of μ_f varied between 27° and 30°, except for experiment WG05 for which μ_f decreased from 40° to 35° within the scope of the corresponding stick-slip series.

7.4.4 Changes in off-fault activity exponent with normal stress

Based on the previously described variations in fault angle and the relatively large differences in effective, rough surface area (i.e. the fault area between the pre-cut notches), we also expect the stress level on the faults to differ between experiments. To investigate the influence of stress on seismic off-fault activity, we computed shear and normal stresses (see Table 7.1) corrected for notch lengths and progressing fault displacements and compared them to average off-fault activity exponents. For the latter, we compiled the AE events of all ISPs and computed AE density profiles but again excluded events within initial ISPs which showed the strongest deviation from the average γ value. Generally, we observed higher values of γ for experiments WG04 and WG07 ($\gamma = 3.4$ for WG04 and 3.2 for WG07) than for WG05 ($\gamma = 1.8$) and WG08 ($\gamma = 2.6$) (Figure 7.9). This is in agreement with the previously estimated values of γ based on averaging over the latter

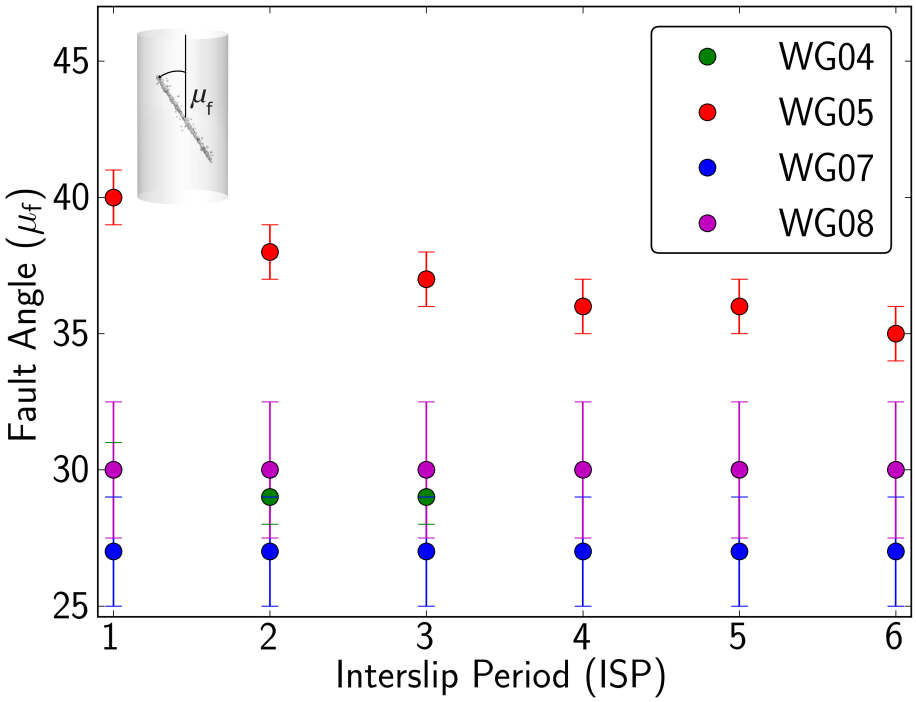

Figure 7.8: Changes in fault angle (μ_f) with successive stick-slip events for all four experiments.

ISPs. These values highlight that for WG04 and WG07, there is a relatively larger proportion of AE activity closer to the fault axis while WG08 and WG05 exhibit larger proportions of AE further away from the fault. The comparably highest off-fault activity and slowest activity-decay was observed for experiment WG05.

Table 7.2 presents an overview of off-fault activity exponents, corresponding goodness-of-fit values (p-values) and the AE rate for individual experiments. The p-value estimates are based on a comparison of KS-distances between observed distributions and Monte-Carlo resampled, synthetic distributions using the estimated power-law parameters (Clauset et al., 2009). Following Clauset et al. (2009), we deem the power-law hypothesis to be plausible if the p-value exceeds a value of 0.1, which is the case for all experiments. In Goebel et al. (2013b), we investigated the influence of hypocentral uncertainties on power-law parameters of the off-fault activity decay, and we find a linear increase in both γ and $Y_{\min}$ as function of hypocentral uncertainty, if the latter follows a normal distribution. The power-law exponent corrected for the influence of location uncertainty,i.e., γ_{corr}, is also displayed in Table 7.2, assuming an average hypocentral uncertainty of 2 mm.

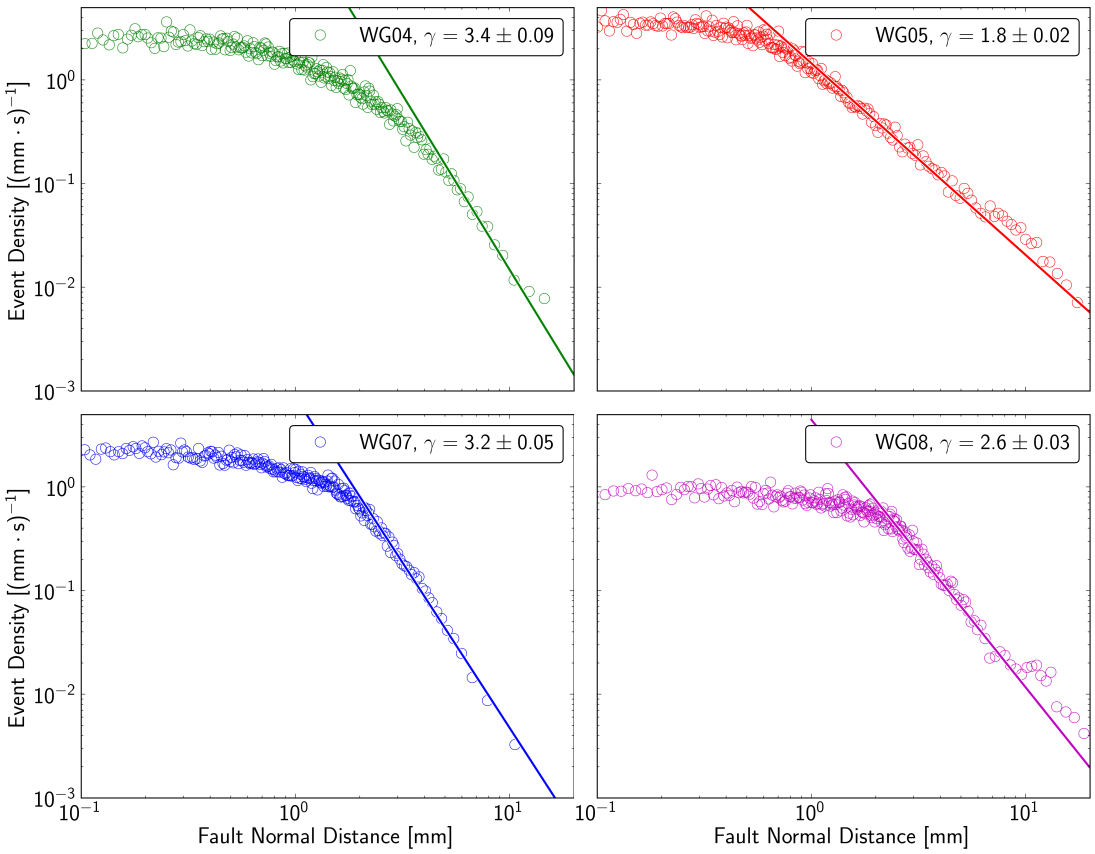

Figure 7.9: Changes in seismic off-fault activity for all experiments. AE densities were computed from all AE events of an experiment, except for events that occurred during the initial ISPs which showed strong deviations from the average value of γ. Power-law exponents and uncertainties are highlighted in the upper right of each frame.

Sample	γ	γ_{ave}	γ_{corr}	p-value	N_{AE}	N_{AE}/s	N_{LSD}	N_{SSD}
WG04	3.37±0.15	3.45±0.14	3.06±0.14	0.21	17363	4.58	3	5
WG05	1.84±0.10	1.91±0.08	1.84±0.08	0.11	20020	4.24	6	5
WG07	3.19±0.12	3.27±0.04	2.92±0.08	0.18	27797	3.51	6	8
WG08	2.58±0.17	2.54±0.09	2.44±0.08	0.29	17890	2.45	6	5

Table 7.2: Overview of off-fault activity and AE rate for the four experiments. γ: off-fault activity exponent, γ_{ave}: average power-law exponent and standard deviation for all ISPs except the initial ISP, γ_{corr}: power-law exponent corrected for hypocentral uncertainty, p-value: goodness-of-fit of estimated γ-values, computed by Monte-Carlo resampling, of the modeled distributions and comparing them to the observed distributions (Clauset et al., 2009). Within the scope of this study, we consider a power-law a valid hypothesis for p-values above 0.10. N_{AE}: Total number of AE events, N_{AE}/s: Number of AE events per second.

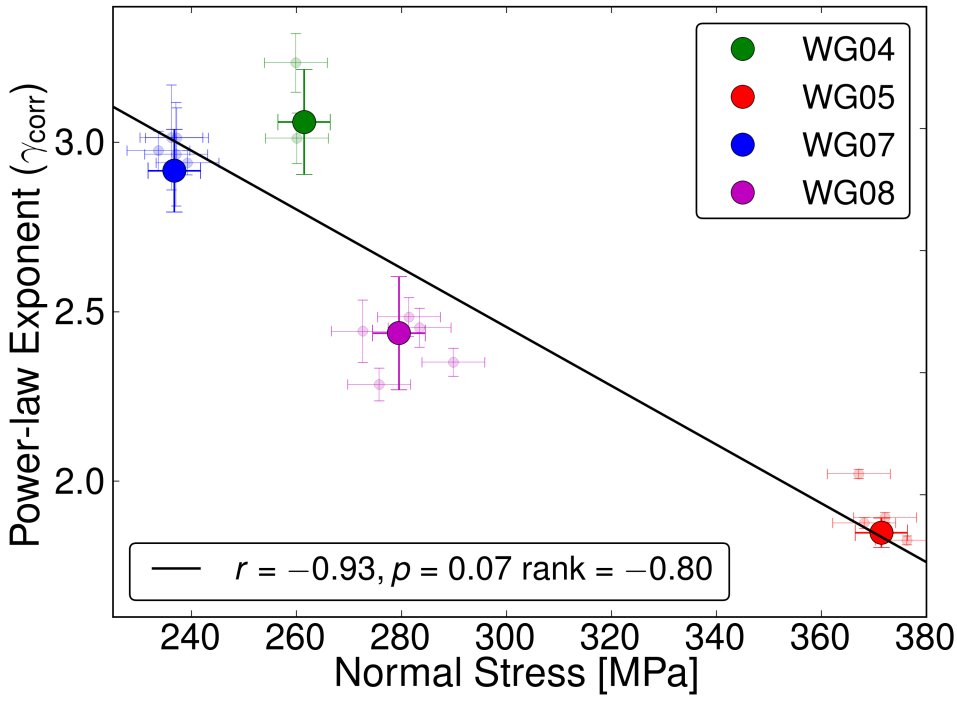

Figure 7.10: Off-fault activity exponent (γ_{corr}), corrected for hypocentral uncertainty, as function of normal stress for the four different experiments. We observed an inverse, linear relationship between γ_{corr} and σ_n. Pearson's correlation coefficient, p-value and Spearman's rank are displayed in the lower left. A linear regression between γ_{corr} and σ_n for all individual ISPs (excluding the initial ISPs, see small, shaded markers) exhibits a correlation coefficient of $r = -0.93$ (Spearman's rank $= -0.88$) which is significant at a 99% level.

Based on the off-fault power-law exponents of compiled AE events for later ISPs, we tested the connection between variations in γ and the normal stress on the fault (Figure 7.10). We observed a general trend of lower off-fault activity exponents with increasing stresses so that γ and σ_n show a negative, linear relationship. The corresponding Pearson's correlation coefficient is $r = -0.93$ (Spearman's rank $= -0.8$) which is significant at a 93% level. If we include γ values of individual ISPs (with ISP $\geqq 2$), the correlation improves further, yielding a value of $r = -0.93$ (Spearman's rank $= -0.88$) which is significant at a 99% level. This indicates that increased normal stresses influence off-fault AE distributions in a systematic way. Larger normal stresses result in a relatively larger proportion of off-fault activity which can explain the relatively low γ-values of experiment WG05, which experienced the largest fault stress level and a comparably slow off-fault activity decrease.

7.5 Discussion

7.5.1 Relating fault structure and AE density distribution

We find a close connection between the seismic activity across complex, laboratory-created fault zones and structural characteristics of these faults. The activity profiles could be characterized by a zone of constant, high AE density close to the principal slip surface, followed by a zone of gradual decrease and a more rapid activity decay at larger distances which could be described by a power-law. Within a previous experimental series (Goebel et al., 2013b), we showed that power-law decay exponents are controlled by both fault roughness and the normal stress on the fault (Goebel et al., 2013b). Higher normal stresses result in an increase in the proportion of effective contact area which may increase the surface interlocking, thus, decreasing off-fault stress-relaxation rates as function of fault-normal distances at load-bearing asperities. The size distributions of these asperities is self-similar for fractal-rough surfaces (Dieterich and Kilgore, 1996). The roughness exponent is directly connected to the spatial extend of the off-fault stresses, as well as brittle failure events which can be described by a power-law with an exponent that is linearly related to fault roughness (Dieterich and Smith, 2009). Our current observations confirm the power-law decay of seismic event distributions with increasing fault-normal distances.

In analyzing sets of post-experimental thin-sections, we scrutinized the possible fault structural equivalents for different zones within the AE density profiles (Figure 7.11). The inner zone of high, constant AE density is connected to high strain and brittle deformation within the fault core which is characterized by micro-scale clasts and gouge material. Between highly deformed fault core and host-rock, we observed a transitional damage zone that showed pervasive fracturing and evidence of local shear deformation. This zone is likely connected to the gradual roll-off in AE density below Y_{min}. Here, we did not include a detailed investigation of changes in the minimum bound of the observed power-law or the characteristics of the roll-off below, which marks the transition to the area of constant AE density close to the fault axis. Both quantities are rather sensitive to variations in rotation angle and the centering of the AE activity profiles. Some of our experiments indicate a continuous broadening of the roll-off zone between power-law activity decay and constant AE density close to the fault with successive stick-slip events (see Figure 7.4). This could be indication of a slip-induced broadening of the transitional damage zone between host rock and fault core. A widening of the damage zone may occur due to wall rock erosion in form of grain fracture and

plugging and subsequent assimilation into the fault core (e.g. Amitrano and Schmittbuhl, 2002).

7.5.2 Fault smoothing and the influence of normal stress and fault formation history

The present experimental series highlights the role of fault roughness and stress in controlling the off-fault distribution of AE events. The off-fault activity exponents were characterized by an initial increase over the first 1–3 ISPs which is likely caused by progressive fault smoothing and reduction in fault complexity. This is in agreement with a previous study during which we inferred an initial reduction in fault complexity based on decreasing fractal dimensions of AE hypocenter distributions (Goebel et al., 2013d). Progressive fault smoothing may also be associated with the formation of one or more preferred slip surfaces which leads to a localization of slip and seismic event activity. Zones of localized slip, which formed after as little as 1–3 stick-slip events, were observed in post-experimental thin-sections (Goebel et al., 2013d). Furthermore, we observed a reduction in secondary cracking and associated AE activity with successive stick-slip events (see e.g. Figure 7.3).

While confirming a linear relationship between stress and γ, experiment WG05 deviated from the previously described trend by exhibiting consistently low γ-values and the initial smoothing was largely absent. This could be explained by an interplay of fault formation and evolution effects. The initial fracture surface for this experiment showed a comparably large angle to the loading axis which changed gradually with successive stick-slip events. This is likely related to changing slip surface orientations and a more favorable alignment with the principal stresses. Moreover, for this experiment, we observed a relatively wider damage-zone and large-wavelength anastomosing crack structures in post-experimental thin-section and CT-scans. The extent of the damage-zone may be connected to repeated variations of principle slip surface orientations. Thus, a combination of initial fault zone orientation, structure, and dynamic changes in structure due to stick-slip fault motion are likely responsible for the observed differences in characteristics of AE distributions.

After the initial fault smoothing process, γ approached a roughly constant value which was mainly controlled by the stress level on the fault. Within the scope of a previous study (Goebel et al., 2013b), we observed that increasing fault normal stresses result in a decrease in γ for experiments on saw-cut surfaces with the same initial roughness but different confining pressures. We compare these results with values of γ from initial ISPs of the current experimental series (Figure 7.12). The two sets of experiments can be described by a negative, linear relationship

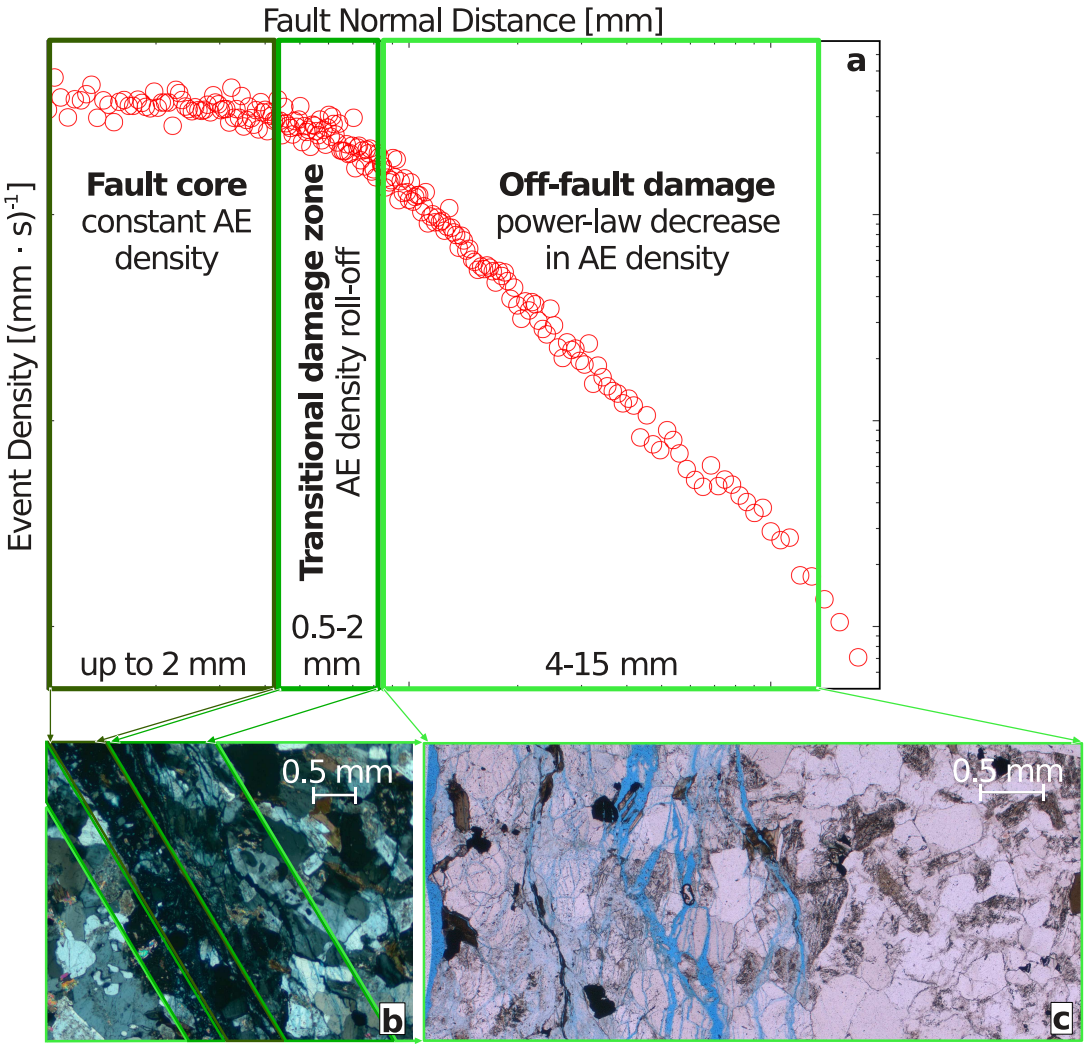

Figure 7.11: Connection between fault structure and across-fault AE density profiles. **a)**: Across-fault AE density displayed on double logarithmic scales (red circles). The fault core is connected to constant AE density, which is followed by a transition zone over which the AE density decrease gradually and the off-fault damage zone which is characterized by a power-law decrease in AE density. **b)**: Thin-section of fault core consisting of highly fractured grains and gouge, and transitional damage zone with highly damaged material that shows evidence of shear. **c)**: Thin-section of off-fault damage zone. Loose particles and gouge have been removed.

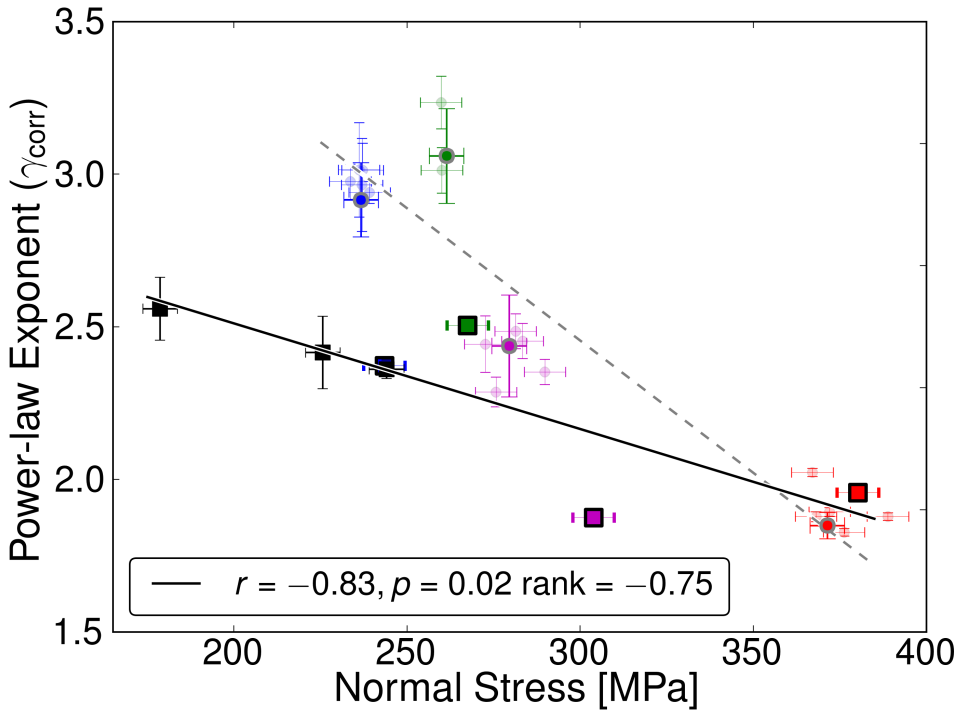

Figure 7.12: Compilation of off-fault activity slopes for experiments conducted on saw-cut surfaces with predefined roughness and saw-cut-guided fracture-surfaces. The black squares represent the saw-cut experiments which exhibited the same initial roughness but different confining pressures (Goebel et al., 2013b). The colored squares correspond to values of γ during the initial ISPs of the four here described experiments (marker colors ares the same as in Figure 7.10). Round markers and dashed line are the same as in Figure 7.10. For both types of surfaces, we observe a similar, weak dependence on normal stress during the initial ISPs (dark solid line represents the corresponding least-squares fit). The γ-values of saw-cut-guided fracture surfaces show a substantially stronger dependence show a substantially stronger dependence on stress during latter ISPs (dashed gray line).

between γ and σ_n (see squares and solid black line in Figure 7.12). This relationship changed with successive stick-slip events so that later ISPs showed a a stronger correlation between γ and σ_n (increase from $r = -0.83$ to $r = -0.93$) as well as a larger decrease in γ with increasing normal stress (dashed line in Figure 7.12, see also Figure 7.10). These results highlight a generic connection between normal stress and seismic off-fault activity but also show that this connection is influenced by fault roughness. Our current experimental series suggest that the seismic off-fault activity-decay close to young, rougher fault surfaces is more strongly controlled by the fault's roughness. Mature, smoother faults, on the other hand, exhibit off-fault activities which are more strongly influenced by the normal stress on the fault.

7.5.3 Additional influences on AE density distributions: fault angle, minimum power-law bounds and profile centering

We conducted a sensitivity analysis of the current results focusing on uncertainties in fault angles (μ_f), the influence of fault curvature and imprecise centering of AE density profiles. This analysis revealed that slight variations in fault angles (up to 3°) had little to no influence on γ while generally leading to a broadening of the zone of constant, high AE density close to the fault axis. We noticed a larger influence of long wavelength fault curvature and inaccurate profile-centering on off-fault activity exponents. To reduce these influences and to avoid an inflation of apparent fault zone width due to fault curvature, we corrected the AE record for fault curvature and recentered individual profiles to maximize the symmetry of both sides of the fault. Poorly centered profiles can generally be identified by a lack of constant AE rate close to the fault axis and a density maximum that does not coincide with the fault axis. This is a result of stacking profiles from both sides of the fault which skew the distributions if the profiles were not centered correctly. While the characteristics of density distributions closer to the fault and the minimum power-law bound were strongly effected by these procedures, the off-fault activity exponents changed only minorly.

7.5.4 Is fault evolution limited to small displacements?

The here observed initial changes in γ and inferred progressive fault smoothing are in agreement with results from an analysis of seismicity distributions in California (Powers and Jordan, 2010). The authors suggest that observed decreases in seismic off-fault activity exponents with increasing fault displacements are indication for continuous fault smoothing, even at large displacements. This interpretation is based on a theoretical study by Dieterich and Smith (2009) that highlights a connection between the spatial extent of off-fault stress relaxation and fault roughness.

While the initial changes in γ indicate fault smoothing with successive stick-slip events, this process may not be continuous. Within the range of displacements of the current experimental series, we observed that faults rapidly reached an approximately constant value of γ suggesting that roughness remained at a stable level thereafter. Similar observations have been made for exhumed crustal fault zones. Here, the reduction in roughness and extension of damage zone widths are predominately active within the first 10–100 m of cumulative fault displacements whereas above only a weak evolutionary signal is observable (Sagy et al., 2007; Savage and Brodsky, 2011; Brod-

sky et al., 2011). Other studies, however, highlight a continuous reduction in fault complexity, based on decreasing numbers of fault step-overs (e.g. Wesnousky, 1988) and geometric disorder (Wechsler et al., 2010), even after hundreds of kilometers. In a recent study, Goebel et al. (2013b) observed a relationship between Hurst exponent and off-fault seismicity decay exponent of the form $\gamma = 3 - H$ for a 2-D fractal rough surface. This is in agreement with theoretical results of the connection between Hurst exponent and fractal dimension of surfaces (e.g. Feder, 1988; Turcotte, 1997). However, most of the off-fault activity exponents of natural seismicity are in the range between 1 and 2 (Hauksson, 2010; Powers and Jordan, 2010) consistent with the spatial extent of off-fault stresses around a fractal rough profile in a 2-D medium ($\gamma = 2 - H$) (Dieterich and Smith, 2009). The apparent difference in the range of power-law exponents between our experiments and natural seismicity may indicate that the activity decay around natural fault zones is controlled by additional factors. Processes within natural fault zones are expected to be complex and are active over a range of scales. In addition to surface smoothing, other evolutionary processes may be active, expressed, for example, in a reduction of fault step-overs. The additional, geometric complexity of natural fault zones may perturb off-fault stresses and expand seismic off-fault activity. Moreover, different evolutionary processes may influence seismicity at different scales and over different periods.

Our results highlight the sensitivity of off-fault event distributions on structure and formation history. These influences complicate a direct mapping between fault roughness and the off-fault activity exponent as suggested by Dieterich and Smith (2009) and Powers and Jordan (2010). Moreover, our experiments highlight the role of increased normal stresses which cause faults to appear seismically rougher, i.e., they exhibit a slower spatial decay of seismic off-fault activity.

7.6 Conclusion

To investigate the relationship between fault evolution and off-fault seismicity distributions, we conducted four frictional sliding experiments on rough fault zones that evolved from an initial fracture surface. The laboratory-created fault structures changed as a result of fault displacement and series of stick-slip events. We observed a connection between the characteristics of across-fault AE density profiles and the extend of fault core, transitional damage zone and off-fault damage zone identified in post-experimental CT-scans. This suggest that the fault-normal distribution of

seismic events is a valuable tool in describing fault structure and possibly also structural variations of faults at seismogenic depth.

The distribution of seismic event densities with respect to the fault center decayed as a power-law outside of the fault core. The power-law exponents increased during the first 1–3 interslip periods as a result of initial fault smoothing and reduction in fault complexity. After that they reached approximately constant values. This suggests that fault evolutionary processes are most active during early stages of fault development. The off-fault activity exponents during later stick-slips were predominantly controlled by the stress state on the fault and fault evolutionary processes were strongly diminished. Consequently, in the absence of substantial fault-roughness variations, the normal stress and off-fault activity exponent are directly connected and exhibit a negative, linear relationship.

Our result emphasize that fault roughness, stress state, and formation history of a fault are important parameters that control near fault seismicity distributions. A differentiation between roughness- and stress-related variations of the spatial distributions of natural seismicity close to faults in nature, can provide important insights into fault zone properties including the seismic hazard potential of individual fault segments.

8 Scaling of laboratory results and minimum earthquake sizes

Laboratory studies have provided invaluable insight into processes that govern the nucleation of slip instabilities and earthquakes. Nevertheless, the large scale-difference between centimeter-scale stick-slip events and kilometer-scale earthquake ruptures are challenging for an extrapolation of laboratory results. The ability to upscale these results generally depends on the physics of the underlying processes, i.e., if macroscopic behavior originates from microscopic organization, for example, in a self-similar fashion. This is suggested to be the case for the faulting process in the laboratory and within the Earth's crust, which is connected to the growth, coalescence and slip upon a network of cracks and faults (e.g. Tchalenko, 1970; Allegre et al., 1982; Main et al., 1990; Meredith et al., 1990; Lockner et al., 1991a,b; Main, 1996; Thompson et al., 2009). Nevertheless, not all results from laboratory rock mechanics experiments translate directly into natural large scale faulting processes. An example for the unsuccessful attempt to extrapolate laboratory findings is the dilatancy-diffusion model (see Scholz et al. (1973) and Anderson and Whitcomb (1973) for details about the model). Based on the observation of sample dilation before rock failure in laboratory compression tests, a model was formulated that predicted a range of precursory signals before earthquake ruptures (e.g. Brace et al., 1966; Nur, 1972; Scholz et al., 1973; Nur, 1974). After initial successes much of the claimed observations of precursors in nature were proven to be artifacts or did not withstand rigorous statistical testing and up to now, no conclusive evidence for near-fault dilation has been found (e.g. Allen and Helmberger, 1973; Kanamori and Fuis, 1976; Lindh et al., 1978; Geller, 1997). This may be caused by the inherent structural and compositional complexity of natural faults (e.g. Ben-Zion and Sammis, 2003; Wibberley et al., 2008; Faulkner et al., 2010) which may inhibit processes that are observable during simplistic laboratory experiments.

An example of a successful extrapolation of laboratory observations is the rate-and-state model that describes frictional behavior of interfaces over a range of scales (Dieterich, 1979; Ruina, 1983). Based on this model a large spectrum of fault behaviors has been explained. Examples of this include the depth-range of the seismogenic zone, fault creep, effective seismic coupling and afterslip distributions (e.g. Marone, 1998; Scholz, 1998). The rate-and-state model was developed based on empirical observations of the response of material interfaces to changes in loading rates, and has been extrapolated to accelerating slip on faults. This model generally describes the change

in friction to a step increase in sliding velocity. This change occurs as an immediate transient response which is commonly an increase in friction followed by a decrease over a characteristic distance (i.e. the critical weakening distance D_c) and subsequent stabilization at a new steady-state friction value (for reviews see Dieterich (1986), Dieterich and Kilgore (1994), Marone (1998) or Scholz (1998)). Earthquake initiation is considered within the context of a nucleating slip patch which under certain conditions will grow unstably thereby radiating seismic energy. Generally, this type of slip event occurs in the laboratory when the frictional strength-decrease ($f_s - f_d$) over the slip weakening distance (D_c) exceeds the unloading curve of the loading frame which is controlled by the machine stiffness (K) (Dieterich, 1979):

$$K < \Delta\tau / D_c. \tag{8.1}$$

Here, $\Delta\tau$ is the change in shear stress which is equivalent to change in frictional strength for experiments at constant normal stress. On crustal faults, a propagating rupture is driven by the elastic energy stored in the surrounding lithology, and slip instability occurs if the rate of strength reduction exceeds the rate of stress reduction (e.g. Dieterich, 1979; Lockner and Beeler, 2002). The stiffness at the center of a rupture patch can describe a function of its size (r), the shear modulus (G) and the patch-geometry (Eshelby, 1957; Walsh, 1971):

$$K = \frac{CG}{r}, \tag{8.2}$$

where C is a geometric constant between 2–3 (Ben-Zion, 2003). The existence of a critical slip-weakening distance that governs the length scale of this strength-breakdown process also necessitates a minimum rupture-patch-size required for the occurrence of slip instability.

Combining Equ. 8.1 with Equ. 8.2, we obtain following expression for the minimum size for the process zone of slip instability, i.e., the spatial region of strength reduction due to rupture growth (e.g. Dieterich, 1979, 1986):

$$r_c = \frac{CGD_c}{\Delta\tau} = \frac{CGD_c}{\sigma_n(f_s - f_d)}, \tag{8.3}$$

where σ_n is the normal stress and f_s and f_d are static and dynamic friction. Using laboratory measured values ($G = 25$ GPa, $D_c = 5 \cdot 10^{-6}$ m, and $\Delta\tau = 0.25$ MPa yields a minimum size for a contained slip instability of $r_c = 0.5$ m (Dieterich, 1979). This type of slip instability has

been observed in biaxial compression tests on large, artificial, laboratory faults (e.g. Okubo and Dieterich, 1984).

8.1 Frequency magnitude distributions and source scaling relations of mining seismicity

Besides the experiments on laboratory faults, mining induced seismicity provides the opportunity to scrutinize the existence of a minimum earthquake size as well as bridging the gap between laboratory and natural earthquakes. Based on the analysis of microseismicity in mines, several studies have claimed that Gutenberg-Richter type frequency-magnitude distributions (FMDs) terminate below a certain magnitude (e.g. $M_{\text{min}} \sim 0$) (Aki, 1987; Iio, 1991; Richardson and Jordan, 2002). Based on the apparent break in scaling, Richardson and Jordan (2002) estimated the source dimension of the apparent smallest tectonic earthquake, assuming slip on a circular crack:

$$r_{\text{c}} = \left(\frac{7M_0^{\text{min}}}{16\Delta\tau} \right)^{1/3}, \tag{8.4}$$

where $\Delta\tau$ is the shear stress drop. This yields an estimate of r_{c}=10–20 m, using the values ($M_{\text{min}} \sim 0.4$, $G = 36$ GPa, $D_{\text{c}} = 1.2 \times 10^{-4}$ m, and $\Delta\tau = 0.3$ MPa) listed in Richardson and Jordan (2002). The authors interpret these results as a difference in source physics and a transition from shear-dominated, tectonic earthquakes to fracture-dominated events in competent rock. Other studies, however, suggested that this change in FMD scaling is likely an artifact of catalog detection limits, rather then being related to earthquake source physics (Boettcher et al., 2009). Boettcher et al. (2009) show FMDs extending down to $M_{\text{w}} = -1.3$ and minimum source size of a complete catalog between 0.3 and 0.7 m. A subsequent study on mining seismicity, recorded with a higher sensitivity seismic array, reported Gutenberg-Richter type FMDs down to $M_{\text{w}} = -4.3$ (Kwiatek et al., 2010). The corresponding seismic moment for their magnitude of completeness is $M_0 = 4.7 * 10^2$ Nm ($M_0 = 10^{1.5M_{\text{w}}+9.1}$ (Hanks and Kanamori, 1979)), the shear stress drops ranged between $\Delta\tau = 1$–10 MPa and corner frequency between $f_{\text{c}} = 0.8$–13.6 kHz. Based on the values of f_{c}, the source dimension of a circular rupture patch can be estimated using Brune (1970):

$$r = \frac{2.34\beta}{2\pi f_{\text{c}}}, \tag{8.5}$$

where β indicates the corresponding shear wave velocity. Depending on the used velocity model the range of source sizes in Kwiatek et al. (2010) is between $r = 0.08$ to 1.3 m. In a follow-up study, Kwiatek et al. (2011) highlighted that mining-induced seismicity shows, analogous to natural earthquakes, self-similar scaling of source-parameters over a broad range of magnitudes ($M_w = -4.1$ to -0.8), underlining the similarities between tectonic and mining-induced seismic events.

8.2 Frequency magnitude distributions and source scaling relations in laboratory experiments

The previously summarized studies on mining induced seismicity highlighted interesting similarities in FMDs and source scaling relationships to natural seismicity. The lower end in the FMD event in Kwiatek et al. (2010) exhibit the approximate dimensions of the largest slip events within our studies, i.e., linear rupture dimensions of about 8 cm. Based on the fault dimensions and measured slip during large stress-drop events, we can estimate an approximate seismic moment for the stick-slip events within our studies:

$$M_0 = GDA, \tag{8.6}$$

where M_0 is the seismic moment, G is the shear modulus and A is the fault area. For an observed range of slip between 0.16 to 0.4 mm and an approximate fault area of $A = 0.003\text{m}^2$, and shear modulus of Westerly granite $G = 24.1$ GPa, we estimate moment-magnitudes using the seismic moment-magnitude relationship in Hanks and Kanamori (1979). For the largest stick slip events, magnitude-ranges are between $M_w = -3.3$ to -3.0. This is in agreement with results from Thompson et al. (2006). Thus, the stick-slip events within our experiments are on the same order of magnitude as the smallest mining-induced seismic events that show self-similar source scaling and Gutenberg-Richter type FMDs. This is important, considering the observed self-similar scaling of acoustic emission sources during laboratory, triaxial compression tests under dry conditions (Harrington and Benson, 2011). In a recent study, we showed extended parallels between the statistics of natural seismicity and laboratory AEs, including Omori-Utsu type aftershock decay, Gutenberg-Richter types FMDs, as well as spatial variations in b-values in the proximity of fault asperity regions (Goebel et al., 2013d). The analogies in seismic event statistics also extend to the

power-law decay of AE density distributions as function of fault normal distance (Goebel et al., 2013b).

The broad parallels in seismic event statistics as well as source-scaling relations indicates a similarity in the underlying mechanisms of seismic event creation in the laboratory, in mines and for natural seismicity in the Earth's crust. The present observations do not provide compelling evidence for a clear distinction between seismic events at different scales.

8.3 Seismic events within a continuum of sizes and slip-velocities

Assuming that the physical processes that govern seismic event characteristics bear a close-knit connection to the statistics of seismic event, we deduce that the underlying physics that lead to the creation of seismic events in the laboratory and on crustal scales are similar. At this point, no conclusive observational-support for the existence of a minimum earthquake, e.g., in form of a possible break in frequency-magnitude distributions or change in source-parameter scaling has been observed.

Besides a lack of distinction of seismically active slip events according to scale, slip on crustal fault occurs also over a range of velocities (e.g. Ide et al., 2007). Creeping faults and large earthquake ruptures may be the end members of this spectrum of slip modes which also includes low-frequency and very low-frequency earthquakes as well as slow-slip events, identified by non-volcanic tremors (Peng and Gomberg, 2010). These slow slip events occur over a range of rupture speeds which may coalesce to form organized rupture in places (Shelly et al., 2006). These results extend the classical view on earthquake nucleation, suggesting a possible range of processes that are involved in the generation of slip events rather than a generic strength break-down process.

9 Conclusion & Outlook

Our results highlight the role of laboratory experiments in understanding micro-seismicity distributions in the proximity of fault zones. Variations in micro-seismicity statistics are connected to fault stress and indicate a fault's position within the seismic cycle. Moreover, micro-seismicity distributions are strongly influenced by fault roughness. They can be used to document fault evolution and structural heterogeneity. The described results do not only apply to near surface processes, but also help understand fault properties at seismogenic depth where most large earthquakes originate. Such connections between physical fault properties and micro-seismicity distributions should be further investigated at larger scales within the Earth's crust. While fault stress and structure are not directly observable under these conditions, other geological observations, for example, fault trace complexity, cumulative displacements, and slip rates, provide a proxy for variations in fault properties in nature. The combination of seismic and geologic observations may significantly advance the understanding of fault evolutionary processes. In particular, this may provide insights into possible increases of structural complexity after initial smoothing for large displacements where fault zones might reorganize. In parallel, fault evolution can also be studied by extending laboratory experiments to larger displacements. Consequently, a combination of laboratory results and natural seismicity studies can further advance the understanding of fault specific hazard potentials and constrain expected earthquake sizes as function of local fault zone properties.

References

Aki, K., 1965, Maximum likelihood estimate of b in the formula $\log N = a - bM$ and its confidence limits: Bull. Earthquake Res. Inst., Tokyo Univ., v. 43, p. 237–239.

Aki, K., 1979, Characterization of barriers on an earthquake fault: J. Geophys. Res., v. 84, p. 6140–6148.

Aki, K., 1981, A probabilistic synthesis of precursory phenomena, *in* Simpson, D.W., and Richards, P.G., eds., Earthquake prediction: An international review, Maurice Ewing Series, v. 4: Washington, D. C., American Geophysical Union, p. 566–574.

Aki, K., 1984, Asperities, barriers, characteristic earthquakes and strong motion prediction: J. Geophys. Res., v. 89, no. B7, p. 5867–5872.

Aki, K., 1987, Magnitude-frequency relation for small earthquakes: A clue to the origin of f_{max} of large earthquakes: J. Geophys. Res., v. 92, no. B2, p. 1349–1355.

Allegre, C.J., Le Mouel, J.L., and Provost, A., 1982, Scaling rules in rock fracture and possible implications for earthquake prediction: v. 297, p. 47–49.

Allen, C.R., and Helmberger, D.V., 1973, Search for temporal changes in seismic velocities using large explosions in southern California, *in* Proc. of the conf. on tectonic problems of the san andreas fault zone, geological sciences, v. 13: p. 436–445.

Amitrano, D., 2003, Brittle-ductile transition and associated seismicity: Experimental and numerical studies and relationship with the b value: J. Geophys. Res., v. 108, p. 2044, doi: 10.1029/2001JB000680.

Amitrano, D., and Schmittbuhl, J., 2002, Fracture roughness and gouge distribution of a granite shear band: J. Geophys. Res., v. 107, p. 2375, doi:10.1029/2002JB001761.

Anders, M.H., and Wiltschko, D.V., 1994, Microfracturing, paleostress and the growth of faults: J. Struct. Geol., v. 16, no. 6, p. 795–815.

Anderson, D.L., and Whitcomb, J.H., 1973, The dilatancy-diffusion model of earthquake prediction, *in* Proceedings of the conference on tectonic problems of the san andreas fault system, v. 13: Stanford University Press, p. 417–426.

Aydin, A., and Johnson, A.M., 1983, Analysis of faulting in porous sandstones: J. Struct. Geol., v. 5, no. 1, p. 19–31.

Bachmann, C.E., Wiemer, S., Goertz-Allmann, B.P., and Woessner, J., 2012, Influence of pore-pressure on the event-size distribution of induced earthquakes: Geophys. Res. Lett., v. 39, L09302, doi:10.1029/2012GL051480.

Barbot, S., Lapusta, N., and Avouac, J.P., 2012, Under the hood of the earthquake machine: Toward predictive modeling of the seismic cycle: Science, v. 336, no. 6082, p. 707–710, doi: 10.1126/science.1218796.

Ben-Zion, Y., and Sammis, C.G., 2003, Characterization of Fault Zones: Pure Appl. Geophys., v. 160, p. 677–715.

Ben-Zion, Y., 2003, Appendix 2: Key formulas in earthquake seismology: Int. Handbook of Rarthquake and Rngeneering Seismol., v. 81, p. 1857–1875.

Bender, B., 1983, Maximum likelihood estimation of b values for magnitude grouped data: Bull. Seismol. Soc. Am., v. 73, no. 3, p. 831–851.

Beroza, G.C., and Zoback, M.D., 1993, Mechanism diversity of the Loma Prieta aftershocks and the mechanics of mainshock-aftershock interaction.: Science, v. 259, no. 5092, p. 210.

Bhat, H.S., Dmowska, R., Rice, J.R., and Kame, N., 2004, Dynamic slip transfer from the Denali to Totschunda faults, Alaska: Testing theory for fault branching: Bull. Seismol. Soc. Am., v. 94, p. 202–213.

Boettcher, M.S., McGarr, A., and Johnston, M., 2009, Extension of Gutenberg-Richter distribution to $M_w - 1.3$, no lower limit in sight: Geophys. Res. Lett., v. 36, no. 10, doi:10.1029/2009GL038080.

Brace, W.F., and Byerlee, J.D., 1966, Stick-slip as a mechanism for earthquakes: Science, v. 153, no. 3739, p. 990–992.

Brace, W.F., Paulding, B.W., and Scholz, C., 1966, Dilatancy in the fracture of crystalline rocks: J. Geophys. Res., v. 71, no. 16, p. 3939–3953.

Brodsky, E.E., Gilchrist, J.J., Sagy, A., and Collettini, C., 2011, Faults smooth gradually as a function of slip: Earth and Planetary Science Letters, v. 302, no. 1–2, p. 185–193, doi:10.1016/j.epsl.2010.12.010.

Brune, J.N., 1970, Tectonic stress and the spectra of seismic shear waves from earthquakes: J. Geophys. Res., v. 75, no. 26, p. 4997–5009.

Byerlee, J.D., 1970, The mechanics of stick-slip: Tectonophys., v. 9, no. 5, p. 475–486.

Byerlee, J.D., and Brace, W.F., 1968, Stick slip, stable sliding, and earthquakes-effect of rock type, pressure, strain rate, and stiffness: J. Geophys. Res., v. 73, no. 18, p. 6031–6037.

Caine, J.S., Evans, J.P., and Forster, C.B., 1996, Fault zone architecture and permeability structure: Geology, v. 24, no. 11, p. 1025–1028.

Californian Fault Traces, 2010, Quaternary Fault and Fold Database for the United States, California Geological Survey & U.S. Geological Survey: http://earthquake.usgs.gov/regional/qfaults, (accessed February 17, 2012).

Candela, T., Renard, F., Bouchon, M., Brouste, A., Marsan, D., Schmittbuhl, J., and Voisin, C., 2009, Characterization of fault roughness at various scales: Implications of three-dimensional high resolution topography measurements: Pure Appl. Geophys., v. 166, p. 1817–1851, doi:10.1007/s00024-009-0521-2.

Candela, T., Renard, F., Klinger, Y., Mair, K., Schmittbuhl, J., and Brodsky, E.E., 2012, Roughness of fault surfaces over nine decades of length scales: J. Geophys. Res., v. 117, B08409, doi:10.1029/2011JB009041.

Candela, T., Renard, F., Bouchon, M., Schmittbuhl, J., and Brodsky, E.E., 2011a, Stress drop during earthquakes: effect of fault roughness scaling: Bull. Seismol. Soc. Am., v. 101, no. 5, p. 2369–2387.

Candela, T., Renard, F., Schmittbuhl, J., Bouchon, M., and Brodsky, E.E., 2011b, Fault slip distribution and fault roughness: Geophys. J. Int., v. 187, no. 2, p. 959–968.

Chayes, F., 1950a, Composition of the granites of Westerly and Bradford, Rhode Island.: Am. J. Sci., v. 248, p. 378–407.

Chester, F.M., and Chester, J.S., 1998, Ultracataclasite structure and friction processes of the Punchbowl fault San Andreas system, California: Tectonophysics, v. 295, p. 199–221.

Chester, F.M., Evans, J.P., and Biegel, R.L., 1993, Internal structure and weakening mechanisms of the San Andreas Fault: J. Geophys. Res., v. 98, no. B1, p. 771–786, doi:10.1029/92JB01866.

Chester, F.M., and Logan, J.M., 1986, Implications for mechanical properties of brittle faults from observations of the Punchbowl fault zone, California: Pure Appl. Geophys., v. 124, no. 1, p. 79–106.

Chester, F.M., and Chester, J.S., 2000, Stress and deformation along wavy frictional faults: J. Geophys. Res., v. 105, no. B10, p. 23,421–23,430.

Clauset, A., Shalizi, C.R., and Newmann, M.E.J., 2009, Power-law distributions in empirical data: SIAM review, v. 51, no. 4, p. 661–703.

Dieterich, J.H., and Kilgore, B.D., 1994, Direct observation of frictional contacts: New insights for state-dependent properties: Pure Appl. Geophys., v. 143, no. 1, p. 283–302.

Dieterich, J.H., and Kilgore, B.D., 1996, Imaging surface contacts: power law contact distributions and contact stresses in quartz, calcite, glass and acrylic plastic: Tectonophys., v. 256, no. 1–4, p. 219–239, doi:10.1016/0040-1951(95).

Dieterich, J.H., and Smith, D.E., 2009, Nonplanar faults: Mechanics of slip and off-fault damage: Pure Appl. Geophys., v. 166, p. 1799–1815.

Dieterich, J.H., 1986, A model for the nucleation of earthquake slip: Earthquake source mechanics, Geophys. Monograph, v. 37, p. 37–47.

Dieterich, J.H., and Richards-Dinger, K.B., 2010, Earthquake recurrence in simulated fault systems: Seismogenesis and Earthquake Forecasting: The Frank Evison Volume II, v. 2, p. 233–250.

Dieterich, J., 1979, Modeling of rock friction 1. Experimental results and constitutive equations: J. Geophys. Res., v. 84, no. B5, p. 2161–2168.

Dietrich, J.H., 1978, Time-dependent friction and mechanics of stick-slip: Pure Appl. Geophys., v. 116, p. 790–806.

Dor, O., Ben-Zion, Y., Rockwell, T.K., and Brune, J., 2006, Pulverized rocks in the mojave section of the San Andreas Fault Zone: Earth and Planetary Science Letters, v. 245, no. 3, p. 642–654.

Dunham, E.M., Belanger, D., Cong, L., and Kozdon, J.E., 2011, Earthquake ruptures with strongly rate-weakening friction and off-fault plasticity, Part 2: Nonplanar faults: Bull. Seismol. Soc. Am., v. 101, no. 5, p. 2308–2322.

Engelder, J.T., 1974, Microscopic wear grooves on slickensides: Indicators of paleosesimicity: J. Geophy. Res., v. 79, p. 4387–4392.

Engelder, J.T., and Scholz, C.H., 1976, The role of asperity indentation and ploughing in rock friction–II: Influence of relative hardness and normal load: Int. J. Rock Mech. Min. Sci. and Geomech. Abstr., v. 13, no. 5, p. 155–163.

Eshelby, J.D., 1957, The determination of the elastic field of an ellipsoidal inclusion, and related problems: Proceedings of the Royal Society of London. Series A. Mathematical and Physical Sciences, v. 241, no. 1226, p. 376–396.

Faulkner, D.R., Jackson, C.A.L., Lunn, R.J., Schlische, R.W., Shipton, Z.K., Wibberley, C.A.J., and Withjack, M.O., 2010, A review of recent developments concerning the structure, mechanics and fluid flow properties of fault zones: Journal of Structural Geology, v. 32, no. 11, p. 1557–1575, doi:10.1016/j.jsg.2010.06.009.

Faulkner, D.R., Lewis, A.C., and Rutter, E.H., 2003, On the internal structure and mechanics of large strike-slip fault zones: Field observations of the Carboneras fault in southeastern Spain: Tectonophysics, v. 367, no. 3, p. 235–251.

Faulkner, D.R., Mitchell, T.M., Behnsen, J., Hirose, T., and Shimamoto, T., 2011, Stuck in the mud? Earthquake nucleation and propagation through accretionary forearcs: Geophys. Res. Lett., v. 38, no. 18, p. L18,303.

Feder, J., 1988, Fractals: Plenum Press, New York.

Felzer, K.R., and Brodsky, E.E., 2006, Decay of aftershock density with distance indicates triggering by dynamic stress: Nature, v. 441, doi:10.1038/nature04799.

Geller, R.J., 1997, Earthquake prediction: a critical review: Geophys. J. Int., v. 131, no. 3, p. 425–450.

Gephart, J.W., and Forsyth, D.W., 1984, An improved method for determining the regional stress tensor using earthquake focal mechanism data: Application to the San Fernando Earthquake Sequence: J. Geophys. Res., v. 89, no. B11, p. 9305–9320, doi:10.1029/JB089iB11p09305.

Goebel, T.H.W., Becker, T.W., Sammis, C.G., and Dresen, G., 2013a, Off-fault damage and acoustic emission distributions during the evolution of structurally-complex faults over series of stick-slip events: Geophys. J. Int., (in prep.).

Goebel, T.H.W., Becker, T.W., Schorlemmer, D., Stanchits, S., Sammis, C., Rybacki, E., and Dresen, G., 2012, Identifying fault hetergeneity through mapping spatial anomalies in acoustic emission statistics: J. Geophys. Res., v. 117, B03310, doi:10.1029/2011JB008763.

Goebel, T.H.W., Candela, T., Sammis, C.G., Becker, T.W., Dresen, G., and Schorlemmer, D., 2013b, Seismic event distributions and off-fault damage during frictional sliding of saw-cut surfaces with predefined roughness: Geophys. J. Int., (submitted).

Goebel, T.H.W., Sammis, C.G., Becker, T.W., Dresen, G., and Schorlemmer, D., 2013c, A comparision of seismicity characteristics and fault structure in stick-slip experiments and nature: Pure Appl. Geophys., (submitted).

Goebel, T.H.W., Schorlemmer, D., Dresen, G., Becker, T.W., and Sammis, C.G., 2013d, Acoustic emissions document stress changes over many seismic cycles in stick-slip experiments: Geophys. Res. Letts., v. 40, doi:10.1002/grl.50507.

Grassberger, P., 1983, Generalized dimensions of strange attractors: Physics Letters A, v. 97, no. 6, p. 227–230.

Green, H., and Marone, C., 2002, Instability of deformation: Reviews in mineralogy and geochemistry, v. 51, no. 1, p. 181–199.

Griffith, W.A., Nielsen, S., Toro, G.D., and Smith, S.A.F., 2010, Rough faults, distributed weakening, and off-fault deformation: J. Geophys. Res, v. 115, B08409, doi:10.1029/2009JB006925.

Griffith, W.A., Rosakis, A., Pollard, D.D., and Ko, C.W., 2009, Dynamic rupture experiments elucidate tensile crack development during propagating earthquake ruptures: Geology, v. 37, no. 9, p. 795–798.

Gulia, L., Wiemer, S., and Schorlemmer, D., 2010, Asperity-based earthquake likelihood models for Italy: Annals of Geophysics, v. 53, no. 3, p. 63–75, doi:10.4401/ag-4843.

Guo, Z., and Ogata, Y., 1997, Statistical relations between the parameters of aftershocks in time, space, and magnitude: J. Geophys. Res., v. 102, no. B2, p. 2857–2873.

Gutenberg, B., and Richter, C.F., 1944, Frequency of earthquakes in California: Bull. Seismol. Soc. Am., v. 34, p. 185–188.

Hanks, T.C., and Kanamori, H., 1979, A moment magnitude scale: J. Geophy. Res., v. 84, no. B5, p. 2348–2350.

Hansen, A., Schmittbuhl, J., Batrouni, G.G., and de Oliveira, F.A., 2000, Normal stress distribution of rough surfaces in contact: Geophys. Res. Lett., v. 27, no. 22, p. 3639–3642.

Harrington, R.M., and Benson, P.M., 2011, Analysis of laboratory simulations of volcanic hybrid earthquakes using empirical Green's functions: J. Geophys. Res., v. 116, no. B11.

Hauksson, E., 2010, Spatial separation of large earthquakes, aftershocks, and background seismicity: analysis of interseismic and coseismic seismicity patterns in southern California,: Pure appl. Geophys., v. 167, doi:10.1007/s00024-010-0083-3.

Hirata, T., 1989, A correlation between the *b* value and the fractal dimension of earthquakes: J. Geophys. Res., v. 94, p. 7507–7514.

Hirth, G., and Tullis, J., 1989, The effects of pressure and porosity on the micromechanics of the brittle-ductile transition in Quartzite: J. Geophy. Res., v. 94, no. B12, p. 17,825–17.

Hori, T., Kato, N., Hirahara, K., Baba, T., and Kaneda, Y., 2004, A numerical simulation of earthquake cycles along the Nankai Trough in southwest Japan: lateral variation in frictional property due to the slab geometry controls the nucleation position: Earth and Planetary Science Letters, v. 228, no. 3, p. 215–226.

Huang, J., and Turcotte, D.L., 1988, Fractal distributions of stress and strength and variations of *b*-value: Earth and Planetary Science Letters, v. 91, p. 223–230.

Ide, S., Beroza, G.C., Shelly, D.R., and Uchide, T., 2007, A scaling law for slow earthquakes: Nature, v. 447, no. 7140, p. 76–79.

Iio, Y., 1991, Minimum size of earthquakes and minimum value of dynamic rupture velocity: Tectonophys., v. 197, no. 1, p. 19–25.

Imoto, M., 1991, Changes in the magnitude–frequency *b*-value prior to large (M≥6.0) earthquakes in Japan: Tectonophys., v. 193, no. 4, p. 311–325.

Ishimoto, M., and Iida, K., 1939, Observations of earthquakes registered with the microseismograph constructed recently: Bull. Earthquake Res. Inst. Tokyo Univ., v. 17, p. 443–478.

Jaeger, J.C., and Cook, N.G.W., 1979, Fundamentals of rock mechanics: London, Chapman & Hall.

Janssen, C., Wagner, F., Zang, A., and Dresen, G., 2001, Fracture process zone in granite: a microstructural analysis: Int. J. Earth Sci., v. 90, no. 1, p. 46–59.

Kanamori, H., and Stewart, G.S., 1978, Seismological asperity earthquake of February 4, 1976: J. Geophys. Res., v. 83, p. 3427–3434.

Kanamori, H., and Fuis, G., 1976, Variation of P-wave velocity before and after the Galway Lake earthquake ($m_{\mathrm{L}} = 5.2$) and the Goat Mountain earthquakes ($m_{\mathrm{L}} = 4.7, 4.7$), 1975, in the Mojave desert, California: Bull. Seismo. Soc. Am., v. 66, no. 6, p. 2017–2037.

Kato, A., Miyatake, T., and Hirata, N., 2010, Asperity and barriers of the 2004 Mid-Niigata prefecture earthquake revealed by highly dense seismic observations: Bull. Seismol. Soc. Am., v. 100, p. 298–306.

Kim, Y.S., Peacock, D.C.P., and Sanderson, D.J., 2004, Fault damage zones: J. Struct. Geol., v. 26, no. 3, p. 503–517.

Klinger, Y., 2010, Relation between continental strike-slip earthquake segmentation and thickness of the crust: J. Geophys. Res., v. 115, B07306, doi:10.1029/2009JB006550.

Kwiatek, G., Plenkers, K., Nakatani, M., Yabe, Y., and Dresen, G., 2010, Frequency-magnitude characteristics down to magnitude −4.4 for induced seismicity recorded at Mponeng gold mine, South Africa: Bull. Seismol. Soc. Am., v. 100, p. 1165–1173.

Kwiatek, G., Plenkers, K., and Dresen, G., 2011, Source parameters of picoseismicity recorded at Mponeng deep gold mine, South Africa: implications for scaling relations: Bull. Seismol. Soc. Am., v. 101, no. 6, p. 2592–2608.

Lei, X., 2003, How do asperities fracture? An experimental study of unbroken asperities: Earth Planetary Sci. Letts., v. 26, p. 247–258.

Lei, X., Kusunose, K., Rao, M., Nishizawa, O., and Satoh, T., 2000, Quasi-static fault growth and cracking in homogeneous brittle rock under triaxial compression using acoustic emission monitoring: J. Geoph. Res., v. 105, p. 6127–6139.

Lei, X., Masuda, K., Nishizawa, O., Jouniaux, L., Liu, L., Ma, W., Satoh, T., and Kusunose, K., 2004, Detailed analysis of acoustic emission activity during catastrophic fracture of faults in rock: J. Struct. Geol., v. 26, p. 247–258.

Lei, X., Nishizawa, O., Kusunose, K., and Satoh, T., 1992, Fractal structure of the hypocenter distributions and focal mechanism solutions of acoustic emission in two granites of different grain sizes: J. Phys. Earth, v. 40, p. 617–634.

Liakopoulou-Morris, F., Main, I.G., Crawford, B.R., and Smart, B.G.D., 1994, Microseismic properties of a homogeneous sandstone during fault nucleation and frictional sliding: Geophys. J. Int., v. 119, no. 2, p. 219–230, doi:10.1111/j.1365-246X.

Lindh, A.G., Lockner, D.A., and Lee, W.H.K., 1978, Velocity anomalies: An alternative explanation: Bull. Seismo. Soc. Am., v. 68, no. 3, p. 721–734.

Lockner, D., and Byerlee, J., 1990, An example of slip instability resulting from displacement-varying strength: Pure Appl. Geophys., v. 133, no. 2, p. 269–281.

Lockner, D., Byerlee, J., Kuksenko, V., Ponomarev, A., and Sidorin, A., 1991a, Observations of quasistatic fault growth from acoustic emissions: Fault Mech. Transport Properties of Rocks, p. 3–31.

Lockner, D., Byerlee, J., Kuksenko, V., Ponomarev, A., and Sidorin, A., 1991b, Quasi-static, fault growth and shear fracture energy in granite: Nature, v. 350, p. 39–42.

Lockner, D.A., and Byerlee, J.D., 1995, Precursory AE patterns leading to rock fracture: in Proc. 5th Conf. on Acoustic Emission/Microseismic Activity in Geologic Structures and Materials, p. 45–58.

Lockner, D.A., and Beeler, N.M., 2002, 32 Rock failure and earthquakes, *in* William H.K. Lee, Hiroo Kanamori, P.C.J., and Kisslinger, C., eds., International handbook of earthquake and engineering seismology, International Geophysics, v. 81, Part A: Academic Press, p. 505–537, doi: 10.1016/S0074-6142(02)80235-2.

Main, I.G., 1996, Statistical physics, seismogenesis, and seismic hazard: Rev. Geophys., v. 34, no. 4, p. 433–462.

Main, I.G., Meredith, P.G., and Jones, C., 1989, A reinterpretation of the precursory seismic *b*-value anomaly from fracture mechanics: Geoph. J. Int., v. 96, p. 131–138.

Main, I.G., Meredith, P.G., and Sammonds, P.R., 1992, Temporal variations in seismic event rate and *b*-values from stress corrosion constitutive laws: Tectonophysics, v. 211, p. 233–246.

Main, I.G., Meredith, P.G., Sammonds, P.R., and Jones, C., 1990, Influence of fractal flaw distributions on rock deformation in the brittle field: Geol. Soc. of London, Special Publications, v. 54, p. 81–96.

Mair, K., Main, I., and Elphick, S., 2000, Sequential growth of deformation bands in the laboratory: J. Struct. Geol., v. 22, no. 1, p. 25–42.

Malin, P.E., Blakeslee, S.N., Alvarez, M.G., and Martin, A.J., 1989, Microearthquake imaging of the Parkfield asperity: Science, v. 244, p. 557–559.

Mandelbrot, B., 1982, The fractal geometry of nature: Freeman, New York.

Marone, C., 1998, Laboratory-derived friction laws and their application to seismic faulting: Annu. Rev. Earth Planet. Sci., v. 26, p. 643–696.

Marone, C., and Kilgore, B., 1993, Scaling of the critical slip distance for seismic faulting with shear strain in fault zones: Nature, v. 362, no. 6421, p. 618–621.

Marone, C., Raleigh, C.B., and Scholz, C.H., 1990, Frictional behavior and constitutive modeling of simulated fault gouge: J.Geophys. Rese., v. 95, no. B5, p. 7007–7025.

McGarr, A., Spottiswoode, S.M., and Gay, N.C., 1979, Observations relevant to seismic driving stress, stress drop and efficiency: J. Geophys. Res., v. 84, p. 2251–2261.

McLaskey, G.C., and Glaser, S.D., 2011, Micromechanics of asperity rupture during laboratory stick slip experiments: Geophys. Res. Let., v. 38, L12302, doi:10.1029/2011GL047507.

Mendoza, C., and Hartzell, S.H., 1988, Aftershock patterns and main shock faulting: Bull. Seismol. Soc. Am., v. 78, no. 4, p. 1438–1449.

Meredith, P.G., Main, I.G., and Jones, C., 1990, Temporal variations in seismicity during quasi-static and dynamic rock failure: Tectonophysics, v. 175, p. 249–268.

Michael, A.J., 1987, Use of focal mechanisms to determine stress: a control study: J. Geophys. Res., v. 92, p. 357–368.

Mitchell, T., and Faulkner, D., 2009, The nature and origin of off-fault damage surrounding strike-slip fault zones with a wide range of displacements: A field study from the Atacama fault system, northern Chile: Journal of Structural Geology, v. 31, no. 8, p. 802–816, doi:10.1016/j.jsg.2009.05.002.

Mogi, K., 1962, Magnitude-frequency relations for elastic shocks accompanying fractures of various materials and some related problems in earthquakes: Bull. Earthquake Res. Inst. Univ. Tokyo, v. 40, p. 831–853.

Moore, D.E., and Lockner, D.A., 2004, Crystallographic controls on the frictional behavior of dry and water-saturated sheet structure minerals: Journal of Geophysical Research: Solid Earth, v. 109, no. B3, doi:10.1029/2003JB002582.

Moore, D.E., and Rymer, M.J., 2007, Talc-bearing serpentinite and the creeping section of the San Andreas fault: Nature, v. 448, p. 795–797, doi:10.1038/nature06064.

Nadeau, R.M., and McEvilly, T.V., 1999, Fault slip rates at depth from recurrence intervals of repeating microearthquakes: Science, v. 285, p. 718–721.

Nadeau, R. M., W.F., and McEvilly, T.V., 1995, Clustering and periodic recurrence of microearthquakes on the San Andreas Fault at Parkfield, California: Science, v. 267, p. 503–507.

Nanjo, K.Z., Hirata, N., Obara, K., and Kasahara, K., 2012, Decade-scale decrease in *b* value prior to the M9-class 2011 Tohoku and 2004 Sumatra quakes: Geophys. Res. Lett., v. 39, L20304, doi:10.1029/2012GL052997.

Narteau, C., Byrdina, S., Shebalin, P., and Schorlemmer, D., 2009, Common dependence on stress for the two fundamental laws of statistical seismology: Nature, v. 462, p. 642–645, doi:10.1038/nature08553.

Newman, M.E.J., 2005, Power laws, Pareto distributions and Zipf's law: Contemporary physics, v. 46, no. 5, p. 323–351.

Noda, H., and Lapusta, N., 2013, Stable creeping fault segments can become destructive as a result of dynamic weakening: Nature, v. 493, no. 7433, p. 518–521.

Nur, A., 1972, Dilatancy, pore fluids, and premonitory variations of t_s/t_p travel times: Bull. Seismol. Soc. Am., v. 62, no. 5, p. 1217–1222.

Nur, A., 1974, Matsushiro, Japan, earthquake swarm: Confirmation of the dilatancy-fluid diffusion model: Geology, v. 2, no. 5, p. 217–221.

Ogata, Y., 1999, Seismicity analysis through point-process modeling:a review: pageoph, v. 155, p. 471–507.

Okubo, P., and Dieterich, J., 1984, Effects of physical fault properties on frictional instabilities produced on simulated faults: J. Geophys. Res., v. 89, no. B7, p. 5817–5827.

Omori, F., 1894, On the aftershocks of earthquake: J. Coll. Sci. Imp. Univ. Tokyo, v. 7, p. 111–200.

Oppenheimer, D., 1990, Aftershock slip behavior of the 1989 Loma Prieta, California earthquake: Geophys. Res. Lett, v. 17, no. 8, p. 1199–1202.

Parsons, T., 2007, Forecast experiment: Do temporal and spatial b value variations along the Calaveras fault portend M $\geq$ 4.0 earthquakes?: J. Geophys. Res., v. 112, B03308, doi:10.1029/2006JB004632.

Peng, Z., and Gomberg, J., 2010, An integrated perspective of the continuum between earthquakes and slow-slip phenomena: Nature Geoscience, v. 3, no. 9, p. 599–607.

Persson, B.N.J., Albohr, O., Tartaglino, U., Volokitin, A.I., and Tosatti, E., 2005, On the nature of surface roughness with application to contact mechanics, sealing, rubber friction and adhesion: Journal of Physics: Condensed Matter, v. 17, no. 1, p. R1–R62.

Power, W.L., and Durham, W.B., 1997, Topography of natural and artificial fractures in granitic rocks: Implications for studies of rock friction and fluid migration: Int. J. Rock. Mech. Min. Sci., v. 34, p. 979–989.

Power, W.L., and Tullis, T.E., 1995, Review of the fractal character of natural fault surfaces with implications for friction and the evolution of fault zones, eds.: Barton, C. C. and La Pointe, P. R. in: Fractals in the Earth Sciences, p. 89–105.

Power, W.L., Tullis, T.E., Brown, S.R., Boitnott, G.N., and Scholz, C.H., 1987, Roughness of natural fault surfaces: Geophys. Res. Lett., v. 14, p. 29–32.

Powers, P.M., and Jordan, T.H., 2010, Distribution of seismicity across strike-slip faults in California: J. Geophys. Res., v. 115, doi:10.1029/2008JB006234.

Rathbun, A.P., Renard, F., and Abe, S., 2013, Numerical investigation of the interplay between wall geometry and friction in granular fault gouge: J. Geophys. Res., v. 118, doi:10.1002/jgrb.50106.

Renard, F., Candela, T., and Bouchaud, E., 2013, Constant dimensionality of fault roughness from the scale of micro-fractures to the scale of continents: Geophys. Res. Lett., v. 40, p. 83–87, doi:10.1029/2012GL054143.

Richardson, E., and Jordan, T.H., 2002, Seismicity in deep gold mines of south africa: Implications for tectonic earthquakes: Bull. Seismol. Soc. Am., v. 92, p. 1766–1782, doi:10.1785/0120000226.

Rockwell, T.K., and Ben-Zion, Y., 2007, High localization of primary slip zones in large earthquakes from paleoseismic trenches: Observations and implications for earthquake physics: J. Geophys. Res., v. 112, no. B10, p. B10,304.

Ruina, A., 1983, Slip instability and state variable friction laws: J. Geophys. Res., v. 88, p. 10,359–10,370.

Rundle, J.B., Rundle, P.B., Donnellan, A., and Fox, G., 2004, Gutenberg-richter statistics in topologically realistic system-level earthquake stress-evolution simulations: Earth Planets and Space, v. 56, no. 8, p. 761–772.

Saffer, D.M., and Marone, C., 2003, Comparison of smectite-and illite-rich gouge frictional properties: application to the updip limit of the seismogenic zone along subduction megathrusts: Earth and Planetary Science Letters, v. 215, no. 1, p. 219–235.

Sagy, A., Brodsky, E.E., and Axen, G.J., 2007, Evolution of fault-surface roughness with slip: Geology, v. 35, p. 283–286.

Sammis, C.G., and Steacy, S.J., 1994, The micromechanics of friction in a granular layer: Pure Appl. Geophys., v. 142, no. 3–4, p. 777–794.

Sammonds, P., Meredith, P.R., and Main, P.G., 1992, Role of pore fluids in the generation of seismic precursors to shear fracture: Nature, v. 359, p. 228–230.

Sammonds, P., and Ohnaka, M., 1998, Evolution of microseismicity during frictional sliding: Geophys. Res. Lett., v. 25, p. 699–702.

Savage, H.M., and Brodsky, E.E., 2011, Collateral damage: Evolution with displacement of fracture distribution and secondary fault strands in fault damage zones: J. Geophys. Res., v. 116, no. B3, doi:10.1029/2010JB007665.

Schmittbuhl, J., Chambon, G., Hansen, A., and Bouchon, M., 2006, Are stress distributions along faults the signature of asperity squeeze?: Geophys. Res. Lett., v. 33, no. 13, p. L13,307.

Scholz, C.H., 1968, The frequency-magnitude relation of microfracturing in rock and its relation to earthquakes: Bull. Seismol. Soc. Am., v. 58, p. 399–415.

Scholz, C., 1998, Earthquakes and friction laws: Nature, v. 391, no. 6662, p. 37–42.

Scholz, C.H., 2002, The mechanics of earthquakes and faulting, 2 ed.: Cambridge University Press.

Scholz, C.H., Sykes, L.R., and Aggarwal, Y.P., 1973, Earthquake prediction: A physical basis: Science, v. 181, no. 4102, p. 803–810.

Schorlemmer, D., and Wiemer, S., 2005, Microseismicity data forecast rupture area: Nature, v. 434, p. 1086, doi:10.1038/4341086a.

Schorlemmer, D., Wiemer, S., and Wyss, M., 2004a, Earthquake statistics at Parkfield: 1. Stationarity of *b*-values: J. Geophys. Res., v. 109, no. B12, B12307, doi:10.1029/2004JB003234.

Schorlemmer, D., Wiemer, S., and Wyss, M., 2005, Variations in earthquake-size distribution across different stress regimes: Nature, v. 437, p. 539–542, doi:10.1038/nature04094.

Schorlemmer, D., Wiemer, S., Wyss, M., and Jackson, D.D., 2004b, Earthquake statistics at Parkfield: 2. Probabilistic forecasting and testing: J. Geophys. Res., v. 109, no. B12, B12308, doi: 10.1029/2004JB003235.

Schroeder, M., 1991, Fractals, chaos, power laws: Minutes from an infinite paradise: W. H. Freemann, New York.

Schulz, S.E., and Evans, J.P., 2000, Mesoscopic structure of the Punchbowl Fault, Southern California and the geologic and geophysical structure of active strike-slip faults: J. Struct. Geol., v. 22, no. 7, p. 913–930.

Scott, D.R., Lockner, D.A., Beyerlee, J.D., and Sammis, C.G., 1994, Triaxial testing of Lopez fault gouge at 150 MPa mean effective stresss: Pure Appl. Geophys., v. 142, p. 749–775.

Shelly, D.R., Beroza, G.C., Ide, S., and Nakamula, S., 2006, Low-frequency earthquakes in Shikoku, Japan, and their relationship to episodic tremor and slip: Nature, v. 442, no. 7099, p. 188–191.

Silverman, B.W., 1986, Density estimation for statistics and data analysis: Chapman and Hall, New York.

Sobiesiak, M., Meyer, U., Schmidt, S., Gotze, H.J., and Krawczyk, C.M., 2007, Asperity generating upper crustal sources revealed by *b*-value and isostatic residual anomaly grids in the area of Antofagasta, Chile: J. Geophys. Res., v. 112, doi:10.1029/2006JB004796.

Stanchits, S., Vinciguerra, S., and Dresen, G., 2006, Ultrasonic velocities, acoustic emission characteristics and crack damage of basalt and granite: Pure Appl. Geophys., v. 163, p. 975–994.

Stesky, R.M., 1978, Mechanisms of high temperature frictional sliding in Westerly granite: Can. J. Earth Sci., v. 15, p. 361–375.

Tchalenko, J.S., 1970, Similarities between shear zones of different magnitudes: Geol. Soc. Am. Bull., v. 81, p. 1625–1640.

Tembe, S., Lockner, D.A., and Wong, T.F., 2010, Effect of clay content and mineralogy on frictional sliding behavior of simulated gouges: Binary and ternary mixtures of quartz, illite, and montmorillonite: J. Geophys. Res., v. 115, B03416, doi:10.1029/2009JB006383.

Thompson, B.D., Young, R.P., and Lockner, D.A., 2005, Observations of premonitory acoustic emission and slip nucleation during a stick slip experiment in smooth faulted westerly granite: Geophys. Res. Letts., v. 32, doi:10.1029/2005GL022750.

Thompson, B.D., Young, R.P., and Lockner, D.A., 2006, Fracture in Westerly granite under AE feedback and constant strain rate loading: Nucleation, quasi-static propagation, and the transition to unstable fracture propagation: Pure Appl. Geophys., v. 163, p. 995–1019.

Thompson, B.D., Young, R.P., and Lockner, D.A., 2009, Premonitory acoustic emissions and stick-slip in natural and smooth-faulted Westerly granite: J. Geophys. Res., v. 114, doi:10.1029/2008JB005753.

Tormann, T., Wiemer, S., and Hardebeck, J.L., 2012, Earthquake recurrence models fail when earthquakes fail to reset the stress field: Geophys. Res. Lett., v. 39, L18310, doi:10.1029/2012GL052913.

Turcotte, D.L., 1997, Fractals and chaos in geology and geophysics: Cambridge university press.

Utsu, T., 1962, On the nature of three Alaskan aftershock sequences of 1957 and 1958: Bull. Seismol. Soc. Am., v. 52, p. 279–297.

Utsu, T., Ogata, Y., and Ritsuko, M., 1965, The centenary of Omori formula for a decay law of afterhock activity: Journal of Physics of the Earth, v. 43, p. 1–33.

Voisin, C., Renard, F., and Grasso, J.R., 2007, Long term friction: From stick-slip to stable sliding: Geophs. Res. Lett., v. 34, doi:10.1029/2007GL029715.

Walsh, J.B., 1971, Stiffness in faulting and in friction experiments: J. Geophys. Res., v. 76, no. 35, p. 8597–8598.

Ward, S.N., 2000, San Francisco bay area earthquake simulations: A step toward a standard physical earthquake model: Bull. Seismol. Soc. Am., v. 90, no. 2, p. 370–386.

Wechsler, N., Ben-Zion, Y., and Christofferson, S., 2010, Evolving geometrical heterogeneities of fault trace data: Geophys. J. Int., v. 182, no. 2, p. 551–567.

Weeks, J., Lockner, D., and Beyerlee, J., 1978, Change in b-values during movement on cut surfaces in granite: Bull. Seismol. Soc. Am., v. 68, p. 333–341.

Wesnousky, S.G., 1988, Seismological and structural evolution of strike-slip faults: Nature, v. 335, p. 340–342.

Westerhaus, M., Wyss, M., Yilmaz, R., and Zschau, J., 2002, Correlating variations of b-values and crustal deformations during the 1990s may have pinpointed the rupture initiation of the M_w=7.4 Izmit earthquake of 1999 August 17: Geophys. J. Int., v. 184, no. 1, p. 139–152.

Wibberley, C.A.J., Yielding, G., and Di Toro, G., 2008, Recent advances in the understanding of fault zone internal structure: A review: Geological Society, London, Special Publications, v. 299, no. 1, p. 5–33.

Wiemer, S., and Katsumata, K., 1999, Spatial variability of seismicity parameters in aftershock zones: J. Geophys. Res., v. 104, p. 13,135–13,151.

Wiemer, S., and Schorlemmer, D., 2007, ALM: An asperity-based likelihood model for California: Seismol. Res. Letts., v. 78, no. 1, p. 134–140, doi:10.1785/gssrl.78.1.134.

Wiemer, S., and Wyss, M., 1997, Mapping the frequency-magnitude distribution in asperities: An improved technique to calculate recurrence times?: J. Geophys. Res., v. 102, p. 15,115–15,128.

Wiemer, S., and Wyss, M., 2002, Mapping spatial variability of the frequency-magnitude distribution of earthquakes: Advances in geophysics, v. 45, p. 259–V.

Woessner, J., Hauksson, E., Wiemer, S., and Neukomm, S., 2004, The 1997 Kagoshima (Japan) earthquake doublet: A quantitative analysis of aftershock rate changes: Geophys. Res. Lett., v. 31, L03605, doi:10.1029/2003GL018858.

Woessner, J., Schorlemmer, D., Wiemer, S., and Mai, P.M., 2006, Spatial correlation of aftershock locations and on-fault main shock properties: J. Geophys. Res., v. 111, no. B8, B08301, doi: 10.1029/2005JB003961.

Wyss, M., 1990, Changes of mean magnitude of Parkfield seismicity: A part of the precursory process?: Geophys. Res. Lett., v. 17, p. 2429–2432.

Wyss, M., 2001, Locked and creeping patches along the Hayward fault, California: Geophys. Res. Lett., v. 28, p. 3537–3540.

Wyss, M., and Matsumura, S., 2002, Most likely locations of large earthquakes in the Kanto and Tokai areas, Japan, based on the local recurrence times: Physics of The Earth and Planetary Interiors, v. 131, p. 173–184.

Wyss, M., Sammis, C.G., Nadeau, R.M., and Wiemer, S., 2004, Fractal dimension and *b*-value on creeping and locked patches of the San Andreas fault near Parkfield, California: Bull. Seismol. Soc. Am., v. 94, p. 410–421.

Wyss, M., and Stefansson, R., 2006, Nucleation points of recent mainshocks in southern Iceland, mapped by *b*-values: Bull. Seismol. Soc. Am., v. 96, no. 2, p. 599–608.

Wyss, M., Schorlemmer, D., and Wiemer, S., 2000, Mapping asperities by minima of local recurrence time: The San Jacinto-Elsinore fault zones: J. Geophys. Res., v. 105, p. 7829–7844.

Wyss, M., and Wiemer, S., 2000, Change in the probability for earthquakes in southern California due to the Landers magnitude 7.3 earthquake: Science, v. 290, p. 1334–1338.

Xu, S., and Ben-Zion, Y., 2013, Numerical and theoretical analyses of in-plane dynamic rupture on a frictional interface and off-fault yielding patterns at different scales: Geophys. J. Int., v. 193, no. 1, p. 304–320.

Zang, A., Wagner, F., Stanchits, S., Dresen, G., Andresen, R., and Haidekker, M., 1998, Source analysis of acoustic emissions in Aue granite cores under symmetric and asymmetric compressive loads: Geophys. J. Int., v. 135, p. 1113–1130.

Zang, A., Wagner, F.C., Stanchits, S., Janssen, C., and Dresen, G., 2000, Fracture process zone in granite: J. Geophys. Res, v. 105, no. B10, p. 23,651–23,661.

Zhang, P., Slemmons, D.B., and Mao, F., 1991, Geometric pattern, rupture termination and fault segmentation of the Dixie Valley–Pleasant Valley active normal fault system, Nevada, U.S.A.: J. Struct. Geol., v. 13, p. 165–176.

Appendix

Contents

A Hypocenter locations

In the following chapter, we describe the estimation of hypocentral locations based on recorded acoustic emission (AE) waveforms and seismic velocities. We included a description of first arrival time estimates of *P*-waves using an AIC-picker (e.g. Kurz et al., 2005), as well as travel time inversion and hypocenter location estimates. Due to the large number of AE events within each experiments (up to hundreds of thousands) the basic processing steps were streamlined to run in an automated fashion for individual experiments.

A.1 AE arrival time picking

The estimation of seismic event locations depends on both the accuracy of the velocity model and the determination of first arrival times. The latter can be estimated, for example, through comparing the long and short- term-average (STA/LTA ratios) of windowed seismograms of natural earthquakes (e.g. Earle and Shearer, 1994). In contrast to natural earthquakes, both signal and noise of AE waveforms occupy similar frequency ranges (commonly in the kHz to MHz range), and signal-to-noise ratios, which vary throughout the failure processes, are low, thus complicating the usages of standard phase picking algorithms. An algorithm that provides reliable results under the described conditions is the autoregressive AIC-picker (e.g. Zhang et al., 2003; Kurz et al., 2005). The AIC-picker is very accurate if the prospective phase is the strongest arrival (e.g. in case of a direct P-wave and small source-receiver distance), which is generally the case in our experiments, and if the algorithm is applied to short time windows of seismograms that contain the phase of interest. The AIC method assumes that the seismogram consists of locally stationary segments, each modeled as an autoregressive process, and that the signal-onset separates two different stationary processes (Sleeman and van Eck, 1999; Zhang et al., 2003).

We applied the AIC-picker to preselected seismogram segments that triggered the recording system due to exceeding a rock-type-specific amplitude threshold. The P-wave-onsets were then estimated within a 100 μs window containing the threshold-crossing by minimizing the AIC-function suggested by Maeda (1985):

$$\mathrm{AIC}(k) = k \cdot \log(\mathrm{var}(x[1,k])) + (N-k-1) \cdot \log(\mathrm{var}(x[k+1,N])), \tag{1}$$

where x is the amplitude vector, N represents the length of the seismogram, and k ranges through all

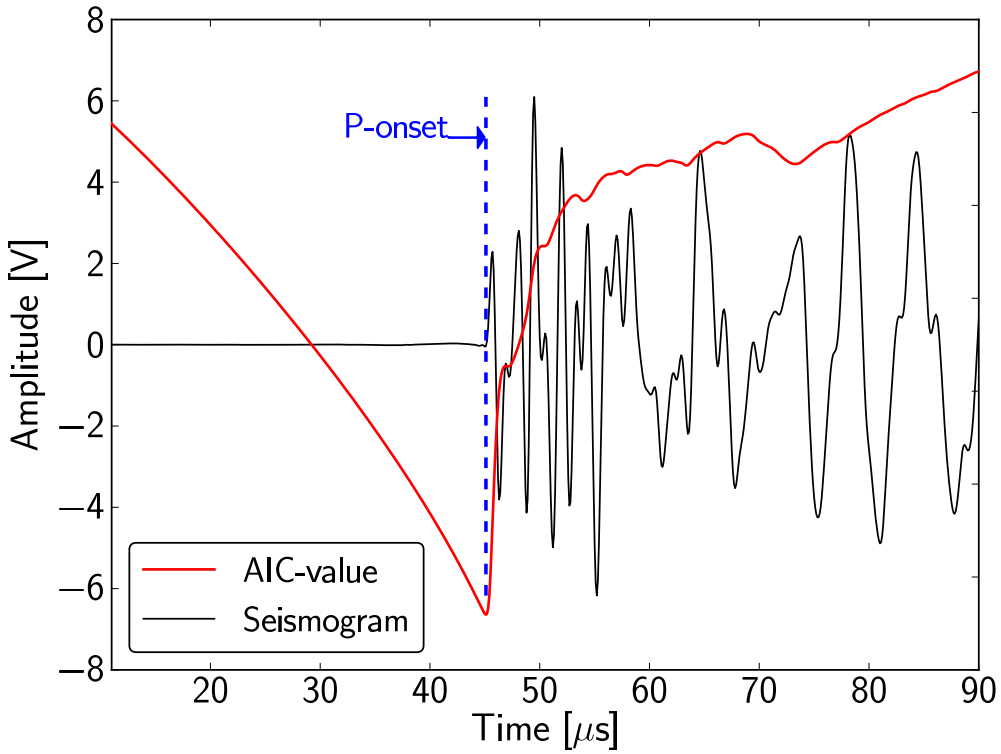

Figure A.1: Example of performance of autoregressive AIC-picker. The black curve represents the observed, bandpass-filtered (0.1–1.5 MHz) seismogram, red are the AIC-values and the blue dashed line is the determined P-onset.

seismogram-samples. We conducted a sensitivity test of the AIC function revealing improved results if applied to waveform envelopes, especially for seismograms with low signal-to-noise ratios. Figure A.1 represents an example of the AIC-picker performance for a time window that contains a clear P-onset of a waveform with high signal-to-noise ratio.

A.2 Travel-time computation

Besides accurate onset times, AE hypocenter locations are based on the estimation of travel times between candidate locations and each sensor of the seismic array. For the travel time computations, we used a layered, anisotropic velocity model and assumed direct, straight ray paths. Seismic velocities were measured directly using piezo-ceramic transducers as active sources. We generally observed a strong seismic anisotropy between radial and axial velocities. This anisotropy was most pronounced during large differential stresses

close to failure. We used five horizontal velocity and one vertical velocity trace to construct the velocity model. The angular dependency of the seismic anisotropy was determined from the measured velocities through elliptical interpolation:

$$r(\theta) = \frac{v_{\mathrm{ax}} v_{\mathrm{rad}}}{\sqrt{(v_{\mathrm{rad}} \cos\theta)^2 + (v_{\mathrm{ax}} \sin\theta)^2}}. \tag{2}$$

Here, v_{ax} and v_{rad} are the axial and radial velocities and r is the seismic velocity as function of take-off angle, θ.

A.3 Travel-time inversion

AE hypocenter locations were determined by minimizing the residuals between observed and synthetic travel times. To this end, we used a downhill simplex algorithm (Nelder and Mead, 1965; Press et al., 1992) which determines local or global minima by following the steepest gradient of the travel time residual close to an initial hypocenter location. An elegant choice of initial hypocenters is crucial to facilitate rapid convergence and can prevent incorrect results due to local minima. Thus, a combination of different algorithms (e.g. grid-search and simplex) for initial hypocentral guesses and subsequent refinements is advisable. For more details about AE event picking and AE hypocenter determinations see Stanchits et al. (2006). Following (Lockner et al., 1991), we required P-onsets of at least 8 stations and a travel time residual of 0.5 μs or less for a successful hypocenter location. Our observed travel time residuals follow a normal distribution with a mean at 0.1 μs for saw-cut experiments and a mean at 0.18 μs for the saw-cut guided fracture experiments (Figure A.2). This difference in travel time residuals is related to the broader damage zone connected to natural fracture surface which influenced local seismic velocities and the accuracy of AE event locations.

A.4 Hypocentral uncertainties

In the following, we will describe uncertainty estimates of onset times and hypocenter locations based on both observed and synthetic events. The latter consisted of up to 1056 events with array-specific travel times and random, Gaussian uncertainties of P-onsets. We determined the corresponding hypocenter locations using a combination of a grid-search and simplex algorithm. The distribution of synthetic travel time residuals

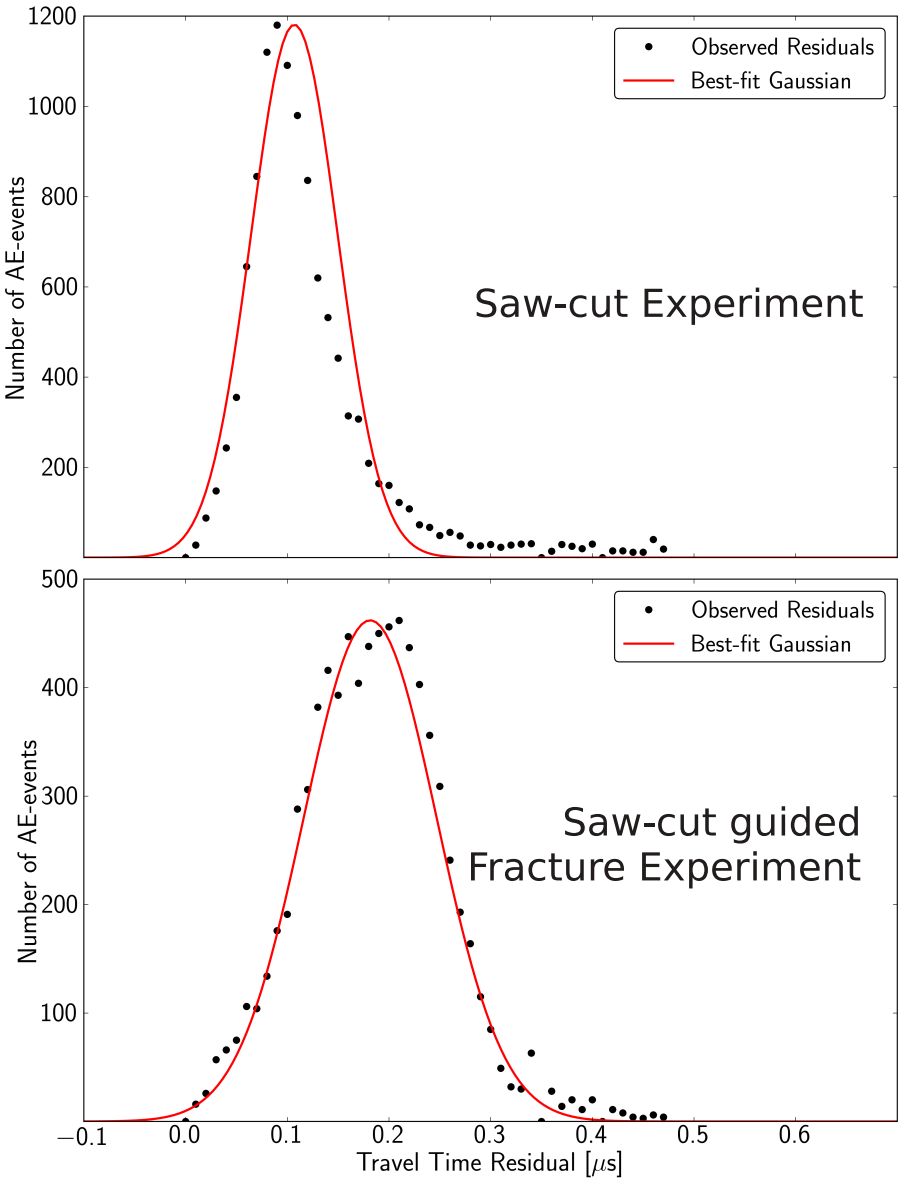

Figure A.2: Average travel time residuals of successfully located AE events (black dots) and Gaussian fit to the data (red curve). The top frame displays the observed travel time residuals for a saw-cut experiments and the bottom for a saw-cut guided fracture experiment.

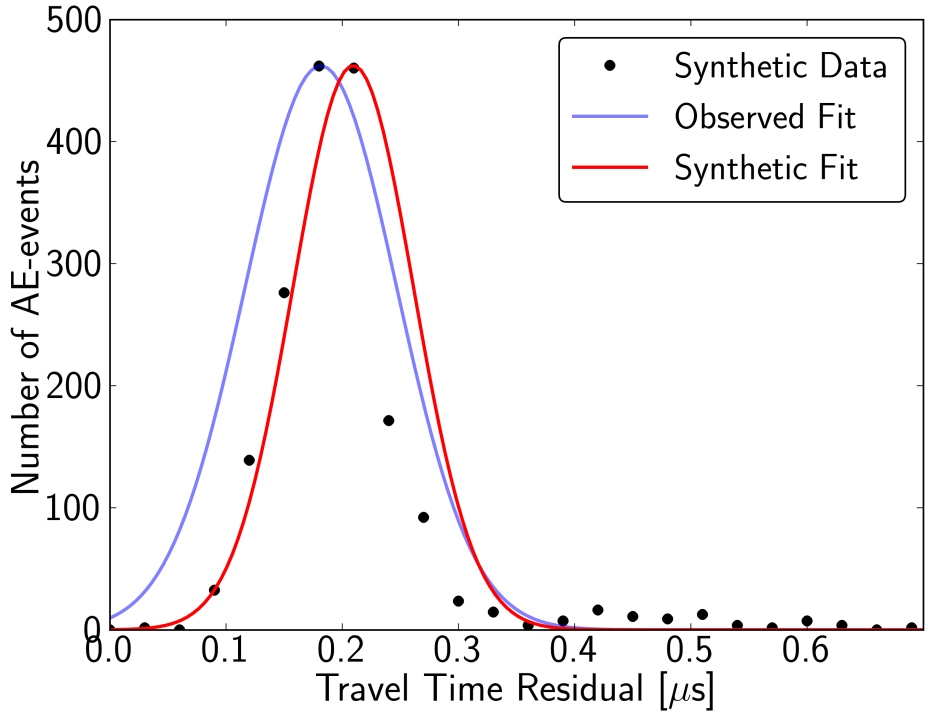

Figure A.3: Distribution of synthetic travel time residuals (black markers) for a pick uncertainty of 0.2 μs which can be described by a Gaussian distribution (red curve). The distribution of synthetic travel time residuals is very similar to the observations (blue curve), thus providing a rough estimate of the expected errors in AE hypocenters.

followed a normal distribution with a mean and standard deviation that were comparable to those of the observed data (Figure A.3). The picking uncertainties for these data was 0.2 μs, which is within the expected range for the observed data.

The uncertainties of the synthetic locations, i.e. the difference between initial hypocenters and hypocenters determined by travel time inversion, could also be described by a normal distribution with a mean at $\approx$ 1.8 mm (Figure A.4). Besides the Gaussian shape, the distribution was characterized by a long tail consisting of few events with large errors resulting in a slight shift of the distribution-fit to higher residuals. Nevertheless, more than 90% of the data were located with a precision of 4 mm or higher. Based on the similarity between observed and synthetic travel time residuals, the hypocentral uncertainties of the synthetic tests can act as a guideline of expected errors within the AE locations. Consequently, we estimated the predominant hypocentral uncertainties between 0.5–4 mm with an average value of 1.8 mm.

The long tails of the synthetic distribution emphasize that, especially for large AE data sets, some outliers

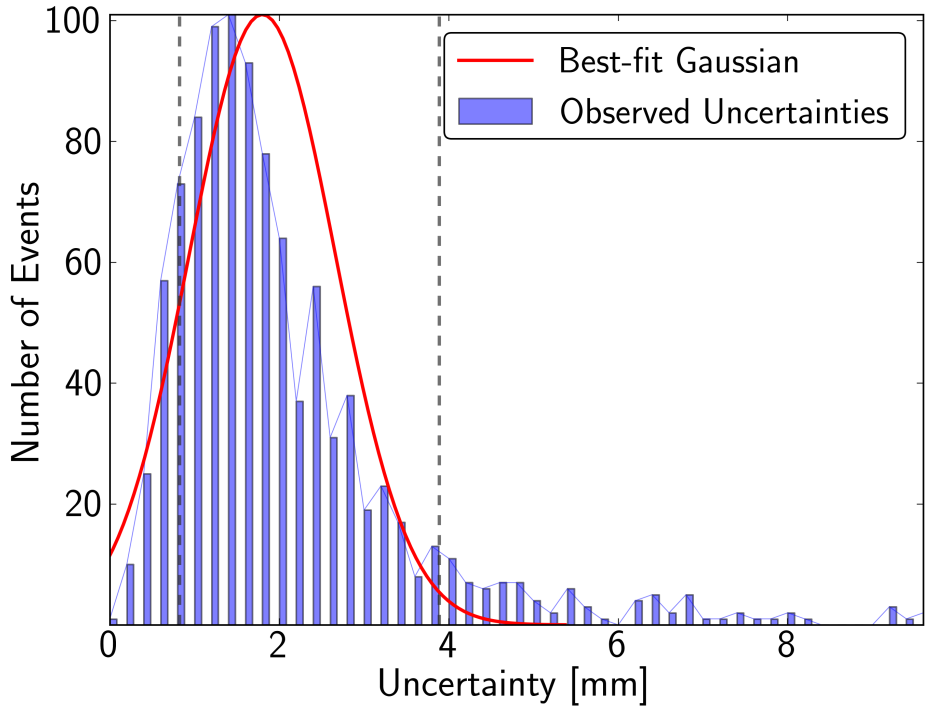

Figure A.4: Uncertainty estimates for the synthetic tests. The blue bars depict the uncertainty histogram and the red curve the corresponding Gaussian fit. The gray, dashed lines represent the 10 and 90 percentile of the data. The distribution of synthetic uncertainties can be described by a Gaussian but it also appears skewed toward larger uncertainties.

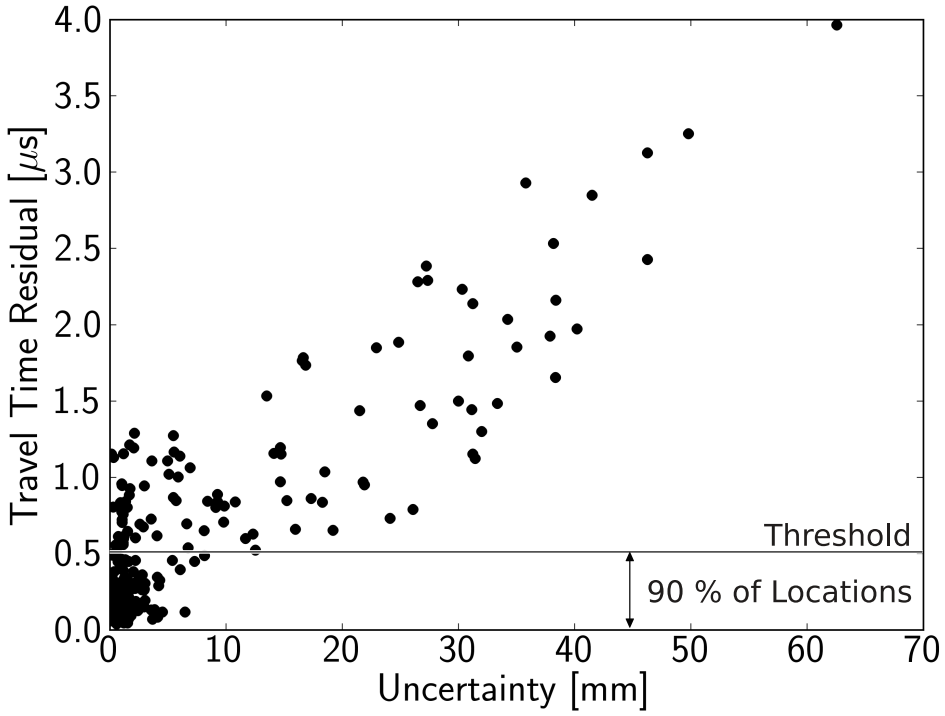

Figure A.5: Connection between travel time residuals and location uncertainty for a synthetic data set. The black horizontal line indicates the 90 percentile of the synthetic residuals which is at $\approx 0.49\ \mu s$. Increasing travel time residuals are generally connected to increasing hypocentral uncertainties. A specific choice of maximum travel time residuals can reduce outliers and hence enhance the quality of the final AE catalog. Synthetic hypocenter locations with small uncertainties but relatively large travel time residuals are likely a result of large errors in origin times.

can be expected. To avoid including events with large errors, we used two additional criterion for successful hypocenter locations: (1) Since the expected volume of AE event locations (i.e. the sample size) is known, we constrained the inversion to locate events only within the sample volume. Alternatively, one could disregard AE locations outside the sample volume after locating the events. (2) Our synthetic tests revealed a general connection between travel time residuals and location uncertainties. Thus, we introduced a threshold of residuals which led to an exclusion AE hypocenters with large uncertainties. The synthetic tests revealed that a residual of 0.5 μs provided an adequate threshold to separate outliers from the bulk of successfully located events (Figure A.5). This result is in agreement with value suggested by (Lockner et al., 1991). A combination of criterion (1) and (2) ensures realistic locations with low residuals of AEs connected to failure processes.

Besides the uncertainty estimates based on synthetic data, we also computed hypocentral errors based

on known source locations. To this aim, we located ultra-sonic pulses emitted throughout the experiments and evaluated the corresponding deviation from the true sensor location (Zang et al., 1998). Based on this method, we estimated average hypocentral uncertainties of $\approx 1.7 \pm 1$ mm which is in agreement with our estimates from synthetic data sets and a previous study on different data sets (Stanchits et al., 2006). Further support for the reliability of these uncertainty estimates is provided through the analysis of off-fault seismicity distributions in Chapter 6. These distributions could be described by a convolution of a power-law and a normal distributions. The latter is connected to the hypocentral uncertainty and exhibited widths between 1.4–2 mm which is comparable to the other uncertainty estimates.

In summary, a combination of different methods enhances the reliability of our estimates for the hypocentral location uncertainty. Compiling the results from the three different methods average hypocenter uncertainties were between 1.4–2 mm.

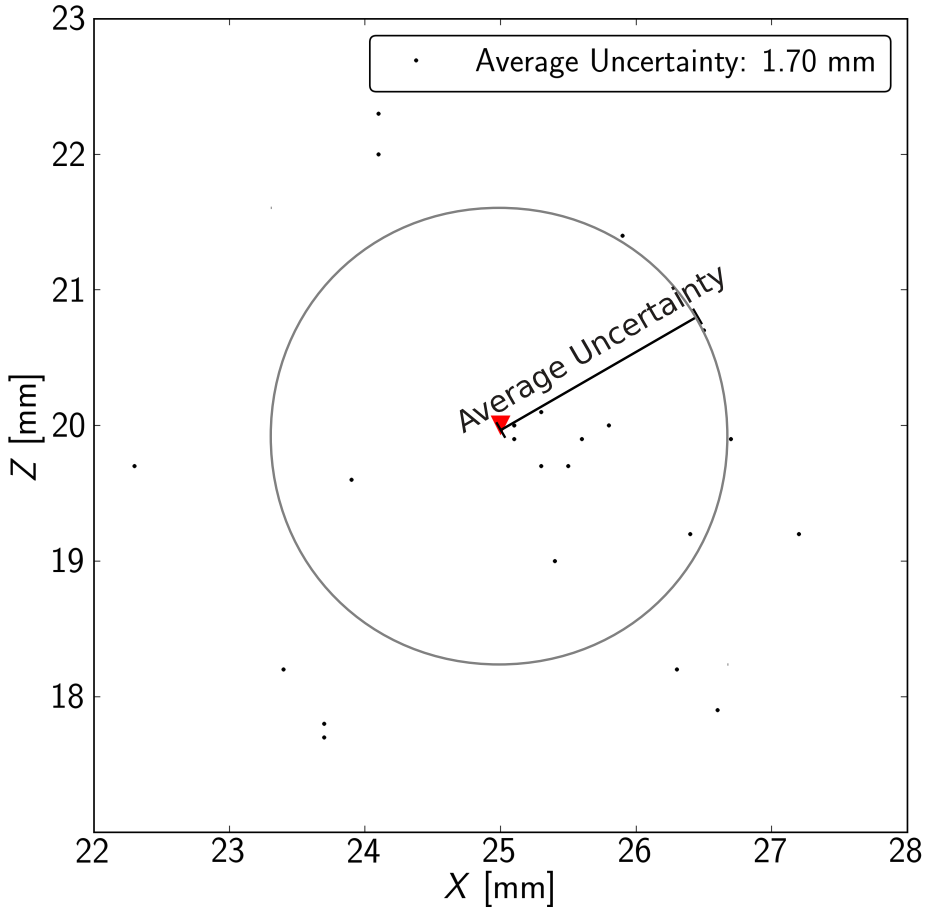

Figure A.6: Uncertainty estimates for one of the experiments using a transducer as pulse sender (red triangle). The small black dots represent the corresponding locations estimated by travel time inversion. The average uncertainty was 1.7 mm.

B Power-law estimates

B.1 Powerlaw distributions in seismological data

Powerlaw distributions arise in many circumstances and can indicate scale invariance of a variable or process. In seismology, powerlaw distributions are observed widely for natural and induced seismicity. For example, the frequency-magnitude distribution (e.g. Gutenberg and Richter, 1944), the rate decrease after mainshocks (e.g. Utsu et al., 1965), the spatial decay of seismic events from mainshocks (e.g. Felzer and Brodsky, 2006), the seismic event density decay away from a fault surface (e.g. Powers and Jordan, 2010) and the general distribution of hypocenters in space (e.g. Hirata, 1989; Wyss et al., 2004) can all be described by different power-laws.

A quantity x obeys a powerlaw if it is drawn from a probability distribution

$$p(x) \propto x^{-\alpha}, \tag{3}$$

where x is the independent variable and α is the powerlaw exponent. This distribution diverges for small values of $x \to 0$ so that it obeys a pure powerlaw only for value of $x \geq x_{\min}$. $x_{\min}$ will be called the minimum bound or minimum cut-off in the following.

B.2 Estimating the powerlaw exponent

There are two commonly used methods for the estimation of powerlaw exponents: (1) a least-squares fit of log-transformed data and (2) a maximum likelihood estimate. The second method should generally be preferred because it is less sensitive to fluctuations in the tail of the distributions (see Section B.6 for details). While least-squares fits may conform to the data in some cases, there are major draw backs in terms of estimating the powerlaw bounds and testing if the data actually obeys a powerlaw or should be described by a different distribution. The latter is addressed in Section B.5.

The maximum likelihood method generally estimates the parameter choices that will maximize the likelihood function of a given distribution for a set of observations. The log-likelihood function of continuously

distributed data that follows a powerlaw is (e.g. Clauset et al., 2009):

$$\begin{aligned} \ln(\mathcal{L}) &= \ln p(x|\alpha) = \ln \prod_{i=1}^{n} \frac{\alpha-1}{x_{\min}} \left(\frac{x_i}{x_{\min}}\right)^{-\alpha} \\ &= \sum_{i=1}^{n} \left[\ln(\alpha-1) - \ln x_{\min} - \alpha \ln \frac{x_i}{x_{\min}}\right] \\ &= n\ln(\alpha-1) - n\ln x_{\min} - \alpha \sum_{i=1}^{n} \ln \frac{x_i}{x_{\min}} \end{aligned} \tag{4}$$

Here, $x_{\min}$ again is the minimum bound, α is the powerlaw exponent, n is the number of data points above $x_{\min}$, x_i are the observed values above $x_{\min}$. Maximizing the log-likelihood function gives the maximum likelihood estimate (MLE) for the powerlaw exponent (e.g. Newman, 2005; Clauset et al., 2009):

$$\alpha = 1 + n \left[\sum_{i=1}^{n} \ln \frac{x_i}{x_{\min}}\right]^{-1}, \tag{5}$$

Thus, the MLE considers only the part of the distribution above $x_{\min}$ and depends on a correct estimate of the minimum bound of the powerlaw.

The expected statistical error in α is simply a function of the powerlaw exponent and the number of observations above $x_{\min}$ (e.g. Newman, 2005):

$$\sigma = \sqrt{n} \left[\sum_{i=1}^{n} \ln \frac{x_i}{x_{\min}}\right]^{-1} = \frac{\alpha-1}{\sqrt{n}} \tag{6}$$

The above described MLE for powerlaw exponents is strictly only valid for continuous data with exponents $\alpha > 1$. Both criteria are generally not met by frequency-magnitude-distributions (FMDs) of earthquakes, for which a different MLE was derived by Aki (1965) and Utsu et al. (1965):

$$b = \frac{1}{\overline{M} - M_c} \log(e), \tag{7}$$

where $\overline{M}$ is the mean magnitude, $e = \exp(1)$ and M_c is the magnitude of completeness corrected for bin size to account for a possible bias of discrete magnitude bin size (Utsu et al., 1965; Guo and Ogata, 1997). The

b value is then defined as the exponent of a FMD:

$$\log N = a - bM, \tag{8}$$

where N is the number of earthquakes with larger or equal magnitude than M and a is a constant representing the seismic activity. The expected statistical error in b is (Shi and Bolt, 1982):

$$\sigma(b) = \frac{b^2}{\log e}\sqrt{\sum_{i=1}^{n}(M_i - \overline{M})^2/n(n-1)}. \tag{9}$$

Here, n is the sample size, M_i is the magnitude of individual seismic events and $\overline{M}$ is the mean magnitude for events greater or equal than M_c. The second term is simply the standard deviation of $\overline{M}$, assuming that mean magnitudes of FMDs follow a normal distribution.

There are several ways to depict powerlaw distributed data. A commonly used method is to show a histogram of the incremented data and to infer a possible powerlaw distribution from an apparent linearity of the observations plotted on logarithmic scales. To avoid large fluctuations within the distribution tail one can choose varying bin sizes, for example, logarithmic bins so that the bins occur equally spaced on logarithmic scales. In case of logarithmically binned data, one has to correct the number of events in each bin by the corresponding width of the bin (Newman, 2005; Amitrano, 2012). A generally more effective way to represent the data is by computing its cumulative distribution, which protects from common binning artifacts within the previous methods. One has to be cautious when comparing exponents of cumulative and non-cumulative distributions. In case of the later, integration of the discrete density function preserves the powerlaw but the exponent appears shifted by -1 (Newman, 2005). The difference in exponents between incremental and cumulative distribution functions is traditionally not observed for FMDs because, following Gutenberg and Richter (1944), the data is represented on a semi-logarithmic scale with linear bin sizes which preserves the same b value in both cases (Amitrano, 2012). The actual powerlaw distributed quantities in this case are the frequency of events and the corresponding seismic energy or moment release (Wyss, 1973; Kagan, 1997; Amitrano, 2012).

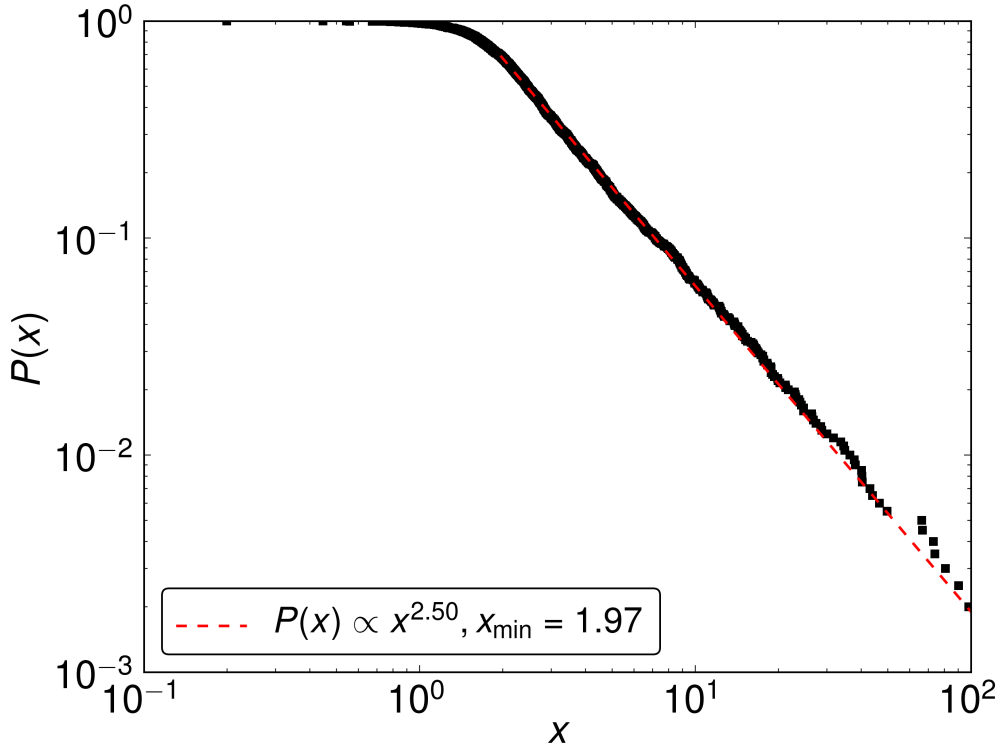

Figure B.1: Synthetic powerlaw data with exponent $\alpha = 2.5$, lower cut-off $x_{\text{min}} \approx 2$. The data follows a normal distribution below x_{min}.

B.3 Creating synthetic powerlaw distributions

In the following, I will describe briefly the creation of synthetic powerlaw distributed data which is invaluable when testing the performance of parameter estimates. To generate random numbers that follow a cumulative powerlaw distribution, one can use:

$$x = x_{\text{min}}(1-r)^{-1/(\alpha-1)}, \tag{10}$$

where r are uniformly, distributed random numbers, and x_{min} and α are the parameters that describe the powerlaw. In nature, one generally observes that the data below x_{min} is not powerlaw distributed. To simulate this behavior, one can convolve x in equation 10 with a normal or exponential distribution. The resulting data shows a powerlaw above x_{min} and a gradual deviation from the powerlaw below x_{min} (Figure B.1).

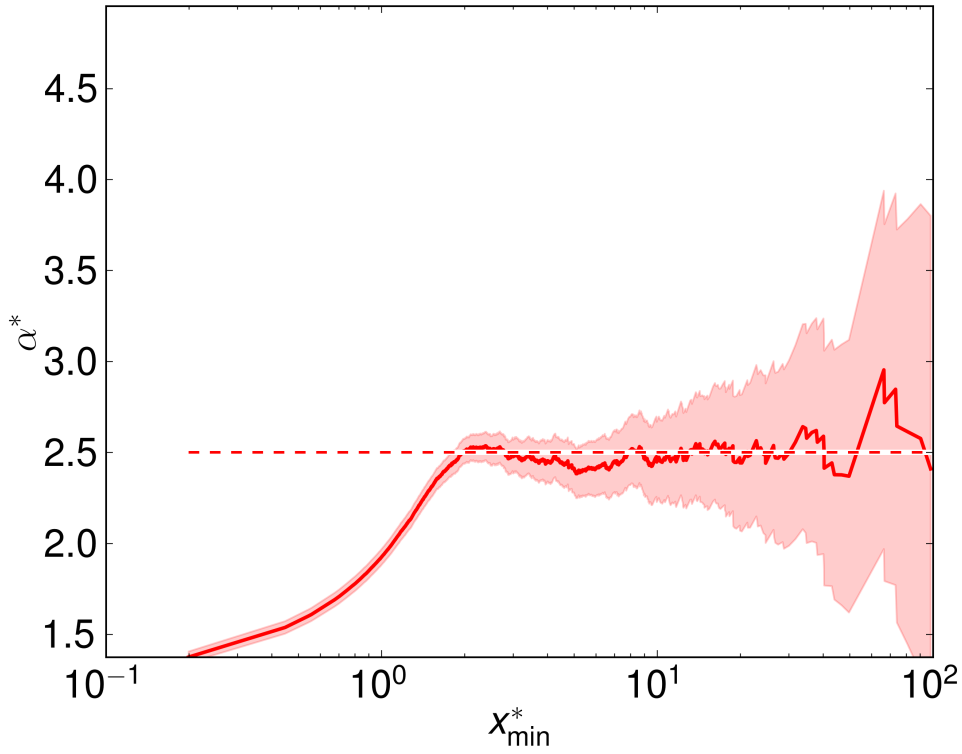

Figure B.2: A powerlaw distribution is characterized by the stability of the exponent α above x_{min}. Shown here are the values of α^* as function of different minimum cut-offs x^*_{min}. The actual value of α is indicated by the dashed line.

B.4 Estimating the lower bound of a powerlaw

The estimation of the powerlaw exponent requires an accurate determination of the lower bound of the powerlaw. Additionally, x_{min} can provide information about the underlying physical processes, for example, the range of scale invariance or the resolution limit of the recording system. A simple but useful way to approximate the minimum cut-off is to compute the powerlaw exponent as function of x_{min} using the MLE (Figure B.2). For a pure powerlaw, the exponent increases rapidly until x_{min} and reaches an approximately constant value above x_{min} over the extend of the powerlaw. Consequently, this method also enables a fairly accurate determination of α for well behaved power-laws. Moreover, plotting α over x_{min} shows characteristics of the distribution and reveals the extend of the powerlaw.

However, the analysis of large sets of powerlaw distributed data require an automated estimate of x_{min}. The possibly fastest and simplest way is by determining x_{min} from the bin with the largest number of data

points in an incremental distribution of the data. This point is generally connected to the maximum curvature of the incremental distribution (Wiemer and Wyss, 2000).

A more advanced method models the distribution of events below $x_{\min}$ using a normal cumulative function and the data above using a powerlaw (Woessner and Wiemer, 2005). The best model parameters are then found from the maximum likelihood estimate of the parameters of both powerlaw and normal distribution. It has been shown that this method performs significantly better than using the maximum curvature method.

The possibly most favorable way to estimate $x_{\min}$ is to include a measure of goodness of fit in the determination of powerlaw exponents. One way to accomplish this is by using the Kolomogorov-Smirnov (KS) distance to evaluate the performance of fits computed for different potential value of $x_{\min}$ between x_i–x_n (Clauset et al., 2009). The KS distance describes the maximum distance between two different continuous, cumulative distributions, here the observed and modeled distributions. It provides an estimate of the probability that both observations are drawn from the same parent distribution assuming that all samples are independent (Woessner and Wiemer, 2005) (the null hypothesis is that both samples are drawn from the same distribution). The best-fit between modeled, powerlaw distribution and observation will minimize the KS distance at the point $x_i = x_{\min}$ which is the minimum cut-off.

B.5 Performance of parameter estimates

The above described methods provide the best parameter estimates for the observed data assuming that the data is indeed powerlaw distributed. To test if this hypothesis is correct one can compare the observations with model realizations based on the estimated parameters $x_{\min}$ and α. To this end, one can use Monte-Carlo re-sampling to create different model representation, compute the KS-statistics and compare it to the KS-statistic of the observed data set (Clauset et al., 2009). The goodness-of-fit (p-value) is then simply the fraction of cases for which the synthetic KS-distances are larger than the empirical distance. Large p-values (e.g. above 0.1 or 0.05) suggest that a powerlaw distribution is a plausible hypothesis whereas small p-values would require a rejection of the powerlaw hypothesis. The failure to reject a possible powerlaw distribution does not indicate that it is indeed the best model for the data and other distribution functions (e.g. exponential or log-normal distributions) may have to be tested, for example, by using a likelihood ratio

test (Clauset et al., 2009).

B.6 Least-squares vs. maximum-likelihood estimates

In this section, we briefly compare the performances of least-squares and maximum likelihood fits. A more extensive study of the two methods can be found in Clauset et al. (2009) and Amorese et al. (2010). We computed series of synthetic distributions using equation 8 with a fixed value $x_{\min} = 1.5$ and powerlaw exponent $\alpha = 1.5$. We varied the sample size (N) of the distributions between 50 and 950, and used Monte Carlo re-sampling to determine the spread of the estimated powerlaw exponents at each sample size for both least-squares and MLE (Figure B.3). Expectedly, both methods show the largest spread of estimated exponents for low sample sizes. For large sample sizes the estimated powerlaw exponents localize closer to its true value. The least-square fits underestimates the true exponent at all sample sizes, probably due to variations in the distribution's tail, and shows an error of ≈ 0.1 for $N \leq 200$. The MLE, on the other hand, provides and accurate estimate of α for $N > 50$ as well as a generally smaller spread in the powerlaw exponents.

This simplistic test shows that MLE should generally be preferred due to its superior accuracy even at small sample sizes. Furthermore, the accurate determination of the minimum cut-off and goodness-of-fit tests both rely on maximum likelihood estimates (Woessner and Wiemer, 2005; Clauset et al., 2009). This is a severe short-coming of the least-squares method which may provide an acceptable fit to the data at large sample sizes but fails to provide means of evaluating the data-fit or for testing the powerlaw hypothesis.

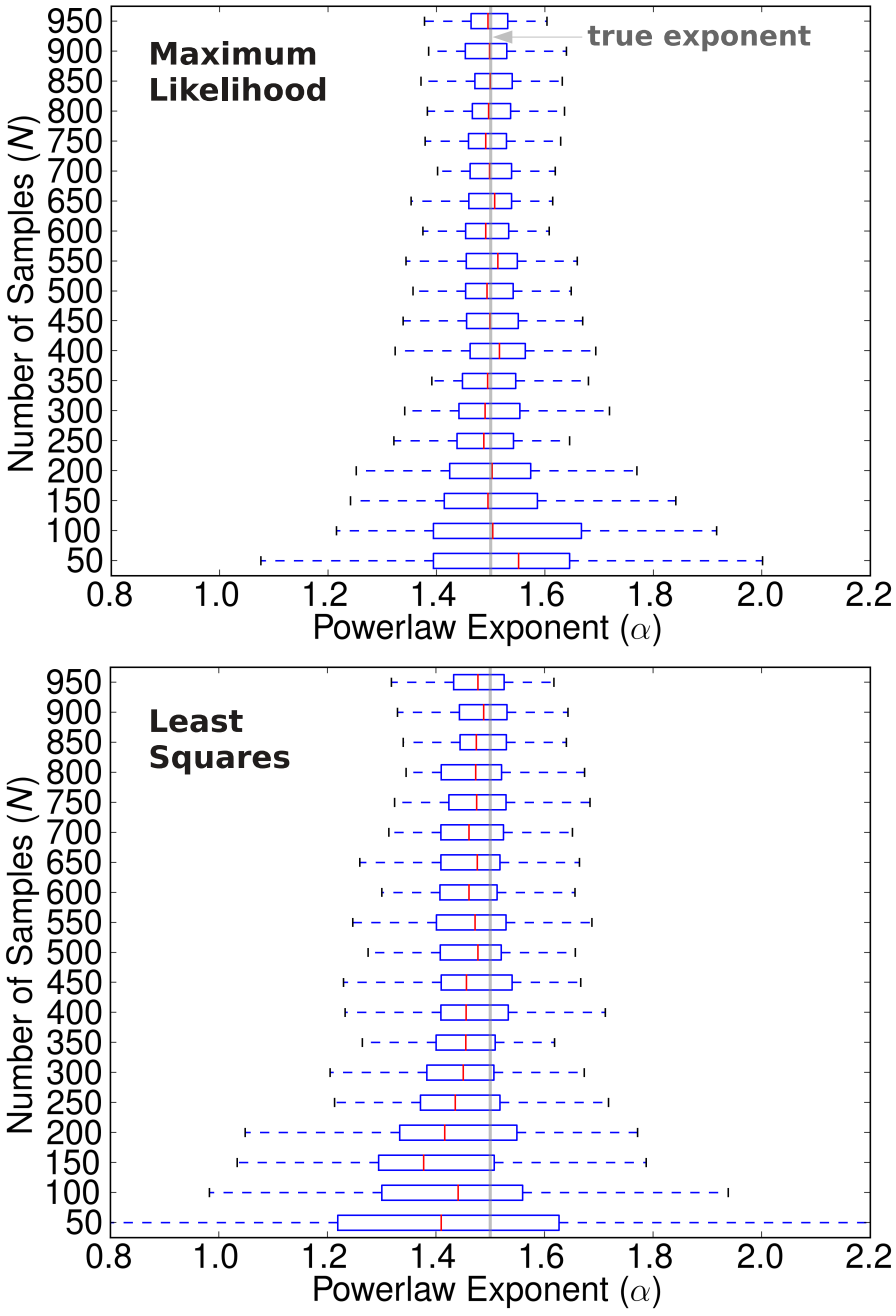

Figure B.3: Comparison between least-squares (bottom) and maximum likelihood (top) estimates of powerlaw exponents. The powerlaw distributed data was created by randomly sampling events between $N = 50$–950 using equation 10 and re-sampling each powerlaw distribution 100 times. The box-plot depicts the range (whiskers) of exponents of the re-sampled synthetic distributions, the 25 and 75 percentile (horizontal box extent) and the mean value of the exponents (red dashes). The true exponent used to create the synthetic powerlaw is indicated by the vertical gray lines.

References

Aki, K. 1965. Maximum likelihood estimate of b in the formula $\log N = a$ - bM and its confidence limits. *Bull. Earthquake Res. Inst., Tokyo Univ.* 43: 237–239.

Amitrano, David. 2012. Variability in the power-law distributions of rupture events. *The European Physical Journal Special Topics* 205 (1): 199–215.

Amorese, D., J. R. Grasso, and P. A. Rydelek. 2010. On varying b-values with depth: results from computer-intensive tests for Southern California. *Geophys. J. Int.* 180 (1): 347–360.

Clauset, A., C. R. Shalizi, and M. E. J. Newmann. 2009. Power-law distributions in empirical data. *SIAM review* 51 (4): 661–703.

Earle, Paul S., and Peter M. Shearer. 1994. Characterization of global seismograms using an automatic-picking algorithm. *Bull. Seismol. Soc. Am.* 84 (2): 366–376.

Felzer, K. R., and E. E. Brodsky. 2006. Decay of aftershock density with distance indicates triggering by dynamic stress. *Nature* 441. doi:10.1038/nature04799.

Guo, Z., and Y. Ogata. 1997. Statistical relations between the parameters of aftershocks in time, space, and magnitude. *J. Geophys. Res.* 102 (B2): 2857–2873.

Gutenberg, B., and C. F. Richter. 1944. Frequency of earthquakes in California. *Bull. Seismol. Soc. Am.* 34: 185–188.

Hirata, T. 1989. A correlation between the b value and the fractal dimension of earthquakes. *J. Geophys. Res.* 94: 7507–7514.

Kagan, Y. Y. 1997. Seismic moment-frequency relation for shallow earthquakes: Regional comparison. *J. Geophys. Res.* 102 (B2): 2835–2852.

Kurz, Jochen H., Christian U. Grosse, and Hans-Wolf Reinhardt. 2005. Strategies for reliable automatic onset time picking of acoustic emissions and of ultrasound signals in concrete. *Ultrasonics* 43 (7): 538–546.

Lockner, D., J. D. Byerlee, V. Kuksenko, A. Ponomarev, and A. Sidorin. 1991. Observations of quasistatic fault growth from acoustic emissions. *Fault Mech. Transport Properties of Rocks*.

Maeda, Naoki. 1985. A method for reading and checking phase times in auto-processing system of seismic wave data. *Zisin = Jishin* 38: 365–379.

Nelder, John A., and Roger Mead. 1965. A simplex method for function minimization. *The computer journal* 7 (4): 308–313.

Newman, Mark E. J. 2005. Power laws, Pareto distributions and Zipf's law. *Contemporary physics* 46 (5): 323–351.

Powers, P. M., and T. H. Jordan. 2010. Distribution of seismicity across strike-slip faults in California. *J. Geophys. Res.* 115. doi:10.1029/2008JB006234.

Press, William H., Brian P. Flannery, Saul A. Teukolsky, and William T. Vetterling. 1992. *Numerical recipes in FORTRAN 77: The art of scientific computing*, Vol. 1. Cambridge university press.

Shi, Y., and B. A. Bolt. 1982. The standard error of the magnitude-frequency b-value. *Bull. Seismol. Soc. Am.* 72: 1677–1687.

Sleeman, R., and T. van Eck. 1999. Robust automatic P-phase picking: an on-line implementation in the analysis of broadband seismogram recordings. *Phys. Earth Planet. Interiors* 113: 265–275.

Stanchits, S., S. Vinciguerra, and G. Dresen. 2006. Ultrasonic velocities, acoustic emission characteristics and crack damage of basalt and granite. *Pure Appl. Geophys.* 163: 975–994.

Utsu, T., Y. Ogata, and M. Ritsuko. 1965. The centenary of Omori formula for a decay law of afterhock activity. *Journal of Physics of the Earth* 43: 1–33.

Wiemer, S., and M. Wyss. 2000. Minimum magnitude of completeness in earthquake catalogs: Examples from Alaska, the western United States and Japan. *Bull. Seismol. Soc. Am.* 90 (4): 859–869.

Woessner, J., and S. Wiemer. 2005. Assessing the quality of earthquake catalogues: Estimating the magnitude of completeness and its uncertainty. *Bull. Seismol. Soc. Am.* 95 (2): 684–698. doi:10.1785/0120040007.

Wyss, M. 1973. Towards a physical understanding of the earthquake frequency distribution. *Geophys. J. Roy. Astr. Soc.* 31: 341–359.

Wyss, M., C. G. Sammis, R. M. Nadeau, and S. Wiemer. 2004. Fractal dimension and b-value on creeping and locked patches of the San Andreas fault near Parkfield, California. *Bull. Seismol. Soc. Am.* 94: 410–421.

Zang, A., F. C. Wagner, S. Stanchits, G. Dresen, R. Andresen, and M. A. Haidekker. 1998. Source analysis of acoustic emissions in Aue granite cores under symmetric and asymmetric compressive loads. *Geophys. J. Int.* 135: 1113–1130.

Zhang, Haijiang, Clifford Thurber, and Charlotte Rowe. 2003. Automatic P-wave arrival detection and picking with multiscale wavelet analysis for single-component recordings. *Bull. Seismol. Soc. Am.* 93 (5): 1904–1912.